Experimental Characterization of Combustion Instabilities and Flow-Flame Dynamics in a Partially-Premixed Gas Turbine Model Combustor

by

Patton Manuel Allison

A dissertation submitted in partial fulfillment
of the requirements for the degree of
Doctor of Philosophy
(Aerospace Engineering)
in The University of Michigan
2013

Doctoral Committee:

Professor James F. Driscoll, Co-Chair
Assistant Professor Matthias Ihme, Co-Chair, Stanford University
Assistant Professor Mirko Gamba
Professor Volker Sick

© Patton M. Allison 2013
All Rights Reserved

For my Parents,
Who taught me not to play with fire,

and

Wally

ACKNOWLEDGEMENTS

It is amazing to me how much support is required for a person to get this point in their academic careers, whether the support is physical, emotional, informational, or financial. I am extremely grateful to have been given all this and more by those who have guided me along the way, especially when the path was unclear.

First and foremost, I must thank my parents for their continuous aid and encouragement throughout my entire life. I have always felt loved, supported, and motivated to do better because of them. They have always been there to raise me back up at my lowest points and celebrate my brightest moments. I hope that this thesis is a reflection of their commitment to my growth and education because without them I would still be on page one. If my mother has taught me anything, it is to always be thankful for the kindness and help I receive from others. If I stand tall, it is not because of my genes, but because of the support and dedication of others.

I have had amazing mentors during my time at Michigan. Professors who have reshaped the way I think about academia and research, in the best of ways. Professor Driscoll has been the greatest resource for both scientific and professional guidance, and I am lucky to have been part of the support system he calls his lab group. I must also thank Professor Driscoll for his continued financial support of my studies, research, and travel. I have been able to work with state-of-the-art equipment and meet the great minds of our field, all over the world because of him. Professors Ihme and Gamba have spent hours of time helping me reason out complex thoughts regarding my project, and have provided insight both in and out of the lab. I must also thank my advisor at Georgia Tech, Dr. Jerry Seitzman. Without his guidance, I would have never fallen in love with combustion and experimental work, particularly the parts involving lasers.

The support staff at Michigan has also made research a much more pleasant experience. The technicians of FXB including Tom Griffin, Dave McLean, Terry Larrow, Eric Kirk, Chris Chartier and Aaron Borgman, have been a great resource for research support. I must thank them for all times they helped me whole-heartedly at 4:30 on a Friday afternoon. If I have met all the requirements of the PhD program, it is only because Denise Phelps has been there to remind me what I needed to get done. She let me focus on the science while she dealt with the red tape. I must also thank Cindy Enoch and Kristin Parrish for all their help regarding the accounting and purchasing of the hundreds of thousands of dollars of equipment that went into my project.

Finally, I must thank my close friends and family, who have motivated and encouraged me the whole way here. I must especially thank my fellow graduate students who have flourished and suffered through graduate school along with me, including Jacob Temme, David Rosenberg, Matt Fotia, Yuntao Chen, Derek Dalle, Aaron Skiba, Tim Wabel, Yasin Abul-Huda, and Robin Klomparens. They have been a great source of insight and have provided welcomed stress relief with nights at Ashley's. May we have many more of those.

To Brianne, she has been my constant champion through to the end. Always understanding of my night owl work habits and my late nights in the lab. Always checking to see if I had remembered to eat and sleep. Always ensuring I stayed positive and motivated to keep moving forward. Always giving 110%, when I could only give 90%, I am blessed to have her love.

Last but not least, I must thank Wally, because he makes all things at the end of the day bearable.

TABLE OF CONTENTS

CHAPTER

LIST OF FIGURES

Figure

LIST OF TABLES

Table

NOMENCLATURE

Symbols

a	POD Temporal Coefficients
A	Cross Sectional Area
c	Speed of Sound
C_p	Specific Heat at Constant Pressure
Da	Damköhler Number
f	Frequency
h	Axial Distance from Burner Face
I	Chemiluminescence Intensity
I_0	Stretch Factor
ℓ	Integral Length Scale
L	Length
Le	Lewis Number
M	Mach Number
Ma	Markstein Number
$\dot{m}$	Mass Flow-rate
P	Pressure
$\dot{Q}$	Heat Release Rate
r	Radial Distance from Centerline
R	Characteristic Outer Radius
R_g	Gas Constant
RI	Rayleigh Index
S	Swirl Number
S_L	Laminar Flame Speed
S_T	Turbulent Flame Speed
St	Strouhal Number
t	Time
T	Temperature
u	Flow Velocity

Greek

β	POD Eigenvector
γ	Ratio of Specific Heats
Γ	Vorticity
δ_{L0}	Unstretched Laminar Flame Thickness
δ_T	Turbulent Flame Brush Thickness
ϵ	Fluid Dynamic Strain
ζ	Time Coordinate Normalized by the Period of a Thermoacoustic Cycle
η	Coordinate Normal to Flame Brush
ξ	Reactedness = (T-T_R)/(T_P-T_R)
Ξ	Plenum-Chamber Coupling Index
υ	Fractional Significance of a POD Mode
Υ	Significance of a Given POD Mode
ϕ	Fuel-Air Equivalence Ratio
Φ	POD Basis Function
ρ	Fluid Density
Σ	Flame Surface Density
τ	Time Lag
Ψ	Surface Area Factor
ω	Chemical Source Term
Ω	Wrinkling Parameter

Subscript

0	Unstretched Condition
b	Burned Mixture
k	Image Number
L	Laminar
m	POD Mode Number
o	Stagnation
P	Products
R	Reactants
T	Turbulent
u	Unburned Mixture

Superscript

$'$	Fluctuating Component
$\dot{}$	Varying per Unit Time
$\bar{}$	Mean Component

Acronyms

CRZ	Central recirculation zone
DME	Dimethyl ether
DNS	Direct numerical simulation
FFT	Fast Fourier transform
FOV	Field of view
FSD	Flame surface density
FWHM	Full width half maximum
GTMC	Gas turbine model combustor
HSPLIF	High speed laser-induced fluorescence
LBO	Lean blowout
LES	Large eddy simulation
LDV	Laser doppler velocimetry
ORZ	Outer recirculation zone
PAH	Polycyclic aromatic hydrocarbons
pdf	Probability density function
PIV	Particle image velocimetry
PLIF	Planar laser-induced fluorescence
POD	Proper orthogonal decomposition
PSD	Power spectral density
PVC	Precessing vortex core
rms	Root mean square
ROI	Region of interest
ORZ	Outer recirculation zone

CHAPTER I

Introduction and Theoretical Background

1.1 Background and Motivation

Reduction of NO_X emissions has driven both aero and aero-derivtive engines designs toward the use of premixed or partially-premixed schemes. Further reduction of NO_X is achieved through lean operation [1]. Lean fueling results in lower flame temperatures, which aids in the prevention of thermal NO_X formed at temperatures over 1800K [2]. As well, if the residence time of the combustor is kept to a minimum, NO_X formation is reduced. Swirl flames are the primary combustion application in gas turbine engines. They enable heat release in a compact fashion, and allow for stabilization and ignition over a wide range of fueling conditions [3, 4]. Swirling flames create high turbulence levels conducive to good mixing, which allows for smaller and shorter combustors. However, operation in this regime is highly susceptible to combustion instabilities. Despite the combustor being one of the most efficient components of the gas turbine engine [5], operational efficiency can be decreased through uneven burning, hotspots, and increased emissions. These instabilities lead to thermoacoustic oscillations as well as destabilization of the flame. As a result of these oscillations, damage can occur to the fuel injector and combustor lining due to large pressure fluctuations.

Combustion instabilities present complex cases of coupling between pressure fluctuations, velocity fluctuations, and heat release fluctuations [6]. In order to be able to successfully apply lean premixed technology to gas turbine based engines, further study is needed to evaluate the behavior and control of instabilities. However, full scale studies of these instabilities present economic, diagnostic, and computational difficulties. Ideally, gas turbine engines would be designed with computational fluid dynamics (CFD). However, many current computational models cannot accurately capture some of the dynamic effects presented through thermoacoustic oscillations and complex flowfield coupling that occurs with the flame.

In order to create better models of these interactions, physical experiments must be carried out which directly evaluate such behaviors. Thus it is far more feasible to study the possible coupling mechanisms on small scale laboratory gas turbine combustors, which are typically representative of only a single fuel nozzle and combustor chamber combination. These smaller combustor setups allow for easier investigations into potential instability mechanisms and flow-flame dynamics. Computational modeling is also greatly simplified at smaller scales with reduced computational cost. Laboratory scale devices have practical relevance in that they can be studied using non-intrusive diagnostics with high accuracy [7]. The collected data can then be used for validation of simulations.

In practical operation, purely premixed combustors are also plagued by global flashback and blowoff issues. Premixed flames also tend to be anchored directly to the fuel injector, which can lead to large amounts of heat transfer and structural damage to the injector face. These scenarios create safety and performance reliability concerns. In order to circumvent some of these problems, partially-premixed systems are applied in which the fuel and air is initially injected separately, and then mixed quickly before burning by employing combinations of swirl, high shear, and turbulence. As well, increasing the time to mix between the injector and flame base will assist in the degree of premixedness achieved. Partially premixed flames can have stratified levels of mixing in which the local equivalence ratio varies spatially. With varying local heat release structure, fluctuating pressure fields may also occur, leading to thermoacoustic oscillations. However, partial premixing provides a middle ground between the emissions and safety/heating concerns respectively involved with purely non-premixed and premixed operation

Partially premixed systems create complex mixing patterns which are difficult to model. Many large eddy simulation (LES) tactics involve modeling the subgrid combustion as either premixed or non-premixed [8–11]. Partially premixed combustion can set up situations characterized by both flamelet techniques. Thus, careful experimental measurements are necessary to assist in the development of better computational models to predict this style of combustion.

1.2 Theoretical Understanding

Gas turbine combustors present a complicated combination of turbulence and combustion interactions. Swirling flow is the primary method for flame stabilization and enhancement of mixing. However, it can also lead to fluid mechanical instabilities like vortex breakdown and precessing vortex cores (PVCs). In combination with fluctuating pressure and velocity fields, combustion instabilities can occur which result in large scale heat release fluctuations. Swirling, turbulent flows are common to all gas turbine combustion studies; however instability presence can be combustor specific. Instabilities can be naturally present [12–15] or artificially induced through pressure field forcing with a loud speaker [16,17]. As well, the mechanism driving the instability can vary depending on the dynamics of turbulence-chemistry interactions and the presence of flow-flame coupling. This section aims to provide the background understanding for some of the underlying physics studied in this experimental work, as well as to shed light on some of the motivations behind these investigations.

1.2.1 Swirling Flows

1.2.1.1 Vortex Breakdown and Central Recirculation Zone (CRZ) Formation

Swirl flows are very important in the stabilization and enhancement of mixing in reacting flows due to the creation of a low velocity central recirculation zone (CRZ) and the formation of outer recirculation zones (ORZ) in confined flows. Recirculation development in swirl flows operates under the following principles [3, 4]:

A) A natural radial pressure gradient is formed due to variation in tangential velocities

B) Upon exiting a nozzle/injector, an axial decay of the tangential velocity occurs, furthering the radial pressure gradient

C) Decaying swirl velocity with flow expansion is necessary for the CRZ

D) Along the central axis of the flow, a negative axial pressure gradient occurs which induces reverse flow and forms a CRZ

E) Should the CRZ become unstable, PVCs can form

Figures 1.1 and 1.2 depict the structure of a flow with a developed CRZ and marked negative axial velocities. Figure 1.1 shows that there may be a PVC present in the shear layer that occurs between the recirculation zone and the downstream directed flow. Figure 1.2 shows an overlay of the tangential velocity field given in green and red, which depicts the swirling component of the flow. Note that the strongest velocities are measured in the shear layer between the CRZ and ORZ, where PVC motion is enabled. Precessing vortex core structures have been previously observed and studied [18] in the GTMC used in this work.

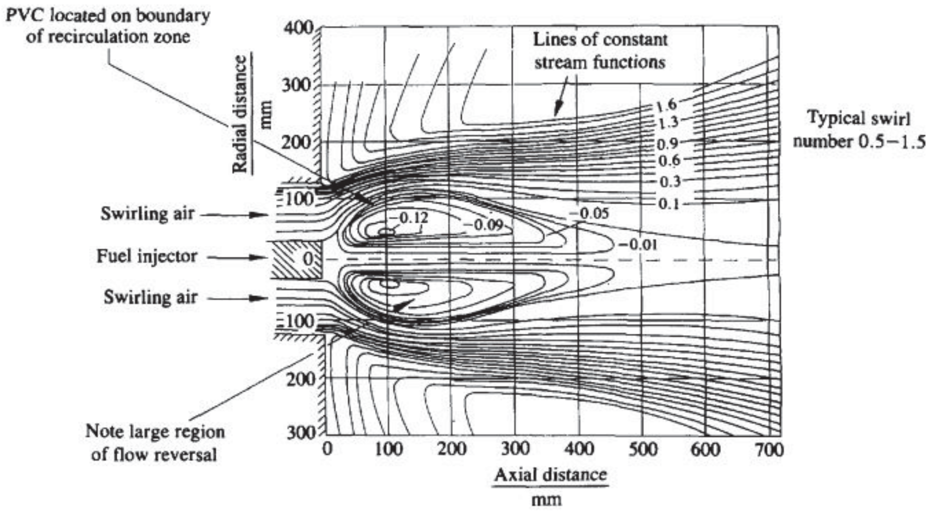

Figure 1.1: Stream distribution at swirl burner exhaust showing typical recirculation zone set up [19].

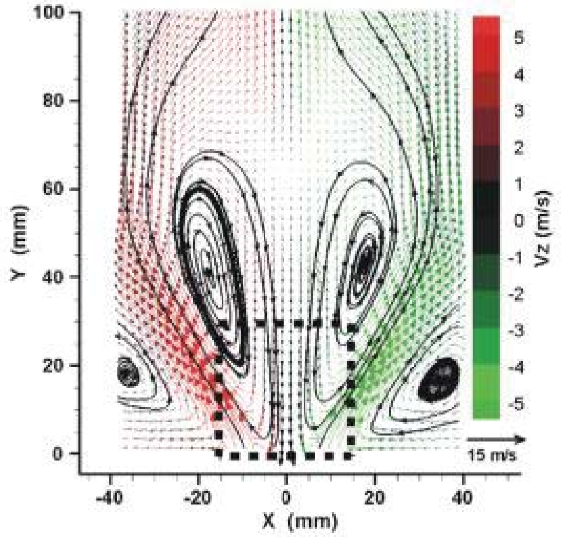

Figure 1.2: Formation of the central recirculation zone and outer recirculation zones due to swirling flow in the GTMC studied by Boxx et al. [20].

The creation of recirculation which transports fluid material back upstream in the combustor has been shown to have many beneficial effects including enhanced stability, as well as better mixing. Studies by Feikema et al. [21, 22] have shown that jet flames with swirling co-axial flows have extended blowout limits and overall lean conditions can be established with non-premixed flames if sufficient swirl is applied. Raman measurements in a premixed gas turbine combustor have shown that exhaust gases can be recirculated and mixed in with the incoming reactants leading to spontaneous ignition in the shear layer [23]. The combination of a low velocity region along with hot exhaust gas recirculation creates regions where the flame can be stabilized and easily sustained. An edge/triple flame can be established in these low strain zones [24].

1.2.1.2 Precessing Vortex Core (PVC) Development and Effects

For swirl numbers greater than 0.5, a central recirculation zone is formed along with the potential for a precessing vortex core. The swirl number, denoting the ratio of tangential to axial momentum flux, is given by:

$$S = \frac{\int_0^R \rho u \nu 2\pi r^2 \, dr}{R \int_0^R \rho u^2 2\pi r \, dr} \tag{1.1}$$

where ρ is the fluid density, u is the axial velocity, ν is the azimuthal velocity, r is the radial dimension, and R is the outer radius of the burner. The formation of a PVC is dependent on the swirl number, vortex breakdown inducing a CRZ, the method of fuel injection, combustor geometry, and the equivalence ratio [25]. Premixing or partial-premixing has been shown to increase the PVC strength while direct axial injection of the fuel has been shown to dampen its effects due to disruption of the shear layer outside the CRZ. If the vortex breakdown is asymmetric and unstable, it will begin to precess around the axis of symmetry. The PVC tends to initially form in the stagnation points caused by the CRZ and then is swept by the fluid motion forming a helical structure as seen in Figure 1.3.

This type of fluid instability can feed into flow-flame coupling and alter the heat release from the flame causing combustion instabilities. The helical motion of the

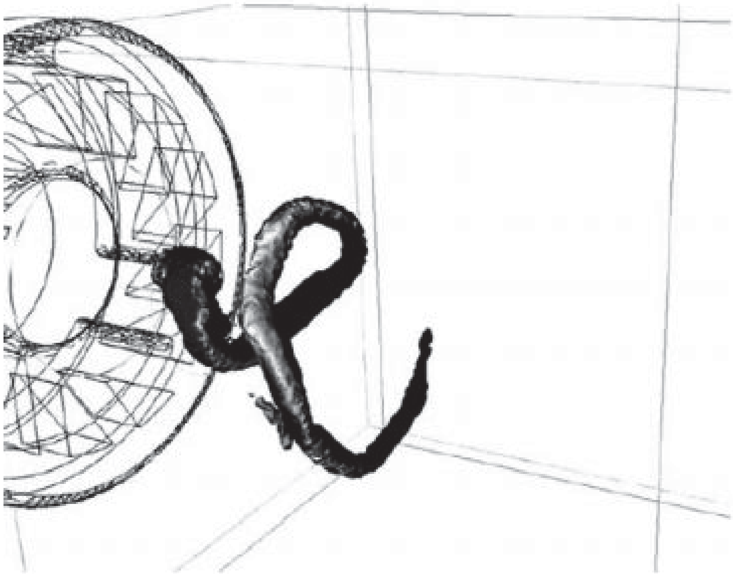

Figure 1.3: Isosurface of low pressure to visualize the isothermal PVC formed at the exit of the swirl burner [26].

PVC can induce a number of interactions such as flame roll up, flame surface area changes, and flame stretch. Stöhr et al. [18] showed that the PVC can interact strongly with the flame in the GTMC causing flame roll up which enhances the supply of hot product radicals to cold injected reactants, aiding in ignition. However, the PVC can also stretch the flame causing local extinction and disruption of the flame surface. It was seen that the balance between the degree of mixing and extinction was linked to the Damköhler number (Da), with increasing stretch occurring in lower Da flames. Decreasing Da causes the flame to extend axially and have elongated reaction zones due to local disruption lower at the flame base. The PVC instability frequency has also been seen to vary linearly with the bulk velocity of the flow [27]. However, even with increasing bulk velocity, the Strouhal number (St) of the flow remained constant relative to the precession rate. This is indicative the PVC is highly coupled with fluctuations convected from the nozzle.

The PVC can also induce large fluctuations in all velocity components which can lead to compression, extension, and wobble of the PVC itself. As well, swirl number fluctuations can cause unsteadiness in the flame and alter the evolution of flame shape and heat release, which depending on satisfaction of the Rayleigh criterion, can cause augmentation or dampening of a thermoacoustic oscillation. Varying swirl number will control the flame spreading angle and liftoff height [28]. According to studies by Palies et al. [29] swirl number fluctuations induced by the PVC can cause parts of the flame structure to interact constructively or destructively. According to the study axial fluctuations are acoustic in nature, while azimuthal fluctations are convective and directed from the swirler exit. Axial fluctuations can cause vortices to be shed from the swirler exit leading to flame rollup and changes in flame area. Combined axial and azimuthal fluctuations cause a breathing motion of the CRZ which is reflected in changes to the flame angle and turbulent flame speed.

While the PVC can affect the flame oscillations by causing alternating patterns of stratified equivalence ratio, the flame also can alter or even destroy the PVC. Suppression of the PVC can occur dependent on the radial location of the flame surface, the equivalence ratio, and the injector of the fuel [25]. Establishment of the flame front in the shear layer where the PVC typically forms will cause the flame stabilization point and the CRZ to move further downstream. This will weaken the CRZ and ultimately the PVC.

1.2.2 Turbulent Combustion Physics

Combustion in the GTMC is inherently turbulent due the nature of the swirling flow. Fluctuations in the velocity and pressure fields lead to wrinkling phenomena in the flame surface and contribute to the fluctuations in heat release which can cause the amplification of combustion instabilities. Turbulent combustion is categorized into premixed and non-premixed modes of operation. The GTMC is operated in a partially-premixed fashion, such that spatiotemporally, both premixed and non-premixed regions exist. Initially, fuel is injected in a non-premixed fashion. However, due to strong recirculation of product gases, swirl, and high shear between recirculation zones, mixing is enhanced and premixed states are quickly achieved. The fuel injector in the GTMC is recessed some 5mm from the burner surface; this distance aids in achieving a mixed state before reactants have been convected to the flame base [30].

While considering the premixed regimes as depicted by Peters [31], the flames examined in this combustor would fall into the "thin reaction zone" regime or into the "turbulent flame front" regime of Chen and Bilger's diagram [32]. Similarly, if non-premixed states are considered, the flames would fall into the "connected flame zones" of Peters non-premixed regime diagram [31] as seen in Figure 1.4. Studies at DLR Stuttgart have reported Reynolds numbers of 15,000 [33]. Given these types of characterizations of premixed flamelets, the analysis of flames discussed in this thesis will operate with the assumption that some degree of premixedness achieved. Reported equivalence ratios will correspond to global values because although the reactants may be thoroughly mixed, the equivalence ratio may spatially vary along the flame sheet. However, this analysis will applied to flamelets observed in a range of 5-30 mm above the injector exit. It is expected that this assumption will hold well particularly for flamelets further away from the injector, whose reactants have had sufficient time to mix.

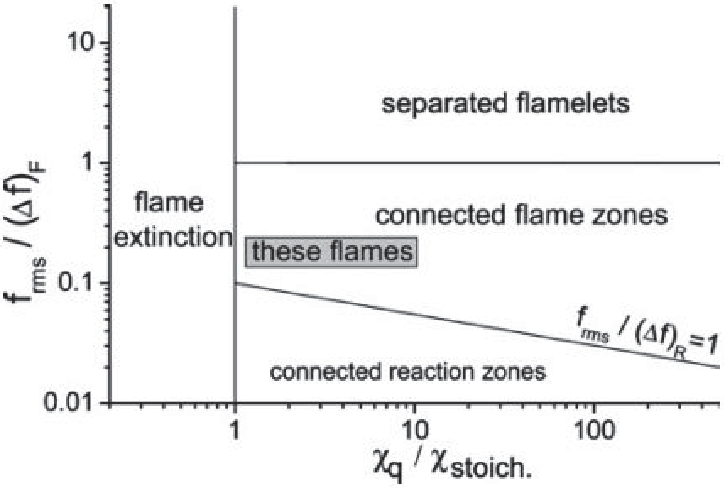

Figure 1.4: Regime diagram for turbulent non-premixed flames. Flames investigated lie within the boundary of the box in the connected region [31].

In Driscoll's [34] review of premixed turbulent combustion, the following relation for turbulent flame speeds is presented:

$$\frac{S_T}{S_{L0}} = I_0 \int_{-\infty}^{+\infty} \Sigma \, d\eta \tag{1.2}$$

$$\frac{S_T}{S_{L0}} \propto I_0 \Sigma_{max} \delta_T \tag{1.3}$$

where S_T is the turbulent burning velocity, S_{L0} is the unstretched laminar burning velocity, I_0 is the stretch factor, Σ is the flamelet surface area per unit volume, Σ_{max} is the maximum value of flamelet surface area per unit volume, η is the coordinate normal to the flame brush, and δ_T is the turbulent brush thickness. The turbulent flame speed is also seen to be a function of the following parameters:

$$S_T = f\left(\frac{u'}{S_{L0}}, \frac{\ell}{\delta_{L0}}, Ma_T\right) \tag{1.4}$$

where $u^{'}$ is the fluctuating component of the velocity, ℓ is the integral length scale, δ_{L0} is the unstretched laminar flame thickness, and Ma_T is the turbulent Markstein number. Finally the maximum flame surface density (FSD), Σ, can be related to the flame surface area by:

$$\Sigma_{max} = \frac{1}{\delta_T}\frac{A_T}{A_L} \tag{1.5}$$

where Σ_{max} is measured along the mean reactedness, $\bar{\xi} = 0.5$ contour at the center of the flame brush, as seen in Figure 1.5.

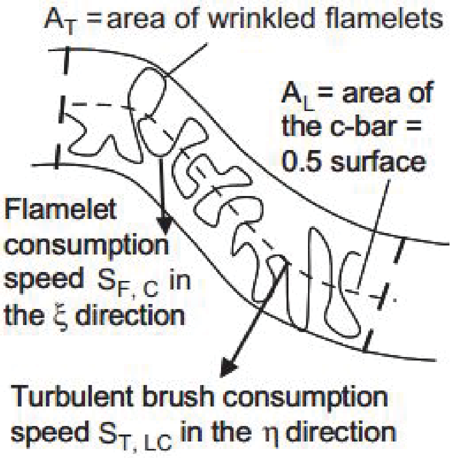

Figure 1.5: Schematic of the wrinkled area and the area of the $\bar{\xi} = 0.5$ contour at the center of the flame brush [34].

Given these relations, it can be seen that increases in the turbulence intensity as defined as the ratio of $u^{'}/S_L$, will lead to larger turbulent flame speeds which are correlated with increased turbulent flame surface areas and/or densities. However, this relation may also be considered from the other point of view. Fuels with higher laminar flames speeds will have larger turbulent flame speeds for a given turbulence intensity level, which implies that these fuels may also be characterized by having increased flame surface density. The chemical source term, proportional to the heat release, can then be modeled as follows [35]:

$$\bar{\dot{\omega}}_c = \bar{\rho}_u S_{L0} I_0 \bar{\Sigma} \tag{1.6}$$

which indicates that the mass flow of unburned mixture through the flame per volume per second is related to a given flame area propagating through the mixture at S_{L0}. This can be related to the heat release from a flame with the assumption that all of the unburned mixture is consumed as it passes through the flame. The final result from these equations is that the heat release from a flame is maximized with fast turbulent flame speeds created with high turbulent intensities and large flame surface densities. It is important to note that this source term can vary locally within a flame given that there are local variations in FSD and S_{L0}. Whereas FSD is altered by flame stretch due to gradients between the reactants and flame front, the local unstretched flame speed is altered by changes in the local reaction rate due to unequal diffusion of heat and unburned mixture [36]. As well, even for perfectly premixed mixtures, one cannot assume that the equivalence ratio will be convected as a plane wave to flame front, but rather oscillations can lead to stratification of ϕ along the front [37].

Of particular importance to this study is flame wrinkling due to vortex-flame interaction in which an eddy passes through or by the flame front. The interaction is controlled by the stretch rate and the residence time during which the stretch is applied. The strength and wrinkling of the reaction layer is then set by thermo-diffusive processes in which wrinkling can be convected downstream and diffused. The thermo-diffusivity of a fuel given in terms of the Lewis number (Le) can determine the sensitivity of the flame to vortical interaction. In a study by Lee et al. [38], turbulent propane flames with varying Le were investigated. The study concluded that for flames which were more thermo-diffusively unstable (Le<1), the flame surface was more strongly convoluted in response to increasing turbulence intensities. In addition to having more flame surface, flame with Le<1 also exhibited more frequent formation of flame pockets and large-scale folded features.

1.2.2.1 Flame Surface Density

Flame surface density is an important parameter in the accurate modeling of turbulent propagation speeds. There is a strong experimental need to measure and investigate the effects of flame surface area changes for model validation. Experimentally flame surface density has been typically evaluated from CH PLIF [39] or OH PLIF [40, 41] images where the local curvature and length of the flame surface is determined from edge detection. PLIF images are converted into binary pictures with an applied intensity threshold. This binary image corresponds to the progress variable such that a value of 1 represents products and a value of 0 represents reactants. The instantaneous contour of the surface is then measured from these binary maps [42].

CH PLIF is useful in that the CH radical is a marker for the heat release zone itself and its topography most closely follows the flame sheet. However, CH PLIF is disadvantageous due to the low overall concentration which leads to low signal. As well, CH PLIF is most suitable for edge detection in connected flame surfaces. However, at high turbulence intensities, broken structures can be created by partially-premixed flames. This creates two types of zones, a fuel consumption layer and diffusion/oxidation layer. The latter is not captured well by CH PLIF images [43], but is captured with OH PLIF, as seen in Figure 1.6 at the top edge of flame. In situations such as these, the mean FSD may be underestimated with the use of CH PLIF.

The measurements of Filatyev et al. [39] were compared to DNS calculations of

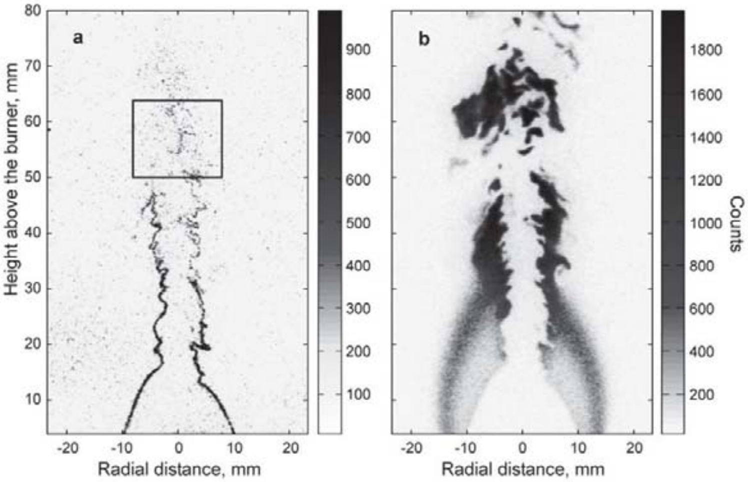

Figure 1.6: Single shot images of CH (*left*) and OH (*right*) PLIF for use in the determination of FSD measurements. The CH PLIF is unable to capture surface elements in non-connected flame zones as seen in the box in the CH image [43].

Bell et al. [44]. From the DNS simulations, the entire FSD of a slot burner was measured using the actual 3-D flame sheet. This calculation was compared to the 2-D experimental CH PLIF derived flame surface density. The result revealed that the 2-D method can underestimate the actual Σ by 25-33%. This type of systematic error must be accounted for in the comparison of experimental and computational data. This suggests that 2-D statistical data needs to be corrected. Filatyev also suggests the use of a wrinkling parameter, Ω, given by:

$$\Omega = \frac{1}{2}\int_{-\infty}^{+\infty} \Sigma \, dy \tag{1.7}$$

which gives a measure of the degree of wrinkling across a flame. It is useful in qualitatively determining how wrinkling changes spatially [45].

1.2.3 The Nature of Combustion Instabilities

Combustion instabilities are the result of a complex combination of unsteady flowfields, acoustic disturbances, resonances, composition inhomogeneities, and turbulence chemistry interaction. They have been the subject of many investigations, with each work providing a little more insight into this remarkable and bottomless topic. The study of instabilities is motivated by the development of industrial combustion systems, gas turbine research, and propulsion efficiency improvement. The instabilities arise from the coupling of pressure, velocity, and heat release oscillations, when the Rayleigh criterion [46] is satisfied. This criterion suggests that when the pressure fluctuations are in phase with the heat release fluctuations, the source term, given in Equation 1.8, can add energy to the acoustic energy conservation equations [47].

$$\Phi = \frac{(\gamma - 1)}{\gamma p_o} p' \dot{q}' \tag{1.8}$$

Unsteady heat addition will add energy to the acoustic field if the magnitude of the phase between p' and $\dot{q}'$ is between 0 and 90 degrees. Energy will be removed from the field is the phase difference is between 90 and 180 degrees, and the instability amplitude will be dampened.

There have been several reviews on the topic conducted by Lieuwen [48], Dowling and Stow [49], and Ducruix et al. [50]. The review by Lieuwen provides a detailed background on the modeling and physics of acoustic interaction with turbulent premixed flames. Dowling and Stow's paper focuses on instability in gas turbine combustors and the types of acoustic modes represented. As well, the coupling between these higher order modes are presented along with modeling challenges. The work by Ducruix et al. sets on categorizing instabilites based on the source of the oscillation, or rather what is feeding energy into the system. The interactions given in Figure 1.7 have been grouped into five mechanisms:

1. Interactions of flames with boundaries
2. Flame vortex interactions

3. Heat release fluctuations driven by acoustic waves
4. Unsteady strain effects leading to surface area changes or reaction rate changes
5. Mixture inhomogeneities due to convective effects

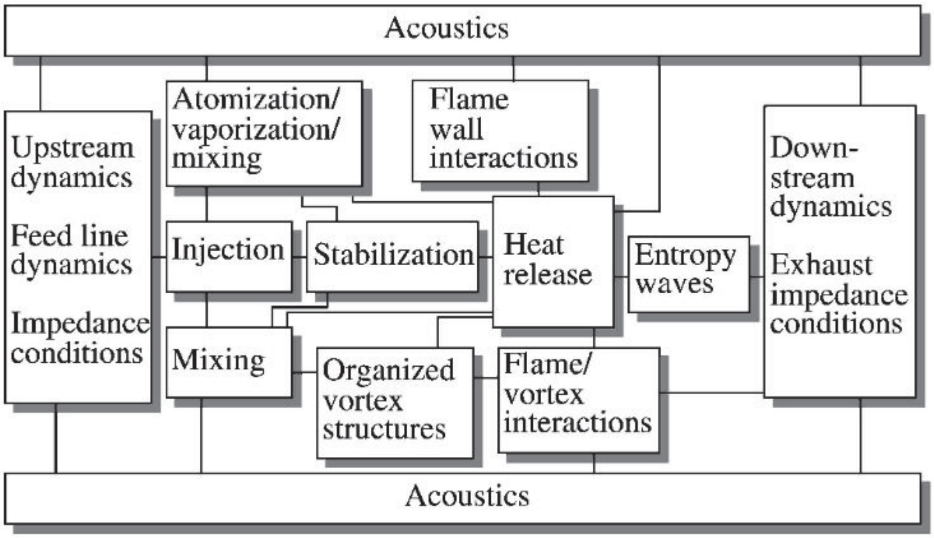

Figure 1.7: Basic interactions leading to combustion instabilities [51].

The review of instabilities given in this thesis will follow this method of categorization and present relevant studies within each grouping.

1.2.3.1 Acoustic Mechanisms

This section will cover background material and studies on instabilties driven by the modulations of the acoustic field by pressure fluctuations. These include organ tone and Helmholtz resonations. The mechanism can best be described by the following:

$$p' \to u' \to A' \to \dot{q}' \tag{1.9}$$

where pressure fluctuations lead to velocity fluctuations, which cause flame surface area oscillations, finally resulting in heat release rate modulation.

Organ tone resonances correspond to standing waves in which the frequency of the mode is given by:

$$f = \frac{c}{L} = \frac{\sqrt{\gamma R_g T}}{L} \tag{1.10}$$

will scale with the speed of sound and some characteristic length of the resonator [52]. For many combustion systems, quarter wave modes are present due to the geometry resembling an open-closed ended pipe. The harmonic wave is anchored at the inlet, but is free moving at the outlet. This type of resonation leads to sinusoidally varying pressure fields throughout the combustor. Pressure fluctuations at the inlet can cause bulk oscillations in the reactant mass flow. In a premixed gas turbine combustor, Meier et al. [53] reports that the chemiluminescence signal fluctuates in accordance with an oscillating pressure field which is causing mass flow pulsations near the injector at 290 Hz. As well, Polifke et al. [54] observed that the instability was activated by a threshold on the pressure drop across the injector which lead to mass flow rate fluctuations. A quarter-wave mode was detected in a propane fired dump combustor in which fuel-rich and fuel-lean instabilities have been reported by Samaniego et al. [55]. The dual-mode behavior of this burner was shown to be mass flow dependent and affected by fluid mechanical oscillations of the injected streams impinging upon each other. It was also suggested that a pressure node for a standing wave can be anchored outside of the exhaust of the burner, allowing for resonating wavelengths that are physically longer than the device.

The Helmholtz mechanism refers to oscillations created by geometries resembling a Helmholtz resonator, which is characterized by a large volume, V, connected to a thin neck of area, A, and length, L. The frequency of this resonator is given by:

$$f = \frac{c}{2\pi}\sqrt{\frac{A}{VL}} \tag{1.11}$$

The volume of air behaves as a spring on the mass of air in the neck, which is analogous to a simple harmonic oscillator system. The pressure in the volume oscillates in a bulk mode, such that it does not vary within the volume. Steinberg et al. have demonstrated that the pressure within the GTMC fluctuates in this manner for methane-fueled conditions [56]. The geometries of the combustors become very important with this type of mechanism. The combination of a plenum and a combustion chamber can create dual-Helmholtz resonators [57]. However, given large changes in area between the two volumes, they become effectively decoupled and can resonate at two distinct frequencies [58]. In an industrial swirl burner, Zähringer et al. [59] have shown that the exhaust chimney length directly scales the observed frequency leading to a Helmholtz conclusion. She has also grouped the observed acoustics into two modes; those controlled by the swirler and naturally present and those controlled by Helmholtz resonances due to the burner design.

Due to the complex geometry and addition of heat release to the flowfield in gas turbine combustors, the dimensions of the combustor and trends of the instability do not always follow those of a perfect Helmholtz resonator. As such, corrections and modifications to Helmholtz theory have been applied. Schildmacher et al. [60] makes a correction on the neck of the resonator, such that the new length L' = L + r, where r is the radius of the neck. As well, with this correction, they argue that their burner follows Helmholtz theory because the frequency of the instability is close to the predicted frequency (with the length correction applied), it varies with the square root of the plenum temperature, and it does not depend on ϕ or the combustion chamber temperature. Selamet and Lee have derived a 2-D analytical method for handling non-standard neck sizes and configurations, particularly for cases where the neck may extend into the volume [61].

1.2.3.2 Convective Instability Mechanisms

Convective-acosutic mechanisms are those that scale with some characteristic velocity in the system, rather than the speed of sound, as given:

$$f = \frac{U}{L} \tag{1.12}$$

Frequently, these mechanisms are also related to equivalence ratio oscillations because inhomogeneities in the mixture composition at the injector are convected to the flame. The structure of convective instabilities is based on the following:

$$p' \rightarrow \phi' \rightarrow \textit{flow convection} \rightarrow \dot{q}' \tag{1.13}$$

where pressure fluctuations lead to equivalence ratio fluctuations, which are then convected to the flame, finally resulting in heat release rate modulation. The process is noted by inherent time delays between the ϕ oscillation and $\dot{q}'$ due to the time required for convection. A schematic for this process as been created by Lieuwen et al. [62] as seen in Figure 1.8.

Rockwell et al. [63] have shown that fluid dynamic oscillations based on frequencies lower than acoustic tones are set by Strouhal number scaling. Higher frequency oscillations through cavities can be determined by organ tone resonances which are speed of sound dependent and velocity dependent. These two types of mechanisms can be coupled in a convective-acoustic mode as addressed in studies by Yu [64] and Lieuwen [62] . Both of the references characterize an acoustic coupling between the flow velocity and a convected entropy wave. Lieuwen describes this wave as being propagated to the flame and exciting a new wave, which moves upstream and impinges on the injector nozzle. He has also provided a simple low order mechanism for premixed systems to describe the feedback which motivates thermoacoustic oscillations where equivalence ratio fluctuations drive heat release oscillations which, in

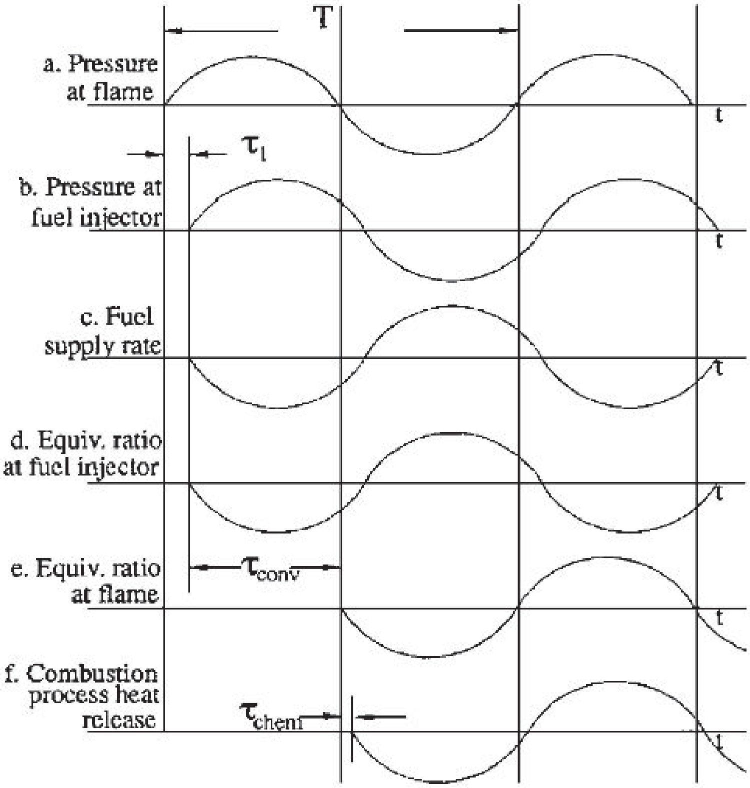

Figure 1.8: Schematic showing the time evolution of disturbances responsible for a combustion instability [62].

turn, cause pressure fluctuations. Yu performed a parametric change of combustor length and inlet velocity to show that changing the convection time for the reflected entropy wave will result in acoustical changes.

1.2.3.3 Turbulence-Chemistry Interaction Mechanisms

Large changes in flame surface area can also lead to oscillations if the total heat release from the flame. As well, changes to the local reaction rate along the flame surface can alter local flame speed leading to greater fuel consumption and thus a larger heat release. These two methods are often the result of local strain due to turbulence effects acting on the local surface as depicted in the coupling processes below.

$$p' \rightarrow u' \rightarrow \mathit{flow} \rightarrow \epsilon' \rightarrow A' \tag{1.14}$$

$$p' \rightarrow u' \rightarrow \mathit{flow} \rightarrow \epsilon' \rightarrow \dot{\omega}' \tag{1.15}$$

These types of strain effects are often well represented by vortex rollup of the flame sheet, in which surface area is increased and local flame speeds change due to the recirculation of hot products. This type of behavior occurs in the GTMC as studied by Stöhr et al. [65], and depicted in Figure 1.9. In this mechanism, flow perturbations produce vorticity, leading to area and heat release changes, which can strongly affect both premixed and non-premixed flames. Non-premixed flames are more susceptible to the second mode of strain interaction due to sensitivities on species gradients as the flame is approached. However, premixed flames may also be affected if the strain leads to local extinction.

Variation of the global equivalence ratio will also change the response of an instability due to the flame speed scaling with ϕ [66, 67]. It should be noted that this is different than equivalence ratio oscillations. Here the scaling is global to the flame. The flame may exhibit very different behaviors for certain ranges of ϕ, such as those observed by Huang et al. [68], where the flame exhibits a hysteresis mode, given that the combustor will transition from stable to unstable dependent on ϕ. This type of bifurcation in behavior can also be due to changes in anchoring of the flame. Flames which are anchored to the injector because of higher flame speeds will have reduced mixing if the reactants are injected as partially-premixed. As well, the lifted flames will be more affected by the recirculation of products [69].

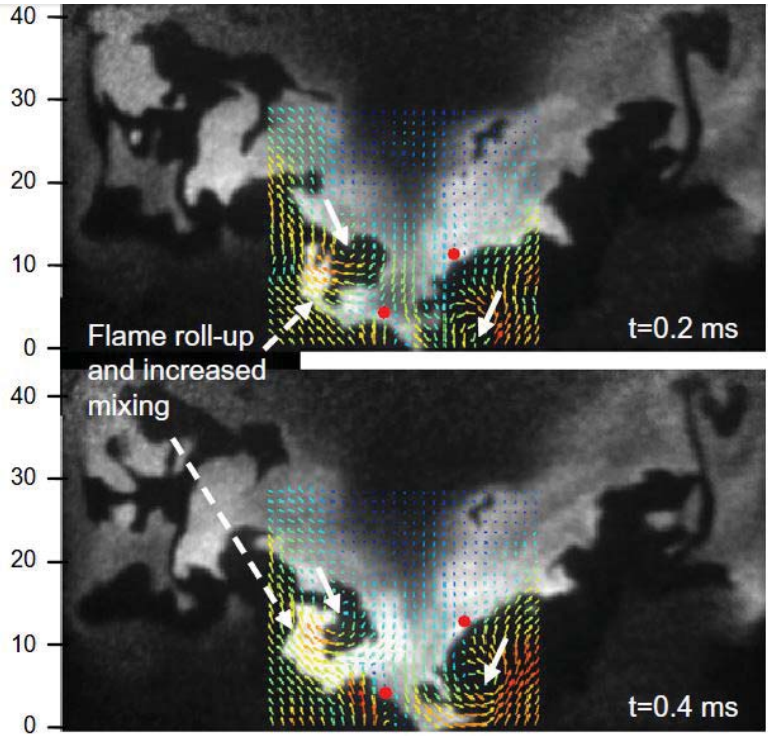

Figure 1.9: Series of combined OH PLIF and PIV images depicting flame roll-up due to interaction of the flame sheet with vortices created by the precession of the PVC [65].

1.2.3.4 Third-Party Mechanisms

Third party mechanisms involve those in which the amplification of the instability is produced by neither the flame nor the flow, such as in the case of impinging flames on a wall. The structure of the process is as follows:

$$A' \rightarrow \dot{Q}' \rightarrow p' \tag{1.16}$$

where interaction with the wall causes a large area change, driving heat release and pressure changes. Studies by Schuller et al. [70] , Durox et al. [71], and Fernandes and Leandro [72] have investigated noise radiated from flames impinging on a surface by both forced and self-excited oscillations. As well, vortex interaction with a wall or surface can cause a third party effect if the vortex carries fresh reactants which are auto-ignited upon interaction with the object [73].

$$\Gamma' \rightarrow \dot{Q}' \rightarrow p' \tag{1.17}$$

1.2.4 Formaldehyde Flame Marking and Combustion Chemiluminescence

Formaldehyde(CH_2O) is formed as a combustion intermediate of hydrocarbon combustion given the following general reaction pathway for methane [74]:

$$CH_4 \rightarrow CH_3 \rightarrow CH_2O \rightarrow HCO \rightarrow CO \rightarrow CO_2 \tag{1.18}$$

Formaldehyde is produced in the low temperature oxidation regions and is an indicator of the first stage of preheat processes, including fuel oxidation, ignition, and stabilization. Within turbulent flames, the planar measurement of formaldehyde can be used to visualize the spatiotemporal evolution of the flame. While CH and OH PLIF have been proven to be good markers for the flame front [75], formaldehyde has only recently been seen to be able to provide similar edge tracking on the fuel side of a flame. Santoro et al. [76] and Joedicke et al. [77] have both used formaldehyde in edge tracking of flames, and Joedicke in particular used it to mark the base point of triple flames which are controlled by low temperature chemistry. Bombach and Käppeli [78] used simultaneous CH and CH_2O PLIF to show the spatial location of each signal relative to each other.

Li et al. [79] performed measurements simultaneously of CH, OH, and CH_2O PLIF to evaluate formaldehyde's use as a marker. Figure 1.10 depicts comparisons between the CH and formaldehyde PLIF. Their results show that CH_2O lies in the inner part of the flame towards the preheat zone in broad regions, however, there may be some overlap of the CH and CH_2O layers. Some of the broadening of the CH_2O layers may be due to interferences with fluorescence from polycyclic aromatic hydrocarbons (PAHs). However, the majority of the broadening is due to turbulence-chemistry interactions.

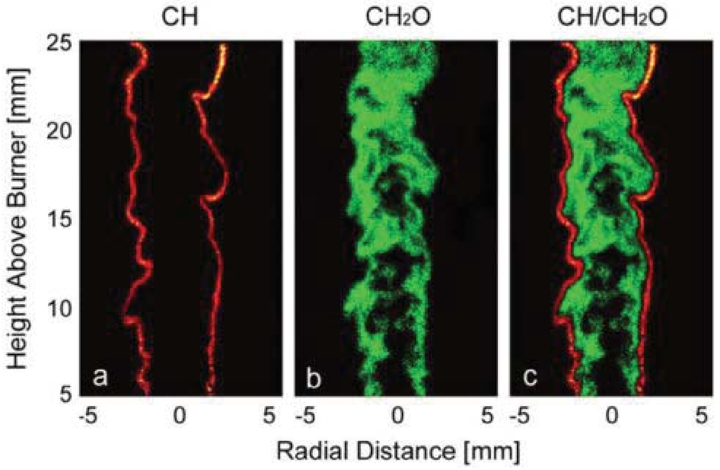

Figure 1.10: Single shot images of CH (*left*) and CH_2O (*center*) PLIF for use in the determination of edge tracking and flame marking [79].

Numerical simulations of turbulent premixed flames using the Peters mechanism [80] indicate the following conclusions regarding formaldehyde:

A) For moderate strain rates (100-1000 s^{-1}), the peak mole fraction of CH_2O remains relatively constant

B) For strain rates from 100-1000 s^{-1}, the thickness of CH_2O layers are independent of strain, but for higher strain, the layers become thinner

C) The thickness of CH_2O layers will increase rapidly with increasing turbulence intensity. This matches experimental observations of thickening of preheat zone with increasing turbulence intensity.

D) Formaldehyde lacks a consumption mechanism in low temperature regions but is consumed at higher temperatures ($T>1500K$) by H, O, and OH. This leads to accumulation of CH_2O in the preheat zones, as seen in Figure 1.11.

E) Evidence of CH_2O in regions of $T<1200K$ is due to eddy transport from the reaction zones, since the chemical reactivity in this region is otherwise quite low.

F) The distribution of formaldehyde in the temperature coordinate is independent of turbulence intensity, denoted as D_t/D, in Figure 1.11.

G) The peak formation rate of CH_2O corresponds to the location of the peak heat release and maximum of CH concentration.

H) The differentiation in gradient magnitude between the low temperature preheat side and high temperature reaction side allows for discrimination of CH_2O signals from PLIF images such that the flame edge can be marked by the largest magnitude CH_2O gradient.

The ability to discriminate between low temperature side and high temperature side of the PLIF signal is important in being able to distinguish flame edges. Dhanuka et al. [81] has used this gradient criterion to mark flame surface and measure flame surface densities in a gas turbine combustor using a Jet-A fuel at elevated temperatures and pressures. The potential for flame marking in temporally resolved measurements have been investigated by Gabet et al. [82] for PLIF images taken at 10 kHz. The original obstacle to this process was the low laser pulse energies typically created by high speed laser systems. High speed measurements of these structures allow for the temporal development of the flame to be studied. Distributed low-temperature reaction zones have also been studied in flameless turbulent combustion [83] using formaldehyde PLIF.

Combustion chemiluminescence can be used as a metric to evaluate heat release, flame motion, and shape, which are important in characterizing unsteady processes. Chemiluminescence is the the natural radiative emission from electronically excited species which are formed in the flame. The intensity of the emission is proportional to the concentration of the excited molecule. However, chemiluminescence measurements are line of sight integrated, meaning that they can only provide information

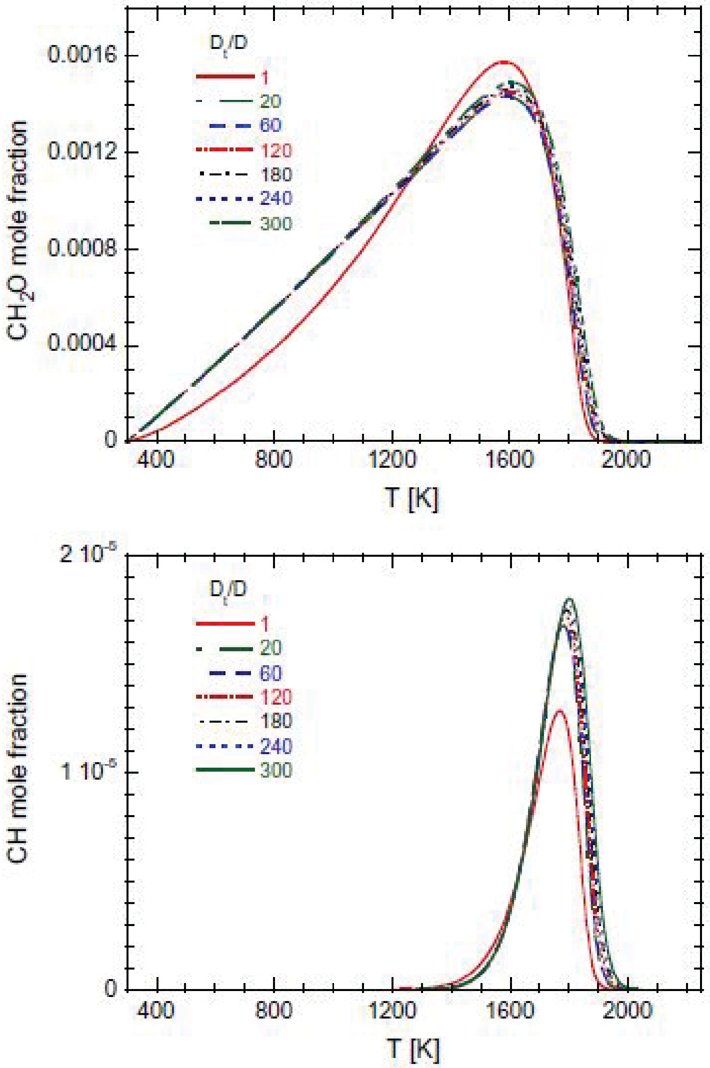

Figure 1.11: Numerically simulated mole fractions of CH_2O and CH as a function of local flame temperature with varying and increasing turbulence intensity, D_t/D [79].

as to the global quality of the flame. Primary emissions from a flame are due to CH*, OH*, CO_2*, and C_2* [84]. While CO_2* and C_2* are broadband signals, CH* and OH* emissions occur over very narrow bands. Overall emission is due to the heat release rate and equivalence ratio, such that the signal is linearly proportional to the heat release. However, this linearity assumes that dilution, radiation losses, and strain/curvature effects are negligible. As well, locally the relationship between the signal and heat release is exponential. Extreme strain can lead to suppression of the chemiluminescence signal without flame extinction. This may explain why turbulence can reduce the overall signal from a flame.

In turbulent, partially-premixed flames, spatial variations in equivalence ratio, strain, and curvature can cause the local exponential dependence on heat release to vary. If the local exponential scaling varies along the surface of the flame, the relationship between the overall emission and overall heat release is now different. However, the spatial variations can average out such that the relationship between the emission is still related to the global equivalence ratio. The effect of partial-premixing is to slightly increase the emitted signal for a given equivalence ratio. As a result of these effects, the interpretation of overall chemiluminescence signals can serve as a qualitative descriptor of flame behavior. Quantitative conclusions and comparisons from this data may be skewed.

In general, chemiluminescence of radicals, particularly OH*, have been widely used for general and local heat release measurements [12, 40, 55, 71, 85–89]. Cross-correlations of radical emissions have also been used for equivalence ratio detection [90] and instantaneous heat release distribution [91]. The emission signal can also be shown to be correlated with the pressure fluctuations in a burner. If one considers the flame to be a monopole source of sound, the pressure at the detector is related to the fuel consumption, Q, by the following [70]:

$$p(r,t) = \frac{\rho_\infty}{4\pi r}\left(\frac{\rho_u}{\rho_b} - 1\right)\left[\frac{dQ}{dt}\right]_{t-\tau} \tag{1.19}$$

where τ is a delay due to the phase shift created by the convection of the sound wave to the detector. Next the rate of variation dQ/dt can be estimated by assuming:

$$Q = kI, \mid k = f(\phi) \tag{1.20}$$

where I is the emission intensity of radicals created in the reaction zone, or a combination of radicals (i.e CH*, OH*), and k is a constant of linearity, proportional to the equivalence ratio. It can then be derived that:

$$p(r,t) = \frac{\rho_\infty}{4\pi r}\left(\frac{\rho_u}{\rho_b} - 1\right) k \left[\frac{dI}{dt}\right]_{t-\tau} \tag{1.21}$$

This formulation allows the interpretation of unsteadiness of pressure fluctuations during combustion instabilities to be correlated with chemiluminescence fluctuations, as a result of heat release and flame surface area oscillations, as follows:

$$p(r,t) = \frac{\rho_\infty}{4\pi r}\left(\frac{\rho_u}{\rho_b} - 1\right) S_{L0} \left[\frac{dA}{dt}\right]_{t-\tau} \tag{1.22}$$

1.3 Previous Work Related to the GTMC

The GTMC used in this thesis was acquired from the DLR Institute for Combustion Studies in Stuttgart, Germany where it has been the subject of a wide array of investigations conducted by the Department of Combustion Diagnostics, headed by Dr. Wolfgang Meier. The GTMC has been used in a variety of laser diagnostic surveys since 2003. This section will give a brief overview of the different types of diagnostics applied and some of the conclusions from those studies. The next segment, Section 1.4, will discuss the work conducted at the University of Michigan and how it is different and/or complementary to the work from DLR.

The primary focus of most studies on the GTMC , both at DLR and at Michigan, has been placed on understanding combustion instabilities and flow dynamics. Preliminary studies on the GTMC involved identification of a 290-310 Hz self-excited acoustic fluctuation for a particular operating condition, fueled with methane. Phase-resolved laser diagnostics were then applied to look at changes in the velocity-field from particle image velocimetry (PIV), OH and CH distributions from PLIF, and temperature/concentrations from 1-D Raman scattering, along the evolution of an acoustic cycle [92–94]. Formaldehyde PLIF was applied in a single study [95] to show complementary structure and behavior to OH PLIF measurements which were also phase-locked to the oscillation. Duan et al. [96] conducted phase-resolve LDV measurements which show large fluctuations in the axial and radial velocity components corresponding to changes in inflow and recirculation zone sizes. This study was used in the work done in Chapter 4 to determine ideal locations for LDV measurements to prove swirler flow rate redistribution. Phase-resolved measurements of 2-D temperature fields have been conducted with two line OH PLIF [97, 98]. Both these studies identified structures in the temperature field corresponding to fluctuations in the shear layer between the recirculation zones.

DLR identified three canonical flame cases as described in Weigand et al. [33] and Meier et al. [30]. Flame A is a standard, high flow rate swirling flame with no resonance present, Flame B is a swirling flame experiencing a thermoacoustic oscillation near 300 Hz, and Flame C is operated near lean blowout (LBO). Flame B will become their standard operating point for studying unstable flames. It is a methane fueled condition with $\phi = 0.75$. These two studies applied LDV, PIV, OH and CH PLIF, and Raman scattering to look at flowfield structures, temperature, species distributions, and turbulence-chemistry interactions. In these studies, the combustor is identified as partially premixed due to the recession of the fuel injector below the burner face. Studies have also been conducted in a similar combustor geometry using a premixed swirling injector to make comparisons to the GTMC [99]. This paper applied high speed diagnostics to look at similar patterns in unsteadiness with varying premixedness.

Simultaneous measurements, often conducted time-resolved with high speed laser diagnostics, have been the hallmark of DLR studies, beginning with Sadanandan et al. [100]. This study showed OH PLIF and PIV maps overlaid for the entire field of view in the GTMC. Presently, focus has been placed on the interaction between acoustics, flame structure, and vortical structures such as the PVC. Some studies have correlated high speed PIV and OH PLIF to examine flame roll-up due to the flame surface and PVC motion at 525 Hz [20, 101]. Transverse cuts, parallel to the burner face, of PIV and OH PLIF measurements also show the effect of swirl and spiraling structures which aid in mixing of reactant and products. Studies by Steinberg et al. [40, 56] have shown that by doubly phase-resolving the flow, the effects of the PVC precession and thermoacoustic oscillation can be separated and analyzed independently. As well, 3-D representation of the PVC are reconstructed from high speed PIV data. The precession rate of the PVC is also shown to correlate with the acoustic frequency and can alter the fluctuation rate of changes in flame surface area. Proper orthogonal decomposition of the PIV data has also shown which coherent structures represent the majority of the kinetic energy in the flow. Stöhr et al. [65] has extended this work by looking at POD decompositions of flames at various thermal powers. His work has also shown that the base of the PVC lies with in the stagnation point created by the CRZ.

Two investigations have been conducted involving the base of the flame. The first study by Stöhr et al. [102] focused on identification of structures which signal LBO . He concluded that the flame root is inherently unstable during LBO due to high strain rates which can cause intermittent extinction of the flame root. Lean blowout will occur is the flame root remains extinguished for a critical amount of time. The second study analyzes flame kernel events to track OH pockets for possible autoignition [103]. It was determined that auto-ignition was not the primary cause of flame kernels, but rather wrinkling and breakup of the flame surface gets swept around giving the appearance of through-plane transport in OH PLIF images.

Three other rather independent studies were conducted involving the GTMC. Investigations by Wehr et al. [104] and Lammel et al. [105] were conducted at elevated pressure. The first paper represents a proof of concept for high pressure Raman scattering measurements, which become very difficult due to interferences from soot and the presence of windows. The second study involves soot formation observations with laser induced incandescence and coherent anti-stokes Raman scattering techniques. Finally, oxyfuel flames were observed in the GTMC and it was determined that the flame stabilization mechanisms vary between methane/air flames and methane/O_2 flames [106].

1.4 Thesis Goals and Uniqueness

The primary goal of this thesis is to investigate a laboratory scale gas turbine model combustor (GTMC) and provide insight regarding the instability mechanisms present and how they effect fuel-air mixing, stabilization, flame shape and motion, and the flame surface in comparison to flames without instabilities present. As well, the coupling between the flame and flowfield structures, like the precessing vortex core (PVC), will be analyzed. This data will allow modelers to evaluate the physics and accuracy of flame dynamics captured by the computations of unstable flames.

The current study focuses on partially-premixed flames that are the result of stratification of fuel-air mixing. These flames capture some of the emissions reductions captured by fully premixed flames without the risks, such as flashback and lean blowout. However, they are susceptible to natural combustion instabilities. The gas turbine model combustor used in this study is unique in that exhibits a natural instability which the result of several simultaneous instability modes and mechanisms. Many instability studies focus on combustors of simple design which are then artificially forced to resonate. The oscillations which are then induced are usually the result of a single acoustic mechanism. The GTMC represents a complex and realistic design for gaseous-fueled gas turbine combustors, featuring complex flow patterns, with several active self-excited mechanisms. A goal of this study is to identify which mechanisms are present and how they couple with each other and the flowfield.

Through harmonic excitation of the combustion, the flame transfer function of the system can be measured by scanning through excitation frequencies to yield gain and phase information. While this information is important for modeling of turbulent combustion processes, it represents only a black box to the study of instabilities because the underlying physics and flame dynamics are neither captured nor explained by flame transfer functions. They serve as an input-output check for model validation, but are not capable of ensuring the proper thermoacoustic interactions are represented. This study aims to focus on the details of the instabilities in terms of global parameters.

Previous studies, particularly those at DLR Stuttgart, have focused on a single operating condition using methane. While a single experimental operating point is satisfactory for a discussion on instabilities in the GTMC, it does not fully explore the breadth of regimes that instabilities can influence. Parameters such as thermal power, equivalence ratio, temperature, and fuel type will be varied in this work to see how they affect the presence and strength of the thermoacoustic coupling. By observing large scale structure phenomena such as flame shape and motion, the dynamics of the flowfield and mixing can be used to explain what enables satisfaction of the Rayleigh criterion and what aspects cause amplification or dampening. Due to the coupling between several mechanisms, data trends often do not follow the exact scalings as predicted by theoretical models. The conclusion of Chapter 3 discusses the reasons for these difference and suggests new modeling ideas.

Mixing and flowfield studies have been previously conducted in the GTMC through the use of high-speed PIV and 1-D Raman scattering. A different approach in this work is used to explain what large scale differences occur between resonating and non-resonating flames. Point-wise laser Doppler velocimetry (LDV) measurements are applied to measure the change in distribution of flow rate through the two swirlers in the GTMC. Whereas PIV data from DLR is used to explain the effect of vortical structures on resonating flames, the LDV data presented explains what is the flowfield criteria necessary to set up the proper conditions for a flame to resonate. The collected 1-D Raman scattering dataset provides an average reference for mixing in the GTMC, but it cannot give an instantaneous view of the entire combustor field. By performing fluorescence measurements of tracers added to the fuel, the 2-D instantaneous distribution of unburned fuel can be observed. While this does not give the same information as the Raman measurements, it presents the spatial localization of where fuel is directed, dependent on the operating conditions and fuel type. This data will be used to interpret how an unstable flame distributes fuel differently than a stable flame.

The goal of Chapter 5 is to investigate changes in flame surface density and wrinkling coupled with the instability. As well, how does the presence of the PVC effect the flame surface motion and location, while comparing resonating and non-resonating flames. Studies from DLR have shown the PVC motion at 525 Hz and that its effects are visible in high-speed OH PLIF images. Formaldehyde PLIF measurements have been made using dimethyl ether (DME) and ethylene for resonating and non-resonating flames for a range of flow rates and equivalence ratios. The uniqueness of this study lies in the use of high-speed formaldehyde PLIF which allows for time-resolved measurements of flame surface area changes. A previous study of phase-resolved formaldehyde PLIF at DLR (see Section 1.3) captured the oscillations near 300 Hz, but were unable to measure any rapid changes in the flame or the influence of the PVC. High-speed OH PLIF was applied at DLR to flame surface tracking and FSD observations. This study is complementary to those measurements in that formaldehyde represents the reactant or "cool" side of the flame where OH concentrations are low. As well, formaldehyde does not suffer from issues associate with OH PLIF, such that OH is in super-equilibrium near the product side of the flame but also highly present in the exhaust gases. Formaldehyde is typically only produced in thin regions marking the preheat zone of the flame.

Proper orthogonal decomposition (POD) has also been applied to the scalar field of formaldehyde signal intensities. POD has been used by Steinberg et al. [40, 56] and Stöhr et al. [65, 107] to decompose the velocity field from PIV measurements into modes consisting of prevalent coherent vortical structures. The POD of the scalar formaldehyde conducted in this study depicts the coherent flame structures and their significance in the flow. As well, the oscillation of each mode can then be attributed to an acoustic or PVC-induced fluctuation, or some combination of the two.

Overall, this study attempts to investigate the major controlling parameters behind instability presence and frequency/amplitude. Turbulent combustion responses to fuel flame speed and heat release will be shown to scale with the instability in Chapter 3 and ultimately correspond to the flame surface fluctuations and structures observed from the HSPLIF and POD modes in Chapter 5. Unburned fuel localization and flame shape/motion measurements in Chapter 4 will identify the global physical structure of the flame and mixing requirements needed to enable satisfaction of the Rayleigh criterion and encourage amplification of the instability. Together these results aim to shed light on the dynamic processes and parameter sensitivities of the physics of combustion instabilities and flow-flame coupling.

1.5 Outline

- **Chapter 2:** Describes the GTMC used in this investigation as well as the experimental methods applied. The range of operating conditions and fuels studied are discussed. An overview of the new Michigan high speed formaldehyde planar laser induced fluorescence (PLIF) system is given, as well as descriptions of the laser Doppler velocimetry (LDV), acetone PLIF, and high speed chemiluminescence measurements conducted. A discussion on the application of dimethyl ether (DME) in high speed laser diagnostics and its advantages/disadvantages is provided.
- **Chapter 3:** Addresses the characterization and identification of thermoacoustic modes that are naturally active in the GTMC. As well, correlations between the instability frequency/amplitude and factors such as fuel flame speed, equivalence ratio, burner temperature are presented. Data has been collected from conditions with syngas fueling in which the mixture composition of the syngas strongly alters the performance of the combustor. A comparison of observed trends and some low-order models are presented along with a discussion involving the scaling parameters of the trends.
- **Chapter 4:** Discusses fuel-air mixing in the GTMC and its effect on combustion instabilities. Velocity measurements are presented which show that the air mass flow rate between the two swirlers fluctuates. Rayleigh indices are given to prove correlations between flame shape and instability strength/presence. Acetone PLIF

measurements illustrate the localization of unburned fuel in the GTMC for a variety of fuel and fueling conditions. Evidence is presented to suggest that the motion of the PVC controls the flame shape and location.

- **Chapter 5:** Presents data collected from high speed formaldehyde PLIF measurements which capture flame surface wrinkling and oscillatory motions due to coupling with the instability and PVC in DME and ethylene flames. Flame surface density measurements are compared between resonating and non-resonating conditions. Air mass flow rate and equivalence ratio trends are also provided. Turbulent flame speed effects are discussed with regards to FSD variations and changes in formaldehyde signal centroid motion. Proper orthogonal decomposition (POD) is applied to the data to construct images of the primary coherent mode structures present. Mode time series are reconstructed from the POD to depict the motion induced by each of the primary modes. The effects of the precessing flame surface during a given motion cycle are examined.

- **Chapter 6:** The conclusions from the previous chapters are presented and reiterated.

· Several coupled acoustic modes are present, with main scaling contributions from dimensions, flow rate, and flame speed.

· Flame shape and anchoring are important indicators of instability presence/strength.

· Frequency scaling can be captured with low order models.

· Swirler air flow rate switching does occur and affects instability presence/strength.

· Precession of flame base affects liftoff cycles, which controls vertical flame motions and responses to the instability.

· POD mode analysis shows flame motions are correlated with thermoacoustic oscillations and the PVC precession rate.

· Increased flame surface correlates with increased instability strength due to an increase in heat release per given volume.

CHAPTER II

Experimental Apparatus and Methodology

2.1 Experimental Apparatus

The swirl burner, known as the gas turbine model combustor (GTMC), was developed by Meier and colleagues at DLR Stuttgart. It has the advantage that it is of canonical axisymmetric swirler-design yet it exhibits the fundamental physics associated with gas turbine flames; it contains two swirling air streams which surround an annular fuel stream.

2.1.1 University of Michigan Gas Turbine Model Combustor (GTMC)

A gas turbine model combustor (GTMC) as seen in Figure 2.1 is used to study acoustic behavior and flow-flame dynamics. The injector consists of a central air nozzle, an annular fuel nozzle, and a co-annular air nozzle. Both air nozzles supply swirling air at atmospheric pressure and temperature from a common plenum. The inner air nozzle has an outer diameter of 15 mm and the annular nozzle has an inner diameter of 17 mm and an outer diameter of 25 mm. The reported swirl number is approximately 0.55. Non-swirling fuel is provided through three exterior ports fed through the annular nozzle which is subdivided into 72 0.5 mm x 0.5 mm channels. The exit plane of the central air nozzle and fuel nozzle lies 4.5 mm below the exit plane of the outer air annulus. The exit plane of the outer air annulus will be referred to as the burner face. The combustion chamber has a square cross section of 85mm in width and 110 mm in height. The exit of the burner has a tapered lid which leads to an exhaust chimney with a diameter of 40 mm and a height of 50 mm. The burner is typically operated with 3 metal blank walls and a single quartz window, with a thickness of 1.5 mm, for flame visualization. The burner was fired using methane, dimethyl ether, propane, ethylene, and syngas fuels. An external cylindrical chamber was used for fuel mixing, particularly carbon monoxide and hydrogen for syngas formation, and fuel line separation. This chamber allowed for the equal division of the fuel flow into three separate lines which lead to the fuel ports on the burner.

2.1.2 Burner Core Components

The core of the burner refers to steel parts which when assembled, form the swirlers and fuel passages, as seen in Figure 2.3. Although there no premixing in the burner, it has been described as partially premixed due to the liftoff height between the flame base and the burner face. This liftoff height is facilitated by the recession of the fuel annulus and central air nozzle. With the present swirling, some degree of mixing can be achieved in this distance. The degree of premixed-ness is a function of the liftoff height, fuel density and swirling velocity. The liftoff height has been seen to vary across fuel types and during operation of a given fuel, when thermoacoustic oscillations cause flame front oscillations. Therefore mixedness is an unsteady, fuel dependent property. The curved lip of the outer swirler tends to direct flow radially, while the shape of the inner nozzle directs flow axially.

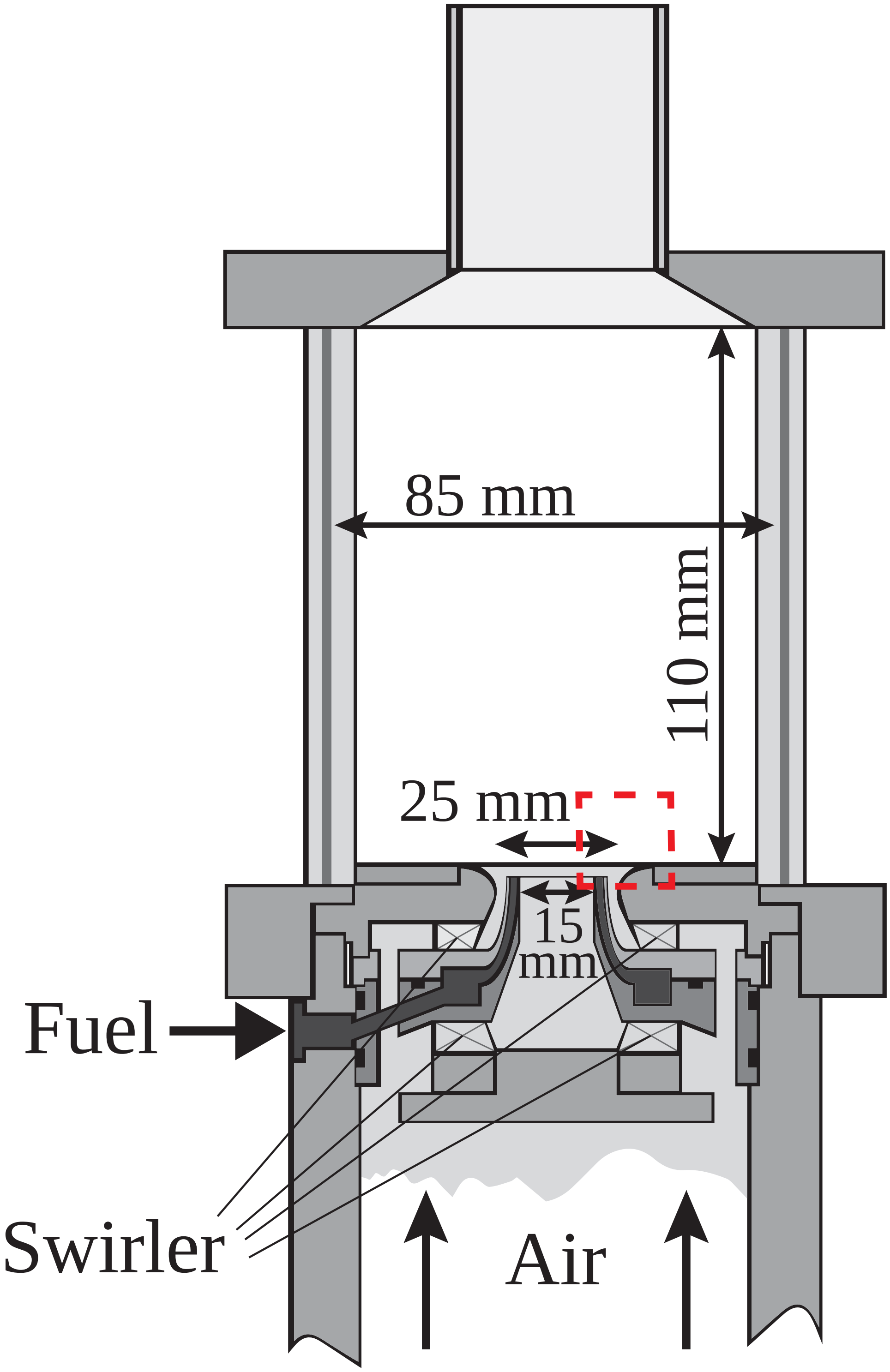

Figure 2.1: Schematic drawing of the Gas Turbine Model Combustor used in this study. The red dashed box indicates the region of interest for LDV and acetone PLIF investigations [33].

Figure 2.2: Images of the standard GTMC configuration in operation.

Figure 2.3: Images of the core components of burner and the core assembled.

2.2 Flow Control and Operation of the Combustor

Mass flow rates for the air and individual fuel lines leading to the burner were controlled by sonically choked orifices, and were calculated using Equation 2.1. Air was provided from the shop air line using the building supply. This air was quite humid and rusty due to the steel pipes, however the air flow was filtered twice to reduce the water and particulate content. The use of bottled air become unreasonable because each bottle would only allow for 15 minutes of run time. An external cylinder, as seen in Figure 2.4 was used to split the fuel flow into three even flows to be sent to the ports in the burner. This cylinder was also used to ensure the syngas mixtures of hydrogen and carbon monoxide were properly mixed before being sent to the GTMC. The burner was ignited by either using a spark plug mounted in one of the walls, or by hand using a propane torch when all the windows were in place. The burner was operated to warm up to a constant core temperature and then data was collected. Before a subsequent data trial could be conducted, the burner was cooled back to room temperature, and the warm up procedure was repeated.

$$\dot{m} = \sqrt{\frac{\gamma}{R_g}(\frac{2}{\gamma + 1})^{\frac{\gamma+1}{\gamma-1}}}\frac{p_o A^*}{\sqrt{T_o}} \tag{2.1}$$

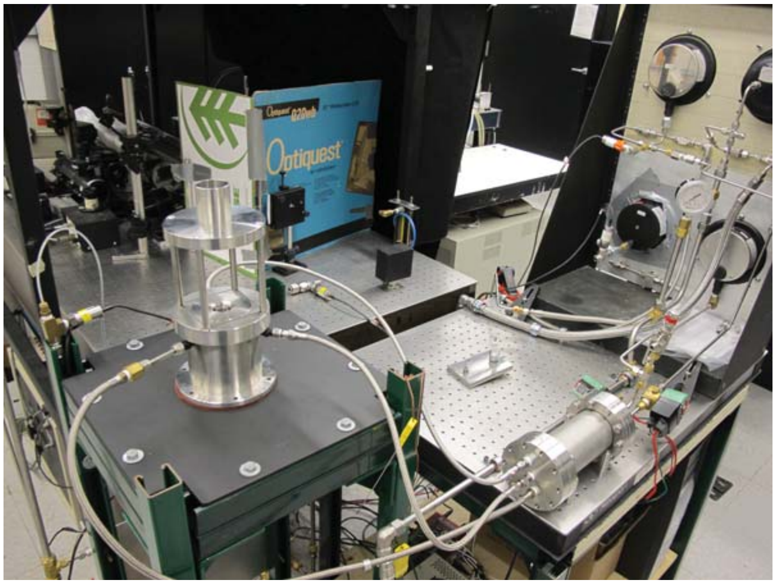

Figure 2.4: Experimental set up for flow control and distribution of fuel to the GTMC.

2.2.1 Control of Burner Temperature

The frequency and amplitude of the instability is sensitive to the temperature at which measurements were taken. Ideally, the burner would be operated until the entire structure has reached thermal equilibrium, a process which takes up to 30 minutes of continuous operation. Due to concerns regarding the windows and warping of the structure, the data was collected at a lower reference temperature. In order to ensure repeatability of the data, measurements were taken at the same reference temperature. However, the proper location to take this temperature needs to be discussed. It was observed that the frequency response of the instability did not scale with the exhaust temperature, nor the temperature of the burner walls. This was evaluated with thermocouples placed at the exit of the chimney, the inlet of the chimney, in a screw hole at the top of a window post, and with a surface thermocouple on a wall. All of the locations did not yield consistent repeatability in the measurements. For the same exhaust or wall temperature, two very different frequencies could be observed.

However, it was determined that the temperature of the burner core components scaled with the frequency response. A thermocouple was then fed through the plenum up into one of the passages of the outer swirler. The temperature in this location increases as the burner face heats up, it acts as a proxy to the actual temperature at the burner face, as opposed to a preheat temperature of the air. Thermocouple measurements taken at the end of a run immediately after flame is extinguished, from a downstream position, indicate that the unburned air temperature at the fuel exit, 4.5 mm below the burner face, had risen from 300K to 310K. Due to this small increase, it will be assumed that there will be no preheated air effects, on parameters such as flame speed, and that the core temperature is representative of the heat transfer from the flame to the burner face. The length of the swirler passage and average reported inlet velocity dictate that the residence time through the burner core is on the order of a few milliseconds. Due to this short time, the degree of air preheating is limited. The temperature at this location will be referred to as the burner core temperature. For the measurements in this thesis, data was typically collected at a core temperature of 333 K, which corresponds to warm up times of 2-3 minutes, depending on the flame. This temperature metric yielded consistent results between repeated warm up and cool down cycles of the GTMC. The total heat flux to the incoming air is low, however, the heat flux to the burner surface is much higher. The measured temperature within the core increases proportional to the burner face, however the temperature at the face is significantly higher than the 333 K.

2.2.2 Flow Control Error

The uncertainty in the flow control by sonically choked orifices can be calculated by:

$$\frac{\Delta \dot{m}}{\dot{m}} = \sqrt{\left(\frac{\Delta P_o}{P_o}\right)^2 + \left(\frac{\Delta A*}{A*}\right)^2 + \frac{1}{4}\left(\frac{\Delta T_o}{T_o}\right)^2} \tag{2.2}$$

The resolution of the air pressure gauge was 1 psi and the fuel pressure gauges were accurate to 0.25 psi. The assumed error in the orifice diameters was about 2% and due to variation of temperature in the room, the temperature error is estimated at 3%. The experimental uncertainty associated with this method gives 2.9% error on the air mass flow rate and 2.7% error on the fuel mass flow rate. The reported equivalence ratios are accurate to within 3.97%.

2.3 Experimental Operating Conditions

Table 2.1 lists the operating parameters investigated. The hydrocarbon fuels and syngas mixtures of 20% and 25% hydrogen were burned over a range of equivalence ratios and air mass flow rates. The syngas mixture of 25% H_2 was chosen because its flame speed over the range ϕ = 0.65 - 1.0 closely matches that of ethylene. As well, the 20% H_2 mixture matches ethylene flame speed from ϕ = 1.1 - 1.2. The flame speed was matched between these fuels to understand their effect on the instability, independent of flame speed influences. Syngas gas mixtures of 30-45% hydrogen were only burned at an air mass flow rate of 282 g/min for a smaller range of equivalence ratios to study stability limits.

The operating conditions were chosen for comparison around the data collected at DLR. Weigand et al. [33] identified the instability at 308 Hz in methane flames at air flow rates of 282 g/min and an equivalence ratio of 0.75. Out of three flames investigated at DLR, he identified this operating condition as Case B. Within this thesis, this condition will also be referred to as Case B. The parameter variations in flow rates are centered around this condition, such that the flow rates vary from 60% to 125% of Case B flow rates.

Table 2.1: Operating conditions for acoustic characterization studies.

Fuel	Air Flow Rate [g/min]	Φ_{Global}	S_L (Φ=1) [cm/s]
Syngas, H_2/CO			
20 % H_2	170 – 354	0.75 – 1.2	60
25 % H_2	170 – 354	0.65 – 1.1	68
10 – 45% H_2	282	0.75 – 1.1	35-105
Methane	170 – 354	0.65 – 1.2	40
Propane	170 – 354	0.65 – 1.2	44
DME	170 – 330	0.65 – 1.2	45
Ethylene	170 – 354	0.65 – 1.2	65

2.4 Chemiluminescence Imaging and Pressure Measurements

High speed videos of the total line of sight flame chemiluminescence were taken using a Phantom V9.0 high speed camera. Videos were taken at a frame rates of 2500 fps with an exposure of 220μs at 768 x 768 pixels. The resolution of each of the images is 114 μm/pixel. Videos taken simultaneously with the high-speed formaldehyde PLIF measurements were taken at 4 kHz at 576 x 576 with a resolution of 118 μm/pixel. A Nikon 50mm lens was used with the aperture typically all the way open to f/1.2.

A PCB piezoelectric transducer, model 062-A01, was used to measure the frequency performance of the burner. The transducer was located in the plenum to avoid thermal damage and wear associated with application in the wall of the combustion chamber. As well, the background noise in the transducer was reduced in the plenum compared to the combustion chamber. The frequency behavior, with the exception of a phase shift, is not affected by the location of the transducer between the plenum and combustion chamber. For Rayleigh index measurements, the transducer was mounted in the wall of the burner because the phase shift will skew the index calculation.

For a given equivalence ratio and air mass flow rate, pressure measurements are taken at a set temperature for 5 seconds at 20 kHz, yielding 100,000 data points. The pressure data was collected using a LeCroy Waverunner 6100A oscilloscope. The gain of the piezoelectric amplifier was set to 10. A power spectral density (PSD) is then calculated for each data set to give frequency and amplitude data. The strength of a resulting frequency peak is determined by integrating the PSD curve with the full width half maximum (FWHM) as the bounds of integration. The complete set of 100,000 data points is divided into 8 overlapping bins of 20,000 points. A Hanning window is applied to each bin, and then the PSD is calculated. Depending on the initial conditions, acoustic frequency varied between 230 Hz and 500 Hz. The reported frequencies are accurate to 0.5% and the calculated amplitude is accurate to 3%.

2.5 Laser Doppler Velocimetry

Velocity measurements were taken using a TSI LDV system using a Ar-ion laser at 514.5 nm with data rates at around 1 kHz and 3000 collected samples. The Innova 90 laser was operated at 1W. A 121 mm focusing lens was used with a 50 mm beam spacing to produce fringe spacings of 1.245 μm. The scattered light was collected in a backscatter method, as seen in Figure 2.6, and processed by a TSI IFA 655 digital burst correlator. The radial velocity of the flow was measured at a single point located a distance of 5 mm above the burner face and 20 mm from the axial centerline, as given in Figure 2.5. A single measured location was deemed sufficient to investigate the presence of a swirler switching effect. Duan et al. [96] previously showed that the radial velocity at this location oscillates over a range of 6 m/s over the course of a single acoustic cycle through phase resolved measurements. The axial velocity at this location undergoes a much smaller range of fluctuation. The primary velocity fluctuation is due to radial flow and thus increases in radial flow can be correlated to increased mass flow through the outer swirler.

Based on the LDV statistics, the turbulence intensities, as defined by the standard deviation divided by the mean of the radial velocity, varied from 25% in syngas and cold flow case to 40% in resonating hydrocarbon flames. The 95% confidence interval around the mean, for a total of 3000 collected samples, is 1.5% of the mean velocity in resonating flames, and 0.9% in syngas and cold flow. Continuous operation of the seeder resulted in the windows becoming coated with seed. Often if the windows were very hot, the seed could become permanently embedded in the glass. Similar behavior was observed by Stopper et al. [108], and as a result, run times were limited to smaller data sets.

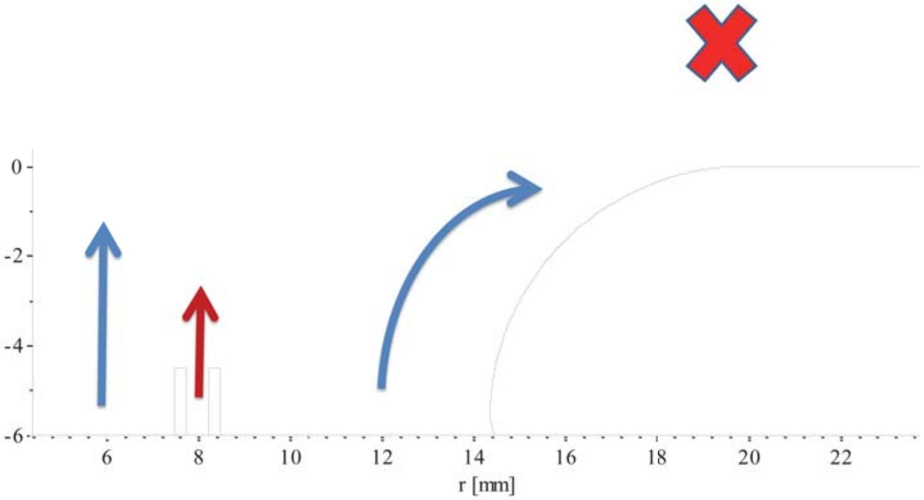

Figure 2.5: Measurement location for LDV radial velocities relative to the inner and outer swirler, r = 20mm, h = 5 mm.

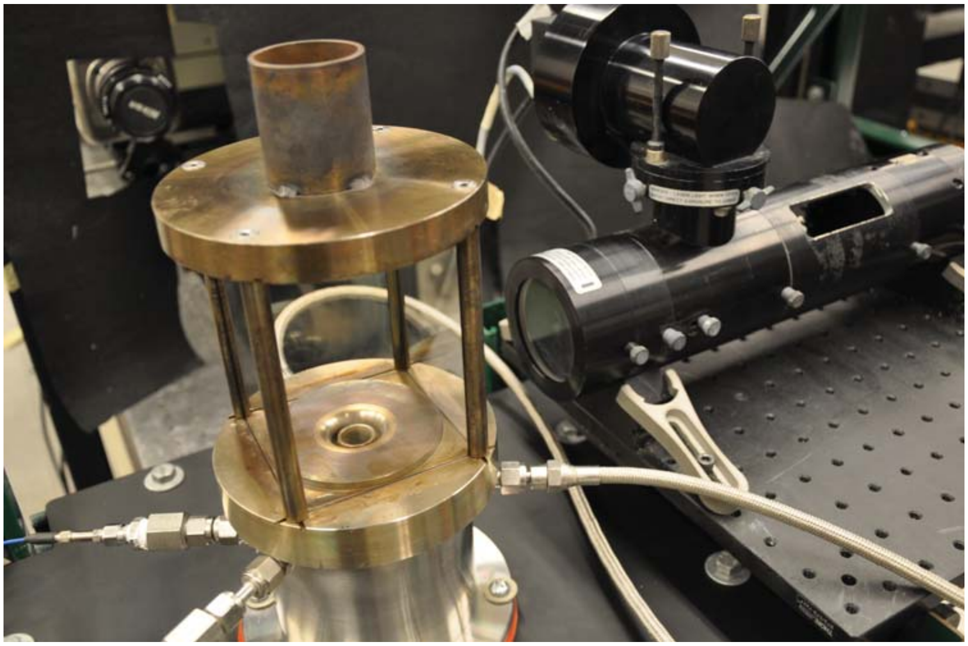

Figure 2.6: Arrangement of the LDV setup in a backscatter configuration to measure radial velocities.

2.5.1 LDV Seeding

Due to the humid shop air, clumping of the particles in the seeder became an issue. The data rates were not always consistent because the clumping would sometimes cause the seeding density to be uneven. The problem was mitigated with the use of

3M Zeeospheres, which are a blend of SiO_2 and Al_2O_3. The particle diameters varied from 4.2-5.2 μm. These particles tended to resist clumping due to the humidity.

2.6 Acetone Planar Laser Induced Fluorescence

The acetone PLIF measurements were taken as part of a separate ongoing study to investigate flame index in partially premixed flames [109,110]. This study involved the use of tracking fuel and air flow with tracers, specifically acetone for the fuel and NO_2 for the oxidizer. This investigation uses the acetone PLIF results from that study. Five fueling cases for methane, propane, and ethylene, as given in Table 2.2 were studied. The methane case, M-1, matches the fueling conditions of Weigand's Case B. The propane cases, P-1 and P-2, from the flame index study are given in Table 2.2. P-1 attempts to match similar fueling conditions to Case B, except with propane rather than methane. The acetone seeding in the propane was achieved by bubbling the propane through an acetone bath. The bath had a bypass line, through which the flow of propane could be controlled. Heat tape, connected to a PID temperature controller, kept the acetone in the bath at a constant temperature to more precisely control the acetone concentration.

As suggested by prior studies [111,112] and a previous flame modeling study [109], acetone makes an excellent fuel tracer, which fluoresces from 400 nm to 500 nm when excited by a 266 nm laser. A diagram of the layout of the lasers, cameras, and burner for the simultaneous acetone and NO_2 PLIF system can be seen in Figure 2.7. The acetone PLIF was achieved with a frequency quadrupled Nd:YAG laser (Spectra Physics GCR-130), Laser 2, at a wavelength of 266 nm. The 266 nm laser was run at 30 mJ/pulse. The laser had a pulse length of 6 ns, and pulsed at a rate of 10 Hz.

The laser beams were formed into sheets and focused using one or more cylindrical lenses, and then passed through 10% pick-off mirrors to a dye cell with an optically thick Rhodamine 6G solution to correct for the non-uniformity of the laser sheet. The distances were set up such that the laser sheets would be focused inside the dye cell. The remaining 90% of the laser sheets were then combined using a dichroic beam splitter, and passed through the burner. At the test section, the 266 nm laser sheet had a height of 10 mm, and a 1/e thickness of 250 μm at its focal point. A knife edge was used to create a sharp edge in the observed PLIF signals and the fluorescence observed in the dye cell, so that the two images could later be aligned, as suggested by Clemens [113].

The acetone fluorescence was also observed by an ICCD camera (Andor iStar DH734-25F-03), ICCD 2, with an interference filter (Omega Optical 500ASP) to allow light at wavelengths of 400 nm to 500 nm to pass. The camera was fitted with a 105 mm f/2.8D Micro-Nikkor lens. A CCD (Sony XCD-X710) imaged the dye cell, and was fitted with a 50 mm f/2.8 Nikkor lens. The acetone camera was gated to turn on 50 ns before the arrival of the 266 nm laser pulse. The gate width was set to 100 ns. A total of 450 images was taken or each condition.The ICCD had a pixel array of 1024 x 1024 pixels. The camera was re-focused each day to ensure the best possible images.

2.6.1 Acetone PLIF Errors

The signal to noise ratios for each of the cases studied are given in Table 2.3. The values are determined by examining a region of interest of uniform intensity in the acetone scalar field. The signal to noise is defined as the ratio of the average to standard deviation of the signal in this ROI. The values here indicate that the acetone PLIF signal is very clear relative to the noise. The resolution of the camera was 22 μm/pixel. After each day of trials, a series of background images was

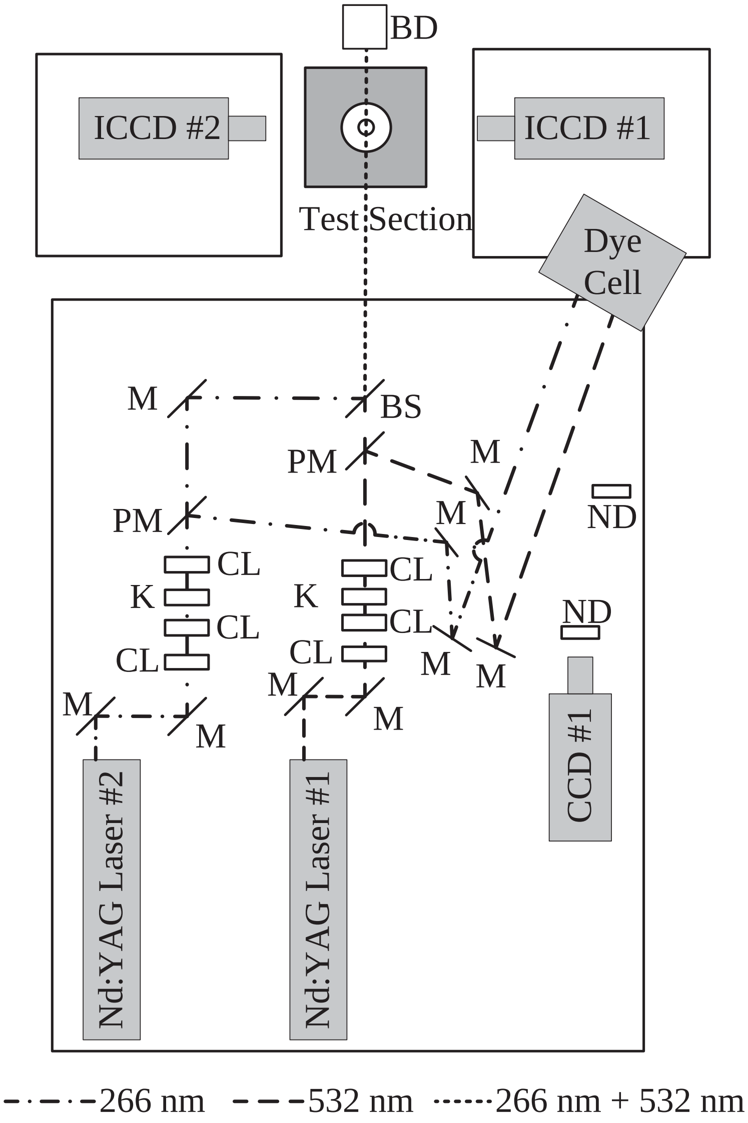

Figure 2.7: System layout for flame index measurements. Results in this study are based on the acetone PLIF measurement used to track fuel location.

taken for image corrections. Image corrections involved dark field, white field, and laser sheet corrections, as well as background corrections for the laser intensity and chemiluminescence from the flame.

Some error may be introduced in terms of how effective a tracer the acetone is for the various fuels. Acetone proved to be a very good tracer of propane according to Chemkin simulations which used a hybrid GRIMech-acetone mechanism. Propane and acetone have very similar molecular weights. However the addition of acetone

Table 2.2: Operating conditions for acetone PLIF measurements of unburned fuel localization.

Case	Air [g/min]	Fuel [g/min]	Phi	NO_2 [ppm]	Acetone Mole Fraction [%]	Fuel
M-1	304	17.4	0.76	5000	20.9	Methane
P-1	300	16.9	0.77	5000	21.9	Propane
P-2	302	26.6	1.21	5000	21.3	Propane
P-3	173	15	1.2	5000	20.4	Propane
S-1	304	36.7	0.65	5000	16.6	25% H_2 Syngas

Table 2.3: Signal to noise ratios for acetone PLIF measurements of unburned fuel localization.

Case	Signal to Noise
M-1	45.45
P-1	24.28
P-2	18.7
P-3	14.79
S-1	18.16

to propane tended to slightly decrease the flame speed of the mixture [114], which may have altered some of the instability characteristics, yet the frequency response of the flame only varied by a few Hz from pure propane flames in the same configuration. For tracer addition to methane, the acetone tended to begin to breakdown at lower temperatures, but the gradients of the consumption of each fuel were similar. However, the addition of acetone to the methane only changed the flame speed by 7% [115]. The ability of acetone to track syngas flames is more difficult to determine. As a heavier molecule, it tracks CO consumption better than hydrogen consumption through the flame. As well, due to differential diffusion, hydrogen and CO consumption profiles are not similar.

2.7 High-speed Formaldehyde Planar Laser Induced Fluorescence

High-speed methods for PIV and PLIF have been developed for laser diagnostics that enable time-resolved measurements of rapidly evolving flowfield and flame parameters [116–118]. However, high-speed formaldehyde PLIF has only recently become feasible with the advancement of laser technology to produce large pulse energies at the proper excitation frequencies. Gabet et al. [82] have conducted studies at 10 kHz in a pulse-burst laser system and Olofsson et al. [119] used a multi-YAG set up to perform 3D PLIF measurements of a bunsen flame.

In this study the 4_0^1 transition in formaldehyde is excited using a frequency-tripled diode pumped Nd:YAG Quantronix Hawk HP laser at 355 nm. The excitation at 355 nm hits the weak side bands of the transition [120, 121]. Through the use of a dye laser or an OPO, other bands which exhibit stronger absorptions could be used. Pulses around 339, 353, or 370 also have lower interference from C_2 and PAHs. However, the advantages of using the output direct from the laser are higher pulse energies and better beam profiles.

The run conditions for the set of high-speed formaldehyde experiments is given are Table 2.4. The laser power at 4 kHz was 38.8 W and at 2.5 kHz was 30.75 W. Due to the high divergence of the laser beam, the sheet height was 25 mm at the burner centerline, even though the beam diameter at the laser aperture was 3 mm. The laser beam was focused into a sheet using a single 500 mm cylindrical lens, with an 355 - 532 nm anti-reflective coating. At the test section, the laser sheet had a height of 25 mm, but expanded 1.5 mm over the width of the burner because the beam divergence was not corrected.

The 1/e thickness of the beam was 990 μm at its focal point, which was measured by rotating the sheet, and measuring the thickness of the Rayleigh scattering profile in air. This sheet is relatively thick compared to most sheets applied in PLIF. However, the minimum waist size is limited by the beam parameter product, M^2, of the laser beam. The theoretical limit for the waist formed by a given optic scales with M^2 [122]. For this laser, the M^2 was 35 according to the laser specifications, whereas typical 10 Hz Nd:YAG lasers have values less than 10. This limits the minimum thickness of the sheet formed with a 500 mm lens to 780 μm. A smaller focal length lens could have been used, but then the Rayleigh range of the focus was half the width of the field of view. The Rayleigh range scales with the square of the beam waist [123].

Table 2.4: Operating conditions for high-speed formaldehyde PLIF studies.

Fuel	Air Flow Rate [g/min]	Φ_{Global}	Frame Rate [kHz]	IRO Gate [ns]	IRO Gain [%]	Pulse Energy [mJ]
DME	170 – 282	0.75 – 1.2	4.0	200	60	9.7
Ethylene	282	0.75	2.5	100	65	12.3

The formaldehyde fluorescence was observed using a combination of a LaVision HS-IRO intensifier and a Phantom v711 high-speed camera, as seen in Figure 2.8 (Courtesy of Yuntao Chen). A 105 mm Nikon micro-Nikkor f/2.8 lens was used and the image resolution was 76 μm per pixel. The intensifier and camera were operated at the same frequency as the laser. A GG-385 filter was used to remove laser light interference below 385 nm. The lens has a UV coating and also acts as a filter for scattering from the laser sheet. The primary emitted fluorescence occurs in the range 350-550 nm, which means there is some interference due to chemiluminescence. A polarizing beam splitter was used to check that the direction of polarization of the beam was horizontal. Interferences from Raman scattering and C_2 and PAH LIF are greater with vertically polarized light [82, 124]. High speed chemiluminescence and pressure measurements were also simultaneously taken.

2.7.1 System Timing and Synchronization

The HSPLIF system was synchronized using an SRS DG-645 Digital Delay Generator. The DG-645 was used to trigger the laser, camera, and the IRO, and also to disable the IRO, when not in use to lengthen its lifetime. The triggering times are depicted in Figure 2.10. The Phantom camera was opened for the maximum exposure of 390 μs at 2.5 kHz. However the camera only receives light when the intensifier gate is open. The intensifier gate was set to 200 ns for DME and 100 ns in ethylene, to reduce chemiluminescence interference. The laser was timed to fire in the middle of the camera exposure at 100 μs. The timing of the IRO was optimized by moving the IRO gate window around the laser pulse, to determine which trigger time resulted in the best signal. Studies have shown that the fluorescence lifetime of formaldehyde is 1-10 ns, when excited with a 35 ps pulse [125, 126]. The laser pulse at these conditions is 130 ns. Since the IRO is gated in 100ns increments, a 200 ns window is needed to capture all of the fluorescence signal. Clipping of the signal was observed with a 100 ns IRO gate, with DME flames.

2.7.2 Applicability of Dimethyl Ether

The chemical properties and reaction parameters of DME under laminar flame conditions are very similar to propane [127]. This makes DME is good candidate as a replacement for propane in high-speed PLIF measurements. DME is the simplest ether and it easily decomposes into CH_3 and CH_3O, which then lead to the formation of formaldehyde. The advantage of DME lies in ability to produce significant

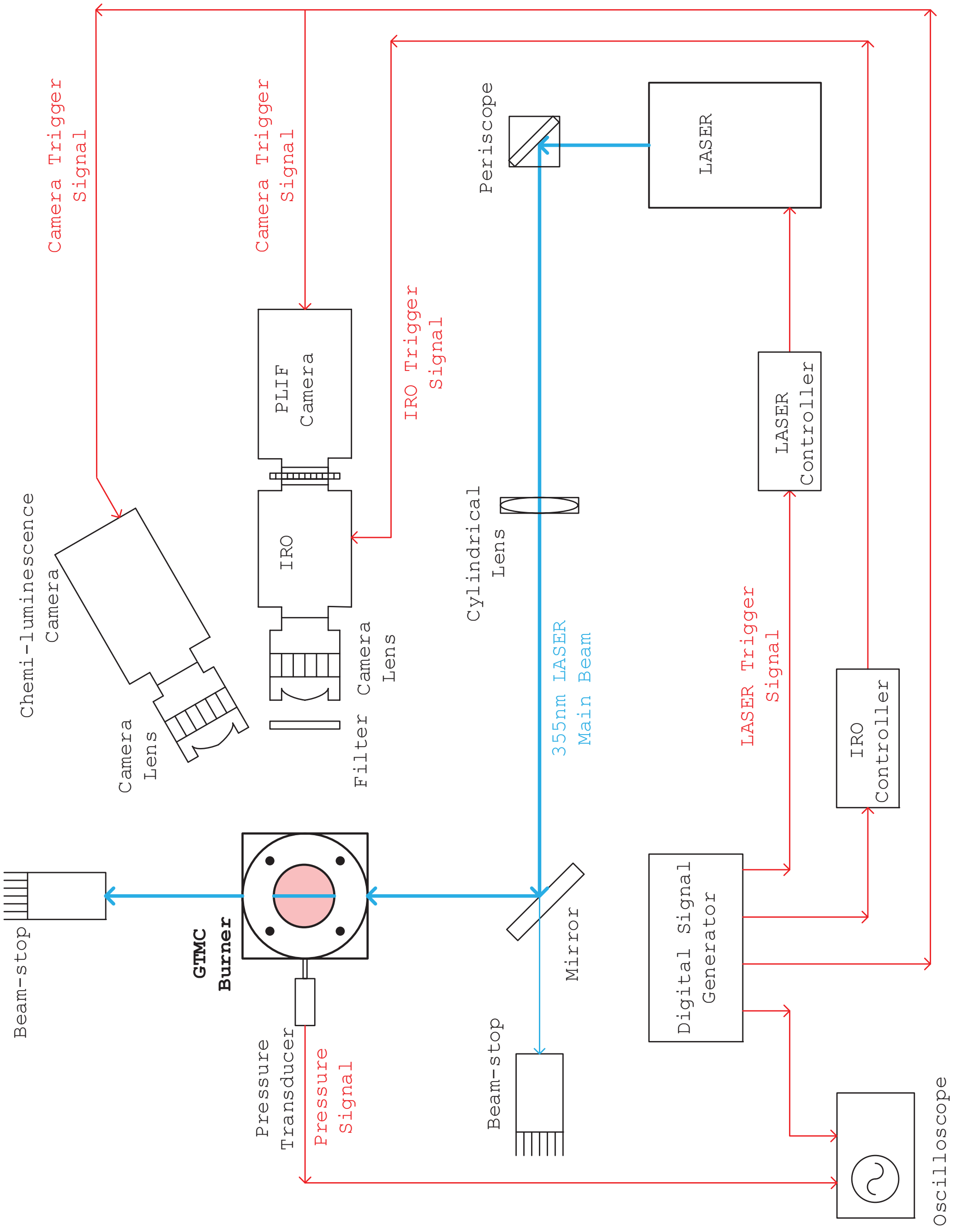

Figure 2.8: Experimental layout for high-speed formaldehyde PLIF measurements. (Courtesy of Yuntao Chen)

amounts of formaldehyde in the preheat zone. Figure 2.11 compares the production of formaldehyde in DME and methane, where it can be seen that the concentration in DME flames can be 10 to 100 times greater depending on the state of mixing. This characteristic of DME is useful in HSPLIF because the low pulse energies make the measurement almost impossible in other fuels. This means that reasonable signal to noise ratios can be achieved at pulse energies less than 10 mJ per pulse.

Gabet et al. [128] used DME in a comparison study of non-premixed methane flames. The main disadvantage concluded from this study was that DME breaks down into formaldehyde in the cool flame region of 900-1200 K. In methane flames, formaldehyde production peaks around 1500-1600 K. From Figure 2.11 the peak formaldehyde concentration shows a greater degree of spatial separation from the high temperatures and CH peak which mark the primary reaction zone, particularly in non-premixed flames. Therefore, care must be taken when interpreting the spatial location of signal in PLIF images. Nonetheless, formaldehyde from DME can be used to effectively mark the preheat-zone surface and formaldehyde reaction layer due to high signal intensities from fluorescence. As well, in premixed situations, the steepest formaldehyde gradient marks the peak of the CH layer, as a point of reference.

2.7.3 Formaldehyde PLIF Corrections and Errors

The PLIF images were background corrected for ambient light in the room and for flame chemiluminescence. Shot-to-shot corrections were not possible at the high frames rates, therefore an average correction taken from 150 images was applied. The luminosity from the flame was reduced by having a short gate time, but corrections were still needed. Another correction was needed to account for laser reflections off of walls and windows. Since the quantitative comparisons were not made and there was no need to place the formaldehyde on an absolute scale, whitefield corrections were not applied. The laser sheet intensity distribution was measured by replacing the combustion chamber with a dye cell filled with Rhodamine 6G dye in methanol. The cell was placed at the focal point of the sheet. The laser was operated at full power, but a beam-splitting polarizing cube and a glass flat were used to pick off 1% of the total power to be sent to the dye cell. This was done to prevent damage to the dye and cell if the full power of the laser were focused in the cell. The fluorescence was measured with the IRO and Phantom v711.

The images were filtered using a median 3x3 cell filter to reduce random noise in the image. After background corrections and filtering, the signal to noise ratios varied between 6.5-11.2 for the DME cases. In ethylene flames, the SNR was 6.3. This results in errors of 9-16% in DME flames and 16% in ethylene flames. The method for determining which edges were considered flame markers applied a gradient threshold. This threshold was conservatively picked to prevent selection of surfaces that do not involve flame markers.

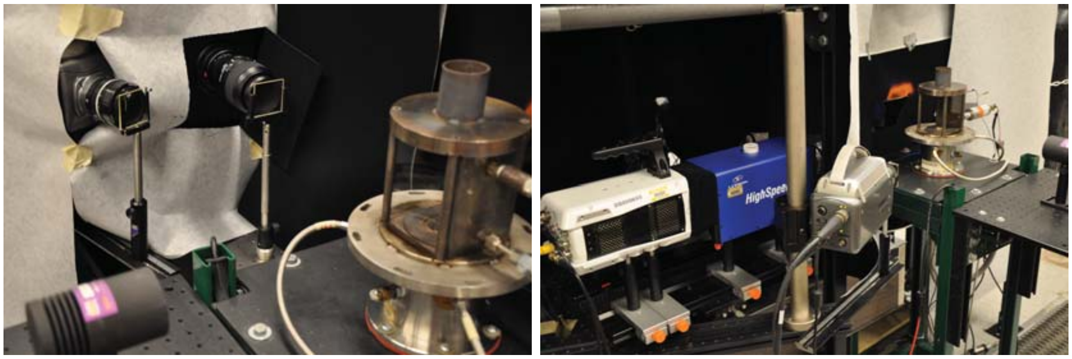

Figure 2.9: Pictures of camera, filter, and IRO layout relative to the GTMC.

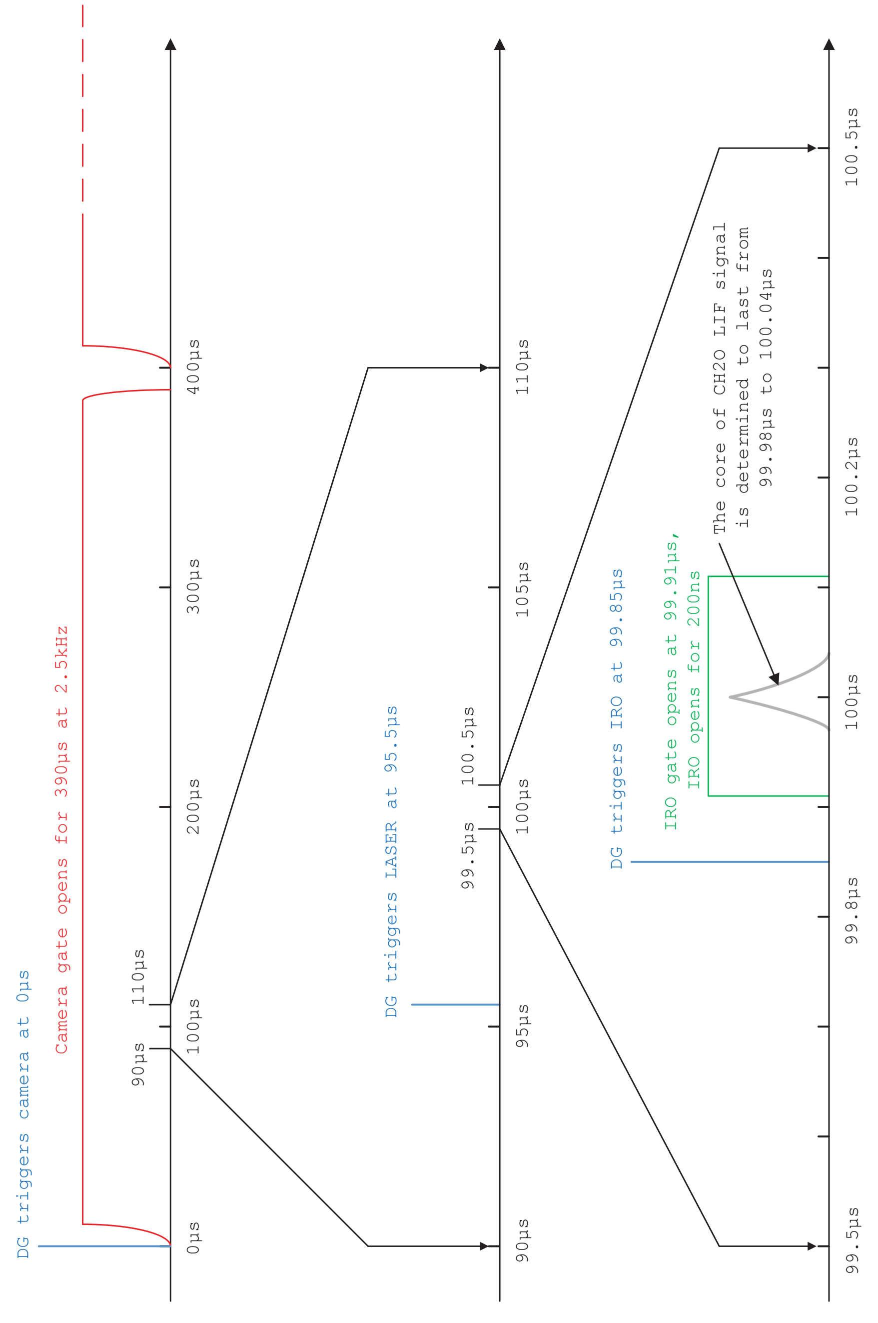

Figure 2.10: Timing diagram for triggering of laser, camera, and IRO. (Courtesy of Yuntao Chen)

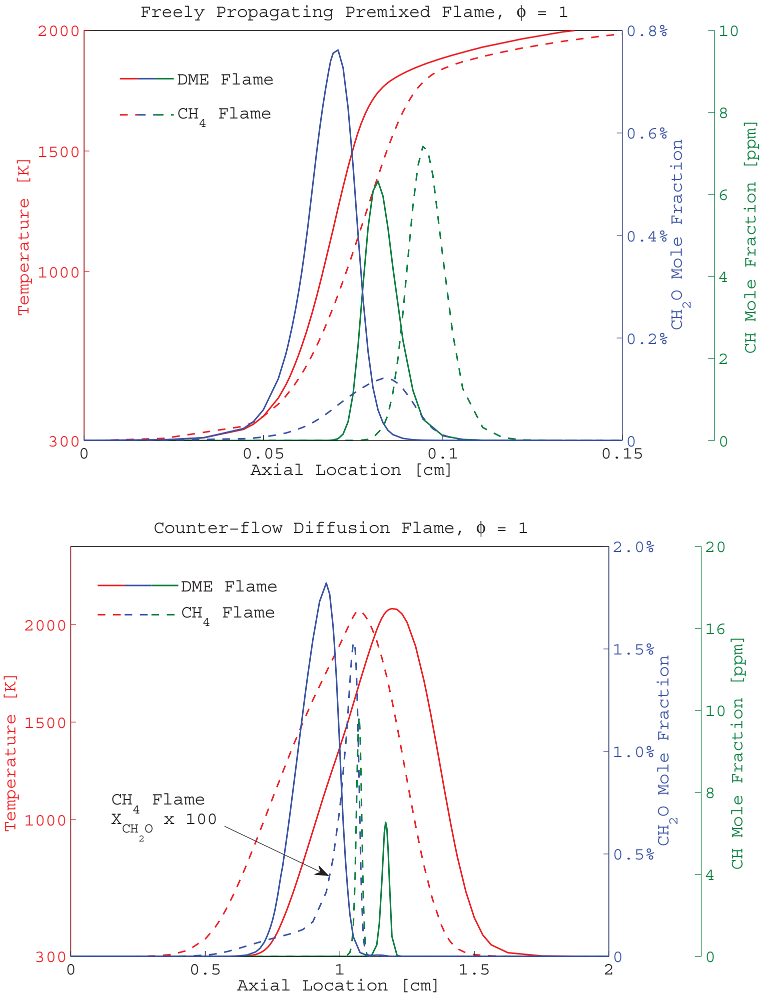

Figure 2.11: Chemkin simulations of formaldehyde production in the preheat zone for methane and DME flames. Premixed (*top*) and non-premixed (*bottom*). (Courtesy of Yuntao Chen)

CHAPTER III

Characterization of Natural Combustion Instabilities

3.1 Overview

The GTMC exhibits a natural combustion instability that is unforced. The goal of this chapter is to identify what types of acoustic and convective modes control the instability and how does the instability scale with a variation of flow parameters and modifications to the geometry. These parameter variations were conducted on a number of fuels, including methane, propane, DME, ethylene, and syngas. However, a common observation among all these fuels is that particular flame shapes are highly correlated with the presence of the instability. It will be seen that the combustor responds to Helmholtz and convective-acoustic resonances. Concepts from models developed by Hathout and Schuller will be used to explain how these modes are coupled in a single mechanism. As well, the fueling parameters alter the coupling by changing convective time scales and the phase difference between the oscillations of the pressure field and heat release.

3.2 Flame Shape and Satisfaction of the Rayleigh Criterion

The GTMC operates in three different acoustic regimes: 1) acoustically unstable and resonating, 2) acoustically stable and non-resonating, and 3) acoustically intermittent where the flame will transition back and forth between the first two modes.

This intermittent mode can be considered the marginal status between quiet and loud flames. Huang [89] and Polifke [54] have studied transitioning and bi-stable flames and shown that changes in flame anchoring and shape are important in this process. The results provided in this chapter do not involve intermittent cases, but will focus on acoustically unstable flames and flames that abruptly transition to non-resonating cases without reverting back. The frequency response of the instabilities observed are typically represented on a clean power spectrum consisting of a single resonant peak, with narrow bandwidth, a seen in Figure 3.1. This suggests that while several mechanisms may be at play, they are balanced and reflected as a single resonance, as opposed to several frequencies being observed.

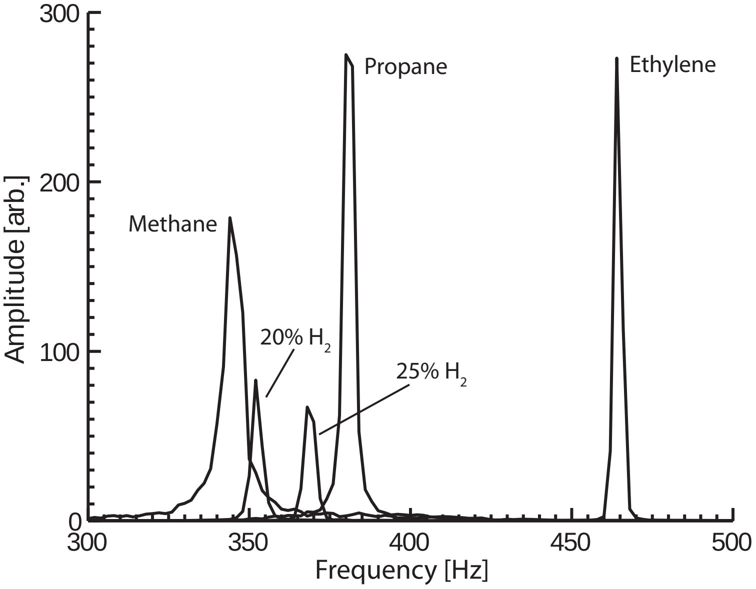

Figure 3.1: Typical power spectrum plots for the variety of fuels investigated in this thesis.

Measurements showed that the intensity of the acoustic response was linked to the flame-shape, and three distinct flame-shapes could be identified (see Figure 3.3b,d, and f). Specifically, it was observed that the instability was amplified when the flame had a flat disk-like shape (see Fig. 3.3f) that was slightly lifted. Flames that were anchored or highly lifted (light off heights less than 2mm or larger than 20mm) were generally quieter. Flames that were directly anchored to the fuel annulus were generally non-resonating. Within the unstable resonating mode, two types of shape fluctuations were observed. The first type involved a flame liftoff height oscillation where the flame would move up or downstream. Steinberg et al. [40] have shown that the flame height oscillations are due piston-like pumping of the PVC and recirculation zones. The CRZ and flame move together in an oscillatory fashion. The second motion was a change from a flat disk shape to a V-shape flame as seen in Figure 3.2, with varying degrees in between.

The change in flame shape has been observed to be correlated with the bifurcation of air flow rate through each swirler. However, when coupled with the flame blockage and pressure fluctuations, the air flow can be redistributed. A side experiment was conducted to evaluate the flame shape change when the entire air flow was redirected through only a single swirler. When flow is directed through the central nozzle, the flame is V-shaped and quieter than the nominal flame. When the inner swirler is blocked, the flow passes through only the outer swirler. Due to the curved lip of the injector at the outer swirler, a larger radial velocity is imparted to the flow, which is conducive to stabilizing a flat flame. It can be inferred that changes in flame shape as described are the result of some degree of flow redistribution, as described in Chapter 4.

A Rayleigh index was calculated according to the method described by Pun et al. [88] for resonating and non-resonating syngas flames, and for a flat propane flame. The Rayleigh index is a numerical metric to measure how well the pressure field and heat release are in phase, as described by Rayleigh's criterion, which was discussed in the Introduction. There are several ways of defining this metric, but they all try to

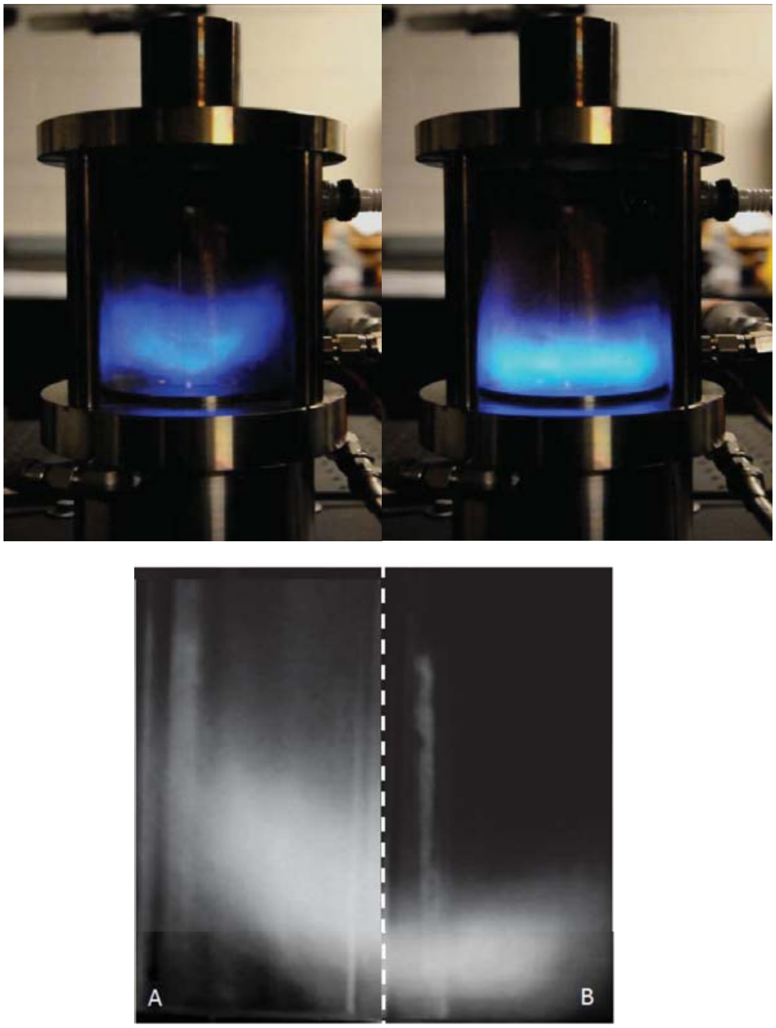

Figure 3.2: Flat and V-shaped flames as exhibited in the GTMC. Flat flames are correlated with the presence of the instability and V-shaped flames are correlated with steady combustion.

relate the local pressure and local heat release fluctuations. Equation 3.1 describes how to calculate this correlation factor:

$$RI = \int_0^1 \frac{p'q'}{p_{rms}\bar{q}} d\zeta \tag{3.1}$$

where ζ is the normalized time coordinate by the period of the thermoacoustic cycle, such that each integration results in an averaging of the coupling of every cycle. The local value of the fluctuating heat release field is correlated to the intensity of the local chemiluminescence pixel. By considering a pixel by pixel based, a 2D Rayleigh map can be constructed. However, the correlation provided here is a temporal one, it does not correlate spatially to itself, such that the pixels are treated individually. The assumption applied in calculating these values for the 2-D fields is that the pressure is operating as a bulk mode in the combustion and shows no spatial variation. The assumption has been observed to be true for methane flames [56]. Figure 3.3 depicts the Rayleigh index field alongside average chemiluminescence images of each respective flame. Each pair represents a left of centerline and right of centerline Rayleigh index and average chemiluminescence image, respectively. Rayleigh indices greater than zero represent thermo-acoustically amplified flames where the pressure field and heat release are in phase, and indices less than zero represent dampening. Figures 3.3a and 3.3b show the flame profile for a non-resonating syngas flame. The index field is populated by values that are close to zero or slightly negative which is indicative of a field with little coupling between the pressure and heat release. Figures 3.3c and 3.3d display the same characteristics for an unstable, resonating flame and there exists a strong region of amplification surrounded by dampened regions, similar to that shown by Kang et al. [129] in a low-swirl combustor.

Figures 3.3e and 3.3f depict a larger region of coupling for a flat propane flame. Also given are the Rayleigh indices for methane and DME flames in Figure 3.4. Note that for these flames, the degree of amplification is much weaker than in propane, however, these flames are still resonating. There are noticeable differences in the flame shapes between the resonating flames and the stable syngas flames. The stable flame shows better anchoring and has an axially extended V-shape profile. While the unstable syngas flame is not as flat as the propane flame, its profile is wider at its base than the stable syngas flame, which implies a higher degree of premixing.

The change in flame shape may also be attributed to the swirler redistribution mechanism. An increase in the flow rate through the central nozzle will lead to a higher axial velocity and a longer V-shape flame. Higher flow rate through the outer swirler will support a flat flame with enhanced mixing. Flat flames are acoustically compact and concentrate heat release in a smaller portion of the burner than an axially extended V-flame. Thus, V-flames are less efficient at applying thermal energy toward acoustic amplification. An explanation for why flat flames are louder than V-flames is provided in Section 3.9.

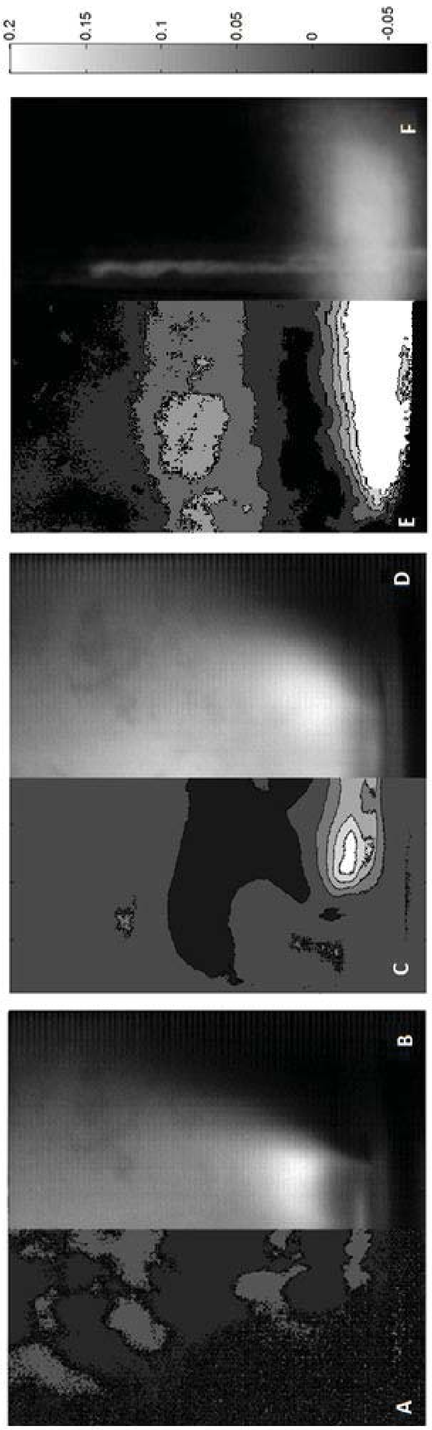

Figure 3.3: Rayleigh index (*left*) and time-averaged chemiluminescence (*right*) of syngas and propane flames for $\phi = 1$, air $\dot{m} = 282$ g/min. (a,b) Stable syngas flame, 40% H2, 60% CO. (c,d) Unstable resonating syngas flame, 25% H2, 75% CO. (e,f) Unstable resonating propane flame.

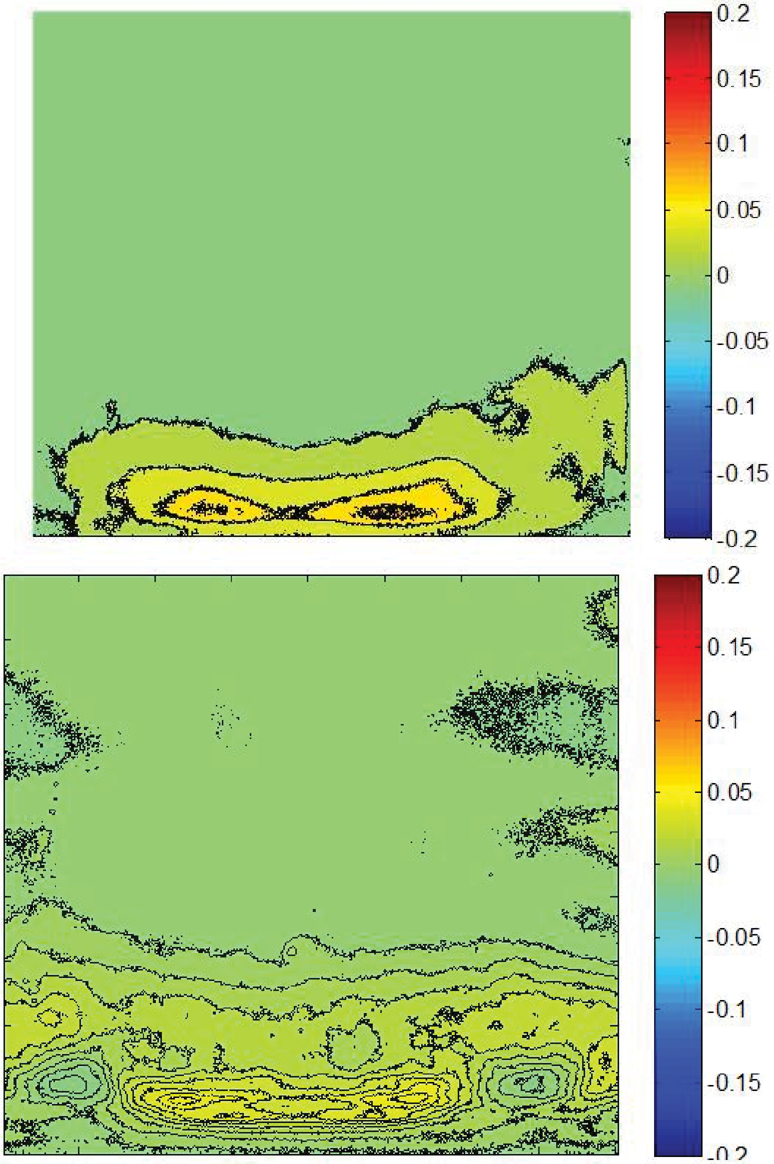

Figure 3.4: Rayleigh indices for methane (*top*) and DME (*bottom*) flames, for $\phi = 1$, air $\dot{m} = 282$ g/min.

3.3 Equivalence Ratio Variation

Figure 3.5 shows the measured frequency and amplitude response of the pressure oscillation with varying equivalence ratios. The equivalence ratio reported here is a global value, since there is no premixing. However, it is expected that once the gases leave the injector there will be some degree of premixing over the liftoff height. The frequency response generally increases with equivalence ratio, except for alkanes which show non-monotonic trends. Although this is suggestive of a flame speed scaling, the frequencies for matched fuels are not similar. The 25% syngas mixture matches the ethylene data only at $\phi = 1$. The fuel-rich ethylene data does not match the 20% syngas data, which have the same flame speed. This indicates flame speed is not the direct controlling factor; rather, another parameter, perhaps indirectly coupled with flame speed, controls the acoustic performance. These trends also cannot be attributed solely to changes in the speed of sound due to variation in the adiabatic flame temperature. The speed of sound only varies with the square root of the temperature, which does not capture the range of frequencies observed.

The amplitude behavior with equivalence ratio shows varying trends with each fuel. Propane shows a decrease in instability strength, while ethylene flames resonate more powerfully with increasing equivalence ratio. Both syngas mixtures show little variation in strength. It is evident that these behaviors are not all consistently scaled with the increase in global heat release.

3.4 Air Mass Flow Rate Variation

Instabilities that are of a convective-acoustic type display a frequency that varies with the gas velocity, while those that are pure organ tones or Helmholtz types do not. To investigate these effects the air mass flow rate was varied. Figure 3.6

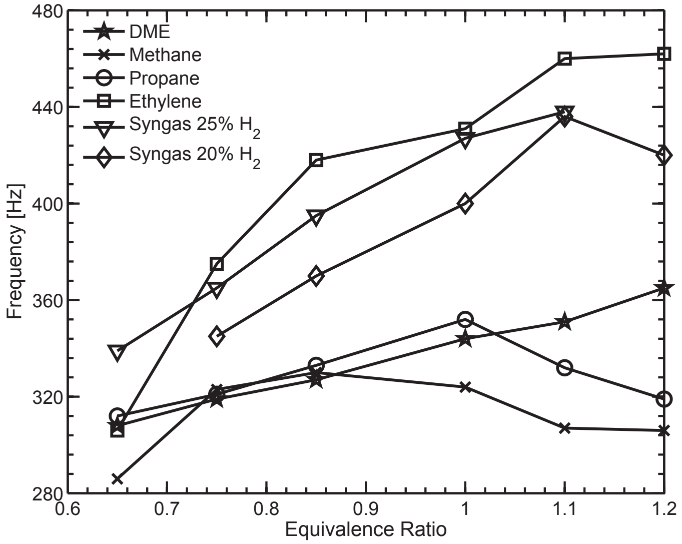

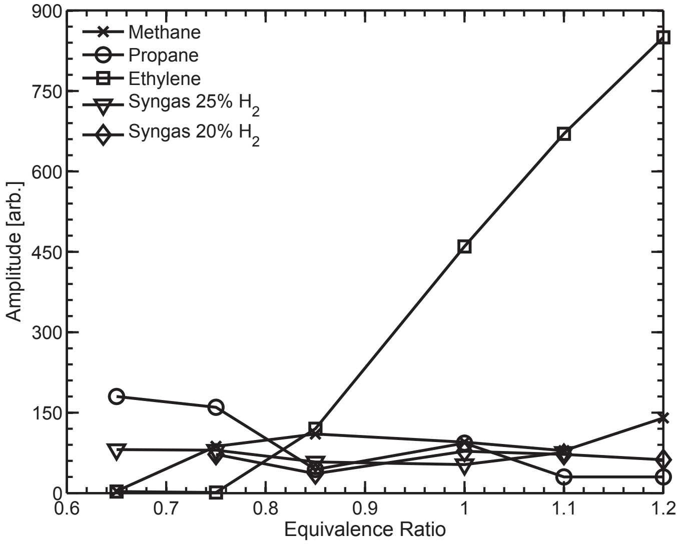

Figure 3.5: Frequency as a function of equivalence ratio (*top*) and PSD amplitude as a function of equivalence ratio (*bottom*) for air $\dot{m}$ = 282 g/min.

indicates that the frequency of the instability increases with an increase in the mass flow rate. This suggests that the instability depends on a Strouhal number and has a convective-acoustic component. The frequency data in Figure 3.6 are similar for the syngas (25% H2) and ethylene, which have the same flame speeds. The relationship between these two fuels also may have similar anchoring and mixing properties at $\phi = 1$.

The amplitude data for the syngas and the hydrocarbon fuels are very different. While syngas drops in amplitude strength, thermoacoustic instabilities are amplified at higher flow rates for hydrocarbons. Ethylene proved to be significantly louder than all other fuels, as seen where it is rescaled by a factor of five. In comparison to hydrocarbons, the lift-off height is reduced for syngas mixtures. When this effect is combined with higher inlet velocities and the high diffusivity of hydrogen, reduced mixing can occur. The nominal flame shape is also different between the types of fuels presented. The hydrocarbon flames are typically observed to be flat, whereas the syngas flames have a wide V-shape, which tends to make them quieter.

Convective-acoustic effects are typified by equivalence ratio oscillations, particularly in partially-premixed systems. Due to this type of mixing, inhomogeneities in fuel-air ratio can create packets of fluid capable of causing heat release fluctuations. These packets must be convected to the flow, where unsteady heat release causes pressure fluctuations which are reflected back to the injector, furthering the formation of uneven mixing. The frequency of the feedback is set by the characteristic time of the cycle for packets to be convected to the flame and then have pressure waves reflected back. This characteristic time is reduced if convection speeds are increased, thus increasing the frequency of the instability.

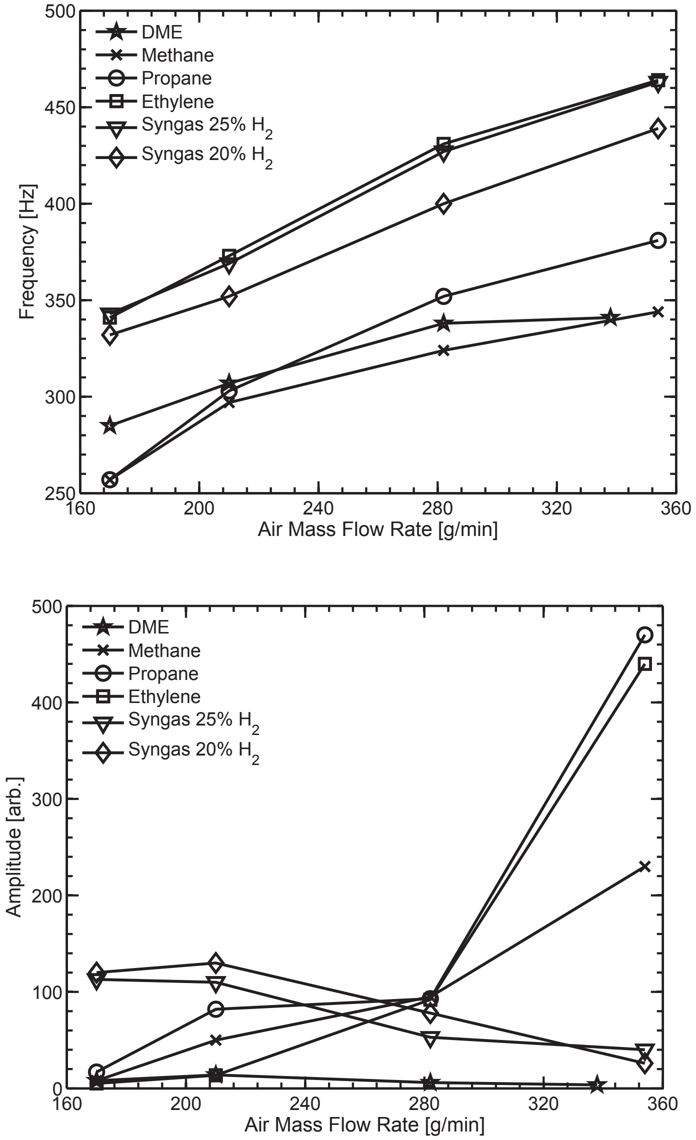

Figure 3.6: Frequency as a function of air mass flow rate (*top*) and PSD amplitude as a function of air mass flow rate (*top*), for $\phi = 1$. Ethylene amplitude data rescaled down by a factor of five.

3.5 Syngas Composition Variation

The frequency at a given equivalence ratio is approximately independent of the hydrogen concentration as shown in Figure 3.7. From this figure, it can be seen that with increasing hydrogen-content (resulting in decreasing molecular weight) the flame speed increases until a hard cutoff occurs, in which the instability is rendered inactive and the flame becomes non-resonating. The concentration at which this "quiet" limit occurs is equivalence ratio dependent, but the limit is extended for richer flames. Within the range of equivalence ratios considered, the maximum cutoff occurs near 43% H_2. Transitions such as these were observed in the hydrocarbon fuels, but these shifts were correlated with the swirler distribution mechanism and dramatic flame shape changes. As well, this shift is quasi-stable for syngas, where once the flame is non-resonating, it will not transition back to unstable. Hydrocarbon fuels can display intermittent behavior where resonant transitioning can occur.

The amplitude of the dominant pressure signal is not equivalence ratio independent. As the "quiet" limit is approached, the instability strength is reduced until silent. This type of behavior suggests that thermoacoustic instabilities can be reduced by increasing the hydrogen content of the fuel. By also operating fuel-lean, the amount of hydrogen required to silence the flame is reduced. The data also suggests that a critical combination of flame speed, diffusivity, and fuel density may control the acoustics for syngas. Lewis number effects may also play a role in setting the critical limit at which syngas flames transition. The transition point occurs very quickly over a small percentage change in composition. Syngas flames are thermo-diffusively unstable due to the nature of the mixture components and may respond to the applied strain differently than hydrocarbon flames.

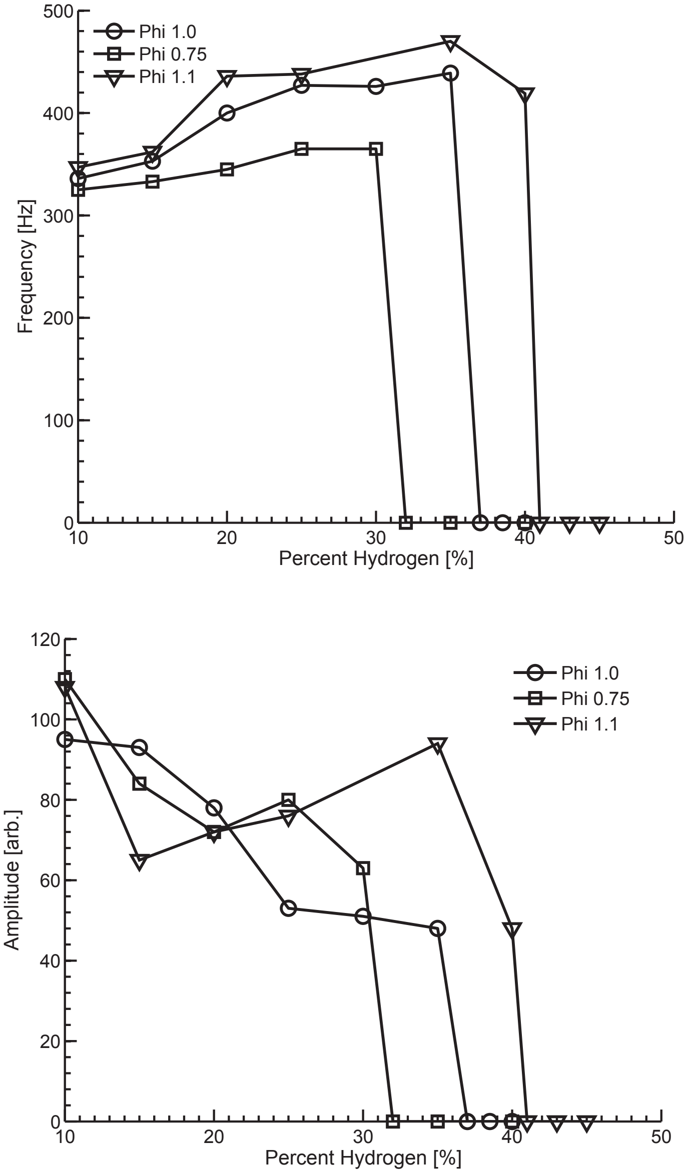

Figure 3.7: Frequency as a function of hydrogen composition (*top*) and PSD amplitude as a function of hydrogen composition (*bottom*) ; for air $\dot{m}$ = 282 g/min.

3.6 Flame Speed Correlations

Figure 3.8 shows the relationship between the observed frequency and the laminar flame speed of a given mixture at all studied equivalence ratios for air $\dot{m} = 282$ g/min. Flame speed data for propane and methane [130], ethylene [131, 132], and syngas mixtures [133,134], were acquired from published literature. An approximately linear relationship between frequency and flame speed can be seen. However, the slope of each curve differs, thus each fuel behaves in different manner. Flame speed affects several things: liftoff height, the speed at which the flame flashes back after it is forced to move downstream, and flame shape. As well, with turbulent combustion, the turbulent flame speed and degree of wrinkling are all linked to the laminar flame speed. Within the range of equivalence ratios studied, syngas mixtures above 43% hydrogen are non-resonating, which implies that flame speeds above 110 cm/s may result in quiet flames in this burner.

The flame speed of the fuel appears to play a role in the acoustic behavior, however it may be a secondary effect between factors which directly scale the flame speed, such as heat release, local reaction rate, molecular weight and diffusivity. Several fuel-air mixtures studied have the same flame speed of 40 cm/s, yet they exhibit varying trends. Molecular weight is known to control thermo-diffusive instabilities in flames which could play a role in the acoustic instability-mechanisms that were studied, as suggested by the present data. The propagation speed of a turbulent flame depends on the molecular weight of the fuel; if the reactants are thermo-diffusively unstable the flame becomes more wrinkled and propagates faster than a stable mixture, even when the laminar burning velocities are matched. As well, the temperature dependence of these fuels can also affect the location of the stabilization.

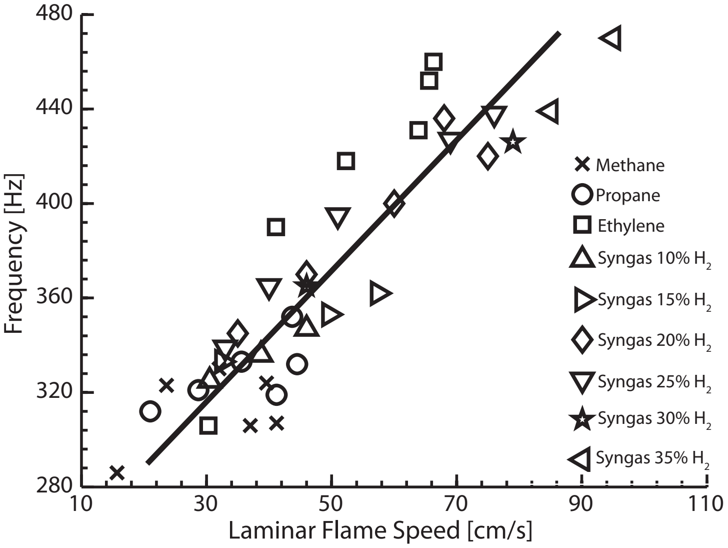

Figure 3.8: Frequency as a function of laminar flame speed for fuels studied at air $\dot{m}$ = 282 g/min, for varying ϕ = 0.65 - 1.2.

3.7 Speed of Sound Variations

For the measurements presented thus far, the data was taken at a consistent burner core temperature as described in Chapter 2. This section presents frequency measurements due to variation of the burner temperature, as well as some interesting behavior that occurs as the burner warms up. The ideal situation to avoid temperature effects is to have the burner warm up until it has reached thermal equilibrium. However, that would require up to 30 min of continuous operation before data can be collected. As a result of concerns regarding deformation of the injector, warping of the window posts, and damage to the thin quartz windows, the burner was operated to a consistent temperature (333 K), and then measurements were made. However, as the burner warmed up, measurements were made in 11K increments. Figure 3.9 depicts the increase in frequency observed as the burner core temperature increases. It is important to note that the temperature in the burner core serves as a proxy to the actual temperature inside the combustor chamber, thus the temperature dependence shown does not necessarily exhibit a square root dependence.

Figure 3.10 shows an interesting behavior observed where banding occurs which causes jumps in the dominant frequency. Each band displays a general increase in the frequency and a new band will appear at a frequency 10-20 Hz higher. For propane flames, a jump to the next band occurs near 337K. The color of each band represents the amplitude of that particular peak. There exists a slight overlap at the end of each band with the onset of the next peak. In order to be consistent, data presented in this chapter have been recorded within the first band. A series of power spectrum plots, showing how the transition from one peak to another occurs as a jump is approached, is given in Figure 3.11.

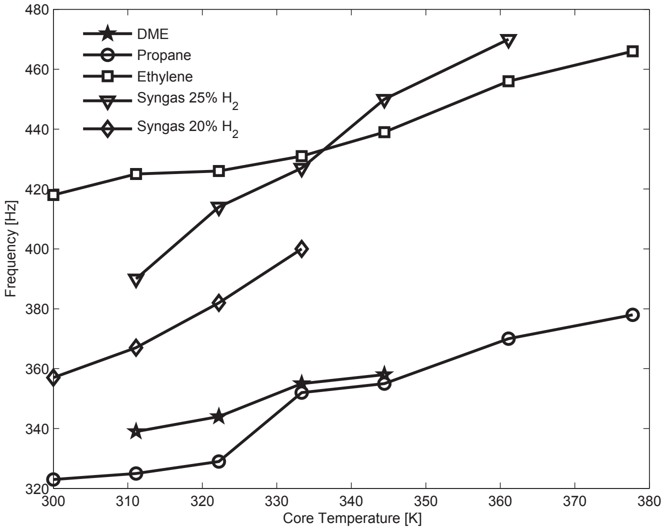

Figure 3.9: Frequency as a function of burner core temperature for fuels studied at air $\dot{m}$ = 282 g/min, $\phi = 1.0$.

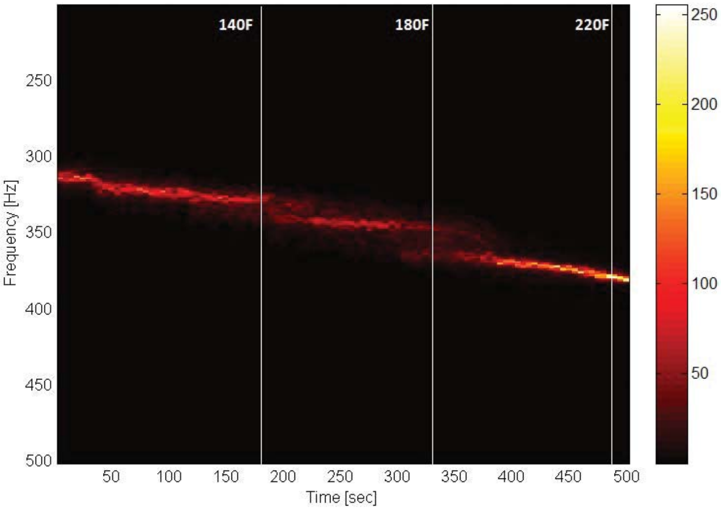

Figure 3.10: Amplitude (arbitrary units) at each frequency of the power spectrum as the burner core temperature is increased reveals banding, for propane, air $\dot{m}$ = 282 g/min, ϕ = 0.75.

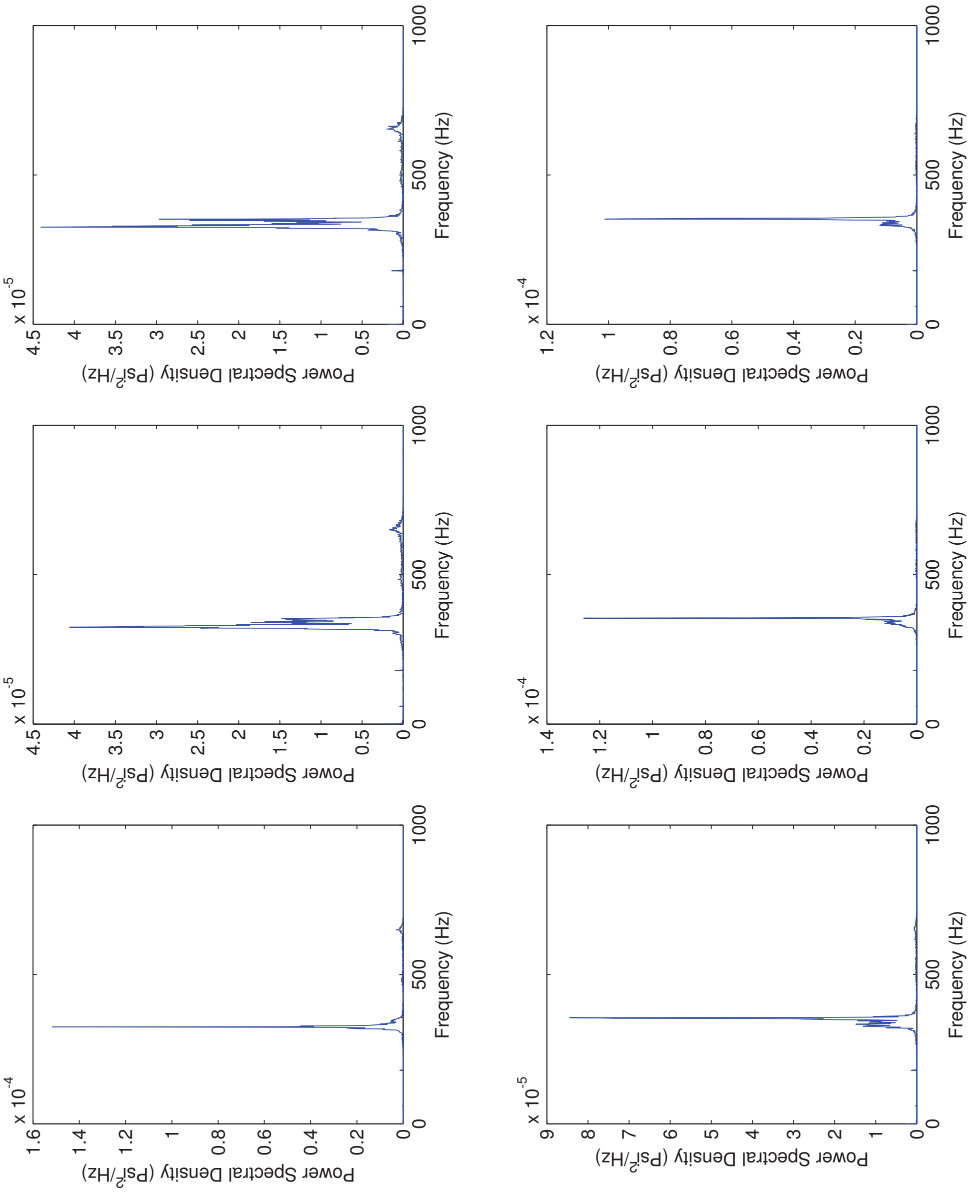

Figure 3.11: Power spectrum plots depicting the transition from one temperature band to another with increasing burner temperature, in propane flames, air $\dot{m}$ = 282 g/min, $\phi = 0.75$.

3.8 Burner Configuration Variations

The dimensions of the GTMC combustion chamber, exhaust tube, and plenum were varied to investigate Helmholtz and organ tone behavior. When the combustion chamber length was varied from 75 to 300 mm, no frequency shift larger than 8% was observed. This result indicates that a standing quarter wave, which scales with combustor length, is not present. The combustor diameter was reduced to 50 mm resulting in an 11% shift to a lower frequency. However, this also results in the flame being disturbed. This variation in combustor chamber volume also indicates that there is no Helmholtz mode associated with the chamber itself.

The volume of the plenum was also varied to determine if an organ tone or Helmholtz resonance is associated with its dimensions. Figure 3.12 depicts the drop in frequency with increasing the plenum volume by increasing its overall length. This variation may imply that the plenum of the burner acts as the Helmholtz resonator, with the turbulent combustion in the chamber driving the resonance.

The largest frequency changes were observed in variations involving the exhaust tube, as seen in Figure 3.12. These measurements were taken at an equivalence ratio of $\phi = 0.75$. However, the burner was allowed to warm up to a higher temperature before measurements were collected. This was done to allow for the extended chimney length to equilibrate more evenly. As well, all metal walls were used in the chamber with no optical access provided. This was done to prevent the shattering of windows that occurred with increased instability amplitude as a result of chimney dimensional variation. The observed trends indicate that decreasing the diameter of the chimney or increasing its length will decrease the observed frequency. Both these variations will also strongly increase the amplitude of the resonance. However, the trends appear to begin to asymptote at small diameters and long extensions. This insensitivity may suggest that the combustion coupling no longer responds to alterations of the exiting flow pattern. As well, any further reduction of the diameter results in extremely strong chugging pulsations which unseat the chamber from the plenum.

The final modification to the burner involved variation of the combustor walls. For complete optical access, the metal walls can be replaced with 4 thin quartz window sheets. Variation of the number of glass windows in place showed that the observed frequency was reduced. The difference in the measured frequency between having all metal walls and all quartz windows was 20Hz. This difference may be due to increased heat transfer out of the combustor due to the thin windows in comparison to the much thicker metal walls. This would lower the overall temperature in the burner and decrease the speed of sound in the chamber.

3.9 Application of Helmholtz Theory in a Conceptualized Model

The GTMC provides a complex combination of heat release coupled with pressure perturbations provided by the resonances of particular volumes. Based on the results of Section 3.8 it can be concluded that the plenum is acting as a Helmholtz resonator which is driven by heat release in the combustion chamber. The chimney acts on the chamber to affect the degree of heat release by changing the impedance of the system. The chamber itself is not resonating due to its geometry, but rather responds to the fluctuations created by the plenum geometry.

The standard Helmholtz model is not applicable in this system because it ignores the applied heat release. As well, the geometry of the standard resonator does not capture the effects of the inlet, the swirler ducts, and the chimney. The one principle

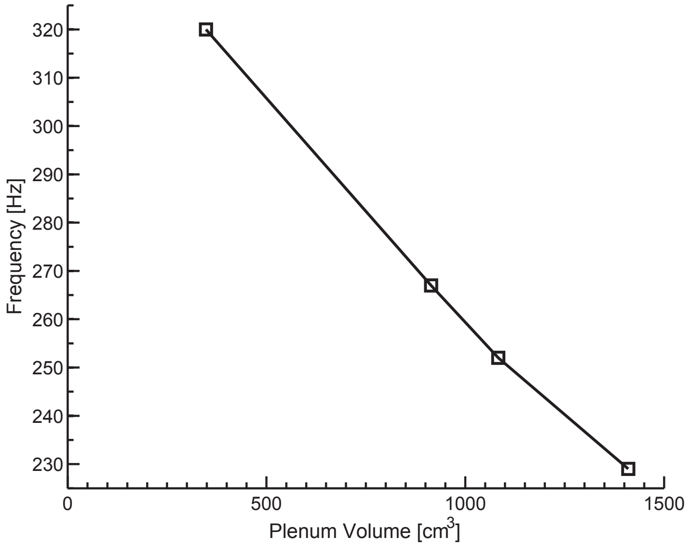

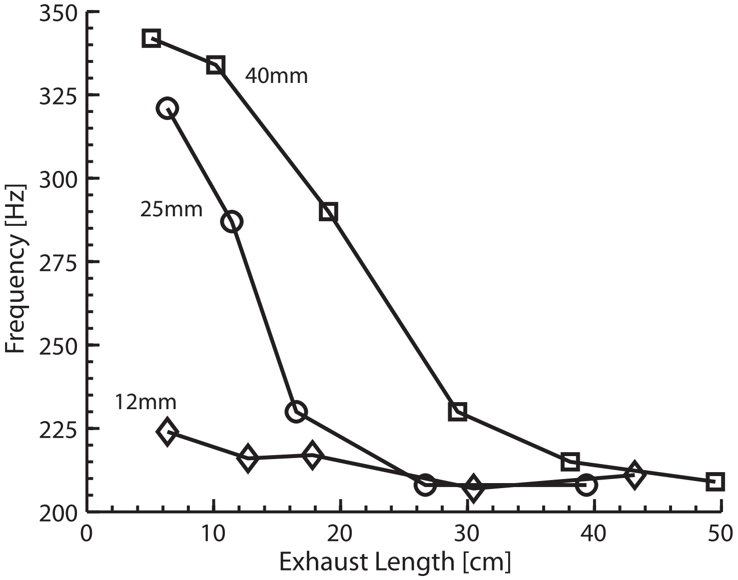

Figure 3.12: Frequency variation with increasing plenum volume (*top*), for propane at air $\dot{m}$ = 282 g/min, $\phi = 0.75$ and frequency response to variation of chimney geometry at elevated temperatures (*bottom*), for propane at air $\dot{m}$ = 282 g/min, $\phi = 0.75$.

that does apply is location of the forcing. Helmholtz resonators are activated by white noise perturbations acting on a slug of fluid mass in the neck of the resonator. The forcing comes externally, and the volume resonates causing the fluid mass to oscillate. In this model, the velocity perturbations within the volume are small, but the mass in the neck moves in response to the pressure fluctuations like a mass on a spring represented by the volume. As well, there is a certain degree of damping to the volume.

There are many combustion driven models for resonators available, however the trends observed in the GTMC are best captured by concepts applied by Hathout et al. [135] and Schuller et al. [58]. The Hathout model captures the effect of heat release on a Helmholtz resonator, while also incorporating flame and fueling parameters which affect the heat release. The Schuller model is able to apply a similar geometry to the GTMC and explain how the chamber can be decoupled from the plenum which acts as a Helmholtz resonator. These two models will be applied to conceptually explain the trends observed in the GTMC.

The Hathout model focuses on a Helmholtz resonator as depicted in Figure 3.13, where the combustion occurs inside the volume and drives it. The governing equation, derived from the manipulation of the mass, momentum, and energy equations for this system, is given by:

$$\frac{\mathrm{d}^2 p'}{\mathrm{d}t^2} + \frac{1}{V}\left[c_i^2 A_i \frac{\partial p_i'}{\partial x}(L_i, t) - c_e^2 A_e \frac{\partial p_e'}{\partial x}(L_e, t) \right] = \frac{\gamma - 1}{V}\frac{\mathrm{d}Q'}{\mathrm{d}t} \tag{3.2}$$

where the subscripts e and i represent the exit and inlet parameters respectively. Equation 3.2 can be further simplified with the assumption that the pressure distribution in the ducts is negligible, which arrives at the driven Helmholtz equation:

$$\frac{d^2 p'}{dt^2} + 2\zeta\omega\frac{dp'}{dt} + \omega^2 p' = \frac{\gamma - 1}{V}\dot{Q}' \tag{3.3}$$

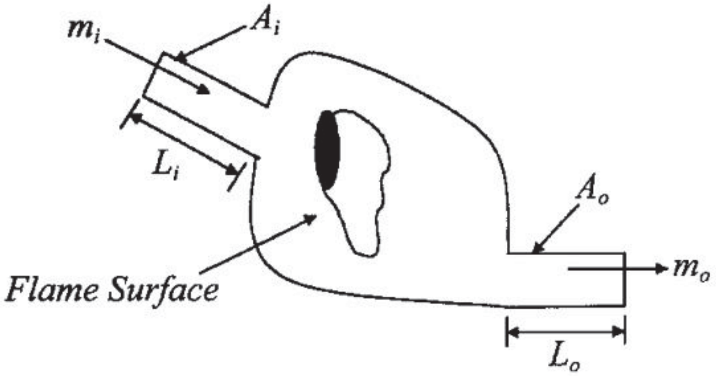

Figure 3.13: Schematic diagram of a combustor exhibiting a Helmholtz-type resonance [135].

The frequency, ω, given here is the Helmholtz frequency if the boundaries are acoustically open. The Helmholtz frequency for a dual ducted volume is given by:

$$\omega_H = \sqrt{\frac{c_i^2 A_i}{L_i V} + \frac{c_e^2 A_e}{L_e V}} \tag{3.4}$$

These equations represent the acoustics of this type of chamber. The effect of heat release is captured through the development of an equation which relates the heat release to basic fueling parameters, the flame speed, heat of combustion, velocity fluctuations, equivalence ratio fluctuations, flame surface area, and the dependence of flame speed and heat release on equivalence ratio, and a characteristic time of propagation delay based on the flame speed and a length, such that:

$$\dot{Q}' = d_0 u' + d_1\left[u'_{\tau_f}(t)\right] + d_2\left[\phi'_{\tau_f}(t)\right] + d_3\phi' + d_\phi\dot{\phi}' \tag{3.5}$$

where the coefficients d_n are functions of flame speed variation with equivalence ratio, density, geometry, flame surface density, and heat of combustion. As well, the propagation delay is given by:

$$\tau_f = \frac{R}{\bar{S}_u} \tag{3.6}$$

$$\dot{Q}' = f\left(u', S_u, \tau_f, \phi', \frac{\partial S_u}{\partial \phi}, \frac{\partial \Sigma}{\partial r}, \Delta h_r, \frac{\partial \Delta h_r}{\partial \phi}, \rho\right) \tag{3.7}$$

This model also accounts for flame shape in that there are parameters within the coefficients d_2 and d_ϕ which deal with the spatial location of the flame surface and area fluctuations. Now we have a set of equations which describe the heat release dynamics and acoustics. The coupling mechanism between them arises in the form of equivalence ratio oscillations or velocity perturbations. The instantaneous equivalence ratio at the exit is given by :

$$\phi_s = \frac{\bar{\phi}}{1 + \frac{u_s'}{\bar{u}}} \tag{3.8}$$

However, there is also a convective delay of the inhomogeneity from the nozzle to the flame given by $\tau_c = L/\bar{u}$. The new equivalence ratio perturbation is given by:

$$\phi' = \phi_s'(t - \tau_c) \tag{3.9}$$

Longitudinal perturbation can also be coupled into this model by use of the energy equation to show that the instability can be induced by both fluctuations in u and ϕ. When the combustion dynamics are dominated by a bulk motion, such as in the Helmholtz volume, the instability is mainly controlled by convective effects, which primarily induce ϕ oscillations. However velocity perturbations at the exit of the exhaust port can be created by the motion of the fluid plug in the exit. The differential equation takes the form of the following, when dominated by convective effects:

$$\ddot{\eta} + 2\zeta\omega\dot{\eta} + \omega^2\eta - \beta_1\eta(t - \tau_c) = 0 \tag{3.10}$$

where η represents p' and all of the heat release dependencies are captured in the coefficient β_1. The frequency, ω represents the forcing attained as a Helmholtz resonator. However, no part of this model requires that the forcing occur inside the volume. The forcing due to combustion is only time dependent, not spatially dependent within the volume. The GTMC observations show that the chamber is not resonating in a Helmholtz fashion, rather the plenum is acting as the resonator. To account for this, the physical layout of the model will be altered to account for the actual driving location of the physical flame. This type of layout is captured in Schuller's model as seen in Figure 3.14.

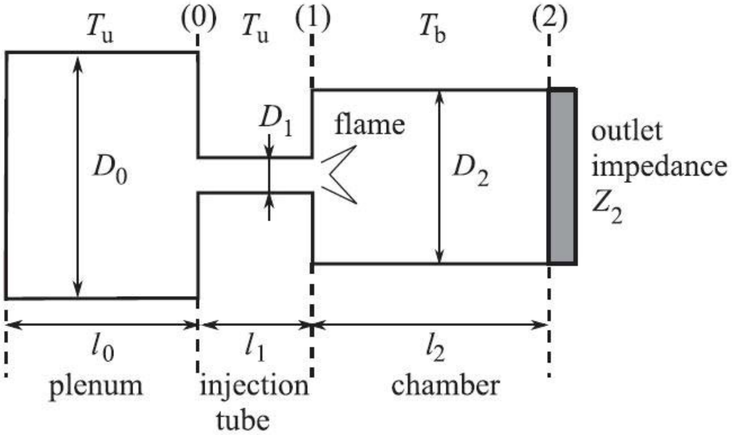

Figure 3.14: Schematic view of a combustor modeled by three coupled cavities with an arbitrary outlet impedance [58].

In this model, the plenum acts as a Helmholtz resonator, but the combustion has been moved to the exterior of the volume and drives the resonance by forcing the plug of air in the neck, represented by the swirler ducts. In the same way that white noise perturbations would drive the resonance of a Helmholtz without heat release, the turbulent combustion performs this role. The equations given previously still hold. The spatial relocation of the driving force is accounted for in the propagation time, τ_f, and the convection time, τ_c. These characteristic times will now take on different values to account for the spatial location and time to convect perturbations to and from the flame.

The Hathout model is able to account for many of the fuel based trends observed in this chapter through the inclusion of heat release in driving the resonance. However, the fact that the chamber does not resonate is only captured in a sense. Similar to how the white noise exists in the "environment" outside the resonator, the chamber and flame represent this "environment" outside the plenum. However the resonance is not coupled in the form of having two geometric resonators. The pressure fluctuations measured in the chamber are due to a reflection of the motion inside the plenum. The Schuller model explains that the two chambers can be decoupled in this manner via a coupling index:

$$\Xi = \frac{A_1}{A_2}\frac{\rho_u c_u}{\rho_b c_b} \simeq \frac{A_1}{A_2}\sqrt{\frac{T_u}{T_b}} \tag{3.11}$$

where the subscripts 0, 1, and 2 represent the cavities in Figure 3.14. The model explains that if Ξ is small ($\Xi \ll 1$), then the plenum and chamber are effectively decoupled. The combustor acoustics are then preferentially controlled by the plenum Helmholtz resonance if the area ratio from the chamber to the injector is small and the temperature jump across the flame is large. For the GTMC, Ξ is typically 0.033, indicating that the chamber will reflect the plenum behavior. The model was examined for the simple case of open combustion chambers and for combustors featuring an exhaust. For the open chamber the net frequency is given by:

$$\omega = \omega_H \left[1 - \frac{1}{2} \Xi \left(\frac{V_0}{V_1} \right)^{1/2} \frac{\omega_H l_2}{c_b} \right] \tag{3.12}$$

In this equation, ω_H is the same as given in Equation 3.4. The chamber effects will modify the frequency and yield a new ω. For small values of Ξ, the length of the combustor, l_2, will have little to no effect on the observed frequency and the observed frequency will be similar to the expected Helmholtz frequency. Note that Equation 3.12 is coupled into Equation 3.10 from the Hathout. This coupling allows for the heat release effects on ω to be accounted for. The Schuller model does not account of any of these effects but rather treats the flame as a compact surface across which the speed of sound changes. The combination of these two models now explains why the chamber geometry does not affect the resonance and how flame parameters are coupled into the process.

The final effect to account for is variation of chimney geometry. The presence of a chimney increases the impedance, ζ, of the system by resisting the outlet flow from the chamber. In examining extremes, zero impedance implies an open boundary and infinite impedance implies a closed combustion chamber. The relationship between the observed ω, the expected ω_H, and the impedance is given by:

$$\begin{aligned} 0 = {} & \left(1 - \frac{\omega^2}{\omega_H^2}\right) \cos\left(\frac{\omega l_2}{c_b}\right) - \Xi \left(\frac{S_0 l_0}{S_1 l_1}\right)^{1/2} \sin\left(\frac{\omega l_2}{c_b}\right) \frac{\omega}{\omega_H} \\ & - i\zeta_2 \left[\left(1 - \frac{\omega^2}{\omega_H^2}\right) \sin\left(\frac{\omega l_2}{c_b}\right) + \Xi \left(\frac{S_0 l_0}{S_1 l_1}\right)^{1/2} \cos\left(\frac{\omega l_2}{c_b}\right) \frac{\omega}{\omega_H} \right] \end{aligned} \tag{3.13}$$

where the exit impedance is given by ζ_2. At minimal impedance, Equation 3.12 is recaptured. The effect of infinite impedance is to lead to the formation of half-wave longitudinal modes within the chamber due to the acoustically closed boundary. However the separation of the longitudinal and Helmholtz modes still occurs for small values of Ξ. The impedance is set as a restriction to the flow at the exit boundary. Decreasing the diameter of the chimney or increasing its length has the effect of increasing the impedance. According to Hathout, the impedance is seen to be inversely proportional to the Mach number of the burned products at the outlet nozzle, such that a reduction of the Mach number causes a higher impedance. In general, impedance is given by:

$$\zeta = \frac{P}{Au} \tag{3.14}$$

where P is the magnitude of the pressure fluctuations at the outlet, A is the area of the outlet, and u is the flow speed through the outlet. This captures the effects of the geometric variations conducted in that decreasing the area of the exhaust increases the impedance. As well, lengthening the exhaust reduces the flow speed through the nozzle by increasing the frictional losses. Impedance in the chimney may act as a relieving effect to pressure oscillations in the chamber, such that larger pressure oscillations are capable at higher impedances. This may explain the increase in amplitudes associated with the geometry variations.

As well, the asymptotic behavior may be explained by an insensitivity of the flame to increased impedance. This may be due to the onset of longitudinal modes in the chamber due to the length or small diameter of the exhaust, which may effectively act as a closed acoustic boundary. The violent chugging motion observed at very small diameters and long lengths may be due to the onset of a half-wave mode in the chamber. The frequency observed by the geometry change is ultimately set by the driven resonance of the plenum in accordance with Equation 3.13. If a plug of fluid is oscillating in the injector at 300 Hz, the fluid above it will also oscillate at 300Hz.

The Hathout and Schuller models can be combined to conceptually explain some of the observed phenomena. The process may be controlled by the equation coupling the heat release to pressure and velocity fluctuations and the equation coupling the frequency to the impedance set by the exhaust geometry. The amplitude of the instability is controlled by the satisfaction of the Rayleigh criterion between the pressure and heat release field. The impedance acts to accentuate pressure fluctuations by acting as a theoretical valve on the exhaust due to an induced pressure drop across the chimney; the dampening of the combustion effect on the plenum is inversely proportional to the exhaust impedance. The turbulence and combustion are the driving forces on activating the Helmholtz resonance of the plenum. However the observed frequency is altered by a combination of flame effects and impedances.

The chamber is decoupled from the plenum due to the low coupling index, such that variations of chamber geometry are not accounted for because the coupling index renders them negligible, as seen in Equation 3.12. However the chamber experiences fluctuations in response to the velocity and pressure fluctuations induced out of the plenum. The frequency of the instability is also controlled by the convection time of these instabilities to reach the flame and reflect back to the injector, thus scaling with the flow velocity. The equivalence ratio perturbations also alter the propagation characteristic time by changing the flame speed, which controls the response time of the flame to induced velocity oscillations.

Although it has been shown that the flame location does not matter in terms exciting the Helmholtz resonance in the plenum, the spatial location of the flame will alter convective time scales which determine the degree to which the instability is excited. The convective-acoustic mode is controlled by two timescales, a convective timescale for perturbations to reach the flame and an acoustic time scale for perturbations to return to the nozzle. The frequency of the mode is inverse to the sum of these scales. As well, the convection time also sets the phase difference between heat release perturbations at the flame and the bulk pressure fluctuations. The convective time scale varies with the flow velocity and distance to the flame. For relatively flat flames, this convective time scale is uniform across the flame surface. However, for V-shaped flames, the distance to the flame varies over the length of the surface, and thus the time scale also varies. This causes different segments of the flame to respond at different times to perturbations. Thus in flat flames, if the phase difference is appropriate, the entire flame contributes to the amplification. However, in V-shapes flames, only a portion of the flame surface may have the correct phase difference to aid in amplification. Since the entire flame is not participating in the process, the instability might not be sustained, and the resonance will not occur.

3.9.1 Application of the Conceptualized Model to the GTMC

The characteristic frequency for the 2-neck Helmholtz resonator is 395 Hz based on Equation 3.4. This frequency is then applied in Equation 3.13 to calculate a new characteristic frequency which accounts for all of the geometric influences of the Helmholtz volume, the exhaust impedances, and the combustor chamber geometry, as well as its degree of coupling. The effect of the impedance and chamber is to drop the characteristic frequency of the Helmholtz resonator. However, it is currently difficult to estimate the magnitude of the impedance and the form its function will take. It is known that the impedance is a function of the diameter and length of the exhaust nozzle. Variation of the combustor chamber length display a 5% alteration to the frequency, which means that despite having a small coupling index, there is a small effect to the characteristic frequency. The new characteristic frequency is then applied to the governing equation, Equation 3.10, which can be solved with substituting the following:

$$\eta = p_c' = Pe^{i\omega t} \tag{3.15}$$

$$\omega = \omega_r + i\omega_i \tag{3.16}$$

The characteristic equation for the complex frequency, after substitution, becomes the following:

$$-\omega^2 - \beta e^{-i\omega\tau_c} + i2\xi\omega_c\omega + \omega_c^2 = 0 \tag{3.17}$$

The definition for ω from Equation 3.16 can then be inserted and the exponential term is replaced using Euler's relation:

$$e^{ix} = cos(x) + isin(x) \tag{3.18}$$

The real and imaginary parts for each side of Equation 3.19 are equated yielding expressions for the real and imaginary frequencies:

$$\omega_i = \frac{\beta}{2\omega_r} e^{\omega_i\tau_c} sin(\omega_r\tau_c) + \xi\omega_c \tag{3.19}$$

$$\omega_r^2 + \beta e^{\omega_i\tau_c} cos(\omega_r\tau_c) + 2\xi\omega_i\omega_c = \omega_i^2 + \omega_c^2 \tag{3.20}$$

These expressions can be simplified through substitution of the following:

$$x = \frac{\omega_r}{\omega_c} \tag{3.21}$$

$$y = \frac{\omega_i}{\omega_c} \tag{3.22}$$

$$A = \omega_c \tau_c \tag{3.23}$$

$$B = \frac{\beta}{2\omega_c^2} \tag{3.24}$$

The simplified equations are then given by the following:

$$y = \frac{B}{2x} e^{Ay} sin(Ax) + \xi \tag{3.25}$$

$$x^2 + Be^{Ay} cos(Ax) + 2\xi y = y^2 + 1 \tag{3.26}$$

The solutions for these equations are given in the plots that follow in Figure 3.15. Each plot depicts the non-dimensionalized frequency which has been normalized by the characteristic frequency determined from the geometry. Each plot represents a different degree of acoustic damping and each of the lines represent varying heat release. Higher values of B correspond to larger heat release effects, as captured by the term β in Equation 3.10. The frequency is plotted against the convective time constant from π to 2π. The important conclusion from this analysis is that the observed frequency can be either greater or smaller than the characteristic frequency depending on the time constant. The effect of increasing heat release and increasing damping is to shift the curves upward to higher observed frequencies. Assuming only minimal impedance effects due the chimney, the observed frequency would typically fall within the range of 300-550 Hz based on a plenum Helmholtz frequency of 395 Hz. This range is representative of the frequencies observed from the parameter variation studies conducted in this chapter.

The time constant is a convective term for inhomogeneities in mixture composition to be convected to the flame and cause unsteady heat release. The unsteady heat release can then cause perturbations to reflect back to the nozzle. The time constant must reflect the time for the inhomogeneity to reach the flame, the time for the flame to respond, and the time for a perturbation to travel back to the nozzle. This time constant can be given by the following:

$$\tau_c = \frac{l_f}{U} + \frac{\delta_f}{S_L} + \frac{l_f}{c} \tag{3.27}$$

where l_f is the liftoff height of the flame, δ_f is the flame thickness, U is the bulk average flow velocity, $\mathrm{S_L}$ is the laminar flame speed, and c is the speed of sound. The first term represents the time to convect to the flame and for the GTMC this value is on the order of 2ms based on a liftoff height of 1 cm and a velocity of 5 m/s. The second term is the time for the flame to traverse through the mixture by a single flame thickness which is approximately 2.5ms based on a flame thickness of 1mm and a flame speed of 40 cm/s. The time for the perturbation to travel back to the nozzle is 20μs, which is based on the liftoff height and the speed of sound, which is estimated to be 500 m/s at the burner face. The time constant is then on the order of 4.52ms. It should be noted that the flame liftoff height is also a function of the flame speed. Higher flame speeds will allow for the flame to stabilize closer the nozzle. The time constant then sets the frequency of the instability relative to the characteristic frequency based on the geometry.

The primary motivator in the GTMC is plenum Helmholtz resonance, driven by turbulent combustion, whose frequency is set by coupling between the resonator, flame/fuel effects, and geometry impedances. The spatial location of the combustion influences the convective time scales of the oscillations, which determines if the instability is amplified or dampened by the degree of satisfaction of the Rayleigh criterion.

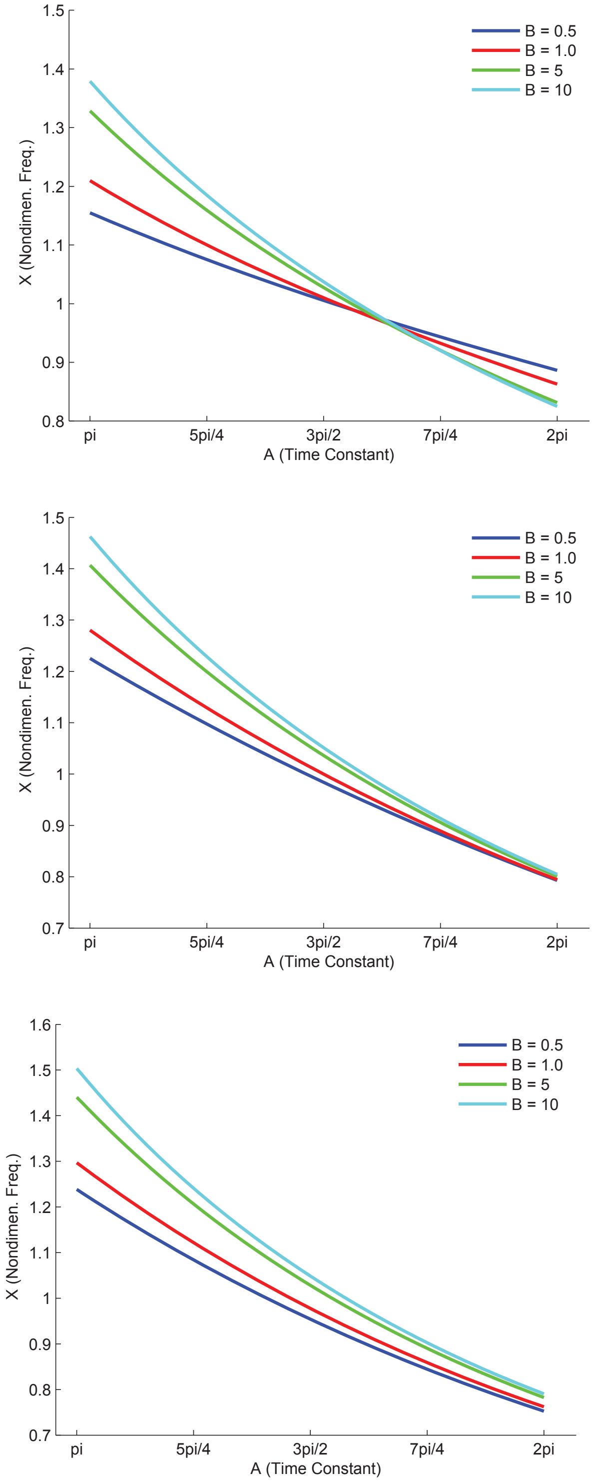

Figure 3.15: Non-dimensionalized frequency as a function of the convective time constant, with varying degrees of heat release, for damping factors $\xi = 0$ (*top*), $\xi = 0.5$ (*middle*), $\xi = 1.0$ (*bottom*).

CHAPTER IV

Fuel-Air Mixing and Instability Interactions

The goal of this chapter is to investigate the effect of each of the components, as depicted by the larger red box in Fig 4.1 in this feedback system, which feed into the combustion process at the flame base. These components will be evaluated by studying fuel-air distributions via PLIF measurements, high speed chemiluminescence videos of flame motion and shape, and LDV velocity measurements of swirler flow rate distributions. LDV measurements of radial velocities in the various flames show velocity fluctuations which correspond to flame motion oscillations captured by high speed chemiluminescence imaging. Fuel-air mixing has been investigated through PLIF measurements, where acetone has been introduced as a fuel tracer. For each fuel type, the spatial distribution of fuel and air in the GTMC has been shown to significantly differ. Flame liftoff height oscillations can be induced by variations in the mixing as well as air flow rate distribution. Flame shape has been correlated with instability strength and presence. Rayleigh indices have been compared to fuel-air distributions to understand how mixing affects instability strength. When air flow is redistributed to the outer swirler, larger radial velocities are recorded. Acetone PLIF images depict low-lying regions of fuel extending towards the outer edge of the burner. This mixing pattern encourages a flat flame shape which is unanchored and oscillates up and down. Rayleigh indices of flat flames indicate stronger acoustic coupling and amplification as compared to cases where the flame may be V-shaped and/or anchored. The latter flames correspond to flow conditions where a lower radial air velocity is observed and the flame is non-resonant.

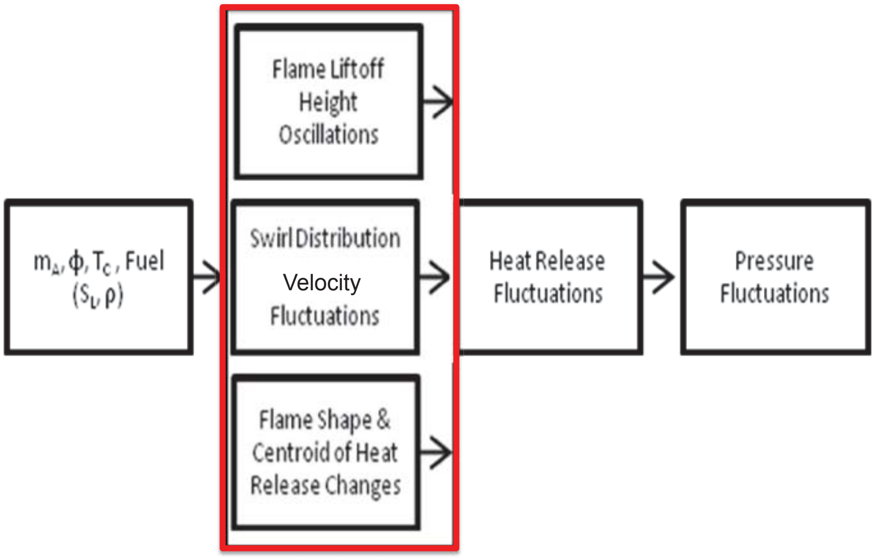

Figure 4.1: Proposed system of thermoacoustic relationships investigated in this chapter

4.1 Swirler Air Flow Redistribution

It has been observed in the GTMC that air flow redistribution can occur between the two independent swirlers, which are fed from a common plenum. Uneven partitioning of air flow between the individual swirlers strongly affects instability strength and shear layer mixing. Swirler flow rate variations can result in large redistributions of heat release which can affect flame shape and the pressure field. LDV measurements of radial velocities in the various flames show velocity fluctuations which correspond to flame motion oscillations captured by high speed chemiluminescence imaging. It is important to note that the bifurcation in flow rate discussed in Section 4.1.1 is not dynamic in time. For resonating flames, a single flow pattern is established and for non-resonating flames another different flow pattern is established. The swirl distribution does not fluctuate in time, rather the distribution can act like an on/off switch with regards to whether the instability is enabled.

4.1.1 Radial Velocity Variations with Air Mass Flow Rate

Figure 4.2 depicts the variation in the radial velocity at the LDV measurement location, as described in Chapter 2. The cold flow case represents a non-reacting measurement with only air flowing. The radial velocity increases linearly with increasing flow rate, as expected. For this non-reacting measurement, a set distribution of air flow rate between the inner and outer swirler has been established and remains unchanging. PIV data from DLR suggests that the split between the outer and inner swirler flow rate is 60/40. The reacting methane case shows interesting behavior. The first data point at 160 g/min represents a flame that is non-resonating. The flame is lifted and has a V-shape. At higher flow rates, the methane flame liftoff height is increased, the shape is flatter, and the flame begins to resonate at 308 Hz. For increasing air flow, the radial fluid velocity remains almost unchanged. For all the propane cases studied, the flames are resonant and flat in shape. The velocity appears to be independent of airflow rate. Of note is the increase in radial velocity observed between the non-reacting and reacting flows. This is suggestive of a redistribution of flow to the outer swirler, which imparts a greater radial flow component.

The syngas trends in Figure 4.3 display very different behavior than the alkane fuels, although ethylene displays the same insensitivity to increased air flow rate. The magnitude of the velocities measured in ethylene are also on par with those measured

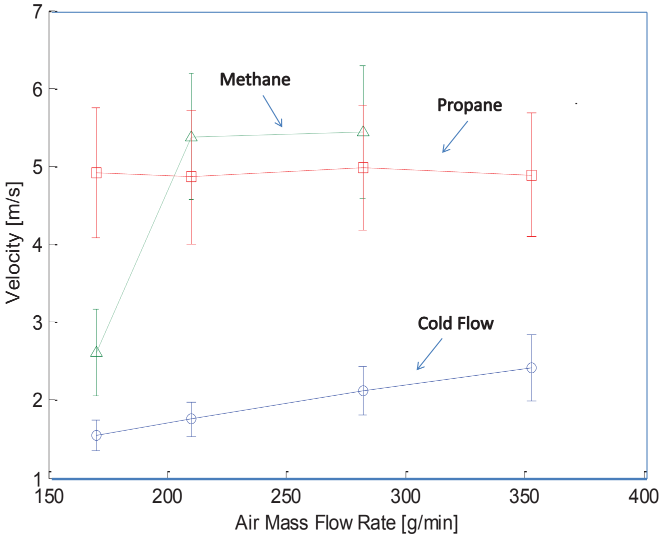

Figure 4.2: Measured radial velocities with varying air mass flow rate. Reacting alkane cases measured at an equivalence ratio of $\phi = 0.75$. Vertical bars represent the rms of the flow indicating turbulence intensities of almost 40% on average for reacting flows.

in methane and propane. The syngas cases represent mixtures of hydrogen and carbon monoxide, where 100% H_2 is pure hydrogen and 0% H_2 represents a carbon monoxide flame. Hydrogen flames are also rather independent of flow rate, however, this may be a response to a different flowfield than is created in alkane and ethylene flames. The pure hydrogen flame is non-resonating and directly attached to the recessed fuel injector lip, as opposed to the fuels which exhibit some degree of liftoff.

Carbon monoxide combustion in the GTMC appears to operate in a flameless mode with a large distributed reaction zone which is highly lifted several centimeters from the burner face. In essence, the velocity response is similar to the cold flow trend because there is little interaction between the flame and injector. The measured cold flow and CO velocities are also very similar. The syngas mixtures all display increasing radial flow with increased flow rate. However the measured velocities are 2-3 times smaller than the hydrocarbon flames, despite the fact that all three mixtures exhibit instabilities. The observed trend implies that syngas flames do not produce the same type of flowfield as hydrocarbon flames, nor do they present the restriction or blockage to the flow.

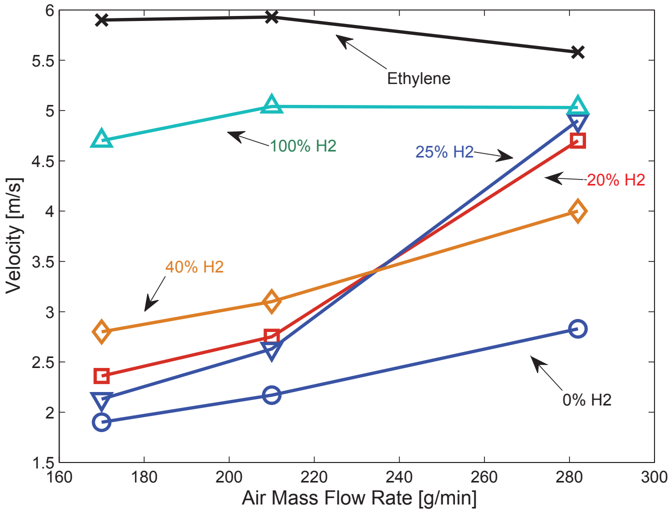

Figure 4.3: Measured radial velocities with varying air mass flow rate. Reacting ethylene and syngas cases measured at an equivalence ratio of $\phi = 0.75$.

The vertical bars in Figure 4.2 do not represent the error of the measurement but rather the rms of the measured velocities. For clarity, the bars were omitted from Figure 4.3. The turbulence intensities for alkanes are typically 40%, indicative of large radial velocity fluctuations, which may be due to contraction of the CRZ and motion of the PVC. As the PVC processes, it may obstruct flow from the outer swirler causing a negative fluctuation in flow. The turbulence intensities are on the order of 25% for syngas flames, which may be due to reduced radial expansion and contraction of the flowfield at the exit of the injector. As a result of higher flame speeds in syngas as well as differential diffusion of hydrogen relative to CO, the injection and stabilization of synfuels may disrupt the formation of the PVC, resulting in smaller turbulent fluctuations. Studies from DLR have captured the motion of the PVC at 525 Hz and evidence will be provided in Chapter 5, that the effect of the precession is detected in the evolution of the preheat zone surface.

It should be clarified that during operation of the burner with an instability present, dynamic switching of the flow from one swirler to the other was not observed. For steady operation, the flow was either dominated by one swirler or the other, there was no rapid back and forth change in flow between the two swirlers. The histograms of the recorded velocities only revealed a single peak, not a rapid bifurcation of flow. As well, the acoustic frequency was not detected in the fluctuations of flow from the swirlers. The power spectrum did not report any particular frequency being present, however this may be due to difficulty in processing for frequency information in the data due to uneven sampling rates in the LDV measurements. in summary, for all cases where the instability is present, the flow through the radial swirler is elevated and in non-resonating cases, the flow rate is low.

4.1.2 Natural Swirler Flow Rate Bifurcation

Figure 4.4 represents radial velocity histograms for an interesting air flow condition unique to the GTMC. As discussed previously, the distribution to each swirler is naturally set by the system and cannot be individually controlled. The cold flow case in Fig 4.2, generally represents a 60/40 split with the outer swirler receiving most of the flow [33]. With the combustion chamber removed from the system, such that the burner is no longer encased, two unique flow patterns can be established for this open air, non-reacting set-up. If a slight back-pressure is applied to the burner face with a bluff object, such as one’s hand, the flow distribution can be set such that the majority of the air flow is directed to the outer swirler.

Interestingly enough, when the blockage or bluff object is removed, the flow pattern through the outer swirler will remain. This results in the open air radial mode as depicted by the solid line histogram in Fig 4.4 , with a mean velocity of 3.1 m/s. However, if a back pressure is reapplied, the flow pattern may switch such that the

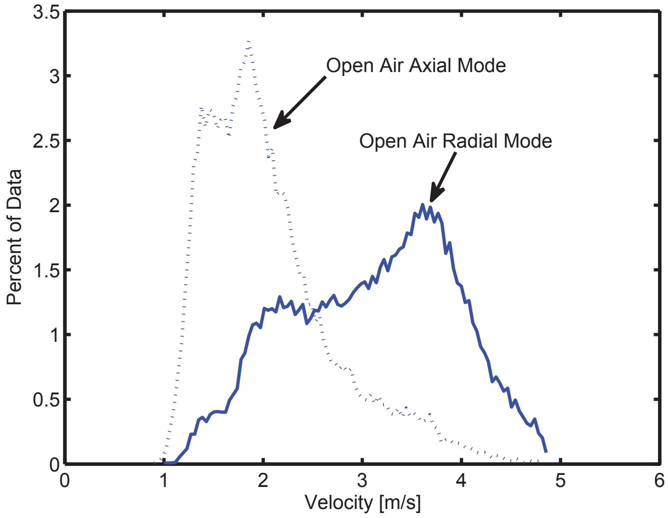

Figure 4.4: Open air, unconfined flow patterns exhibited by applied back pressure to the injector face causing a redistribution of flow from one swirler to the other. Radially dominated flow mode (*solid*). Axially dominated flow mode (*dash*). Air $\dot{m}$ = 282 g/min, non-reacting.

majority of the flow is redirected to the inner swirler. Again, this flow pattern is maintained when the back pressure is removed. The inner swirler has no contoured shape and thus the air flow is generally directed down the axial direction. This results in the open air axial mode as depicted by the dashed line histogram in Fig 4.4, with a mean radial velocity of 2.05 m/s.

This unique set of flow patterns is interesting because it establishes the precedent that higher radial velocities are correlated with flow to the outer swirler and that changes in back pressure to the burner face can cause this distribution of flow to “switch” between the self described radial and axial modes. The presence of a reacting flow also tends to force more flow to the outer swirler as observed with the higher velocities seen in Fig 4.2. It is hypothesized that the flame and recirculation zone created by the swirling flow can affect the back pressure on the injector face which will feedback to the airflow distribution and alter the flame and recirculation bubble. Thus conditions correlated with onset of resonating flames are established with the initiation of a particular flow distribution through the swirlers.

4.1.3 Radial Velocity Variations with Equivalence Ratio

Figure 4.5 depicts the variation of radial velocity with varying equivalence ratio in methane flames. The behavior shows a non-monotonic trend with the measured velocity peaking at an equivalence ratio of 0.75. Similar trends are this are observed in propane flames. However, syngas and ethylene flames do not exhibit any discernible trends . A similar behavior is observed in previous studies [136] of acoustic frequency versus equivalence ratio. The frequency behavior of resonating methane flames is also non-monotonic with increased fueling which suggests a correlation of higher measured frequencies with higher measured radial velocity, for a given air mass flow rate. The vertical bars in this figure also represent the degree of turbulence intensity in the flow.

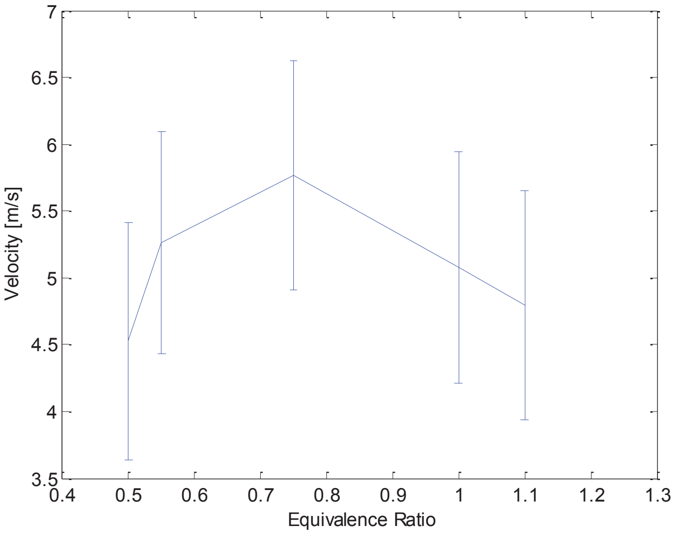

Figure 4.5: Methane, reacting case, radial velocity variation with equivalence ratio, with air $\dot{m}$ = 282 g/min.

4.1.4 Special Case Studies : Lean Blowout and Intermittency

A separate case study was observed for methane flames near lean blowout (LBO). These flames were operated at the Case B air flow rate, but the equivalence ratio was reduced to 0.48, leading to the onset of LBO. At this condition the flame is weakly resonating with a low acoustic amplitude. However the flame is very sensitive to disturbances and will fluctuate between a highly lifted and stable state. When stable and resonating, the flame is flat and displays a higher radial velocity near 4.5 m/s, as seen in Figure 4.6. When the flame is highly lifted, the shape changes to be more V-like and the radial velocity drastically drops to speeds below 2.5 m/s. This suggests that the air flow is being redistributed is a similar to fashion as observed in Fig 4.2, dependent on flame position. These drops in velocity correspond to moments when the flame is about to blowoff. Finally at the end of the time series, after 60 sec, the flame is finally blown off. It can be reasoned that high radial velocities are conducive to flame stabilization.

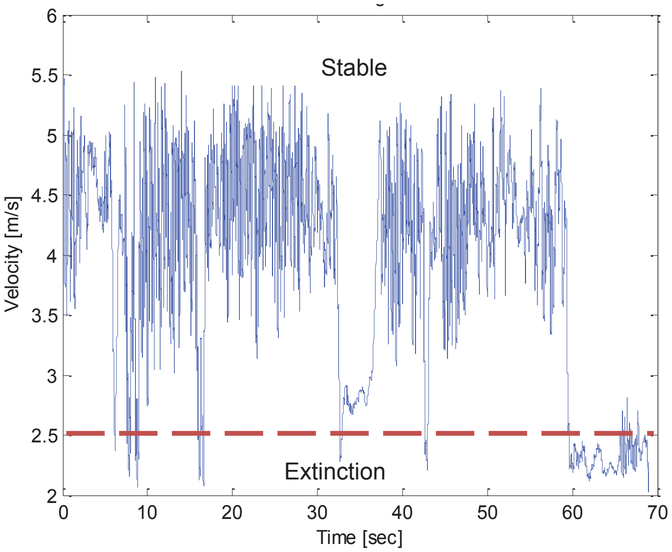

Figure 4.6: Methane flame operated near LBO, air $\dot{m} = 282$ g/min, $\phi = 0.48$. The horizontal dashed line indicates the threshold below which very lean methane flames will be extinguished. However, stable lean flames may exist if higher radial velocities are achieved.

A secondary case study was conducted for an interesting behavior observed in rich propane flames. It was seen that the flame shape would transition between a flat mode and a lifted, V-shape mode, similar to the previous methane LBO case. Figure 4.7 depicts the measured velocities corresponding to this flame motion. This behavior has been displayed as 3 segments in Fig 4.7. Initially, the flame is resonant and flat with a high radial velocity. The flame then transitions some time later to the lifted, V-shape mode, marked by low radial velocities. In the final segment, the flame is seen to dynamically transition back and forth in a “flapping” motion. This flapping motion is naturally occurring and unforced. It is marked by the large fluctuations in velocity, alternating between velocities typical of propane at the fueling condition and velocities seen in cold flow measurements, as the flame shape changes.

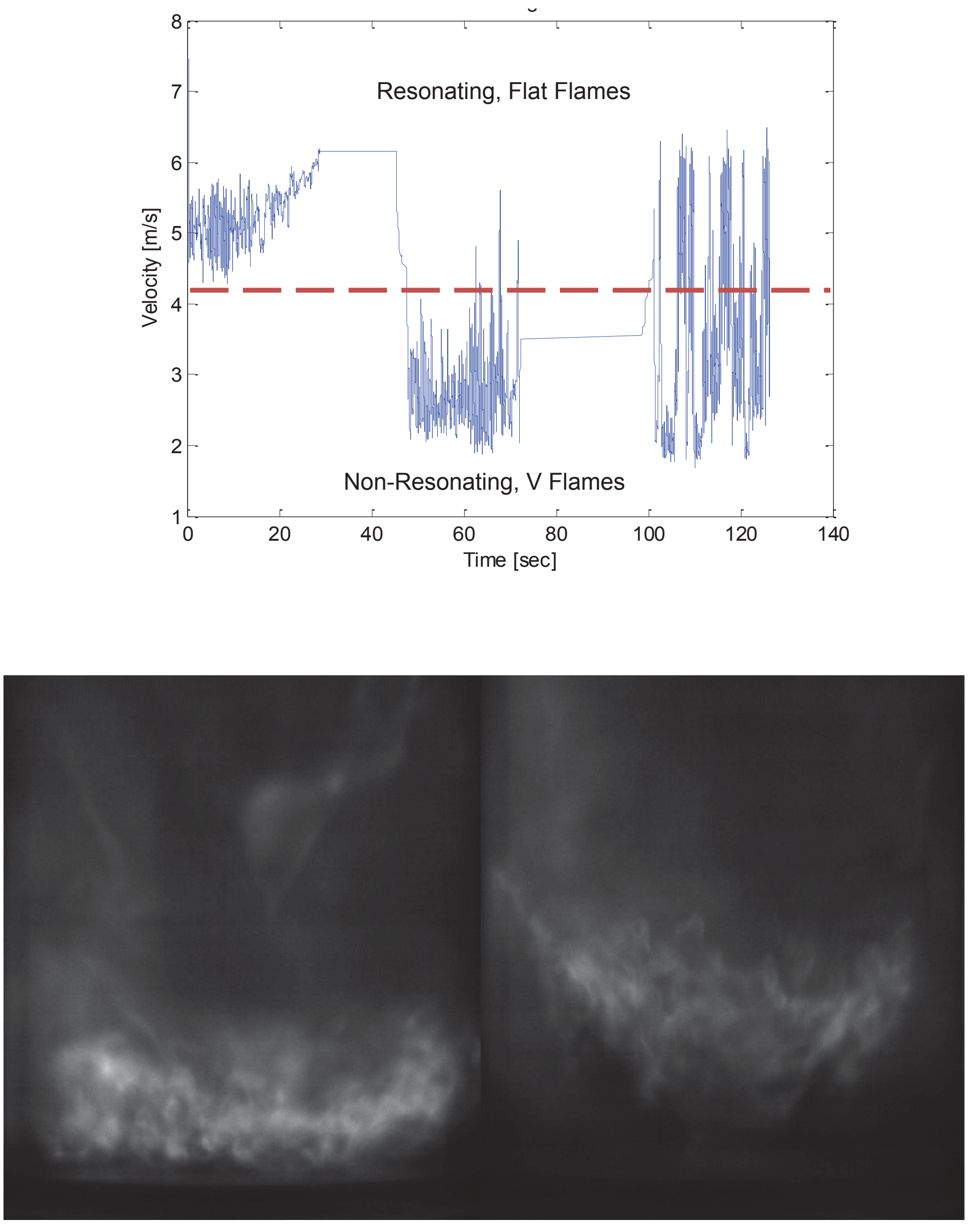

Figure 4.7: (*Top*) Rich propane flames operated at $\phi = 1.4$ for a reduced air flow rate of 160 g/min. "Flapping" captured exaggerated velocity fluctuations. (*Bottom*) Typical flame chemiluminescence images of the two flame shapes exhibited during the flapping motion.

4.1.5 Modification of Swirler Configurations

This investigation has shown that flame shape is controlled by the distribution of air through the two swirlers. An extended set of six case studies were based on modifications to the swirl patterns, using Case B fueling with propane, as outlined below:

Case 1: Inner swirler blocked: Blockage of the inner swirler forces all flow through the outer swirler. As a result, measured core temperatures are biased because of additional cooling of the thermocouple in the outer swirler. To compensate, the burner was allowed to warm up for the same amount of time as would normally be needed to reach temperatures higher than measurements are typically taken at. A flat flame was established, however, the FFT of the instability no longer produces a single clean peak at 320 Hz. Rather a series of peaks are observed in the range of 320-350 Hz, seen in Figure 4.8.

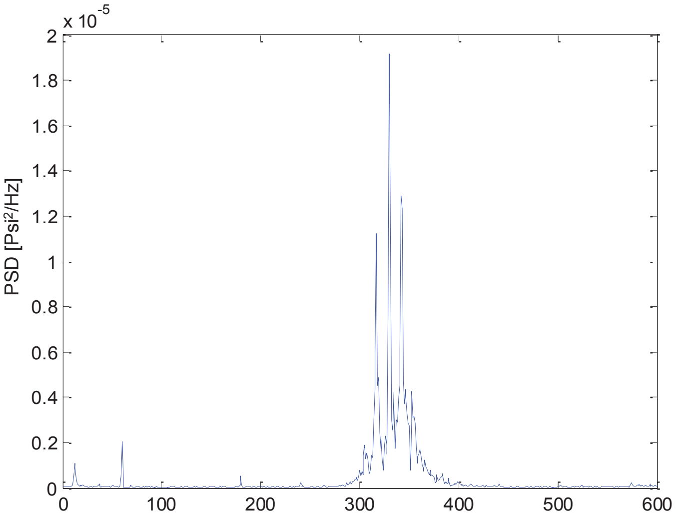

Figure 4.8: Power spectral density plot of propane flames, air $\dot{m}$ = 282 g/min, ϕ = 0.75, where flow through the inner swirler is blocked. Multiple peaks are observed as opposed to a single peak at 320 Hz. This may be due to interferences formed by the cavity created in the nozzle by blocking the swirler.

Case 2: Inner swirler blocked, cavity filled: The second case study also involved blocking the inner swirler. However, when this is blockage is applied at the inlet of the swirler, the hollow cavity that forms the inside of the central nozzle remains open to the burner. The cavity is filled such that the central nozzle acts more like a bluff body plug. With this blockage, flow is still forced through the outer nozzle and a resonating flat flame is established. The resonance of this flame is still in the range of 320-350 Hz, yet a single distinct peak is recovered. This suggests that the empty cavity present during the first case study was affecting the resonance and creating multiple peaks as seen in Figure 4.8.

Case 3: Inner swirler removed: The inner swirler is removed but the plate which holds it in place is left in position, creating an 10mm gap where the swirler was once located. Flow may still travel through the central nozzle but it is no longer swirled, rather is parallel to the the central axis. Air may still travel through the outer swirler. It appears that the majority of flow goes through central nozzle. A highly lifted jet flame observed with no resonant tones. There is no anchored flame noticeable at any flow condition.

Case 4: Inner swirler flow direction reversed: The inner swirler is an axisymetric ring with angled passages cut radially through it. If the swirler is removed and re-installed upside-down, the direction of swirled flow through the central nozzle is reversed. The flow through each swirler is now counter-rotating. Unexpectedly, there is no apparent change in frequency or amplitude due to this alteration, which may suggest that the flow is not very sensitive to flow modification through the center nozzle.

Case 5: Outer swirler blocked: The blockage of the outer swirler was varied from 0% to 100% in 25% increments. The inner swirler was left in its standard configuration. Figure 4.9 depicts the change in the instability frequency. There is little change seen until 75% blockage is applied, such that the frequency of the instability decreases by 5%. While complete obstruction of the outer swirler, a flat flame will not stabilize, rather a highly lifted V-shape, non-resonating flame is observed. This may imply that a critical threshold of radial flow is needed to establish flat flames, which resonate.

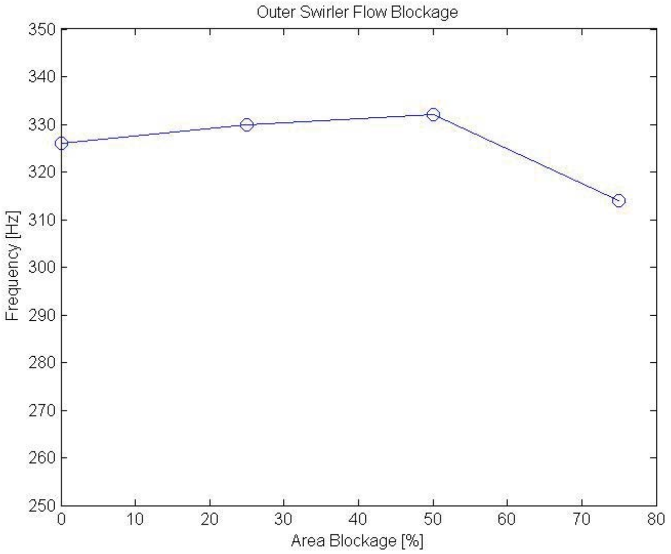

Figure 4.9: Combustion instability frequency of propane flames, air $\dot{m}$ = 282 g/min, $\phi = 0.75$, where the blockage ratio of the outer swirler is increased. A flat flame will not stabilize with the outer swirler completely blocked and no resonance is observed.

Case 6: Inner swirler mounting plate removed: The inner swirler is held in place with a mounting plate on which the flow entering the plenum stagnates upon. This plate has a lip which extends beyond the diameter of the inner swirler, creating a lip, around which flow must ravel to get to the inner swirler, as marked by the red circles in Figure 4.10. This plate was removed to see if this lip had any effect on the flow distribution between the two swirlers due to the modification of the flow path through the plenum. The inner swirler was still left in place, in its standard configuration. With the modification, there was no apparent change in flame shape or instability frequency/amplitude, suggesting that this plate does not play a role in setting the distribution of flow to the swirlers.

Acoustics are highly amplified in the flat flame case whereas they are weak, compared to background noise, when only the inner swirler is used. This finding implies

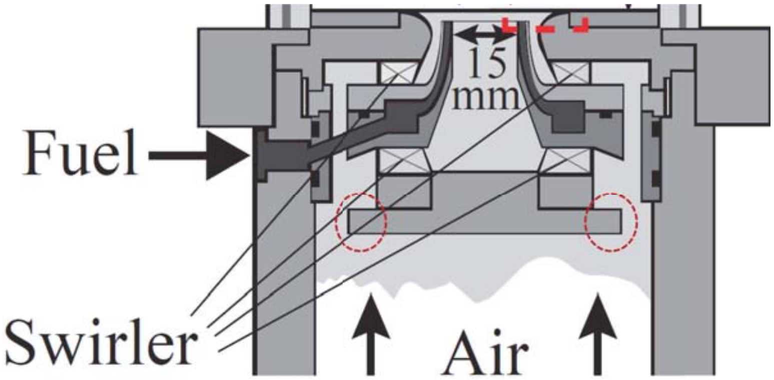

Figure 4.10: Schematic of the internal components of the of the GTMC injector. The mounting plate of the inner swirler was removed to see if the lip of the plate, marked in red circles, had any effect on the distribution of flow to the swirlers.

that there is a coupling between reflected pressure waves, flame shape, and the distribution of air through the swirlers. As a flat shape, the flame acts as larger blockage within the combustion chamber. Reflected pressure waves may act on the incoming air streams influencing flame shape. With a flat flame, the heat release is focused along a smaller location in the burner, which allows for stronger amplification of the existing instability.

4.2 Pressure and Chemiluminescence Correlations

Pressure measurements were taken simultaneously with high speed videos of the line of sight chemiluminescence. These measurements showed detailed flame motions occurring over a given acoustic cycle. For the chemiluminescence images, information regarding the average flame shape, liftoff height, average liftoff fluctuation distance, and frequency of heat release could be investigated.

4.2.1 Cyclic Flame Motions

As described in Chapter 3, flame shape is a potential representation of the instability presence and strength. Figure 4.11 depicts the average chemiluminescence from 6 different flames studied. The general trend observed is that for increasing flame speed, the flame spreading angle decreases and the flame becomes more axially extended. The hydrocarbon-fueled flames in this figure all display an instability varying from 300-400 Hz. Note there is a strong shift in the distribution of the average signal between 25% H_2 and the 40% H_2 synfuels. The 40% mixture represents the maximum boundary of the map for hydrogen composition and instability presence, as seen in Chapter 3. Mixtures with higher hydrogen concentrations do not exhibit instabilities, which may be attributed to better anchoring associated with higher flame speeds.

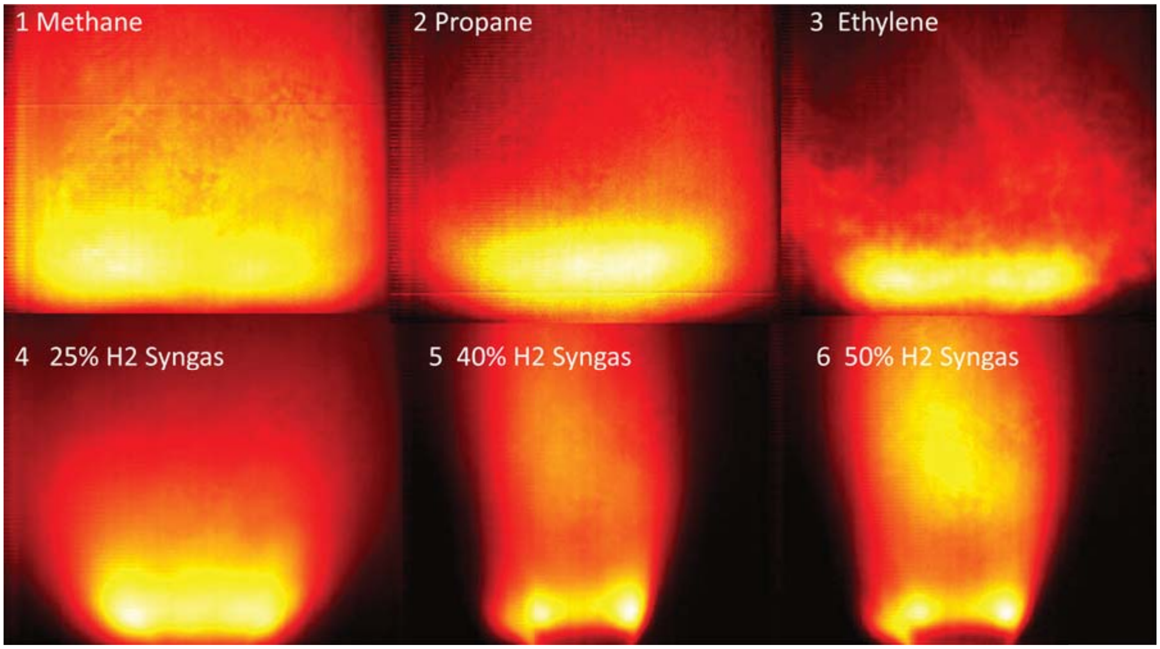

Figure 4.11: Average chemiluminescence signal from six fuels studied in this investigation. Flames that displayed an instability were generally radially distributed, as seen with hydrocarbon fuels and low hydrogen synfuels. Air $\dot{m}$ = 282 g/min, $\phi = 0.75$

Figure 4.12 depicts a typical time series of flame chemiluminescence images for propane at Case B conditions, captured at 2.5 kHz. The series represents the liftoff and flashback motion over a thermoacoustic oscillation. The time separation between each subsequent image is 250 μs. Propane flames at this fueling condition resonate at 320 Hz, which implies that a video taken at 2.5 kHz will have roughly 8 frames

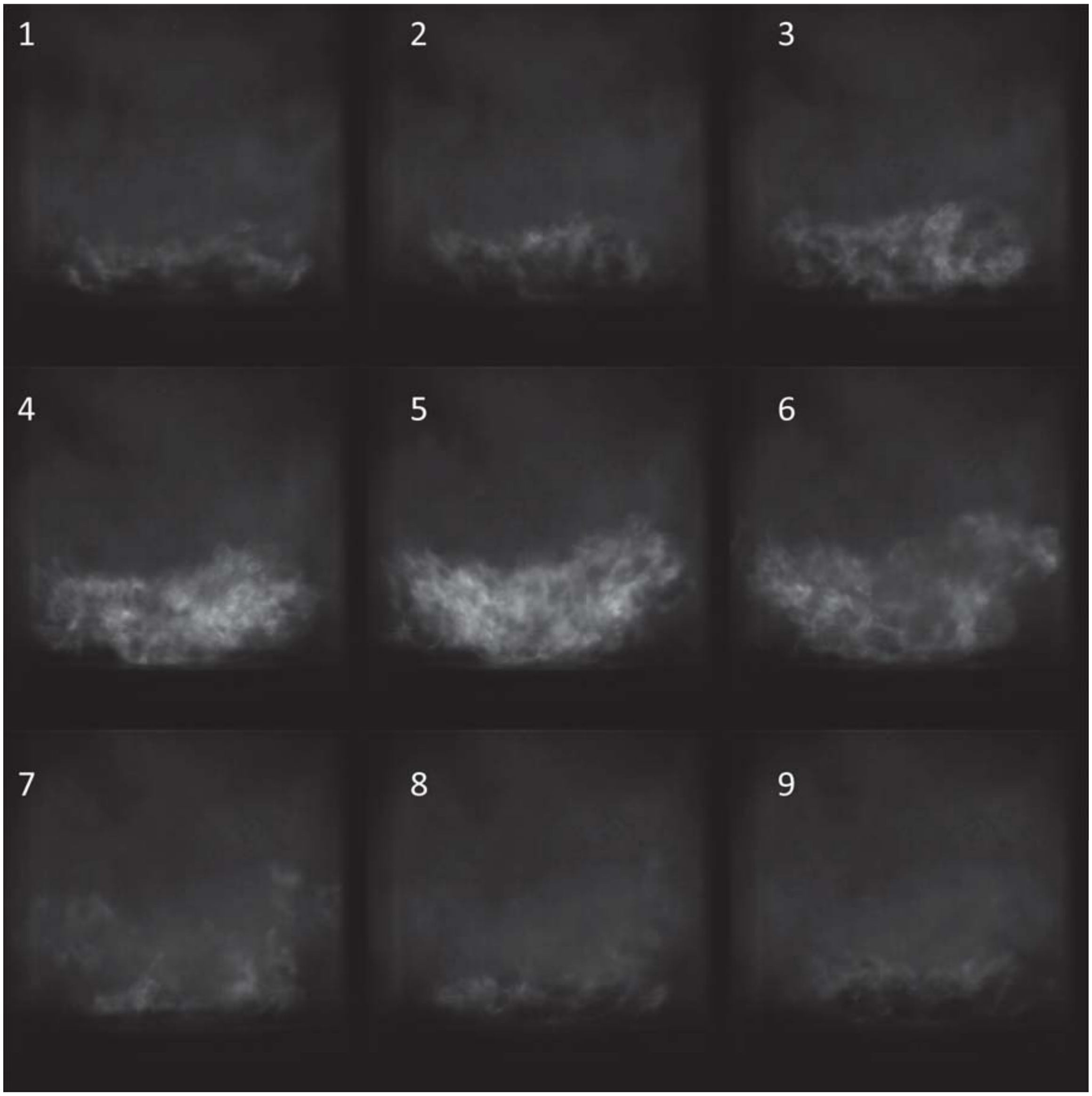

Figure 4.12: Chemiluminescence time series displaying the liftoff and flashback motion of a propane flame. 250 μs separation between subsequent images, Air $\dot{m}$ = 282 g/min, $\phi = 0.75$

per oscillation. Given here is a nine frame series, where frame 9 represents the first image of the next cycle. There are three behaviors occurring simultaneously in these image. The first behavior involves the vertical motion of the flame. The flame starts fairly low on the burner in frame 1 and then the bulk of the flame moves downstream in frames 3-5, only to retreat by frame 8. The second observable process is the large change in the amount of signal and the size of the flame brush. Over the course of the cycle, significant flame surface area is being created and destroyed. By frame 8, at the end of the cycle, the flame appears to be on the verge of being extinguished.

This type of motion is associated with convective acoustic effects causing equivalence ratio oscillations. These fluctuations can be convected by vortex induced rollup of the flame causing a large "eruption" of heat release, when the mixture ignites. Entrained products with the vortex motion can assist in this ignition process. Subsequently, as the flame lifts off, fuel may accumulate at the flame base, only to be captured by the next vortex interaction, causing a repetition of the cycle. The following section on fuel localization will explain where unburnt fuel is positioned.

The majority of liftoff observed occurs at the sides of the flame, the center of the flame is only displays slight motion. PVC motion results in asymmetric downstream transport of vorticity. This asymmetry causes the flame to rock left-to right during oscillations, as seen in frame 6, where the right side is lifted higher. This is due to the helical shape of the PVC, such that vortices are transported in vertically mismatched asymmetric pairs. For another cycle, the left side may be lifted higher than the right. Essentially, while the flame lifts and flashes back, it also rocks left to right. The rocking motion, however, is a 2D representation of the precession of the PVC. This motion will be clarified in the POD analysis in Chapter 5.

4.2.1.1 Transversely Integrated Signal Oscillation Patterns

Figure 4.12 only depicts the motion of a single cycle. It would be more useful to observe changes that occur across several cycles. In order to view this motion over a number of oscillations, each flame chemiluminescence image is transversely integrated and then the resultant vertical columns are plotted in time. The integration is carried out as follows for each 2-D image, I(x,y):

$$I(y) = \int_{-\infty}^{+\infty} I(x,y)dx \tag{4.1}$$

This reduces the 2-D image field, I(x by y), to a 1-D column vector, I(1 by y). This is the vertical distribution of all signal collected in the transverse direction. Figure 4.13 shows plots of how this distribution changes in time for a series of oscillations in propane, ethylene, and syngas flames. For a given plot, each vertical column of pixels represents the integration of a single image at some time, t_i. Each plot is presented on the same color scale limits for comparison. Again, very different behaviors between fuels can be observed. In each plot, the individual vertical groupings represent a thermoacoustic cycle as seen in Figure 4.12. The first thing to note is that the bands vary in thickness between fuels. Since each column represents a 250 μs difference from one image to the next, the frequency of the instability and the frame rate of the video will determine the band's thickness. For propane flames resonating at 320 Hz, 8 vertical columns represent a cycle. For ethylene at 400 Hz, 6 columns depict a cycle. Syngas flames with 25% H_2 oscillate at 360 Hz and are displayed across 7 columns. Syngas flames with 50% H_2 do not oscillate and burn steadily, showing no apparent banding.

The next important observation is the vertical thickness of the flame brush which

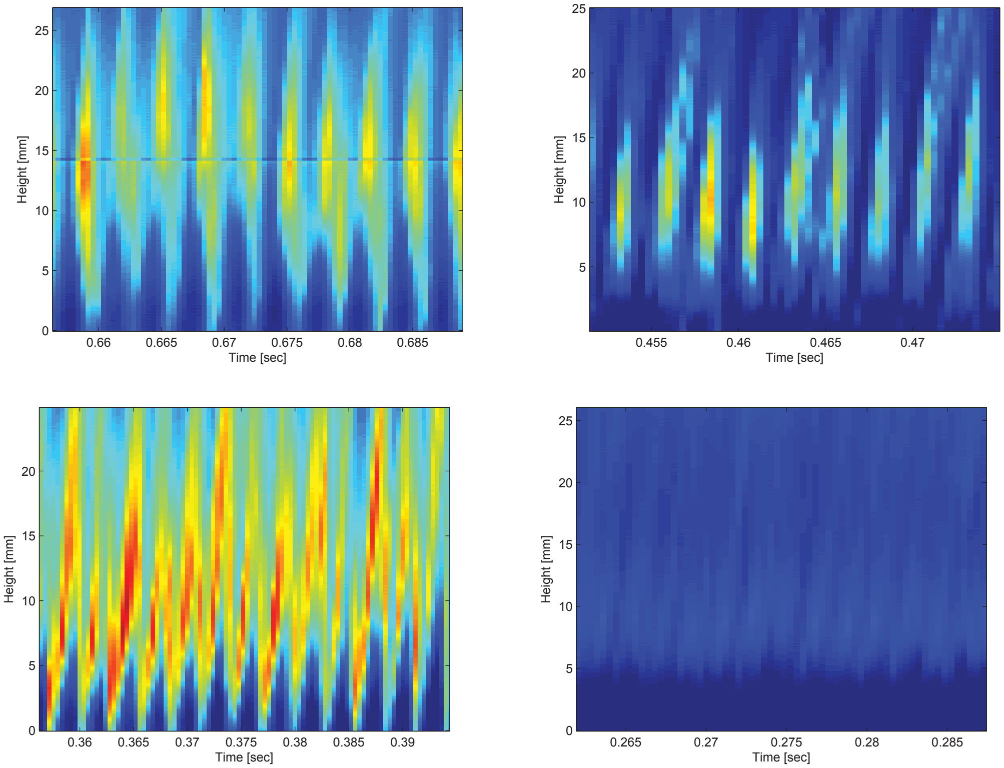

Figure 4.13: Transversely integrated series of flame chemiluminescence depicting periodic changes in flame liftoff and intensity for propane (*top, left*), ethylene (*top, right*), 25% H_2 syngas (*bottom, left*), and 50% H_2 syngas (*bottom, right*), for air $\dot{m}$ = 282 g/min, ϕ = 0.75. Bright color indicates the intensity of the chemiluminescence.

can be demarcated by the full width half maximum (FWHM) of each column. Although this metric is arbitrarily chosen, it gives an adequate representation of where the bulk of the flame lies. The brush thickness for propane is much wider than that for ethylene. The propane brush is about 16 mm in height, whereas the ethylene brush is 10mm wide. The 25% H_2 syngas mixture has a much thinner brush of 7 mm. This appears contrary to Figure 4.13, however if you examine the columns individually, the flame consists of a narrow, but very intense horizontal band, which displays a high degree of vertical motion from one column to the next.

The liftoff height and degree of motion also varies from fuel to fuel. The liftoff height from the base of the flame to the burner is determined by assigning the height that represent 75% of the maximum signal intensity as the bottom edge of the flame brush. The liftoff height for propane and ethylene are similar, at 8 and 6 mm respectively. However the measurement is misleading in syngas flames. In hydrocarbon flames, the liftoff height represents a drastic change in signal from the burner face to flame itself. In general, there exists a gap between burner and flame where little to no chemiluminescence is observed. This is a result of the loose anchoring and stabilization of the flame. The syngas flames are stabilized by being anchored to the injector. Now the majority of the flame brush is lifted, and this brush oscillates vertically. However, there is always some degree of flame structure connected to the burner, such that unlike the hydrocarbon flames, there is never any true liftoff height. This type of structure can be compared to ethylene liftoff from instantaneous chemiluminescence images in Figure 4.14.

The degree of vertical motion also varies between these fuels. Propane flame exhibit a fairly large range of motion, with the flame almost flashing back to the injector. Ethylene flames, however, exhibit a very narrow range of motion over

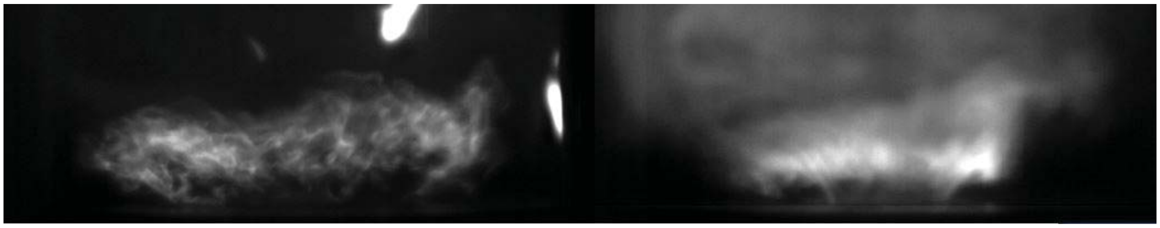

Figure 4.14: Instantaneous flame chemiluminescence images of ethylene (*left*) and 25% H_2 syngas (*right*). Note that there is some flame structure connecting the main portion of the syngas flame brush to the burner. Similar structure is not apparent in the liftoff height for hydrocarbon flames. Air $\dot{m}$ = 282 g/min, $\phi = 0.75$.

about 8 mm. The lower hydrogen content syngas flames exhibit the greatest range of motion. The most intense portions of the flame brush are seen to clearly flash all the way back to the burner face. Note the difference in behavior between propane and syngas. Propane flames typically have some degree of liftoff with little reactivity, however syngas flames typically always have some structure that extends to the burner.

The thickness and intensity of the flame brush also varies over an oscillation cycle. For propane flames, each oscillation band mimics a very narrow ellipse with thinner left/right edges. This indicated that the brush is lengthened in the middle of the cycle and simultaneously experiences an increase in heat release. The profiles at the base of the syngas flames exhibit a sawtooth pattern, implying that the cycle evolves from a fully attached state and slowly liftoffs, but then a much more rapid flashback motion occurs. The higher concentration syngas flame is a steady burning attached flame with no instability present. However, in relation to the other flames, there is no cycling of heat release or liftoff.

The final comment that can be made regarding Figure 4.12 is that there appears to be dim breaks between oscillations in the hydrocarbon flames. This suggests that at some point in each cycle the flame approaches a near blowout condition, where there is almost no visible chemiluminescence detected. This may be due to a combination of equivalence ratio oscillations and high strain effects, causing the mixture to become inflammable and strained to near extinction. The resuscitation of the flame may be due to vortex rollup entraining hot products and mixing with the fresh reactants. In contrast, for syngas, the flame structure always appears to be present over the entire cycle, never reaching a blown out state. This may be due to differential diffusion of hydrogen and carbon monoxide resulting in some portion of the mixture always being flammable regardless of the motion of the flame.

4.2.2 Heat Release and Pressure Coupling

The frequency of the pressure fluctuations were compared to the frequency of the chemiluminescence oscillations. This was achieved by taking the FFT of the total integrated signal fluctuation per frame. The total intensity of each pixel per image was summed resulting in a single total intensity per image. The average intensity was determine from the 2500 images per video measurement. Given this average, the fluctuation of each was calculated by subtracting the average from the integrated value at each image. For every case in which an instability was present, the frequency of the chemiluminescence signal occurred at the same frequency as the pressure fluctuations. This is depicted in Figures 4.15 to 4.18 for propane, ethylene, 25% H_2 syngas, and DME flames. This implies that the pressure and heat release oscillations are coupled, albeit with a phase lag.

4.2.3 Flame Front Motion

Figure 4.19 depicts the frequency of the flame front motion of a DME flame. The flame front was calculated in the same manner discussed previously. The liftoff height is calculated as the distance from the burner required to reach 75% of the

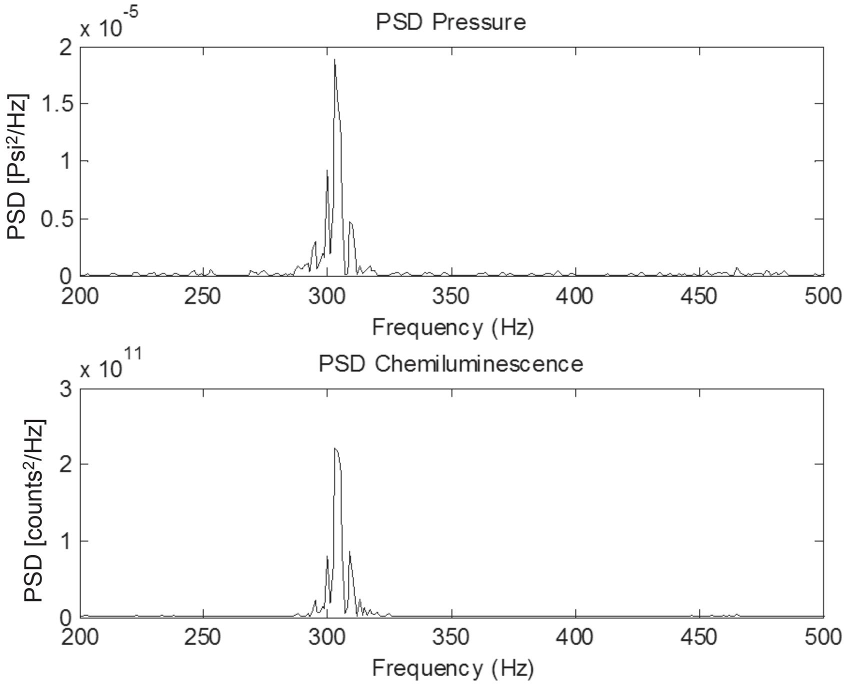

Figure 4.15: Power spectral density of the pressure oscillations (*upper*) and chemiluminescence fluctuations (*lower*) of propane flames, Air $\dot{m}$ = 282 g/min, $\phi = 0.75$.

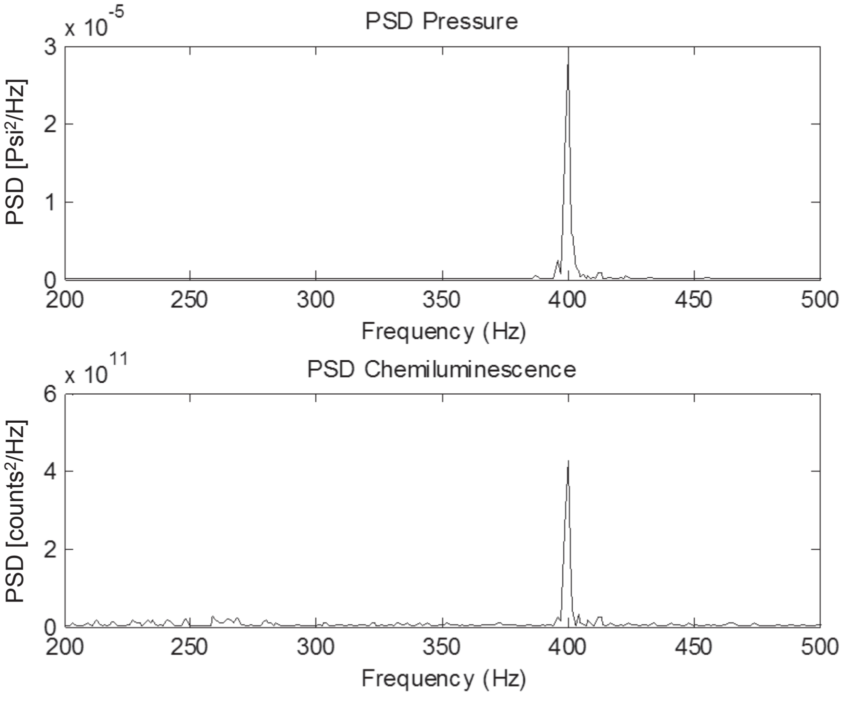

Figure 4.16: Power spectral density of the pressure oscillations (*upper*) and chemiluminescence fluctuations (*lower*) of ethylene flames, Air $\dot{m}$ = 282 g/min, $\phi = 0.75$.

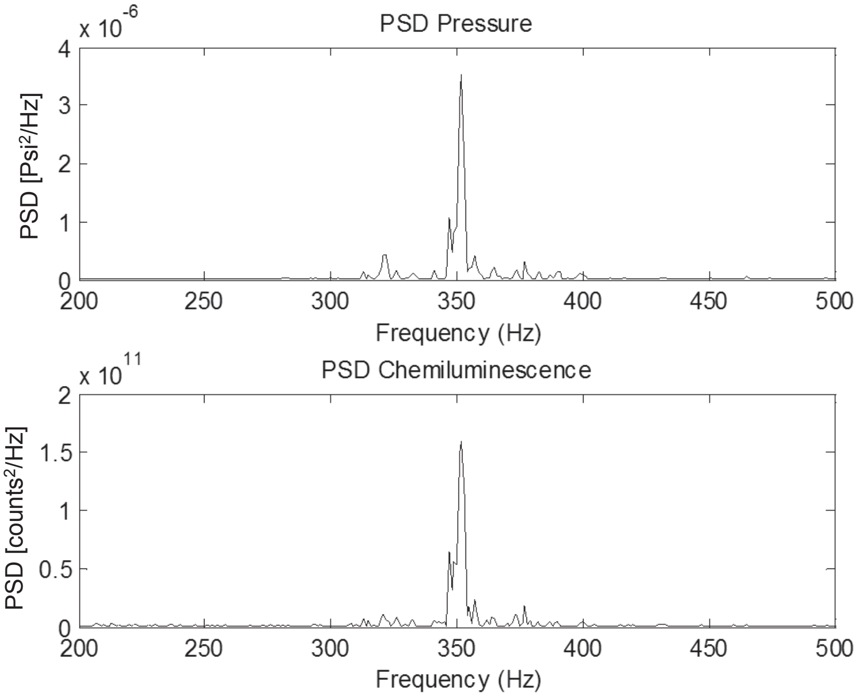

Figure 4.17: Power spectral density of the pressure oscillations (*upper*) and chemiluminescence fluctuations (*lower*) of 25% H_2 syngas flames, Air $\dot{m}$ = 282 g/min, $\phi = 0.75$.

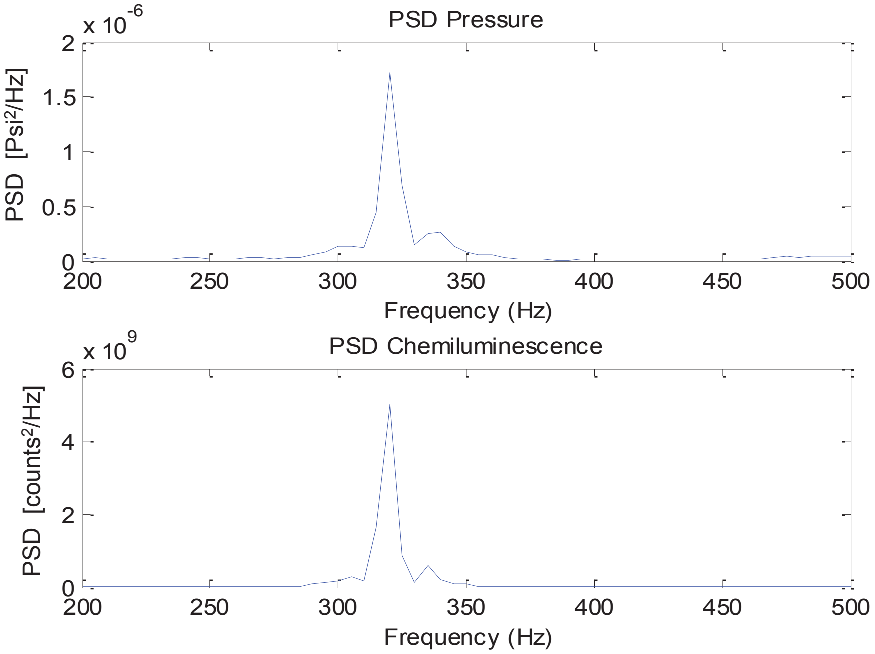

Figure 4.18: Power spectral density of the pressure oscillations (*upper*) and chemiluminescence fluctuations (*lower*) of DME flames, Air $\dot{m}$ = 282 g/min, $\phi = 0.75$.

horizontally integrated signal per image. This results in a series of liftoff distances at each time instant; a single height per image. From this it can be seen that the liftoff motion also occurs at the same frequency as pressure and heat release oscillations. For brevity, only the measurement of DME is given, however, all other resonating flames behave similarly, exhibiting matched frequencies. Knowledge of the liftoff height and time between images allows for calculation of oscillation speeds; how fast is the flame front moving and how far does it move from one image to another.

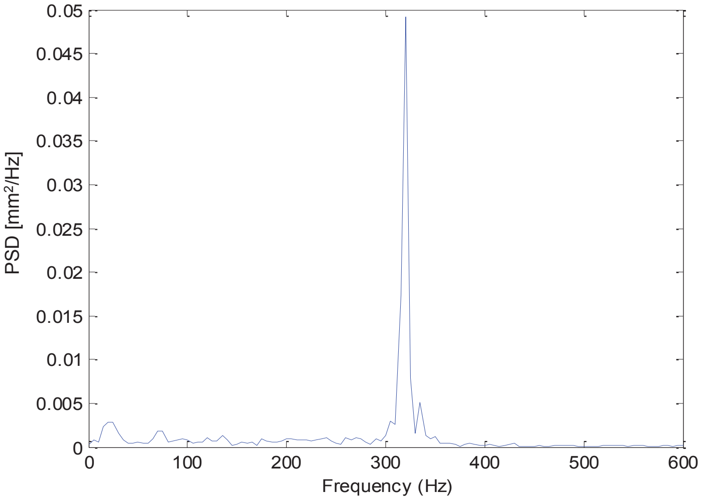

Figure 4.19: Power spectral density of the liftoff motion of DME flames, Air $\dot{m}$ = 282 g/min, ϕ = 0.75. Liftoff motion occurs at the same frequency as the chemiluminescence and pressure fluctuations.

For DME flames, the average liftoff height was 4 mm. Propagation speeds for the flame motion were also calculated for the upstream and downstream motions. The upstream and downstream speeds were 2.5 m/s and 1.9 m/s, respectively. The average propagation fluctuation for a DME flame was 0.52±1.2 mm. For methane flames, the average liftoff height was 6 mm compared to 8 mm for propane flames. For both methane and lean propane, the propagation speeds in each direction were the similar. The upstream and downstream speeds for methane were both 1.5 m/s.

For propane the upstream speed was 7.4 m/s and the downstream speed was 7 m/s. The average propagation fluctuation for a methane flame was 0.6±1.6 mm and for propane, the average propagation distance was 2.9±8 mm. These results indicate a high degree of motion and rapidly changing flame sizes and positions, particularly for propane.

4.2.4 Centroid of Heat Release Measurements

However, while flame liftoff height is a useful metric, it only pertains to the flame base. The condition can arise where the flame base is rather stationary and the flame brush above it thickens, an effect not captured by the previous measurements. As well, the liftoff height calculation assumes that the base of the flame moves vertically as a plane, an assumption inherent to the horizontal integration. As seen in Figure 4.12, the flame may rock from side to side. This is a combination of horizontal and vertical motions where the flame base does not remain parallel to the burner face. In order to get an idea globally of the flame motion, the centroid of chemiluminescent signal can be calculated according to the following:

$$C_x = \frac{\iint\limits_S xI(x,y)dxdy}{\iint\limits_S I(x,y)dxdy} \tag{4.2}$$

$$C_y = \frac{\iint\limits_S yI(x,y)dxdy}{\iint\limits_S I(x,y)dxdy} \tag{4.3}$$

This calculation for the axial and radial location of the chemiluminescence is performed for each image in a 2500 frame series. The result is the time evolution of the center of heat release for the flame. This also allows for the flame motion to be decomposed into radial and axial time-resolved movements. Figures 4.20 - 4.22 depict the resulting power spectral densities calculated from propane, ethylene, and

25% H_2 syngas flames. Interesting results are provided in these plots in that the radial and axial motions are remarkably different. As expected however, the flame centroid fluctuates vertically at the same frequency as the thermoacoustic oscillation for each respective fuel.

The radial motion of each flame captures glimpses of the thermoacoustic oscillation. However, the majority of the energy is located in a spectral band between 10-30 Hz, dependent on the flame. This motion is very slow compared the vertical fluctuations. This behavior almost amounts to a sloshing back and forth. There is no evidence to suggest that this motion is related to the PVC motion, which rotates at around 500 Hz according to measurements from DLR. However, it will be discussed in Chapter 5, that a 15 Hz oscillation is observed in high speed formaldehyde PLIF videos. It is assumed that these low frequency motions in both the chemiluminescence and formaldehyde signals may be due to a slow breathing motion. However, the precession of the PVC helical structure may circumferentially move around at this low frequency. This could be studied with OH or formaldehyde PLIF of the transverse plane, but was not currently conducted. This motion would be represented as a slow left-right motion in the chemiluminescence. Basic scaling suggests that this is may be a transverse oscillation which is proportional to the radial velocity fluctuations and the radius of the burner as follows:

$$f = \frac{U_r'}{2R} = \frac{1.25m/s}{0.085m} = \ 15Hz \tag{4.4}$$

4.3 Flowfield Interaction with Unburned Fuel Localization

Figure 4.23 represents flame motions over the course of an acoustic cycle for a propane flame operated at Case B conditions. The flame lifts off the face of the

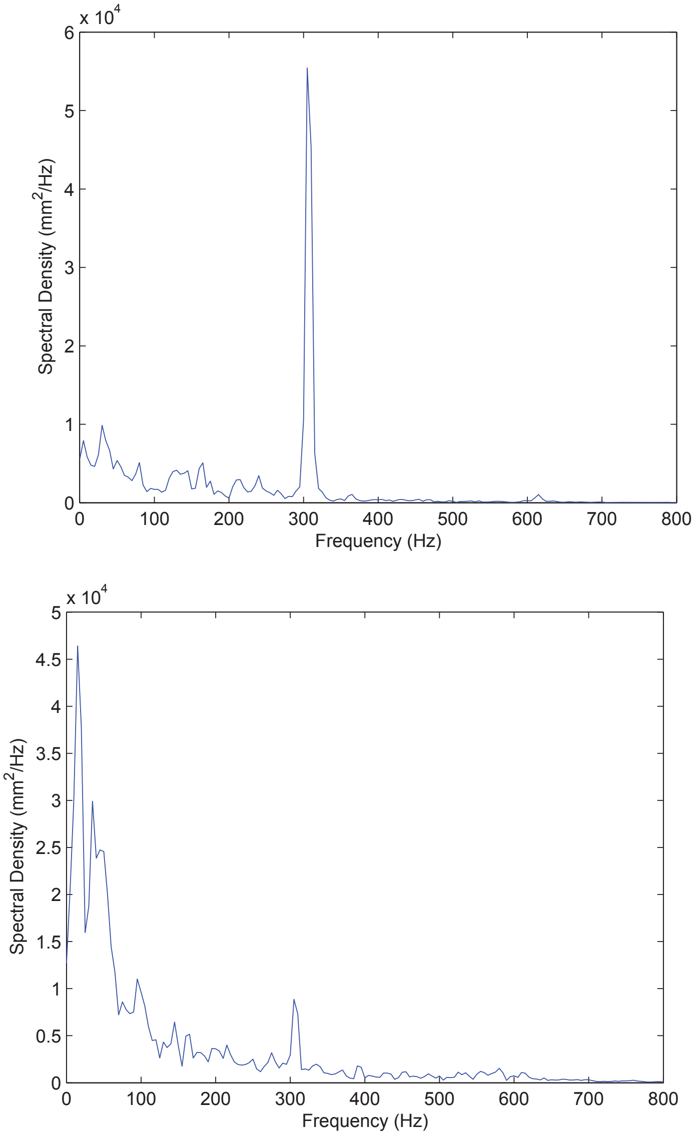

Figure 4.20: Centroid of heat release in propane flames. Axial centroid power spectral density (*upper*). Radial centroid power spectral density (*lower*). Air $\dot{m}$ = 282 g/min, $\phi = 0.75$.

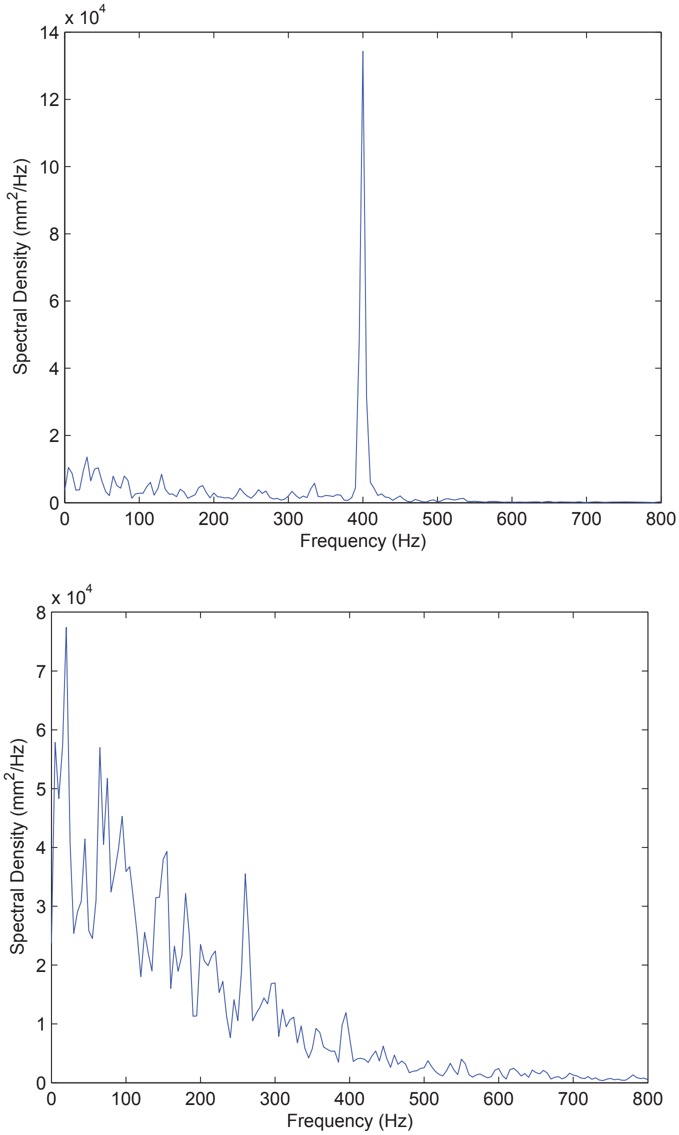

Figure 4.21: Centroid of heat release in ethylene flames. Axial centroid power spectral density (*upper*). Radial centroid power spectral density (*lower*). Air $\dot{m}$ = 282 g/min, $\phi = 0.75$.

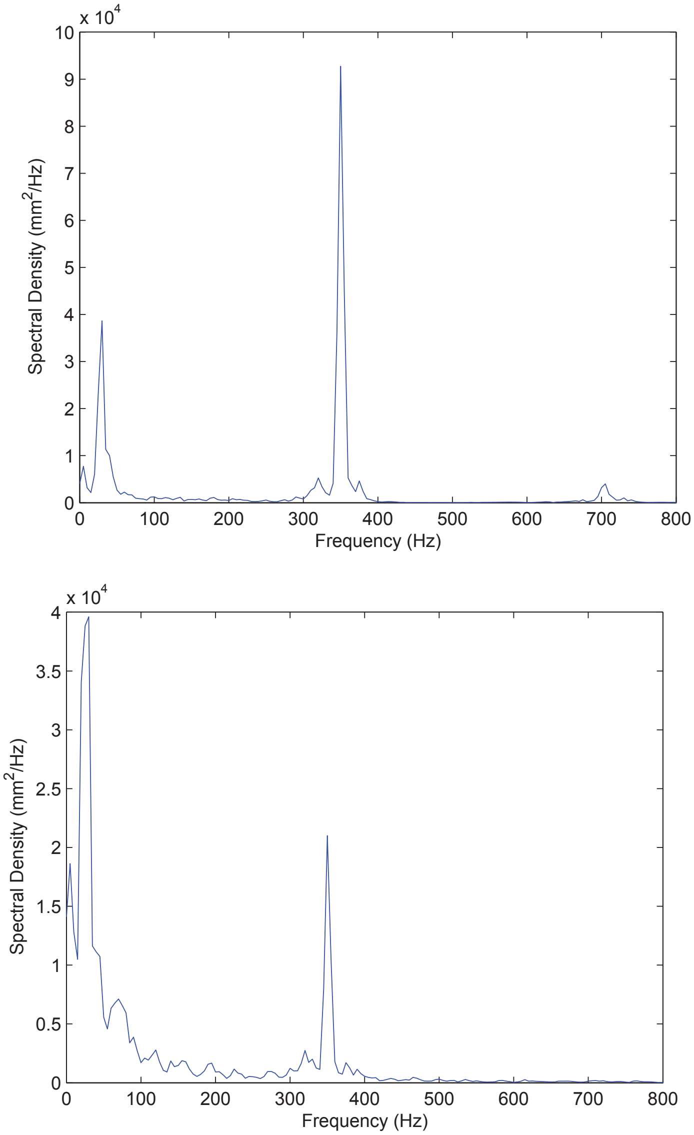

Figure 4.22: Centroid of heat release in 25% H_2 syngas flames. Axial centroid power spectral density (*upper*). Radial centroid power spectral density (*lower*). Air $\dot{m}$ = 282 g/min, ϕ = 0.75.

burner and then returns to a flat shape. The two red circles marked in Scene 2 represent the location immediately above the fuel injector, where the propane is entering. These regions will be further analyzed with acetone PLIF measurements. As the flame moves back upstream to the injector, this region remains partially unburned. In Scene 3, there is still some unburned space in this region until the flame fully propagates back to the burner face in Scene 4. The cycle repeats with the flame then lifting off again. As described in Chapter 2, acetone has been added as a tracer to the fuels. This was conducted as part of a larger study to investigate partial-premixedness and flame index in the GTMC. This section applies the acetone PLIF to look in particular to where unburned fuel is distributed.

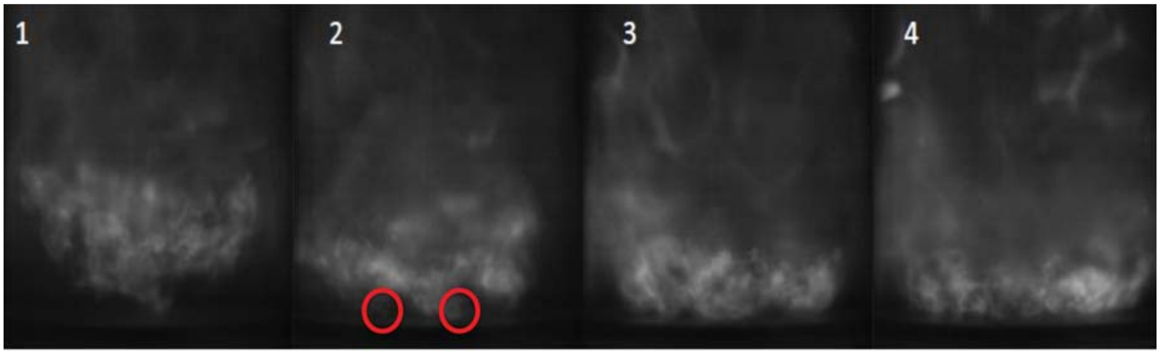

Figure 4.23: Series of propane chemiluminescence images depicting the liftoff cycle motion and the potential for the pooling of unburned fuel beneath the flame in regions marked by red circles. These zones are investigated with acetone PLIF.

4.3.1 Fuel Localization in Lean Methane Flames

Methane was bubbled through an acetone bath to seed the flow for fuel marking. The location of the acetone signal marks regions of unburned fuel. Acetone PLIF measurements were taken over a field of view located above the fuel injector to the right of centerline. Figure 4.24 shows the average acetone signal for 450 images. Two distinct lobes of fuel exist in the burner. Lobe A is located closer to the injector at a radial distance of 12-14 mm. Lobe B is lifted and located at a radial distance of 8-10mm from centerline, which is almost directly above the fuel annulus. Both these lobes are marked with rectangular regions of interest (ROI) in Figure 4.24.

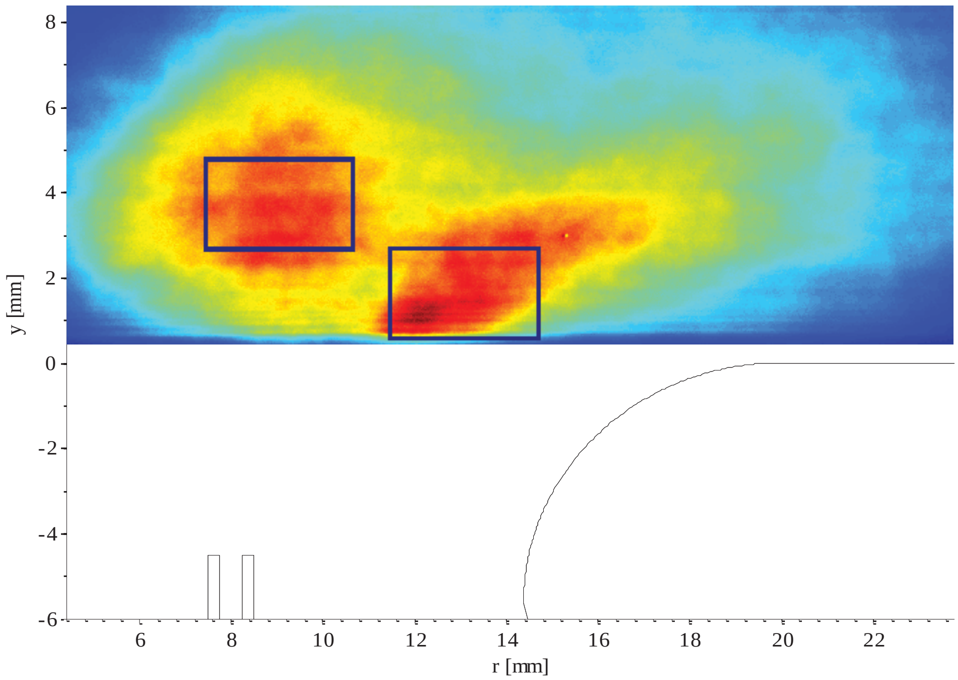

Figure 4.24: Average acetone PLIF signal, marked with regions of interest for methane, with GTMC injector schematic, denoting where unburned fuel is located. Air $\dot{m}$ = 282 g/min, $\phi =$ 0.75.

These two regions have been investigated for dynamic behavior. It has been observed that the unburned fuel location switches between Lobe B, located in the upper left of the image, and Lobe A, located in the lower right, over the course of the data set. In order to develop a numeric metric, the entire signal within the regions of interest (ROI) marked on Figure 4.24 are respectively considered. Each region of interest is equally sized. For each frame in the 450 image set, the total signal in each ROI is summed. A ratio of the signal in region A versus region B is calculated. When this ratio is larger than 1, there is more fuel located near location A. For ratios close to 1, there is an equal amount of fuel located in both regions A and B. For ratios much smaller than 1, the signal at location B is much larger than that at location A. Figure 4.25 depicts sample frames for various calculated ratios of 57, 1, and 0.08. In order to even the scaling range between ratios larger than 1 and ratios less than 1, the following metric has been applied for each ratio per image:

$$Z_i = \log \left[\frac{\iint\limits_{ROI_A} I(x,y)dxdy}{\iint\limits_{ROI_B} I(x,y)dxdy} \right] \tag{4.5}$$

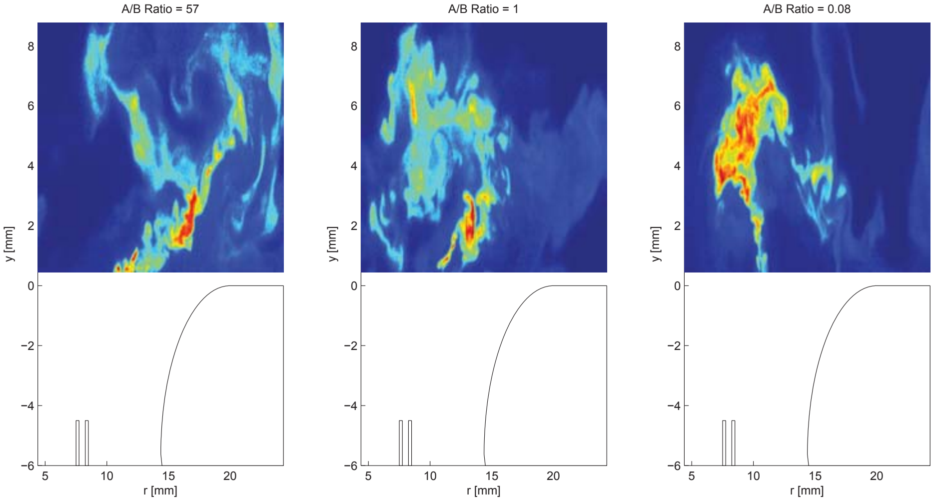

Figure 4.25: Instantaneous acetone images depict three typical cases of fuel localization based on the ROI ratio. (*left*) Ratio = 57. Fuel mostly located in Lobe A. (*center*) Ratio = 1. Fuel evenly distributed between both lobes. (*right*) Ratio = 0.08. Fuel mostly located in Lobe B.

This metric can be used to track the movement of unburned fuel between these two regions as it switches back and forth. These measurements were taken at around 1 Hz. The time sequence of motion captured is not time resolved. However, individual statistics based on each frame can be used to evaluate this motion. Figure 4.26 displays a histogram of the logarithm of these ratios, the metric Z_i, which allows for more balanced scaling. Values near zero correspond to an equal distribution of unburned fuel. Positive values correspond to concentrations favoring ROI A, and negative values correspond to concentrations favoring ROI B. Based on the histogram, 60% of the cases have more acetone in ROI A. There are also several cases where the signal in A is up to 100x lager than in region B. However from the average acetone image, the total signal in each ROI is roughly the same, which indicates that even when the fuel is concentrated to one ROI or the other, the signal strength is equally the same regardless of the lobe that it is in.

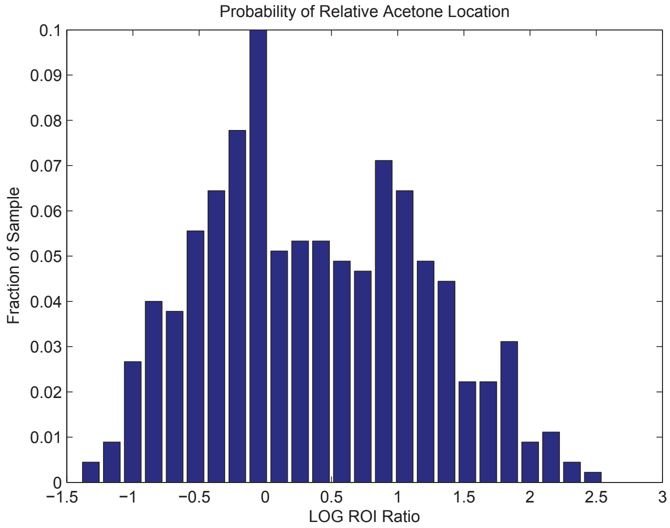

Figure 4.26: Histogram of the values of Z_i identifying where unburned methane fuel is localized. Positive values indicate that the majority of the fuel lies in Lobe A. Negative values indicate that the majority of the fuel lies in Lobe B.

This back and forth motion can be related to the large scale fluctuations in radial velocity which occurs over an acoustic period. The pattern exhibited in the average acetone image is very similar to that of the average formaldehyde PLIF image for non-resonating DME flames. This is not to suggest that this particular methane case was not resonating, however, it suggests that the flow field between the two cases are similar. It will be discussed in Chapter 5, that the flow in non-resonating hydrocarbon flames are dominated by the presence of the PVC, which can cause this rocking motion observed in the chemiluminescence image series. The pattern displayed in the average image may reflect the influence of the precession of the the PVC. For a 2-D cut through the burner, as the PVC moves to a particular side of the injector, the flow is disturbed and directed outward. As the PVC moves to the other side of the injector, the original flow pattern is restored and the fuel move closer to centerline.

According to PIV measurements from DLR, the location of the gap between the two lobes corresponds to the high velocity shear layer between the CRZ and ORZ. The PVC originates from within this shear layer and its movement may be the cause of the localization of fuel on one side or another of the this shear layer.

4.3.2 Fuel Localization in Propane Flames

Similar PLIF measurements were taken in propane for lean ($\phi_{lean} = 0.75$) and rich ($\phi_{rich} = 1.20$) flames. Figure 4.27 depicts the average acetone signal for the lean and rich propane cases. These images show similar dual lobe behavior as compared to the average acetone methane signal. However, for lean propane, the unburned fuel is concentrated to ROI B, whereas for rich propane, the unburned fuel is concentrated to region A. The same ROI ratio was calculated for these lean and rich cases as given in Figure 4.28. The ROIs are spatially located in the same locations relative to the injector as in the methane study. As well, each ROI corresponds to equally sized areas as the methane study.

For the acetone signal in upper plot of Figure 4.27, the signal is on average twice as strong in region B as region A for lean propane. From the top histogram in Figure 4.28, the range of ratios exhibited is larger than that seen in methane. Figure 4.28 shows that for 40% of the time, the signal in ROI B is at least double the signal in A. Likewise, 40% of the time, the signal in ROI A is at least double the signal in ROI B. This suggests, in coordination with the average signal image, that when the unburned fuel is located in ROI B, the concentration is large, compared to when the fuel is in ROI A, where the concentration appears to be weaker. However, when the fuel is located in ROI A, the signal in ROI B must be very weak, in order for the average image to reflect this uneven behavior. For the acetone signal in the lower plot of Figure 4.27, the signal is on average 15% stronger in region A than in region B for rich propane. The lower histogram of Figure 4.28 shows that for 23% of the time, the signal in ROI B is at least double the signal in A. However, 47% of the time, the signal in ROI A is at least double the signal in ROI B. This suggests, in coordination with the average signal image, that the fuel is typically found in ROI A on a frame to frame basis. However, fuel can appear almost equally strong in signal for either ROI.

4.3.3 Fuel Localization in Lean Syngas Flames

The same measurements have been applied to syngas flames, where the carbon monoxide has been bubbled through liquid acetone and then this mixture is combined with the hydrogen to form the final syngas mixture. The average acetone image in Figure 4.29 reveals a very different behavior compared to the alkane cases previously discussed. The syngas fuel location appears to have very little spatial movement based on the average. The signal strength does vary significantly from shot to shot; the *RMS* of the total integrated signal per picture represents 46.5% of the average integrated signal, which indicates a highly fluctuating flow. There appears to be little horizontal motion of the flame, however the degree of vertical motion can be verified by investigating a series of transversely integrated signal images, similar to those produced in Figure 4.13. Figure 4.30 depicts this motion for a series of frames, where each columns represents the horizontally integrated signal. It should be noted that the images are not time-resolved and thus the temporal evolution of

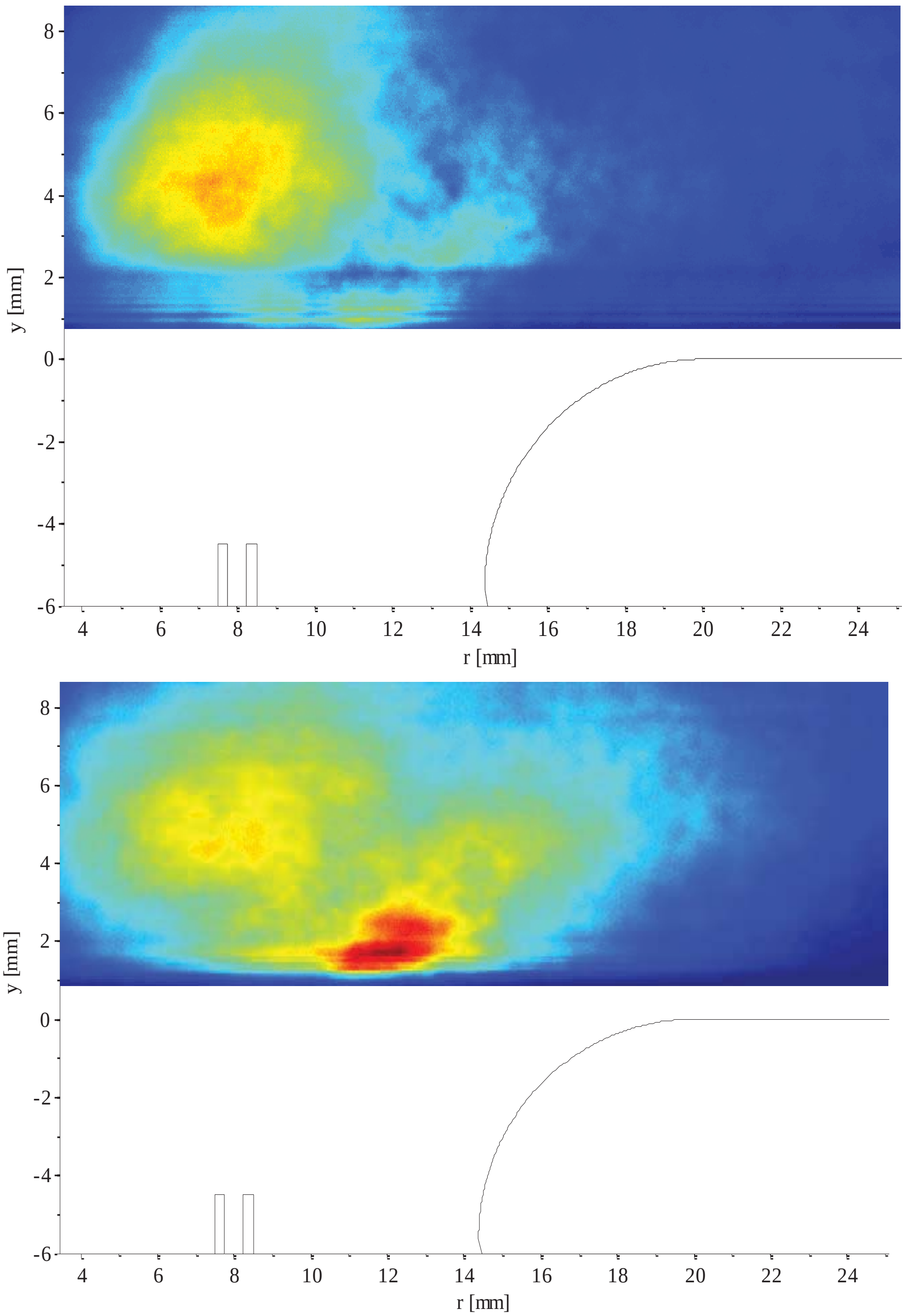

Figure 4.27: Average acetone PLIF signal, for lean propane (*top*) and rich propane (*bottom*), with GTMC injector schematic, denoting where unburned fuel is located. Air $\dot{m}$ = 282 g/min, $\phi_{lean} = 0.75$, $\phi_{rich} = 1.20$.

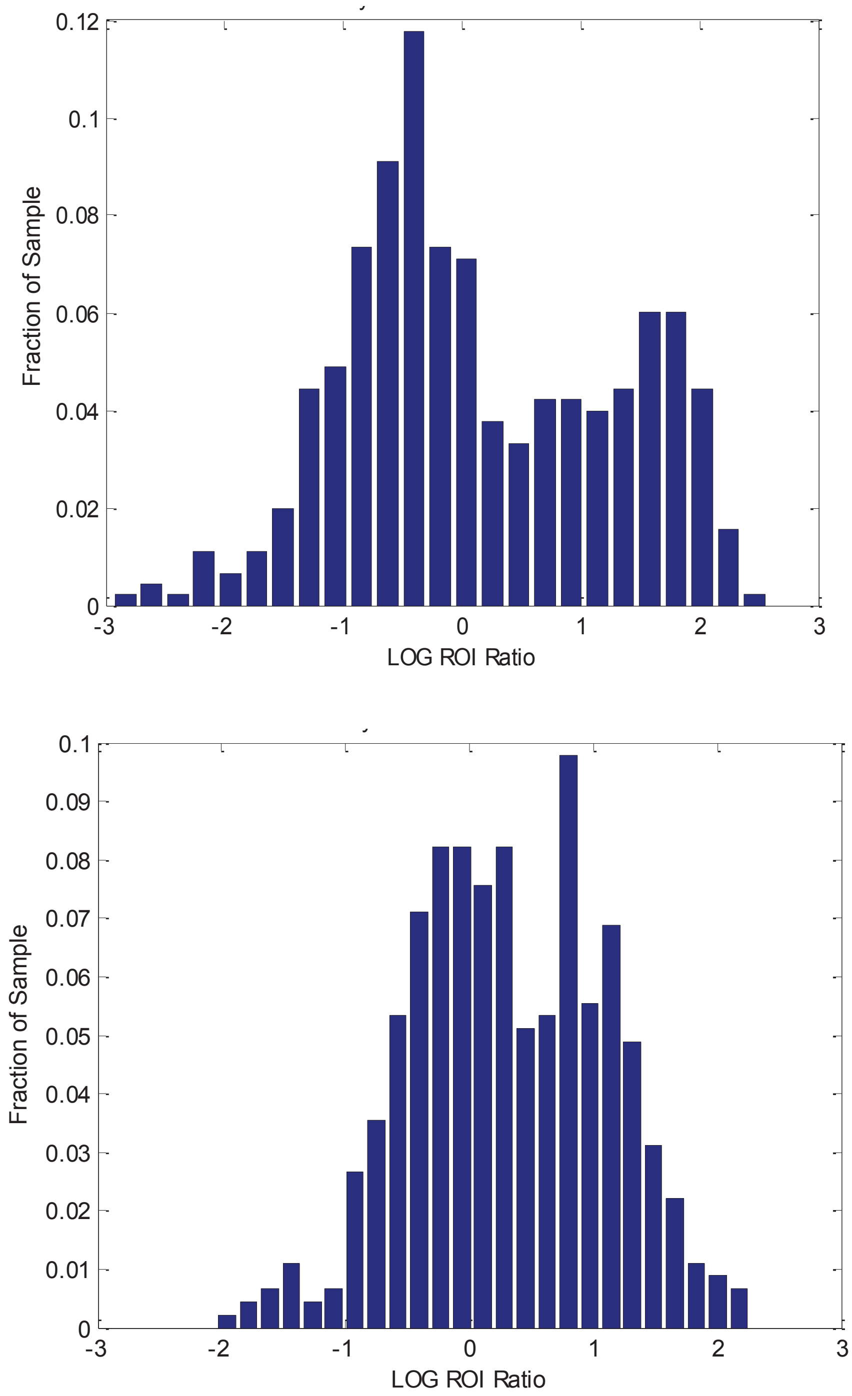

Figure 4.28: Histogram of the values of Z_i identifying where unburned lean propane (*top*) and rich propane (*bottom*) fuel is localized. Positive values indicate that the majority of the fuel lies in Lobe A. Negative values indicate that the majority of the fuel lies in Lobe B.

the motion cannot be determined, however this figure does show that the peak fuel concentrations do exhibit some degree of relative vertical movement.

From the average image, it can be seen that the unburned fuel lies in the shear layer created directly above the injector between the CRZ and ORZ. The lower image of Figure 4.29 shows an overlay of the average unburned fuel location in methane and syngas with the ROIs marked. The syngas layer lies directly in between the two methane lobes. This localization of fuel may be explained by the absence of the PVC in this particular flame. Granted, there is no direct evidence to verify this claim, however the hypothesis is supported by the lack of horizontal motion present compared to other flames. Syngas flames are more directly anchored to the fuel injector and the presence of fuel being directly located in the shear layer suggests that the formation of the PVC may be disrupted. This will reduce and/or arrest the rocking motion created by the PVC over the course of a liftoff cycle.

4.3.4 Special Case: Low Radial Flow Propane

This last case study represents a very different operating and fueling condition. Results from Rosenberg et al. [109, 110] have concluded that the majority of the reactants are quickly mixed and achieve a premixed state. In order to investigate a case in which the majority of the flow is non-premixed, the configuration and fueling of the burner was modified. The outer swirler passages were blocked, and the air mass flow rate was dropped to 60% of the nominal cases while the equivalence ratio was raised to $\phi = 1.2$. This creates a swirled air core flow with a propane fuel co-flow. The shear from the outer swirler is not acting on the flow. As expected, the instability was not present. The resulting flame was highly V-shaped, and very likely there is no PVC present. The average acetone image seen in Figure 4.31 has features similar to the syngas case. The majority of the unburned fuel lies directly above the

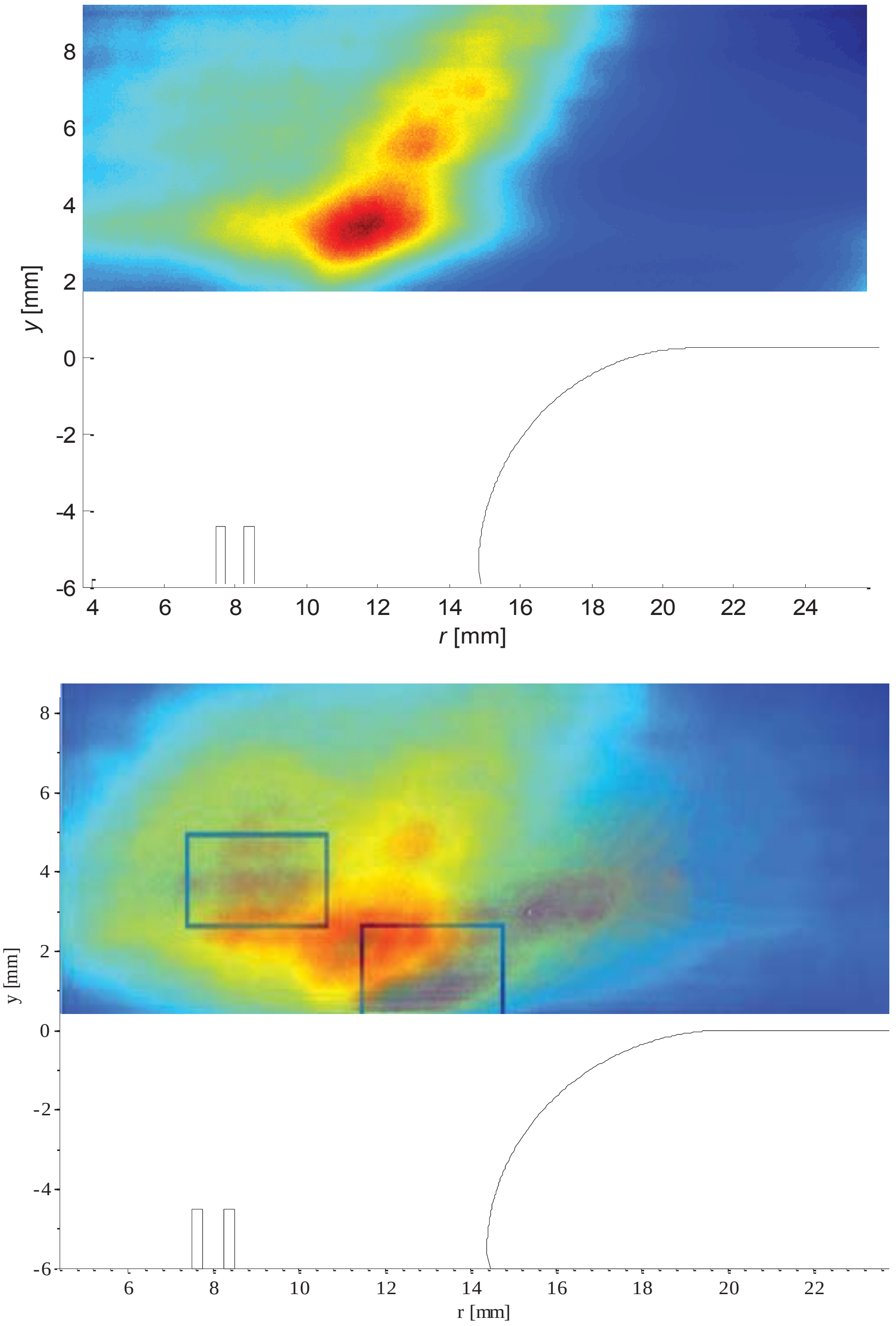

Figure 4.29: Average acetone PLIF signal (*top*) for 25% H_2 syngas flames, with GTMC injector schematic, denoting where unburned fuel is located. Air $\dot{m}$ = 282 g/min, ϕ = 0.65. Overlay of the location of the average syngas fuel location with regards to the average methane fuel location with ROIs marked (*bottom*).

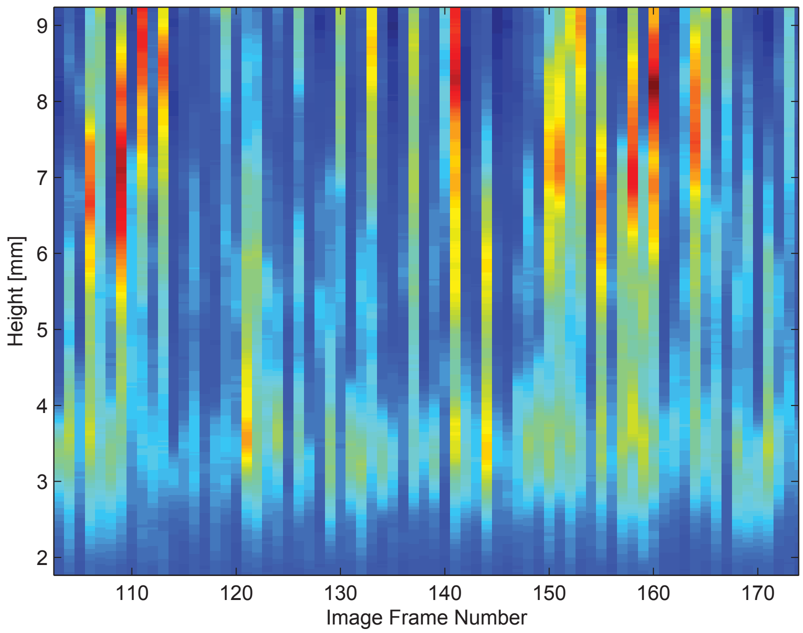

Figure 4.30: Transversely integrated acetone PLIF intensity depicting the vertical motion of syngas fuel location in the GTMC shear layer. This series is not time-resolved; each vertical column represents an individual frame in the series. Time between images is 1 sec.

injector on the outside edge of the central air flow. There may also be some fuel entrained into the swirling air flow. However, the common flow pattern between this case and the syngas case is that the radial flow due to the outer swirler is either very low or non-existent. This may suggest that the formation of flow structures critical to instability coupling and presence require higher radial flow velocities.

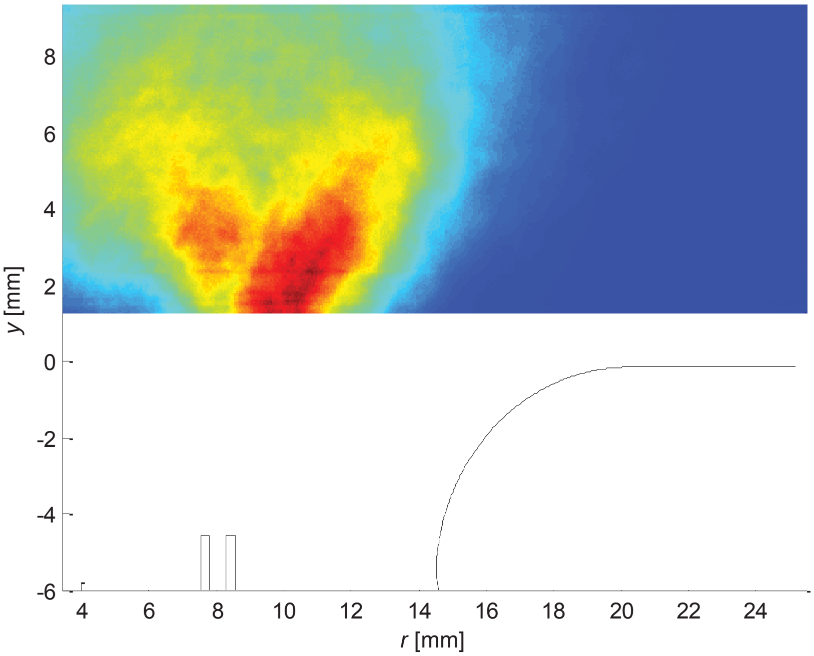

Figure 4.31: Average acetone PLIF signal for low radial flow propane, with GTMC injector schematic, denoting where unburned fuel is located. Air $\dot{m}$ = 173 g/min, $\phi = 1.20$.

CHAPTER V

High-Speed Investigations of Preheat Zone Surfaces

Formaldehyde is created as an intermediate compound in the breakdown of hydrocarbon fuels. It is formed in the low temperature regions on the fuel side of the flame and acts as a marker for the preheat zone of the flame, as was discussed in Section 1.2.4 of the introduction and also explained for DME flames in Section 2.7.2. The steep concentration gradients allow for the marking of the edge of the formaldehyde surface which lies adjacent to the reaction zone layer marked by the formation of CH radicals. The detection of this edge allows for observations of the flame surface structure, as seen in Figure 5.1. High-speed formaldehyde PLIF has been applied at frame rates of 2.5 - 4 kHz to make time-resolved measurements of the evolution of the flame surface in DME and ethylene flames. These measurements allow for the calculation of the flame brush size, flame surface area, and flame surface density. The time resolution of these images also allows for dynamic tracking of these metrics. Proper orthogonal decomposition (POD) has been applied to understand the types of coherent flame structures that exist and how the most significant modes represent particular flame motions in time. The response of the flame surface to variations in air mass flow rate and equivalence ratio has also been observed. Measurements have also been made in ethylene flames for comparison of flame speed effects.

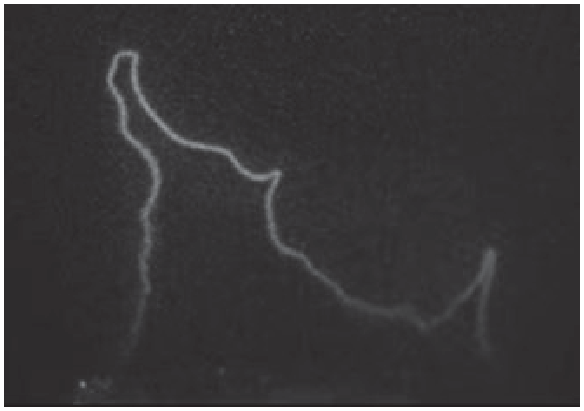

Figure 5.1: Flame surface marking and wrinkling observed in a DME turbulent premixed flame on a meshed Bunsen burner.

5.1 Comparison of Resonating and Non-Resonating Flames

5.1.1 High-Speed PLIF Image Series

The following figures depict a time series of images for non-resonating and resonating DME flames. There are some clear differences between the structures of these two flames. Figure 5.2 represents the evolution of the flame surface in time. This particular flame is non-resonating for the given fueling condition. However, it serves as a good basis for comparison to flow patterns exhibiting instabilities. The first visible difference between these flames is the amount of structure. Both of these flame cases are highly wrinkled. Non-resonating flames appear to be more wrinkled in this series. They have a higher degree of folding and the surface is more convoluted. The flowfield is not oscillating, but is dominated by turbulent eddies and the presence of the PVC. Whereas for the resonating flame, the flowfield is highly oscillatory. It will be proven in the coming sections that evidence of the PVC has been detected in the frequency response of the PLIF measurements.

The structures in the non-resonating flames are generally thinner than in the resonating flames. While brush size in each lobe may be larger, the high gradient edges which mark the flame surfaces are thinner. These same structures are thicker in the resonating flames, which may be due to thickening of the preheat zone due to high turbulence intensities. The interaction of eddies with the flame surface aids in the diffusion of formaldehyde outward from the surface, leading to a wider spatial distribution of the intermediate.

According to the LDV measurements of Chapter 4, the velocity field of non-resonating flames shows a smaller radial component, which causes the flame to be more axially stretched. This motion is exhibited by the non-resonating flames, as more structure extends to the top of the laser sheet. In resonating cases, the flames are flatter due to higher radial velocities. It can be seen in Figure 5.3 that less structure reaches the top of the sheet. As well, there is less structure close to the centerline of the flow.

The motions of the flame surface do show some similarities. There is a left-to-right switching motion from one lobe to the other. One lobe will strengthen in intensity and size as the other wanes. The growth of a given lobe is marked by a large increase in the surface area present, such that the heat release of the lobe must also be increased from one lobe to the next. There is a phase shift that occurs from one lobe to the next. The switching from one side to the other is separated by a time lag and the delay for resonating flames appears to be shorter than for quiet flames. At the maximum size and intensity for a lobe, the other lobe is beginning to also strengthen.

There is also a rocking motion present where, as the flame surface density decreases, the flame surface recedes to the burner face. As the flame surface density increases, the lobe moves away from the burner. This may be caused by asymmetric vortices created by the PVC helix which are convected downstream. From the POD analysis conducted later in this chapter, it will be seen that the PVC does control some aspects of the flame motion. This rocking motion is presented in Figure 5.4, where the white lines roughly indicate the mean flame surface position through the brush in each lobe. The angle of the line in each lobe changes over the switching cycle. The motion is not very drastic but occurs over a range of roughly a centimeter.

Finally, it is important to note that in the given experimental setup for the high-speed formaldehyde PLIF measurements, the GTMC is operated with 3 glass windows and 1 metal wall with pressure ports in the wall. This configuration varies from the configuration for acoustic measurements presented in Chapter 3. For DME fuel, when the extra windows are added, the frequency of the instability is reduced as well as the amplitude of the oscillation. This is consistent with the results from the series of burner modifications investigated. For the HSPLIF setup, DME flames are non-resonating for an equivalence ratio of $\phi = 0.75$. However it resonates for stoichiometric or rich conditions. Despite this discrepancy in instability presence, the data that follows provides insight into the differences between resonating and non-resonating flames, in terms of changes to flame surface and flow-flame interactions.

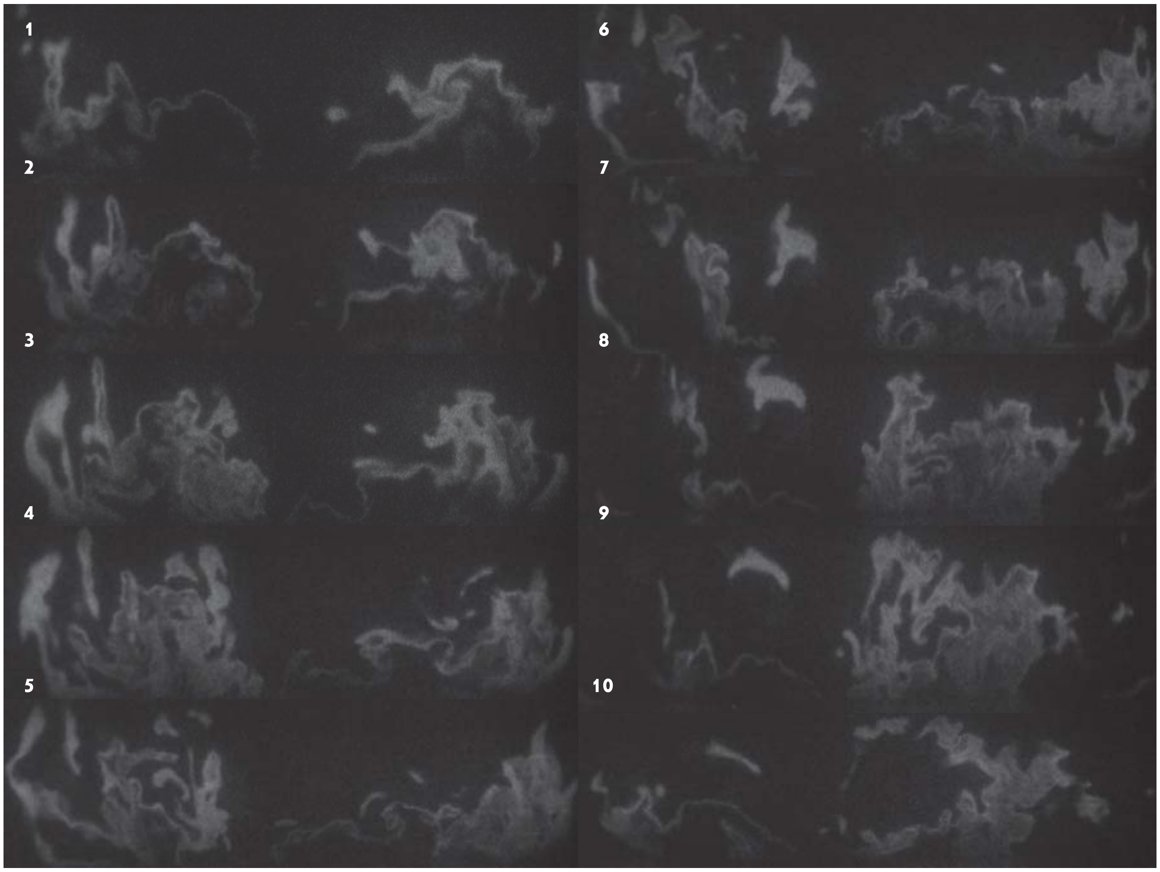

Figure 5.2: Non-resonating flames: Time series of images depicting flame surface motion and rollup due to PVC interaction. DME flames, air $\dot{m}$ = 282g/min, $\phi = 0.75$. Each frame represents a 20mm by 70mm field of view.

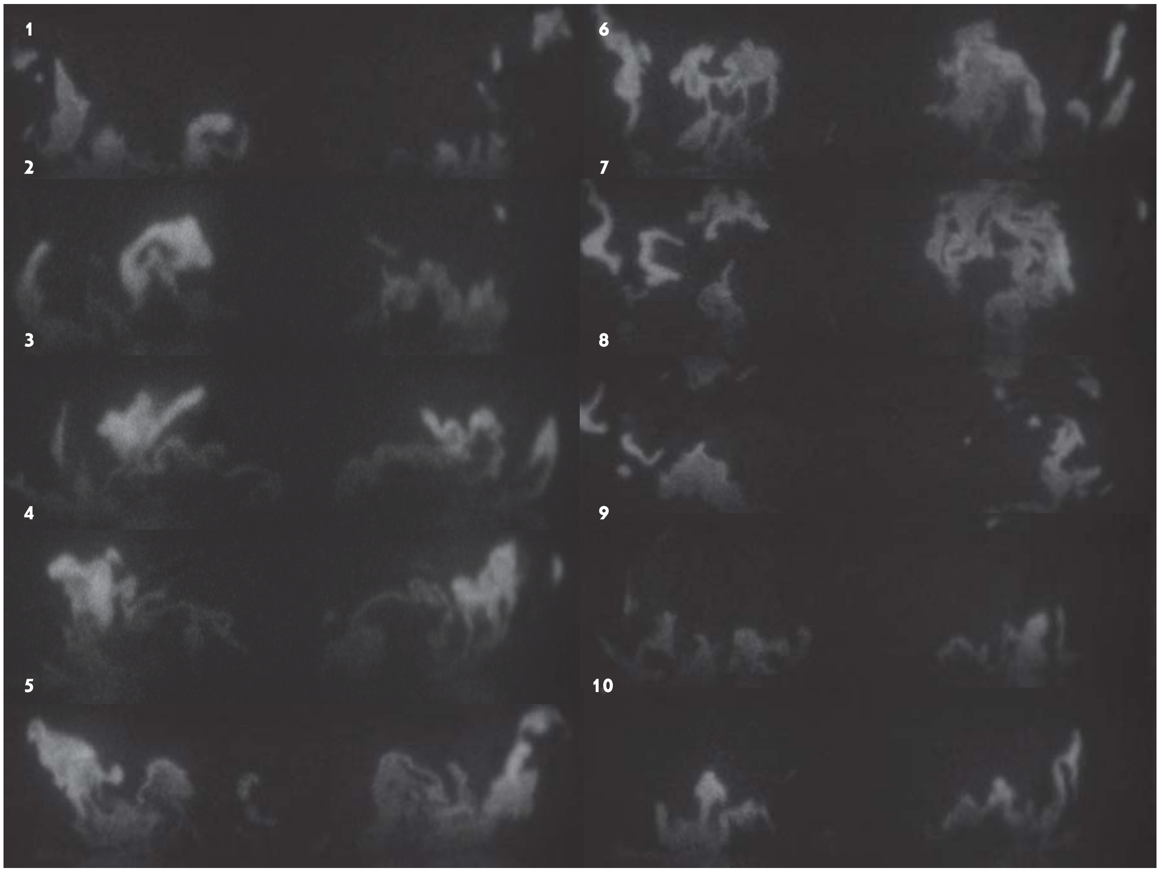

Figure 5.3: Resonating flames: Time series of images depicting flame surface motion and rollup due to PVC interaction. DME flames, air $\dot{m} = 282$g/min, $\phi = 1.2$. Each frame represents a 20mm by 70mm field of view.

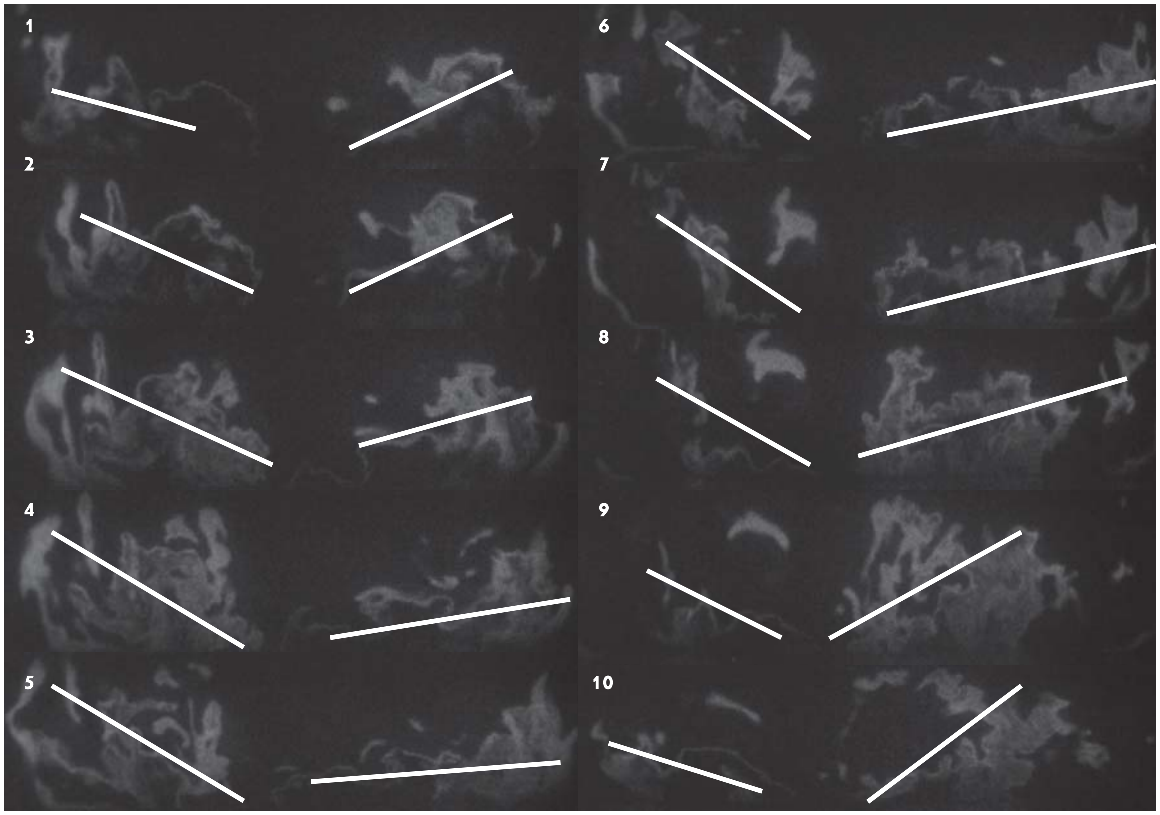

Figure 5.4: Non-resonating time series of images depicting flame surface rocking due to PVC interaction. DME flames, air $\dot{m} = 282$g/min, $\phi = 0.75$.

5.1.2 Integrated Formaldehyde Signal and Surface Motion

For each flame type, the average and RMS formaldehyde 2-D field has been computed for 4000 images, representing 1 second of real-time data, as seen in Figures 5.5 and 5.6. The two cases have very different structure in that the resonating flame is composed of two large lobes where formaldehyde exists. The left and right lobes of the non-resonating flame consists of a two-zone structure. This two-zone lobe structure is very similar to the pattern seen in the fuel localization PLIF images for hydrocarbon flames discussed in Chapter 4. In fact spatially, if the methane fuel distribution is compared to the non-resonating DME formaldehyde distribution, the lobes all lie adjacent to one another. The fuel lobes would lie just under each of the formaldehyde lobes. This suggests that the PVC also may dominate the flame motion for non-resonating flames, as will be determined from the forthcoming POD analysis. The separation of the two zones also appears to lie along the shear layer that exists on the boundary of the CRZ.

The radial distribution of flame surface also varies. The majority of the signal in resonating flames is located further from the center line, than for the non-resonating case. The two-zone lobes of quiet flames distributed the flame surface radially outward. It should be noted that the centerline appears to be free of signal from flame surface, which suggests that flammable mixtures are rarely entrained into the center of the swirling flow. However, the inner zone of the quiet lobes lie much closer to the centerline than the resonating lobes. Again this is due to the redistribution of air flow from the inner swirler to the outer swirler that occurs in resonating cases, which draws more fuel mixture radially outward.

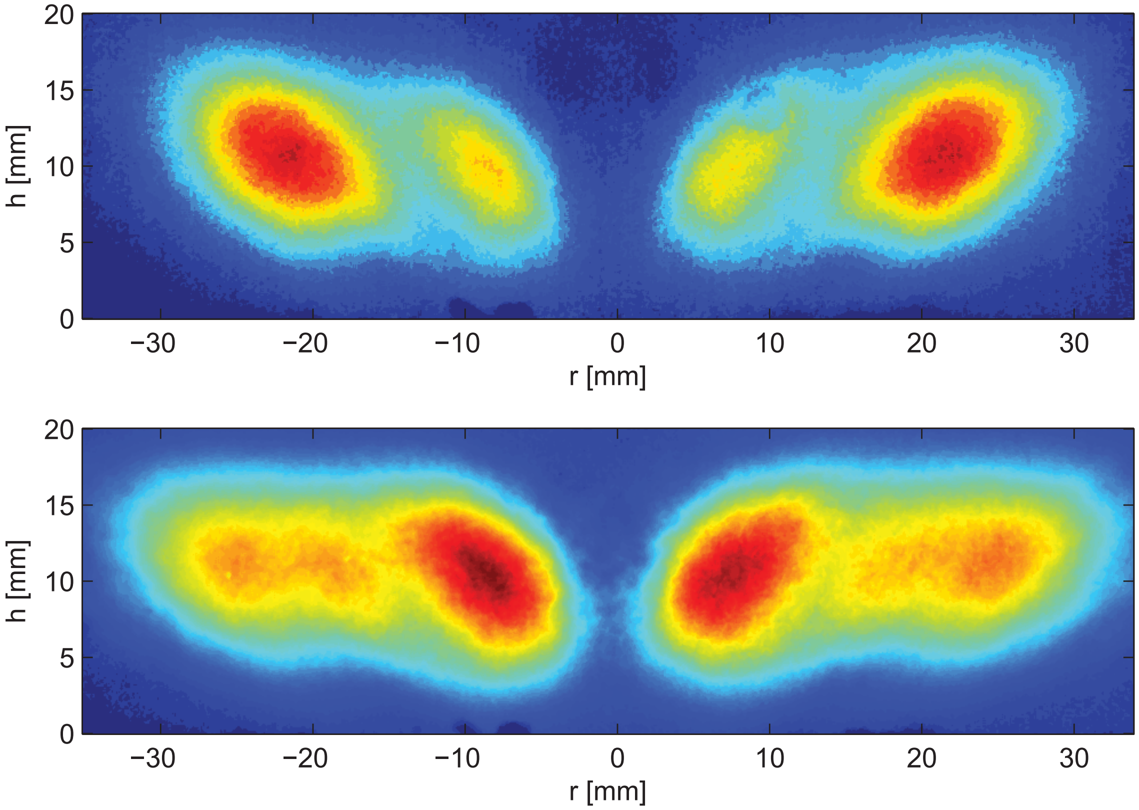

Figure 5.5: Formaldehyde average (*top*) and RMS (*bottom*) distribution for non-resonating DME flames, air $\dot{m} = 282\text{g/min}$, $\phi = 0.75$.

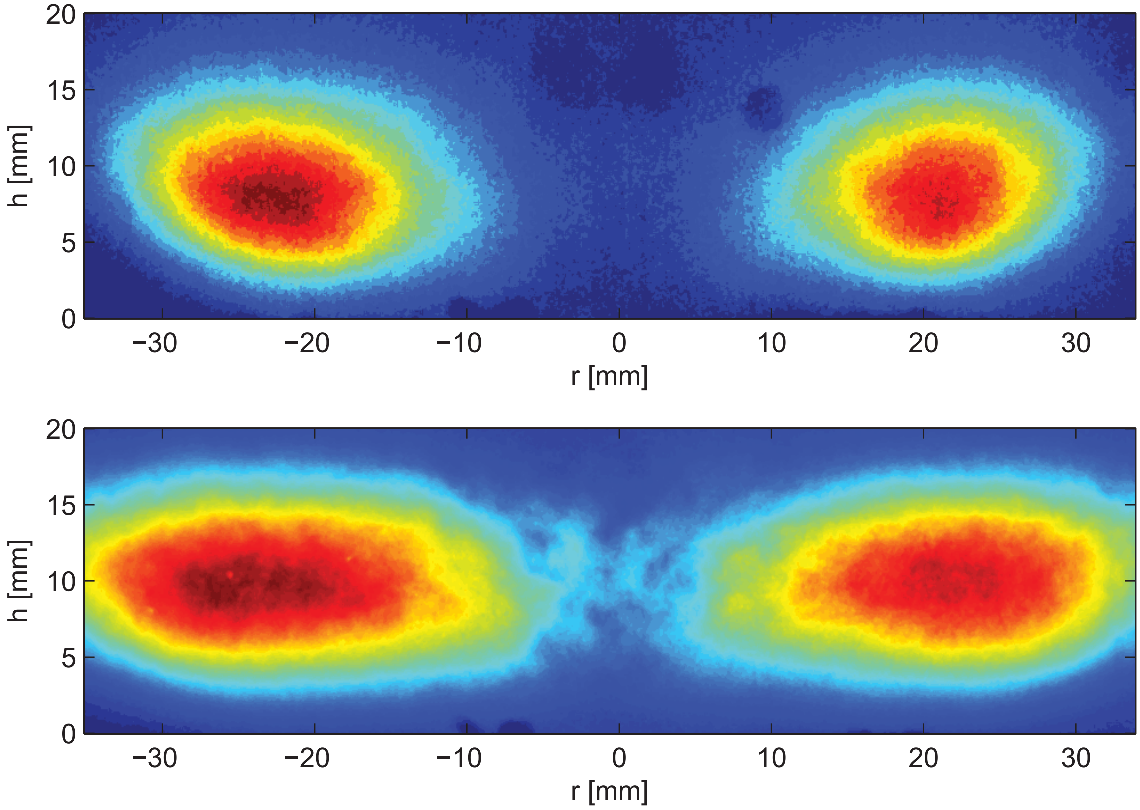

Figure 5.6: Formaldehyde average (*top*) and RMS (*bottom*) distribution for resonating DME flames, air $\dot{m} = 282\text{g/min}$, $\phi = 1.2$.

The RMS fields show that the signal is fluctuating strongly across the burner except near centerline for the resonating case. However, for the quiet flame, the strongest fluctuations occur at the inner zone of each lobe, with fluctuations extending closer to the centerline. This RMS distribution suggests the flowfield has an uneven distribution of turbulence between the inside of the shear layer near the CRZ and outside the shear layer.

If the total signal for the each image is integrated, a single intensity value is calculated per image. The power spectral density of the time series of these integrated intensities can then be calculated as seen in Figure 5.7. For the non-resonating flame, the dominant frequency occurs at around 50 Hz. The remaining spectrum does not show any other coherent fluctuations. The resonating flame clearly oscillates at the same frequency as the measured acoustics at 320 Hz. This suggests that the formation of formaldehyde, and hence flame surface, is coupled with the instability.

However, the switching behavior between the individual lobes must also be investigated. A rectangular region of interest has been considered around each lobe, and the total signal within each ROI has been integrated to yield a single intensity per lobe. Thus, there is a pair of intensities per image in the time series. A power spectral density can be calculated for the time evolution of each lobe, as given in Figures 5.8 and 5.9. Each of the lobes in the resonating case oscillate independently at the acoustic frequency of 320 Hz. There is also some motion at 10 Hz, which is similar to the frequency of radial centroid motion seen in the flames investigated in Chapter 4. This also may be due to a breathing motion.

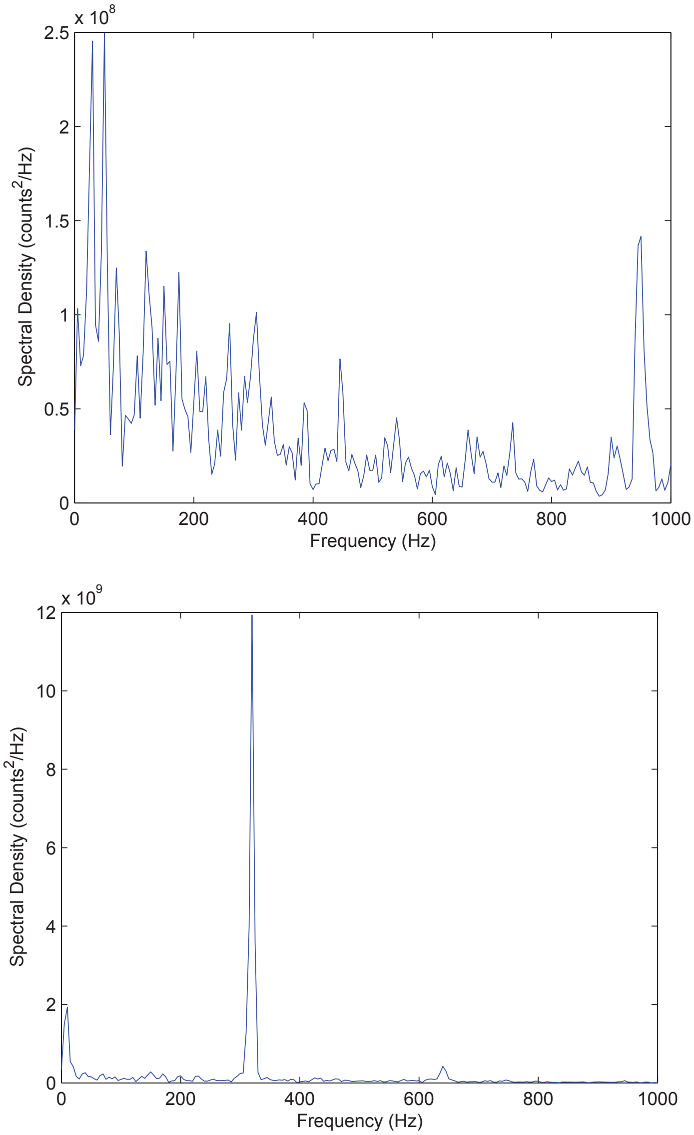

Figure 5.7: Power spectral density of the total integrated formaldehyde signal for non-resonating (*top*) and resonating (*bottom*) DME flames, air $\dot{m}$ = 282g/min, $\phi = 0.75$ and 1.2.

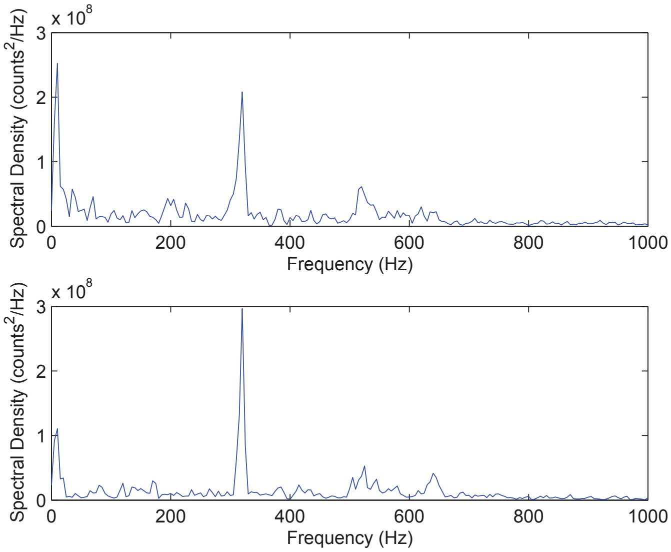

Figure 5.8: Power spectral density of the total integrated formaldehyde signal in left(*top*) and right (*bottom*) lobe ROIs for resonating DME flames, air $\dot{m}$ = 282g/min, $\phi = 1.2$.

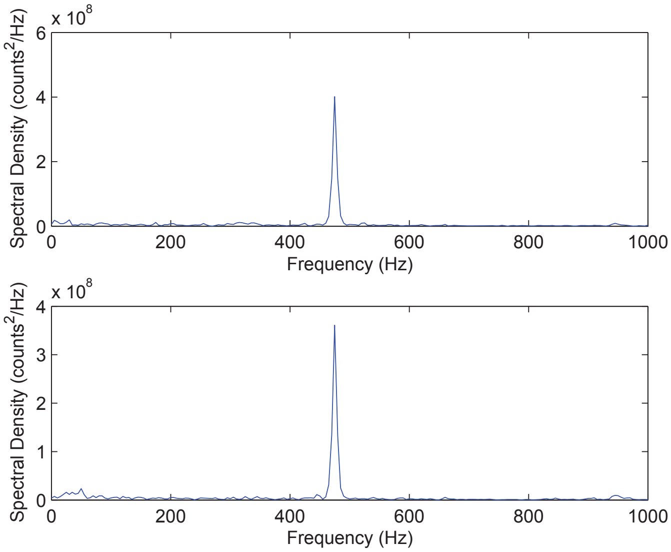

Figure 5.9: Power spectral density of the total integrated formaldehyde signal in left(*top*) and right (*bottom*) lobe ROIs for non-resonating DME flames, air $\dot{m}$ = 282g/min, $\phi = 0.75$.

The lobes in the non-resonating case fluctuate strongly at 475 Hz. This frequency is higher than any acoustic frequency measured with DME in the GTMC. However, high-speed PIV results from DLR have shown that the PVC precession occurs near 500 Hz in methane flames at the same flow rate and equivalence ratio. These power spectrum plots are highly suggestive of the flame being strongly affected by swirling flow structures. This is also the strongest evidence presented that the PVC is affecting the flame surface evolution, as suggested throughout this work. However, it again must be reiterated that the PVC was not measured directly. To measure the PVC motion directly, high-speed time-resolved PIV is required, and this measurement was not conducted at Michigan. Based on the PIV work at DLR which detects PVC motion near this frequency, it is concluded that PVC related effects are being observed. The oscillation within the formaldehyde scalar field is a result of PVC motion influences.

Of importance is the motion of one lobe relative to another. It was previously discussed from the high-speed time series that the non-resonating flames appear to have a longer delay time between each the maximum intensity observed in the oscillation of each lobe. Figure 5.10 shows that for each flame there is some phase shift in the relative oscillation of each lobe. For the non-resonating flames this phase shift is 127° and for the resonating flames the phase shift is 89°. This agrees with the longer delay observed in non-resonating flames. These plots prove that there is a certain degree of switching between the two lobes.

The ratio of the integrated signal in each lobe can also be considered. The power spectral density of this data proved the frequency of switching between the two lobes. Figure 5.11 shows that the frequency response of the switching between the lobes in non-resonating flames is at the suspected PVC precession frequency of 475 Hz.

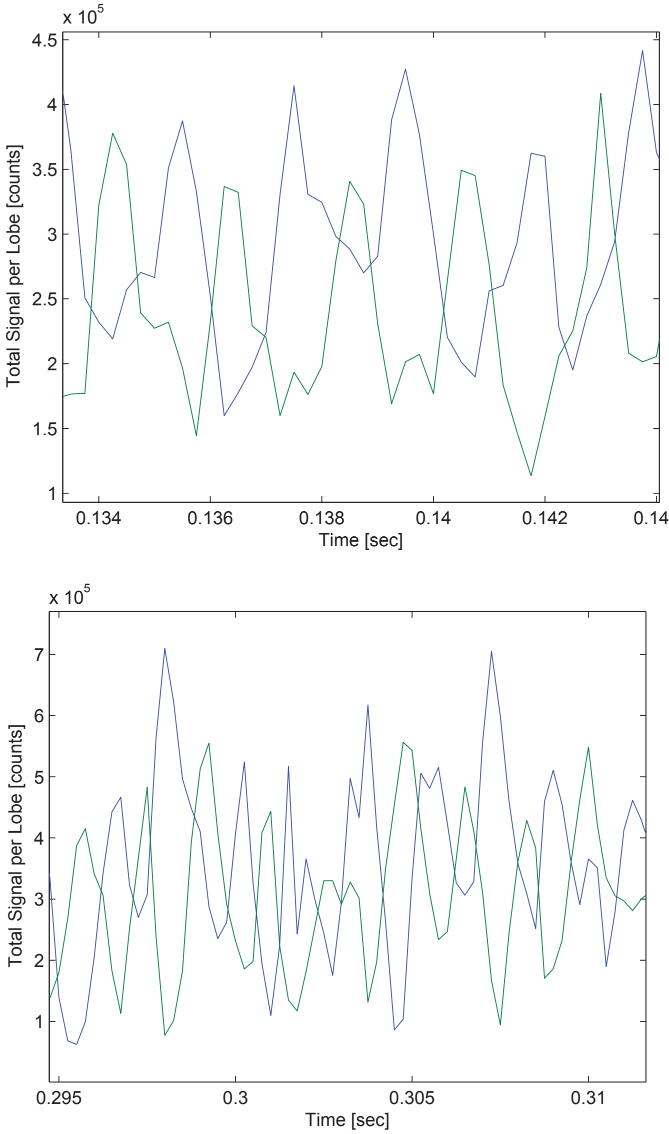

Figure 5.10: Integrated signal strength of each lobe fluctuating in time for non-resonating (*top*) and resonating (*bottom*) DME flames, air $\dot{m} = 282$g/min, $\phi = 0.75$ and 1.2.

The most interesting part of this figure is the response of the resonating flame at 525 Hz. While the total signal fluctuates at the acoustic frequency, the signal from one lobe to the next oscillates at the PVC frequency. This implies that there are PVC effects in the resonating flame occurring simultaneously with thermoacoustic oscillations. As the PVC precesses around, it encourages the creation of flame surface and formaldehyde in each lobe. This is very important because it helps explain some of the flame motions observed.

For the non-resonating flames, further information can be derived from the two zones that compose each lobe. A region of interest was examined encompassing each of the two zone segments of the left lobe. From this an FFT was calculated of each zone as seen in Figure 5.12, which shows that both regions also oscillate at a frequency of 475 Hz. The ratio of these two zones can be taken to see if the signal intensity oscillates from one zone to another, or if the signal of both regions is steady. Figure 5.13 displays that the intensity of each zone fluctuates back and forth between each other at 475Hz. This may imply that the PVC causes the flame surface to sweep from the inside of the shear layer to the outside, where there is a large increase in flame surface production.

The axial and radial centroids of formaldehyde production can also be calculated in a similar fashion to the centroid of heat release computed in Chapter 4. The power spectrum of the oscillation positions of the axial and radial centroids are presented in Figure 5.14 for both non-resonating and resonating cases. The non-resonating flames display vertical motion at 25 Hz, which may correspond to the breathing mode discussed previously. As well the horizontal motion of the centroid occurs at 475 Hz, corresponding to the precession of the PVC. In the resonating case, the vertical motion is consistent with the acoustic mode from the plenum. However the

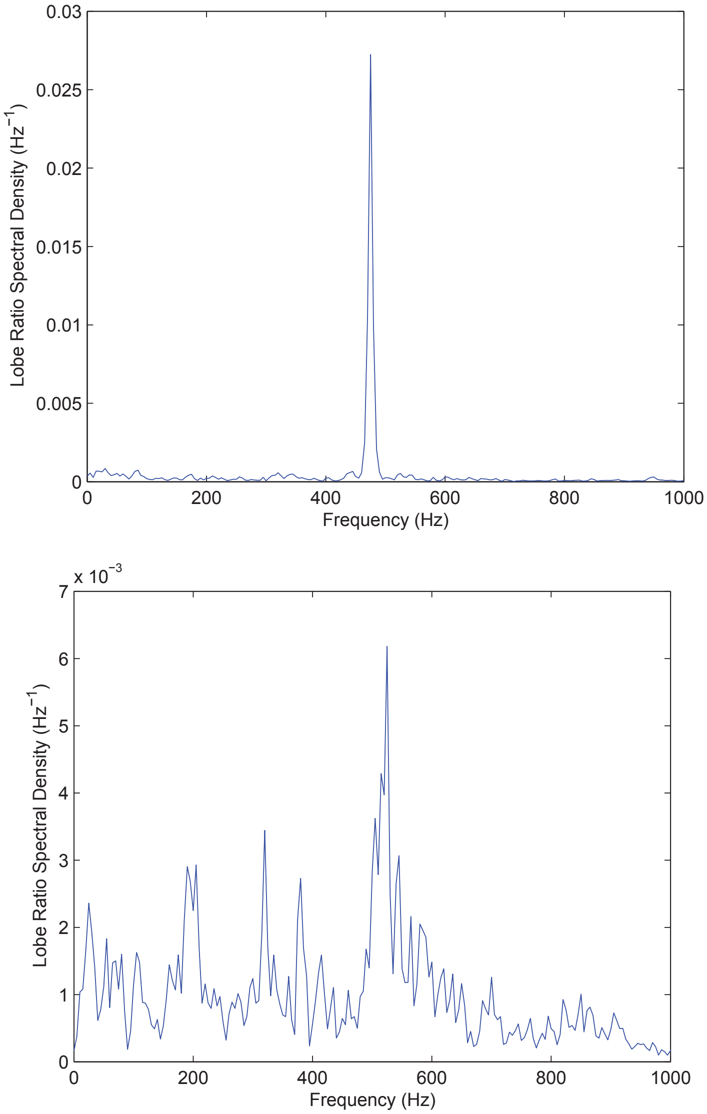

Figure 5.11: Power spectral density of the ratio of total integrated formaldehyde signal in each lobe for non-resonating (*top*) and resonating (*bottom*) DME flames, air $\dot{m}$ = 282g/min, ϕ = 0.75 and 1.2.

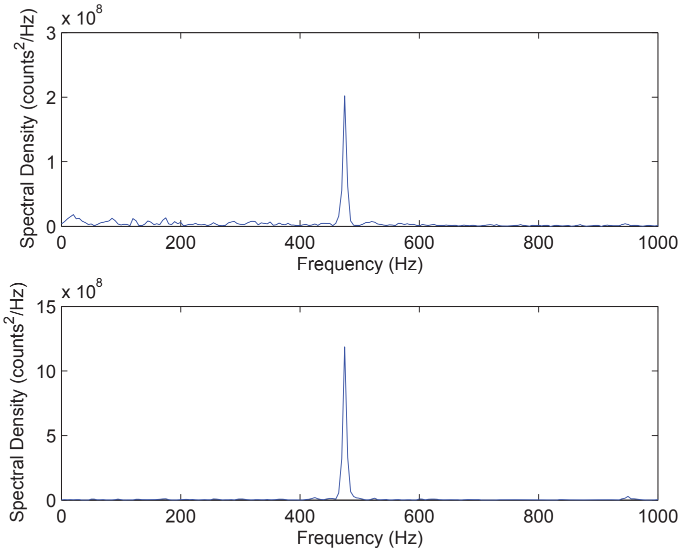

Figure 5.12: Power spectral density of total integrated formaldehyde signal in each zone for non-resonating DME flames, air $\dot{m} = 282\text{g/min}$, $\phi = 0.75$.

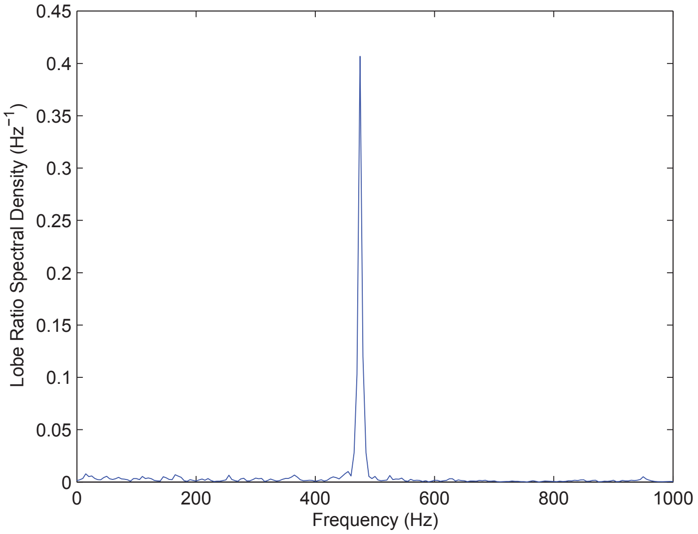

Figure 5.13: Power spectral density of the ratio of total integrated formaldehyde signal in each zone of the left lobe for non-resonating DME flames, air $\dot{m} = 282\text{g/min}$, $\phi = 0.75$.

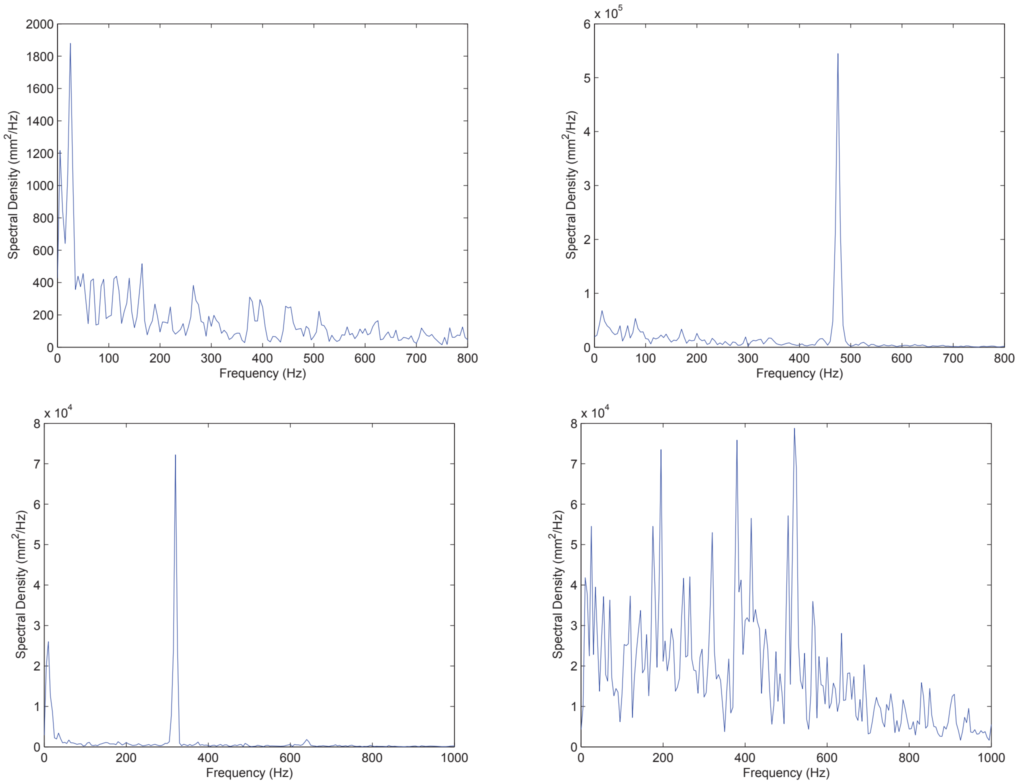

Figure 5.14: Power spectral density of the motion of centroid position in non-resonating flames: axial (*top, left*) and radial (*top, right*); resonating flames: axial (*bottom, left*) and radial (*bottom, right*) for DME, air $\dot{m}$ = 282g/min, $\phi = 0.75$ and 1.2.

horizontal mode is not very clear. The strongest peak occurs at 525 Hz, matching the assumed PVC motion. There is also a peak at 200 Hz, which centroid measurements taken at DLR have shown to be the difference in frequency between the PVC and thermoacoustic motion, in the lab frame.

The data presented in this section clarifies the flame surface differences between resonating and non-resonating flames. The motion of the flame appears to be a combination of PVC and thermoacoustic oscillations which cause liftoff and rocking behaviors. In resonating flames, PVC effects are only evident when the relative motion of each side of the flame is considered, due to the asymmetry of the PVC operating on the symmetric pulsation of the acoustics. Non-resonating flames are seen to couple directly with the suspected PVC motion.

This conclusion reinforces the application of time-resolved PLIF measurements in lieu of high speed chemiluminescence videos. The chemiluminescence captures the acoustic frequency along with the PLIF, but because it is line of sight, it will not capture asymmetric effects such as those due to the PVC. These asymmetries will be averaged out in the line of sight images. Most importantly though, is the ability to distinguish differences in increased heat release. The local heat release can be altered by fluctuations in flame surface area or changes to the local reaction rate. Essentially, a combination of flame length fluctuations could occur alongside local changes in signal intensity for the same amount of flame surface. Chemiluminescence videos cannot distinguish between these two causes and can only report the total effect of increased heat release. However, high speed PLIF measurements can capture these effects independently. With this data set, it can be seen that the in-plane flame length is also fluctuating with the instability.

5.1.3 Wrinkling and Flame Surface Measurements

The formaldehyde signal in the HSPLIF images are a direct marker of the formaldehyde reaction layer in the low temperature preheat zone. However, the steep gradient on the flame side of the formaldehyde layer corresponds with the maximum production of CH radicals in the reaction zone. Flame surface tracking can then be applied through a combination of edge marking and gradient threshholding. Due to the breakdown of DME into formaldehyde at lower temperatures, particularly in non-premixed regions, a gradient threshold must be used to differentiate between edges which indicate flame presence and those which are the result of fuel decomposition. In the GTMC, hot product recirculation is produced by the CRZ, which can move hot, radical-laden gases upstream to mix with the fresh reactants. This can aid in fuel decomposition without the presence of a flame front. However, these regions can be distinguished easily because they often have broad, low value gradients.

5.1.3.1 Flame Surface Marking Procedure

The procedure for marking the formaldehyde preheat surface will be discussed in this subsection to provide an understanding of each step of the post processing. After background corrections and smoothing with a 2x2 kernel filter, a typical image looks like Figure 5.15. The image is then binarized to differentiate between the background and all formaldehyde structures, as seen in Figure 5.16. A canny edge tracking method is applied to each individual image to mark all detected edges, seen in the second image of Figure 5.16. This method was compared with the Sobel edge detection procedure, but it was determined that while the Sobel method detected more connected segments, it did not capture edges that were clearly formaldehyde signal.

Next, the gradient is calculated along the surface of the edge from the instantaneous image. The gradient is calculated using a central difference method on a 4x4 stencil at each edge marker. The gradient at each edge pixel is given in Figure 5.16. A threshold is applied to the gradient magnitude and those edges whose gradient is greater than the threshold are considered markers of the preheat zone surface. Blue pixels designated flame surface in Figure 5.16, while red pixels denote the edges that did not pass the threshold requirement. Those below the threshold are considered markers of fuel decomposition into formaldehyde or noise in the signal causing false edges.

The threshold was varied until the detection of actual flame surface was deemed satisfactory. Figure 5.17 gives the distribution of gradient magnitudes across all detected edges. In this particular instantaneous image, 4,845 pixels were marked as edges. Given the applied gradient threshold of 10 counts/pixel, 1,640 edges were

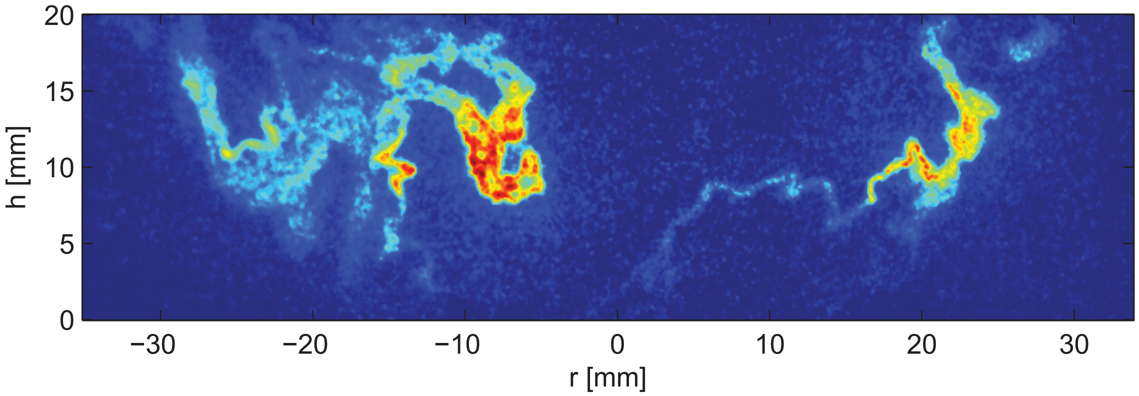

Figure 5.15: Instantaneous formaldehyde PLIF image after background corrections and smoothing. Non-resonating DME flames, air $\dot{m}$ = 282g/min, $\phi = 0.75$.

deemed to represent the flame surface. This represents 34% of the number of edges detected. Variation of the gradient threshold is somewhat sensitive. Lowering the threshold to 8 counts/pixel increases the number of flame markers by 40%, while increasing the threshold to 12 counts/pixel decreases the number of flame markers by 38%. The application of this threshold, in this image, correctly filters out portion of the formaldehyde image not representative of a flame, such as the small pockets in the left lobe, the majority of the distributed signal regions, and islands of signal with thickened edges.

Once the appropriate surfaces have been marked, the image can be reduced to a series of surface contours. Essentially an image consisting of only preheat surface edges. This is conducted for 4000 images in each case study, and frequency statistics can be applied to them. Since each pixel represents a physical segment of flame length, the pixel resolution of the image can be used to convert the edge segments into physical length of flame surface. From this estimate, the total flame length in the laser sheet plane can be studied to see how it evolves in time. Finally, the flame surface density can be calculated by binning the image and measuring the number

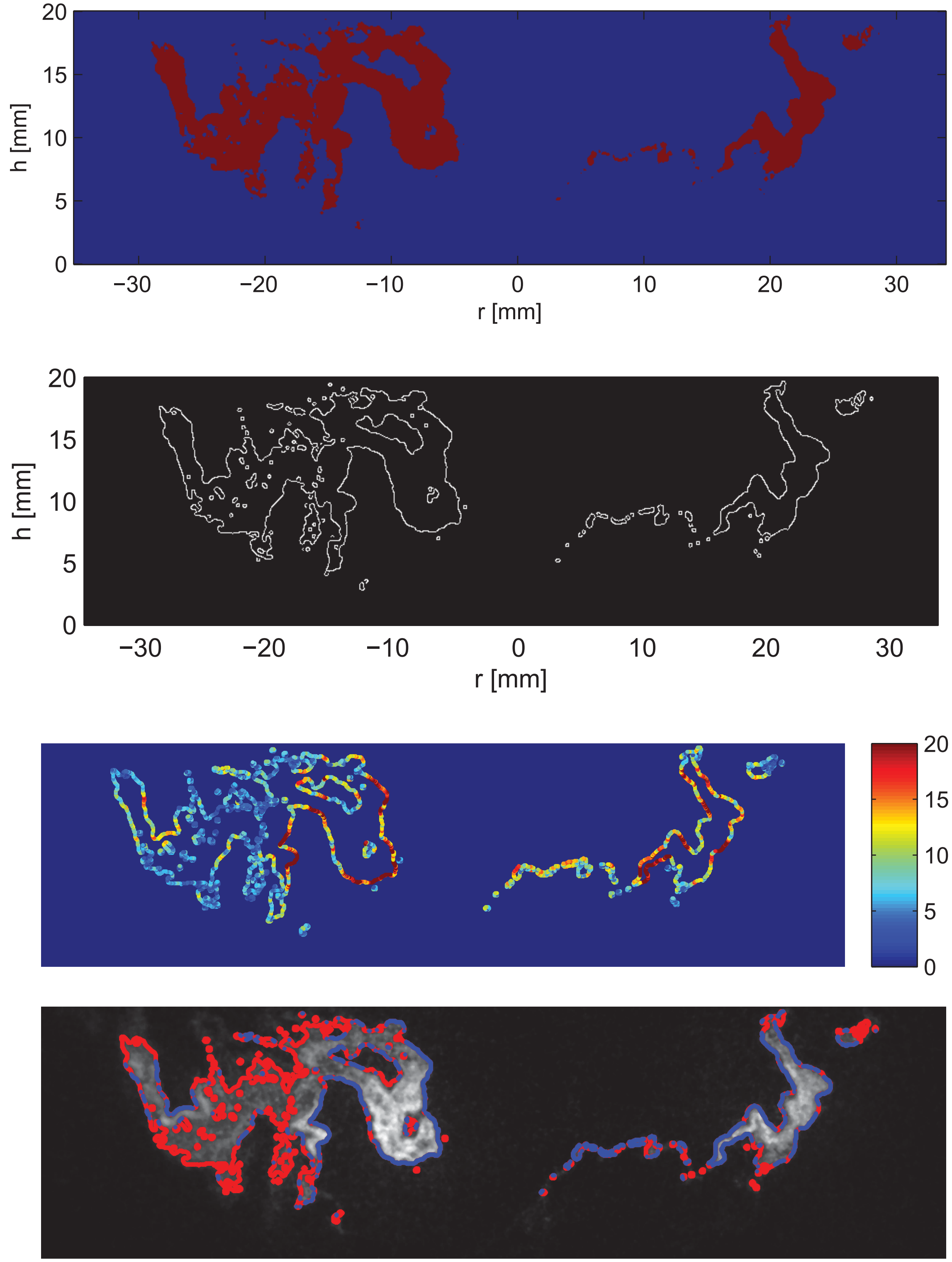

Figure 5.16: Post-processing steps for preheat zone surface marking. *Image 1*: Binarization, *Image 2*: Canny edge detection, *Image 3*: Calculation of gradient along surfaces, *Image 4*: Determination of flame surface through gradient threshold. Blue pixels = Flame surface; Red pixels = Fuel decomposition.

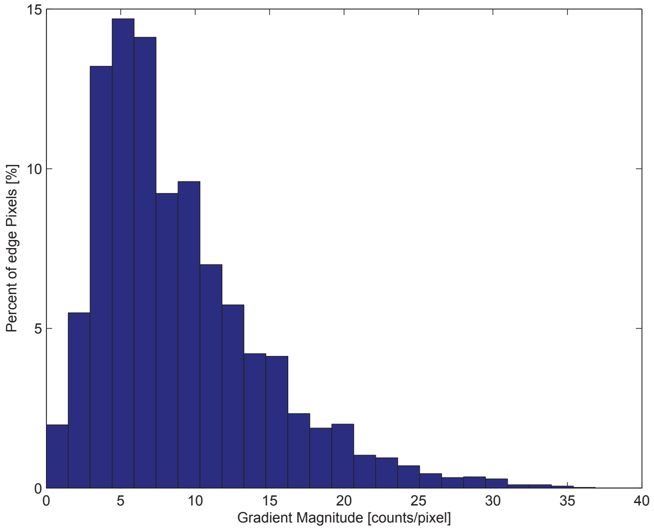

Figure 5.17: Histogram of the calculated gradient magnitudes along the detected edges. Gradient threshold set at 10. Non-resonating DME flames, air $\dot{m} = 282$g/min, $\phi = 0.75$.

of flame surface contours that lie in each spatial bin.

However, it must be discussed that some inherent bias may be introduced through this gradient thresholding method. Due to the selection of primarily steep gradients in the formaldehyde field, the detected edges may be biased towards identifying premixed flamelets. With regards to the resolution limits of the imaging system, often only a few pixels are able to resolve the entire gradient along the preheat surface. Purely premixed regions will have much thinner structures as opposed to non-premixed regions or areas where fuel decomposition has occurred due to hot product recirculation. On a gradient basis alone, non-premixed regions and areas of decomposition will appear to be similar. Without markers for other species, it is difficult to distinguish between the two. In order to be conservative, a higher gradient threshold is consider to prevent regions of decomposition from being included in the metric. While the gradients for diffusion flames can also be steep, these flames are also more susceptible to turbulent transport of formaldehyde away from the flame surface, which can appear to smear the surface. Thus, it may result that premixed regions are preferred by this method. However, it will be seen that both the entire formaldehyde scalar field and the detected edges exhibit the same temporal response to the instability.

5.1.3.2 Flame Surface Density of the Preheat Zone

Flame surface density (FSD) is based on the area of flame surface that lies within a 3-D volume in space. Given that the formaldehyde image measurements are 2-D in nature, the FSD can be estimated by:

$$\Sigma_{xy} = \frac{\delta L_f}{\delta A_{xy}} \tag{5.1}$$

Where the FSD is given by the total flame length inside a certain area that lies in the plane of the laser sheet. The densities presented here are calculated using a 10x10 spatial bin, which corresponds to a 0.75 x 0.75 mm box in actual space. The length of each contour was determined by counting the number of pixels within each box, dividing by the thickness of the contour (1 pixel), and then dividing by the area of the box. Figures 5.18 and 5.19 depict the contour surface along with the calculated FSD for the resonating and non-resonating cases. The contour images provide an idea of the turbulent flame brush for each case. For both cases, there appears to be little flame surface motion along the centerline, although the non-resonating brush approaches the center much more closely than the resonating brush, which is distributed further out to the edges.

The flame surface density plots show that the highest degree of wrinkling occurs at the outer edges of the flame, as seen in high-speed chemiluminescence videos. The non-resonating case shows that the wrinkling is greatest within the two zones per each given lobe. The highest degree of wrinkling occurs at the outside of the shear

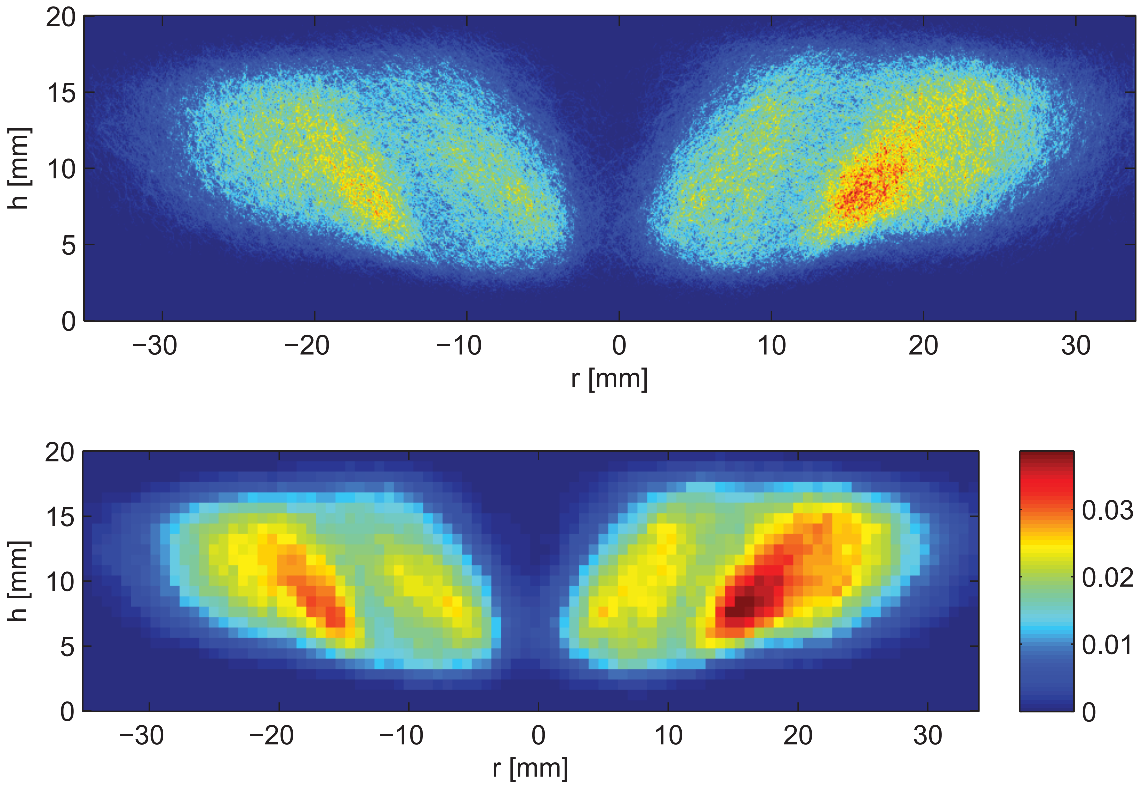

Figure 5.18: Average overlay of all flame surface contours (*top*) and flame surface density (*bottom*). Non-resonating DME flames, air $\dot{m} = 282\text{g/min}$, $\phi = 0.75$.

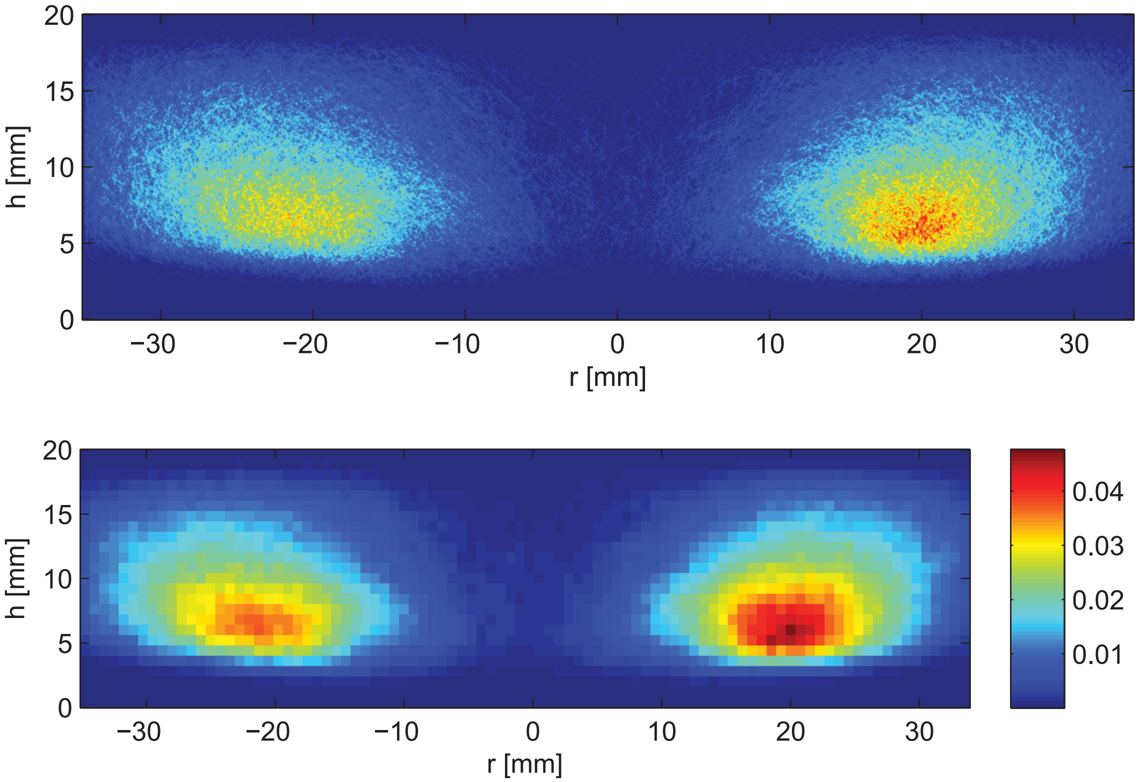

Figure 5.19: Average overlay of all flame surface contours (*top*) and flame surface density (*bottom*). Resonating DME flames, air $\dot{m}$ = 282g/min, $\phi = 1.2$.

layer. This means that the turbulence intensities increase from the center of the flame moving radially outward. For the resonating case, the wrinkling is relegated to two lobes, as seen in the average formaldehyde PLIF images.

The evolution of wrinkling in time can be tracked by measuring the total length of flame surface per image, as seen in Figure 5.20. The average length per image of the non-resonating and resonating case is 143±28 mm and 135±48 mm. The average lengths are about the same, but the difference between the two cases lies in the RMS of the fluctuation, such that resonating flames show larger oscillations. Similarly to the formaldehyde signal, the flame length fluctuates at the acoustic frequency in resonating flames and at a low frequency near 25 Hz for the non-resonating case. If the same lobe based analysis is applied, as seen in Figures 5.21 and 5.22, the results are similar again to the formaldehyde results. In non-resonating flames, the lobe and their ratio fluctuate at the assumed PVC frequency. In resonating flames, the lobes independently oscillate at the acoustic frequency, but relative to each other, the oscillation occurs at what is believed to be the PVC precession rate.

5.1.3.3 Wrinkling Parameter and Flame Surface Area

Wrinkling parameter is a useful metric to look at the distribution of wrinkling across the burner. It is typically defined for jet flames as the change in wrinkling down the length of the flame. However, because this flame is more radially distributed, the parameter has been redefined as seen in Equation 5.2.

$$\Omega = \int_{-\infty}^{+\infty} \Sigma \, dh \tag{5.2}$$

Figure 5.23 shows the distribution of wrinkling radially across the flame for both

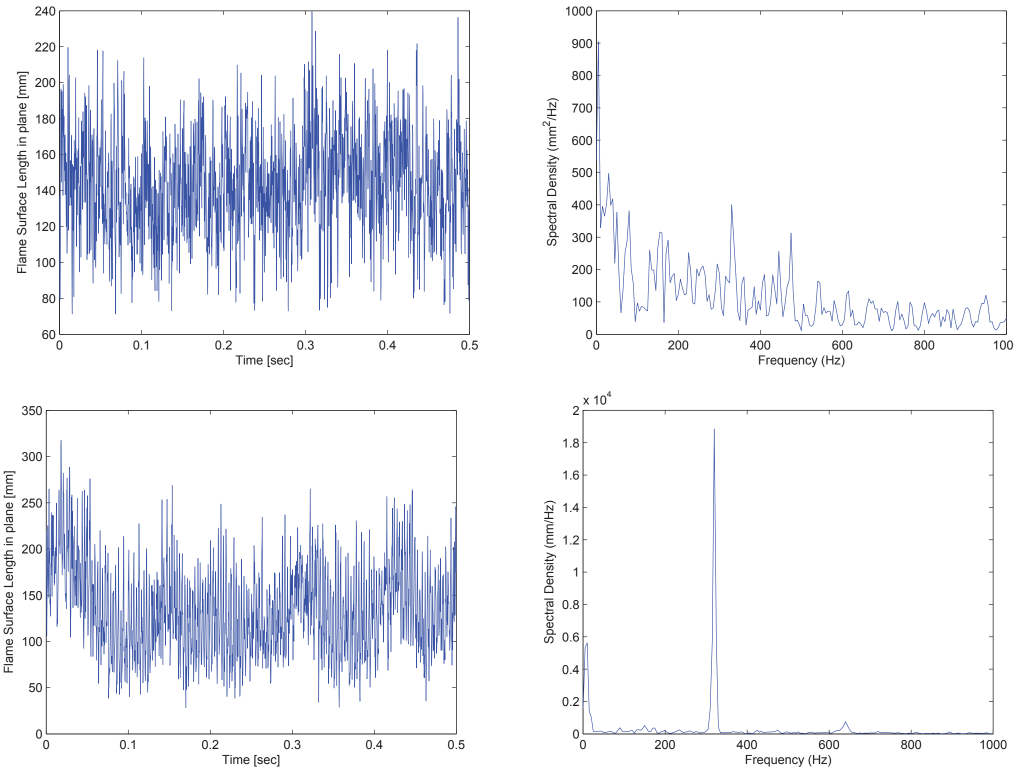

Figure 5.20: Time series showing the fluctuations in flame surface length in the plane of the image and the power spectral density of the oscillation for non-resonating (*top pair*) and resonating (*bottom pair*) DME flames, air $\dot{m}$ = 282g/min, ϕ = 0.75 and 1.2.

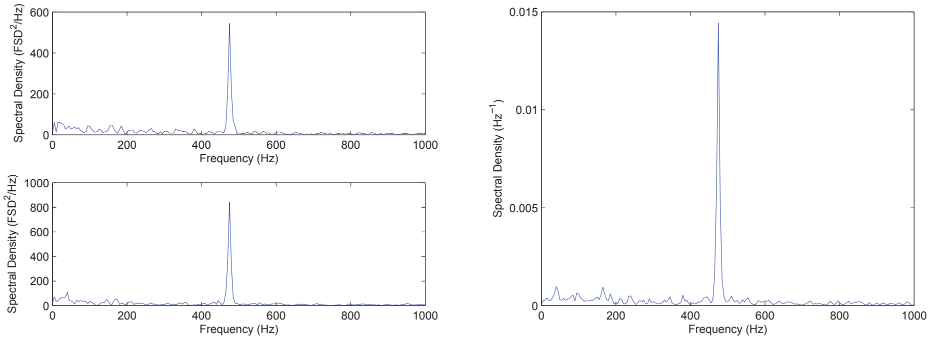

Figure 5.21: Power spectral density of the flame length oscillations in each lobe (*left pair*) and the ratio of flame length in each lobe (*right*) for non-resonating DME flames, air $\dot{m}$ = 282g/min, $\phi = 0.75$.

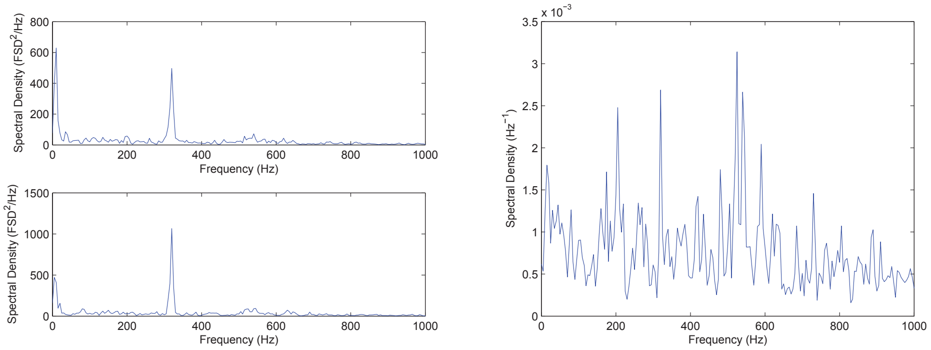

Figure 5.22: Power spectral density of the flame length oscillations in each lobe (*left pair*) and the ratio of flame length in each lobe (*right*) for resonating DME flames, air $\dot{m}$ = 282g/min, $\phi = 1.2$.

cases. The non-resonating case displays an initial rise in wrinkling marking the inner zone of each lobe, followed by a secondary rise marking the outer zone of the lobes. The resonating case displays a Gaussian like distribution across each lobe. As well, the resonating case shows that the maximum wrinkling occurs at a larger radial distance.

With higher turbulence intensities, it is expected that the flame would become more wrinkled and the total flame surface area would increase. This not apparently clear from the measurements of flame length, which give approximately the same average length for both cases. However a more important metric would be the 3D surface area of the flame, which assuming that the flame is axisymetric, can be estimated with the following:

$$dA_{f,3D} \sim rdl_{f,2D} \tag{5.3}$$

This metric weighs the radial distribution of the flame surface, such that wider flames will have a larger area. If the flame is approximated as an inverted cone, the flame length would represent the length of the slanted surface. Two cones can have the same length of slanted side, but will have very different flame surface areas if the flame cone angle is large. This model represents the difference between the two cases. Both flames have roughly the same length, but the resonating flame has a larger cone angle, which distributes surface further away from the centerline. For resonating flames, the average area across all images is 369±128 cm^2, and for non-resonating flames, the average is 305±66 cm^2. The resonating flame displays a larger area by 20% and the range of fluctuations is larger.

Similar to the wrinkling parameter, a surface area parameter, given in Equation 5.4, can be used to give the radially weighted wrinkling of the burner. This metric dictates that wrinkling which is distributed further from the centerline contributes more to the total surface area of the flame. The parameter is also plotted in Figure 5.23. This can help explain that the strength of the instability is due to higher heat release caused by a large surface area, which is created by a high degree of wrinkling, distributed far from the centerline.

$$\Psi = \int_{-\infty}^{+\infty} r\Sigma \, dh \tag{5.4}$$

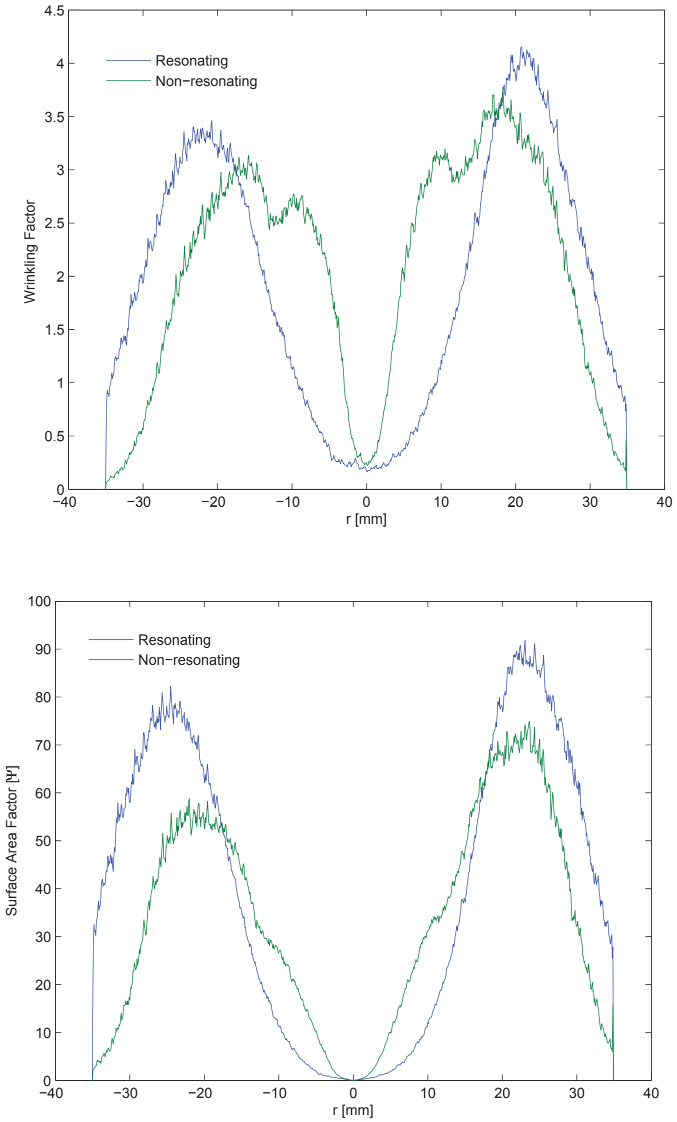

Figure 5.23: Radial distributions of wrinkling parameter (*top*) and surface area parameter (*bottom*), depicting the distribution of wrinkling across the burner.

5.1.3.4 Pockets and Local Extinction of the Formaldehyde Layer

The GTMC flames are exposed to a high degree of strain caused by the stochastic turbulence, recirculation, shear layers, and PVC motion. These effects severely wrinkle the flame and can cause folding and convolutions in the 3D flame surface. Due to the turbulent flame speed, the flame can burn out pockets in its own surface. As well the recirculation of hot products can cause certain parts of the mixture to immediately become flammable, which also causes combustion away from the primary flame sheet. This may be represented by holes in the formaldehyde layer or by isolated islands of formaldehyde signal as seen in Figure 5.15.

As well, the PVC creates vortices which lead to rollup of the flame surface, as seen in Figure 5.24. The combination of high strain along the surface and increased flame speed causes the roll to consume itself, beginning with local extinction along the surface, until the surface is shredded. Local extinction can also lead to flame segments being pinched off. However, it must be noted that not all segments seen in the PLIF images are due to local extinction or kernels of auto-ignited mixture. Some segments can be introduced into the plane of the laser via through-plane transport of flame fragments.

5.2 Proper Orthogonal Decomposition of the Formaldehyde Scalar Field

Proper orthogonal decomposition (POD) is a statistical tool that allows for the extraction of unsteady coherent structures in turbulent flow. It allows for decomposition of the flow into energy containing modes, based on the significance of the mode. From a sequence of k temporally-resolved scalar field measurements, the POD provides a set of k spatial eigenmodes , $\Phi_j(x, y)$, temporal coefficients, $a_j(t)$, and eigenvalues λ_j, such that the eigenmodes form an orthonormal basis for the original

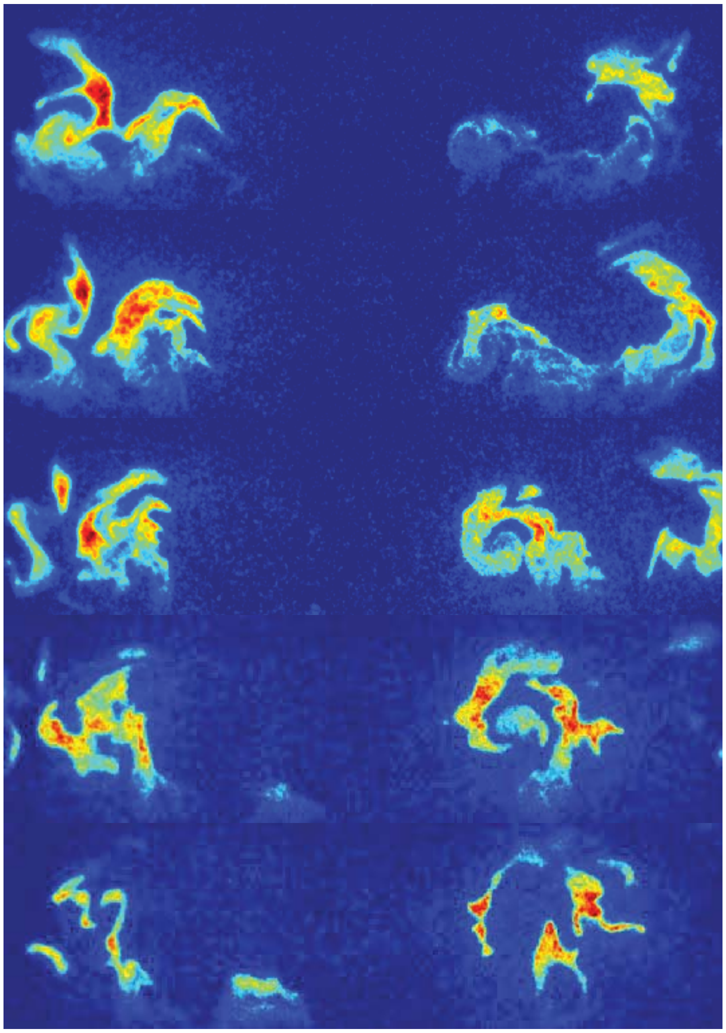

Figure 5.24: Time series of formaldehyde PLIF images showing flame rollup due to interaction with the PVC and local extinction due to high strain.

data set [137]. POD will be applied in this work to the scalar formaldehyde field, in order to study which coherent structures are present and how their motions control the flame surface and are represented in the observed oscillations of the flame.

5.2.1 Application of POD in Combustion

POD analysis has been applied in combustion studies to break down the turbulent flow into coherent structures which dominate the flowfield. Steinberg et al. [40, 56] used POD to be able to separate the velocity field, in high-speed studies of the GTMC, into the most energetic modes of flow. This also allowed for an analysis of how the OH field is coupled to coherent flow structures in the velocity field. Boxx et al. [138] applied POD to the velocity field of quiet and noisy flames in a premixed gas turbine combustor. Stöhr et al. has studied the transverse plane of the GTMC to look at structures in the velocity field in the swirling plane [107].

The previous studies all applied POD to the velocity, however, it is possible to study a scalar field with POD. Danby et al. [139] used decomposition to study structures of a passive and reactive scalar in numerical simulations of auto-ignition in non-homogeneous mixtures. Bizon et al. [140] applied POD to chemiluminescence images of ignition in internal combustion engines.

5.2.2 POD Analysis Procedure

The principal of POD is to develop a set of linear basis modes which are temporally resolved based on the 2D scalar images of formaldehyde. The temporal history of the scalar field can be constituted through the following:

$$I_k(x,y,t_i) = \sum_{j=0}^{k} a_j(t_i)\Phi_j(x,y) \tag{5.5}$$

To calculate the temporal coefficients and eigenmodes, the following procedure was applied:

1. From the set of 3x3 binned images, an m x n matrix, S, was created where each column of S represents an instantaneous 2D field measurement. The columns were created by concatenating the rows within a given image. Each row of S represents a time instant of the series, such that along the a given column is the time history of a single pixel in the image.

2. A spatial correlation matrix is computed by:

$$C = \frac{1}{K}(SS^T) \tag{5.6}$$

3. The eigenvalue problem is solved by:

$$C\beta_m = \lambda_m \beta_m \tag{5.7}$$

4. The basis functions are created by projecting S onto the eigenvector, β_m, where m is each mode:

$$\Phi = S^T \beta_m \tag{5.8}$$

5. Compute the coefficient matrix, a_m^k, by projecting S onto Φ:

$$a_m^k = S\Phi \tag{5.9}$$

The coefficient matrix is now sized K x M, such that each column represents a different mode. The rows of a given column represent the temporal history of the amplitude of the coefficient of mode m. There are K coefficients per mode, one for each time instant, and there are k total modes M, such that a_m^k is square. The structure of a given mode can be computed by applying the average coefficient of a given mode to the average mode structure reconstructed from the matrix Φ. Each column of Φ represents the concatenation of the transposed rows of the image structure of a given mode m. Application of Equation 5.5 can be used to reconstruct the average mode structures for a single mode, or any combination of modes.

Within the coefficient matrix, the mode columns are arranged in decreasing order of significance. When applied to the velocity field, the coefficients can be related to the energy of each mode. However, the same physics are not applicable to the scalar field, rather the mode can be described in terms of its significance, Υ, to the overall structure of the scalar field and its time evolution. The mode significance of a given mode and its contribution to the total flow can be calculated through the following:

$$\Upsilon_m = \sum_{k=1}^{K} (a_m^k)^2 \tag{5.10}$$

$$\upsilon_m = \frac{\Upsilon_m}{\sum_{m=1}^{M} \Upsilon_m} \tag{5.11}$$

It is common the apply POD to the fluctuating field, however the average mode structure can be retained by applying POD to the entire non-average-centered series. Mode 0 will correspond to the average structure. The coefficients of a given mode fluctuate in time and can fluctuate between positive and negative values, as given in Figure 5.25. The switching of sign will be seen to correspond to the oscillation of a particular flow structure. The computational application of the POD procedure in MatLab is based on the work of Chen et al. [141].

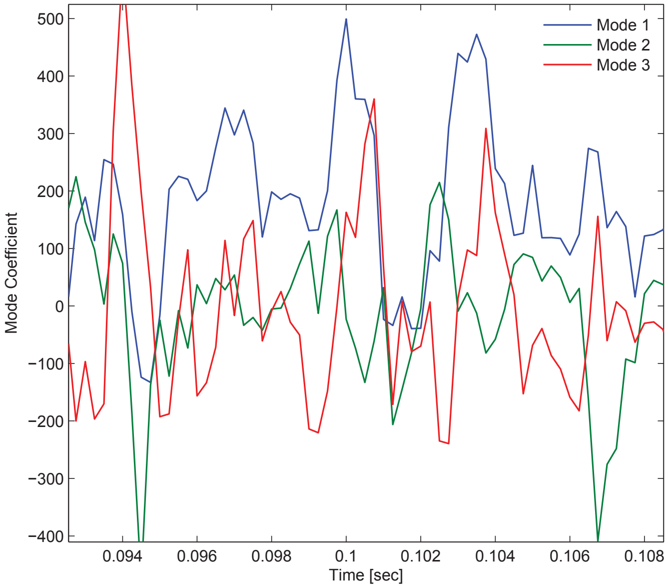

Figure 5.25: Temporal evolution of the mode coefficients for the most significant spatially fluctuating modes of a resonating flame.

5.2.3 POD Comparisons of Resonating and Non-Resonating Flames

The average mode structures for the first 3 modes for non-resonating flames are given in Figure 5.26. Mode 0 corresponds to the temporal average and Modes 1 and 2 correspond the most significant oscillatory modes. Mode 0 matches the structure of the average formaldehyde image given in Figure 5.5, where the lobes consist of two-zones. Mode 0 shows only positive values and the coefficients for this mode oscillate, but are also positive. This indicates that the mode corresponds to an overall pulsation of the entire structure. Mode 1 shows the oscillatory motion of the inner zones of each lobe. The positive and negative values composing the structure indicate that as the coefficients for this mode oscillate, the intensity of each zone will switch from positive to negative. This suggests a side to side motion within the shear layer. Mode 2 depicts four coherent structures which are asymmetrically matched by sign. As the coefficient magnitudes switch sign, the relative strength of the structures will also switch. Mode 2 corresponds to a rocking motion induced by the PVC, because at any given time, there is a matched high-low pair on either side of the injector. This captures the motion from the inner zone to the outer zone per lobe, which is asymmetric across the burner due to the PVC.

Figure 5.27 shows the frequency at which the coefficients for each mode fluctuates. The PSD of Mode 0 captures the low-frequency breathing mode observed earlier in the PSD of the total integrated formaldehyde signal. The overall pulsation of the zeroth structure is a slower breathing mode where the entire structure oscillates in phase. The frequencies of the first and second modes are dominated by the suspected PVC frequency, indicating that the side-to-side and rocking motions are correlated to the PVC motion. Thus the scalar field in non-resonating flames in dominated by a low frequency pulsation and the PVC motion.

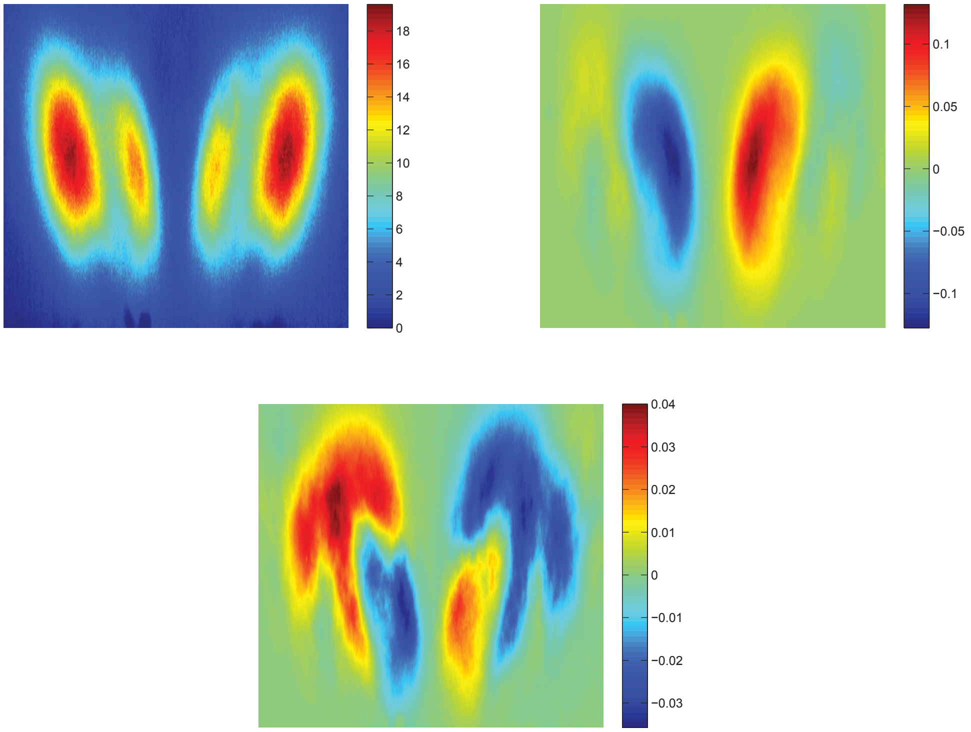

Figure 5.26: Average reconstructions of the most significant POD structures representing the temporal average, Mode 0 (*top,left*), Mode 1 (*top,right*), and Mode 2 (*bottom*) in non-resonating DME flames, for air $\dot{m}$ = 282g/min, $\phi = 0.75$.

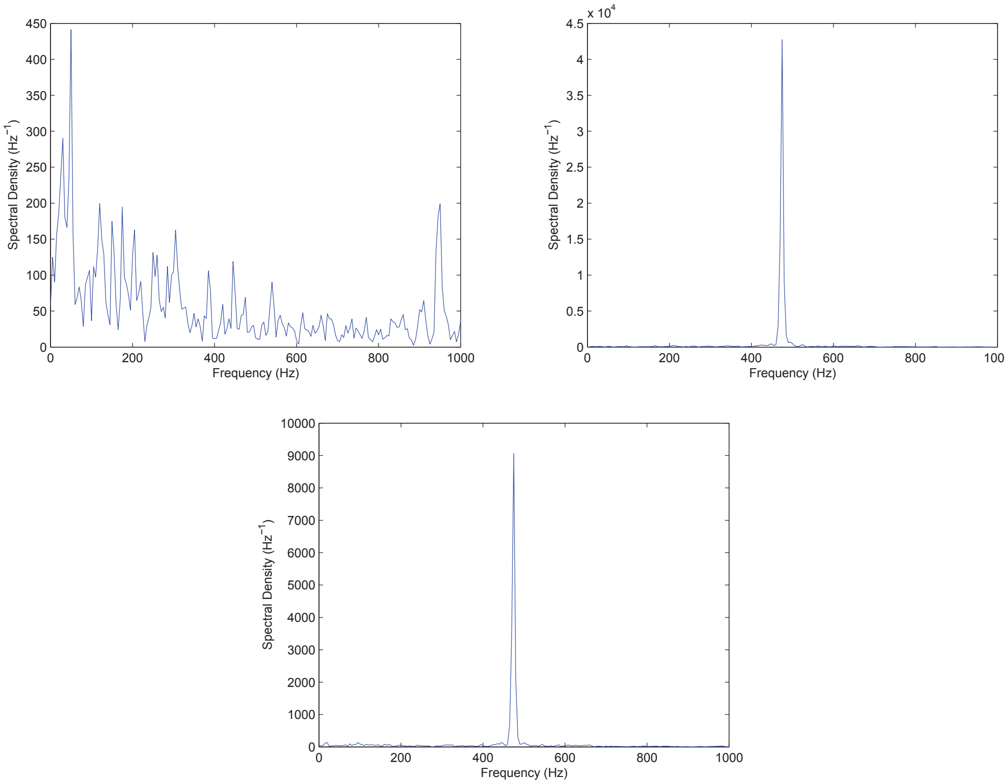

Figure 5.27: Power spectral densities of the temporal coefficients of the most significant POD structures representing the temporal average, Mode 0 (*top,left*), Mode 1 (*top,right*), and Mode 2 (*bottom*) in non-resonating DME flames, for air $\dot{m} = 282\text{g/min}$, $\phi = 0.75$.

The average mode structures for the first 3 modes for resonating flames are given in Figure 5.28. Mode 0 corresponds to the temporal average and Modes 1 and 2 correspond the most significant oscillatory modes. Mode 0 matches the structure of the average formaldehyde image given in Figure 5.6, represented by two large lobes of signal. Similar to the non-resonating flame, the coefficients of Mode 0 are all positive and their variation corresponds to a pulsation at 320 Hz, according to Figure 5.29. There is no motion associated with this mode.

Mode 1 in resonating flames consists of a radial contraction and expansion of the flow, similar to a change in the flame cone angle. In this motion, the flame widens and opens up at the acoustic frequency, as well as at 10 Hz. This motion corresponds to the independent behavior of each lobe. Mode 2 is the most interesting because it depicts two pairs of asymmetric lobes, which oscillate at the acoustic frequency as well as at the PVC precession rate. This is evidence that the PVC also plays a role in the motion of resonating flames. However, based on the frequency behavior of Modes 0-2, the thermoacoustic oscillation dominates the scalar field. The PVC is still present but cannot compete with the instability presence. The motion given in Mode 2 is a combination of rocking and liftoff, due to the acoustics and PVC. An oscillatory cycle of this motion is given in Figure 5.30. As the sign of the temporal coefficients changes, the strength of each lobe also correspondingly changes. However, coefficient magnitude affects all structures equally.

Resonating flame behavior is controlled by both thermoacoustics and PVC motion. However the dominant influence is due to the instability. The flame motions can be clearly identified and attributed to these different driving forces. In comparison to non-resonating flames, the dominant forces include a low frequency breathing and the PVC motion. These forces directly affect the flame surface and control its temporal evolution in terms of its wrinkling and motion.

The significance of each mode to the total scalar field has been calculated in Figure 5.31. For both cases, the first three modes control most of the structure of the flame surface. For the non-resonating flame, the first three modes, including the average, represent 60% of the coherent structures. In resonating flames, 49% of the significance can be attributed to the first three modes. The average field dominates the flame surface behavior and the next few modes indicate the primary fluctuations on the average. The higher modes correspond to the stochastic turbulence-induced structures. Granted, many of these stochastic modes also greatly assist in wrinkling the flame surface, however the primary distribution and motion of wrinkling is controlled by the first few modes. The significance of subsequent modes in non-resonating flames provides little additional contribution. The reconstruction of the highest modes appears to be a time-varying field of white noise. Coherent structures such as those investigated for both cases are not visible in the modes that contribute the other 40% of the field.

The combination of high-speed diagnostics and POD analysis has allowed for the investigation of time-varying structures and their spatiotemporal evolution. Mode decomposition has also proven that the different motions of the flame surface can be attributed to combinations of structures created by the instability and flowfield. The instability presence appears to damp out PVC effects, although its influence is still apparent. These motions can be tracked through high-speed chemiluminescence, and observed in the local unburned fuel distributions and swirler air flow distribution. This analysis links all of the previous studies conducted in this thesis.

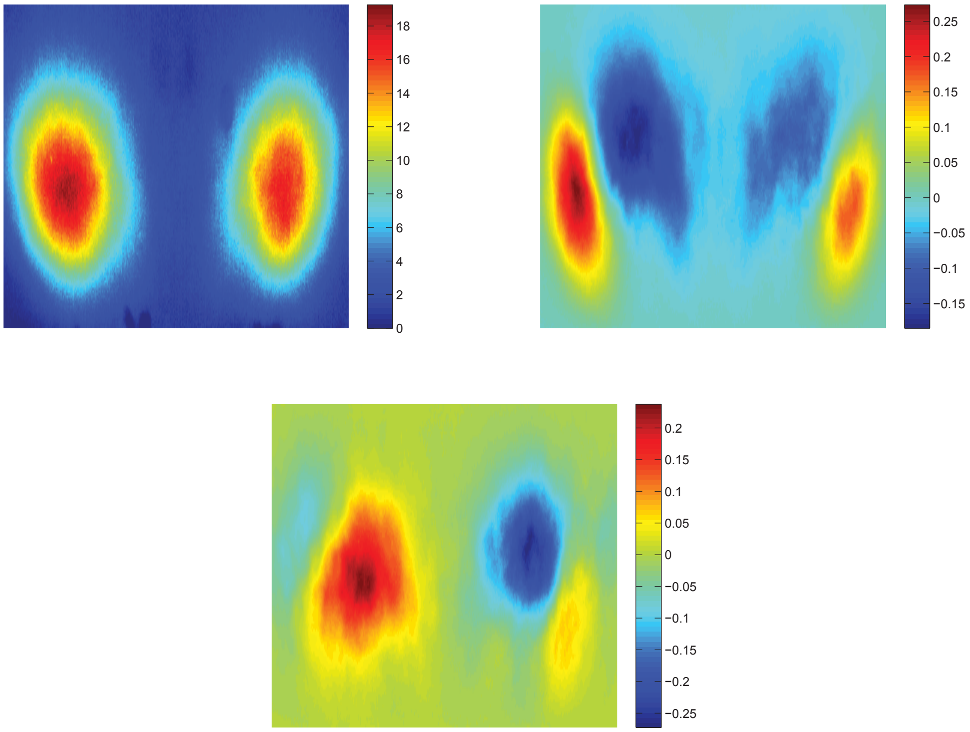

Figure 5.28: Average reconstructions of the most significant POD structures representing the temporal average, Mode 0 (*top,left*), Mode 1 (*top,right*), and Mode 2 (*bottom*) in resonating DME flames, for air $\dot{m} = 282$g/min, $\phi = 1.2$.

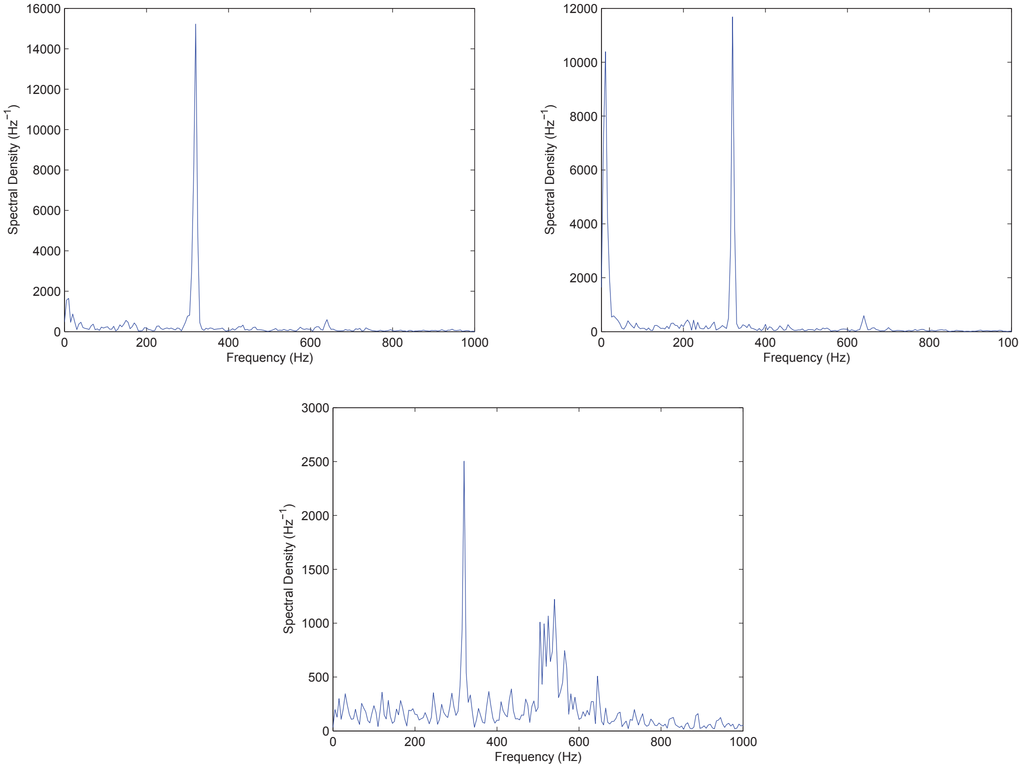

Figure 5.29: Power spectral densities of the temporal coefficients of the most significant POD structures representing the temporal average, Mode 0 (*top,left*), Mode 1 (*top,right*), and Mode 2 (*bottom*) in resonating DME flames, for air $\dot{m}$ = 282g/min, $\phi = 1.2$.

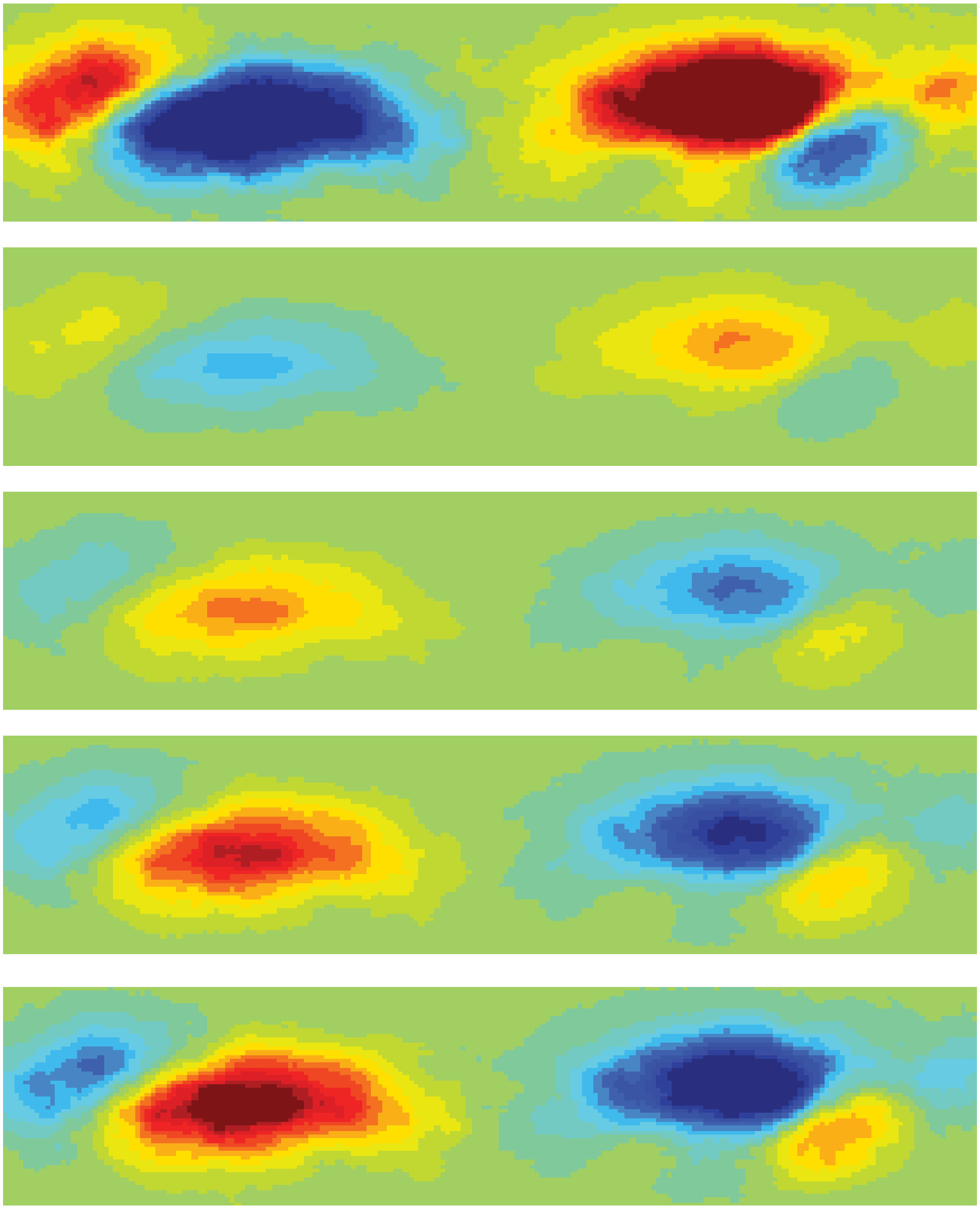

Figure 5.30: Temporal evolution of the second mode structure in a resonating flame, exhibiting effects of thermoacoustic and PVC oscillations. Both liftoff and rocking can be observed, indicating that the flame motion represents a balance of both driving forces.

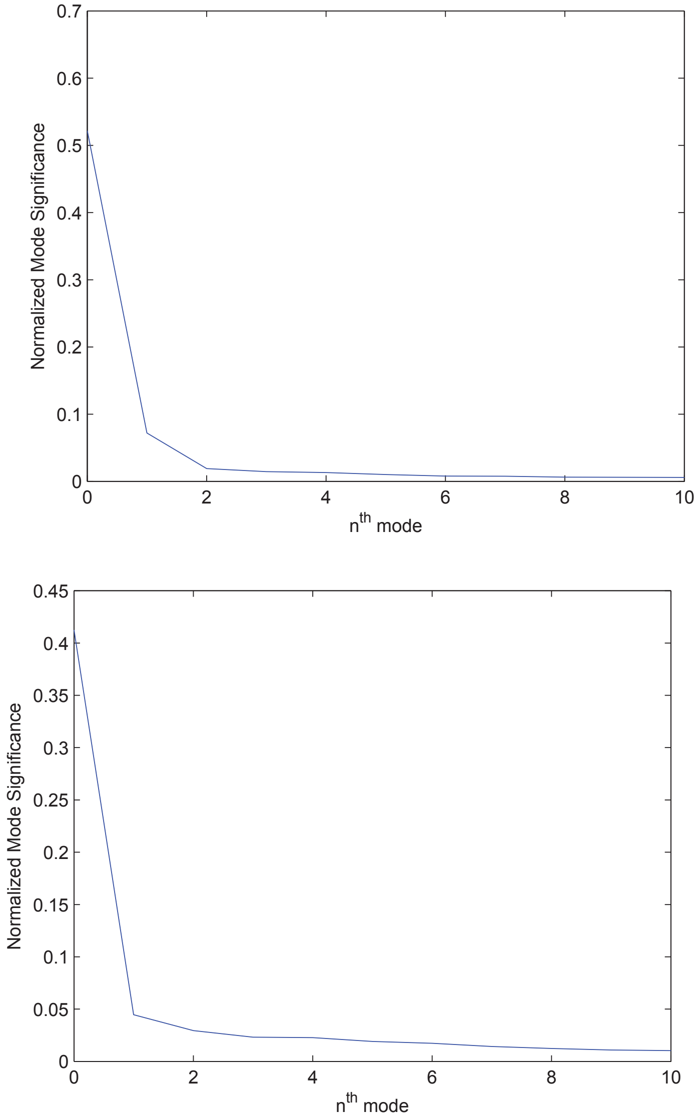

Figure 5.31: Fractional significance of the POD modes relative to the entire scalar field structure in non-resonating (*top*) and resonating (*bottom*) flames.

5.2.4 Summary of Flame Surface Motions

The preceding analyses have identified several motions attributed to both resonating and non-resonating flames. The flame motions have been determined from the centroids of formaldehyde signal and heat release, and from the POD modes. The motion of non-resonating flames is controlled by a low-frequency breathing mode which affects the overall pulsation and vertical motion of the flame. The PVC controls the horizontal and rocking motion. In resonating flames, the acoustic frequency dominates the vertical motion of the flame. The horizontal and rocking motion of the flame is affected by both the acoustic oscillation and the PVC.

5.3 Preheat Surface Response to Parameter Variations

The equivalence ratio and air mass flow rate was varied to investigate changes to the flame surface structure and motion. Varying trends were observed for a combination of cases which resulted in resonating, weakly resonating, non-resonating, and highly lifted V-flames. This distribution of behaviors allowed for observation of the effect of instability processes and PVC interactions. High-speed PLIF was also applied to ethylene flames to study the effect of increased flame speed. Further variation of fueling parameters with ethylene fuel was not possible because of the creation of large unsteady, radiating soot structures which overwhelm the PLIF signal and cannot be filtered out. A well, other fuels could not be used with the HSPLIF system due to the low pulse energies, which can only be applied to fuels which produce large formaldehyde concentrations.

5.3.1 Air Mass Flow Rate Variation

Air mass flow rate variation was conducted at two constant equivalence ratios, ϕ = 1 and 1.2. The air flow rate was varied from 170 to 282 g/min. Decreasing the flow rate tended to reduce the instability strength. The combination of low air flow and high equivalence ratio produced a highly lifted, non-resonating DME flame. Tables 5.1 and 5.2 represent the results of this parameter study. It appears that for weak flames, the observed frequencies are due to both acoustic and flowfield oscillations. When the instability is weak, it cannot damp out the flowfield influence via the PVC. The weakly resonating low flow case at $\phi = 1$ exhibited an average structure similar to the non-resonating flames, with two zones in each lobe.

With increasing flow rate, the phase shift between the switching lobes is decreased and the surface area and RMS area fluctuations increase. The instability becomes stronger with a highly wrinkled flame which fluctuates strongly. The frequency of the lobe ratio exhibits the PVC frequency except in the low flow cases, where it is suspected that there is no PVC present. Not all swirling flowfields can support a PVC. As well, the detected 570 Hz is a harmonic of the 285 Hz observed in the ratio of the lobe signals. Therefore, the 570 Hz may not necessarily be due to a flowfield structure motion at that frequency.

In general, as the air mass flow rate is increased the acoustic and PVC frequencies also increase. As well, the flame lengths between resonating and non-resonating flames are all about the same. However, the degree of fluctuations, given by the RMS, increases for resonating flames. This is also true of the mean surface area and its RMS. Resonating flames have higher degrees of wrinkling and flame surface area, and these metric also oscillate to a greater extent than in quiet flames.

A special case to this investigation was the highly lifted flame. This case may be due to poor mixing as a result of decreased shear and recirculation at low flow rates, combined with increased fueling. Essentially the flame mixture does not become flammable until further downstream. This flame only experiences slow, breathing type oscillations which may be due to thermo-diffusive instabilities in the flame surface. As well ,this flame is much less wrinkled than all other flames studied.

5.3.2 Equivalence Ratio Variation

Variation of the equivalence ratio yielded similar trends to the variation of air mass flow rate. Thus some of these trends may just be related to general increase in the thermal power of the flame. In general the acoustic frequency (if present) and the PVC frequencies shift higher with more fueling. As well, when the flame transitions to a resonating state, the phase shift between the lobe oscillations also decreases. Finally, the total surface area increases with higher ϕ, and the RMS of the area and length fluctuations is increased as well, as seen in Table 5.3.

These variation show that between loud, semi-loud, and quiet flames, there are competing effects for what dominates the flame surface motion. For resonating cases, the instability controls the flowfield and damps out effects due to the PVC. For non-resonating flames, the turbulent structures like the PVC and vortices greatly influence the oscillatory pattern of the flame. However, for weakly resonating flames, the two forces compete and balance is achieved in that the effects of both are observed.

5.3.3 Formaldehyde PLIF in Ethylene Flames

In this particular burner configuration, with all glass windows for optical access, ethylene is weakly resonating at this fueling condition. This also happened to DME flames at the same fueling conditions. During modification of the burner configuration, it was observed that the frequency and amplitude of the instability was decreased as more windows were put place. This suggests that wall boundaries of the burner can also act in a similar fashion to the chimney. It was determined that the chimney controls the impedance of the system by acting as a resistance to the

Table 5.1: Flame surface response to the variation of air mass flow rate at a constant $\phi = 1$.

Fuel Type	DME	DME	DME
Air [g/min]	170	210	282
Phi	1	1	1
Instability Present	Weak	Weak	Yes
Acoustic Frequency [Hz]	280	280	310
FSD Frequency [Hz]	270/570	280	310
Total Formaldehyde Frequency [Hz]	270/570	280	310
Individual Lobe Frequency [Hz]	280	280/345	310
Lobe Ratio Frequency [Hz]	285	345	480
Two- Zone Relative Frequency [Hz]	285	N/A	N/A
Two-Zone Phase Shift [deg]	75	N/A	N/A
Relative Lobe Phase Shift [deg]	110	98	72
Flame Surface Area Mean [cm²]	210	191	326
Flame Surface Area RMS [cm²]	54	65	118
Flame Length Mean [mm]	100	81	103
Flame Length RMS [mm]	24	25	41.5

Table 5.2: Flame surface response to the variation of air mass flow rate at a constant $\phi = 1.2$.

Fuel Type	DME	DME	DME
Air [g/min]	170	210	282
Phi	1.2	1.2	1.2
Instability Present	Highly Lifted	Yes	Yes
Acoustic Frequency [Hz]	15	290	320
FSD Frequency [Hz]	5	290	320
Total Formaldehyde Frequency [Hz]	15	290	320
Individual Lobe Frequency [Hz]	5	290	320
Lobe Ratio Frequency [Hz]	20	379	525
Two- Zone Relative Frequency [Hz]	N/A	N/A	N/A
Two-Zone Phase Shift [deg]	N/A	N/A	N/A
Relative Lobe Phase Shift [deg]	61	89	89
Flame Surface Area Mean [cm²]	85	319	369
Flame Surface Area RMS [cm²]	42	107	128
Flame Length Mean [mm]	42	118	135
Flame Length RMS [mm]	17	35	48

Table 5.3: Flame surface response to the variation of ϕ at a constant air $\dot{m}$ = 282 g/min.

Fuel Type	DME	DME	DME
Air [g/min]	282	282	282
Phi	0.75	1	1.2
Instability Present	No	Yes	Yes
Acoustic Frequency [Hz]	N/A	310	320
FSD Frequency [Hz]	10	310	320
Total Formaldehyde Frequency [Hz]	50	310	320
Individual Lobe Frequency [Hz]	475	310	320
Lobe Ratio Frequency [Hz]	475	480	525
Two- Zone Relative Frequency [Hz]	475	N/A	N/A
Two-Zone Phase Shift [deg]	75	N/A	N/A
Relative Lobe Phase Shift [deg]	127	72	89
Flame Surface Area Mean [cm²]	305	326	369
Flame Surface Area RMS [cm²]	65.6	118	128
Flame Length Mean [mm]	143	103	135
Flame Length RMS [mm]	28.2	41.5	48

mass flow through the system by adding a slight pressure drop at the exit of the system. Similarly, the wall material may change the thermal impedance of the system, such that there is higher heat transfer out of the boundaries when all quartz windows are used. With more heat transfer out of the system, the amplification of the instability cannot be sustained as strongly.

For this weakly resonating case of ethylene, the flow was controlled by both the acoustics and the PVC, which precessed at 480 Hz, as seen in Table 5.4. This is similar to the PVC frequency seen in DME flames. The average formaldehyde structure, given in Figure 5.32, resembles the non-resonating DME flames. The two zone structure to each lobe still exists. However the degree of wrinkling is greatly reduced. All metrics of the degree of wrinkling: surface area, flame length, and the RMS values of these components, are all fractions of the DME statistics. The reason for this decrease in wrinkling may be attributed to the turbulent flame speed. At higher turbulent flame speeds, the wrinkling process is in competition with processes to smooth the flame at small cusps and regions of high curvature. Thus the ethylene flame may be smoothed relative to the DME flame.

Table 5.4: Flame surface response to ethylene fueling.

Fuel Type	Ethylene
Air [g/min]	282
Phi	0.75
Instability Present	Weak
Acoustic Frequency [Hz]	360
FSD Frequency [Hz]	480
Total Formaldehyde Frequency [Hz]	360
Individual Lobe Frequency [Hz]	480
Lobe Ratio Frequency [Hz]	480
Two- Zone Relative Frequency [Hz]	480
Two-Zone Phase Shift [deg]	75
Relative Lobe Phase Shift [deg]	122
Flame Surface Area Mean [cm²]	195
Flame Surface Area RMS [cm²]	41
Flame Length Mean [mm]	102
Flame Length RMS [mm]	20

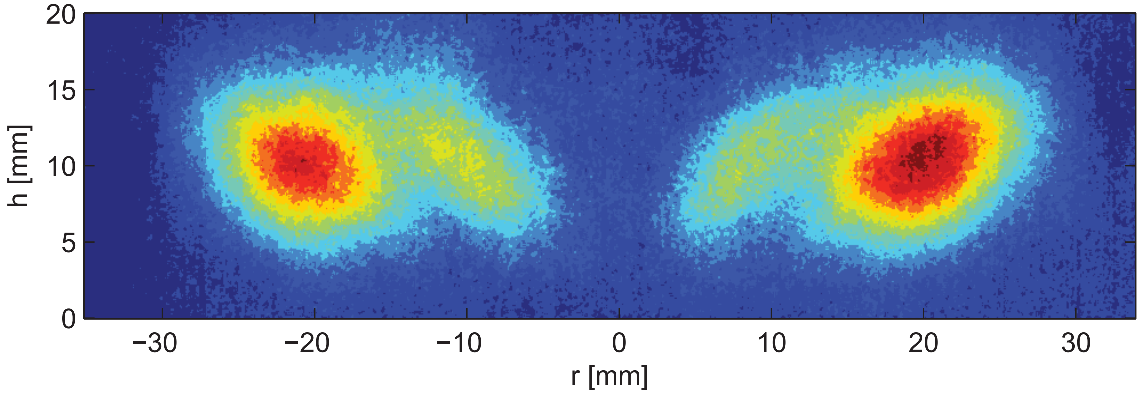

Figure 5.32: Formaldehyde average distribution for weakly resonating ethylene flames, air $\dot{m} = 282$ g/min, $\phi = 0.75$.

CHAPTER VI

Summary and Conclusions

The investigations presented in this work have focused on developing an understanding of combustion instabilities and flow-flame interactions in a partially-premixed gas turbine combustor. The GTMC allowed for the study of a complex flow environment with naturally occurring instabilities which were affected by the operating conditions and geometry of the burner. This study has provided insight into coupled mechanisms and the role of flame geometry. As well, markers in physical flame properties were used to evaluate fluid dynamic coupling. The GTMC is well suited for studies of combustion physics because it presents realistic flowfield dynamics and has excellent optical access. However, the GTMC presents challenges in that there are many active influences on the flame which are all simultaneously coupled.

A wide parameter study was conducted to evaluate the effect of varying equivalence ratio, mass flow rate, preheat temperature, and fuel composition. This parameter study was conducted on a variety of fuels, including methane, propane, ethylene, dimethyl ether, and two syngas mixtures. The burner geometry was also varied to determine natural resonances of the GTMC. These studies aided in the development of a conceptualized model based on Helmholtz theory which explained the observed trends.

LDV measurements of radial velocities were used to show redistribution of the swirler air flow rate, which helps explain the flat flame shape seen in chemiluminescence videos. Variations of the swirler configurations also showed the roles each swirler plays in setting up particular flow patterns. The high speed chemiluminescence videos were used to study the dynamics of rapid flame motions such as the location of the centroid of heat release and the liftoff-flashback oscillation, both of which can be correlated with simultaneous pressure measurements. Acetone PLIF was applied to study the distribution of unburned fuel in the GTMC for methane, propane, and syngas cases.

High-speed formaldehyde PLIF was conducted at 4 kHz in DME flames to observe the differences in preheat surface structure between resonating and non-resonating flames. Proper orthogonal decomposition analysis was also applied to study coherent structures which affect the flame surface and how these structures evolve in time. As well, parameter variations of air mass flow rate and equivalence ratio were conducted to investigate the response of the preheat layer. Finally, high-speed PLIF was also conducted in ethylene flames which have a much higher flame speed than DME.

6.1 Characterization of Natural Instability Mechanisms

The GTMC exhibited a naturally occurring combustion instability that was the result of several integrated mechanisms. The instability resonated at a single peak frequency, despite several influences, indicating that a balance takes place between them.

6.1.1 Parameter Variation

A) A driven Helmholtz mode is present based on the changes in frequency due to altering the volume of the plenum.

B) A convective acoustic mode is present in which the frequency of the instability scales with the air mass flow rate. This is associated with equivalence ratio oscillations in which inhomogeneities in the mixture are convected from the injector to the flame base. Pressure fluctuations are then reflected back to the injector. The time for this cycle to occur scales with the bulk air velocity.

C) The instability frequency tended to scale proportionally to the equivalence ratio, except in alkane flames, which behave non-monotonically. The flame speed may play a role in this trend. However, the 25% H_2 syngas mixture and ethylene have the same flame speed, yet do not exhibit the same trends. As well, the adiabatic flame temperature may play a role, but the variation in frequencies observed would not be accounted for with a change in temperature alone.

D) The amplitude of the instability increases with flow rate for hydrocarbon flames, but decreases for syngas flames. This may be due to decreased mixing in syngas flames because of lower residence times and thermo-diffusive instabilities.

E) Increasing the hydrogen content of syngas mixtures, decreases the amplitude of the instability, due to better anchoring. At a critical limit, the instability will be rendered inactive with higher hydrogen concentrations. The frequency response seems to be insensitive to increasing hydrogen content until the critical limit is reached.

F) The frequency of the instability is directly correlated with the flame speed of each fuel. However, this may be a secondary effect because the flame speed is dependent on several other factors, such as the heat release, reaction rate, diffusivity, fuel weight, and turbulence intensities.

G) The frequency of the instability scales with the burner core temperature. The core temperature is not the exact burner temperature, but rather a proxy for it, such that the flame will not be disturbed by a thermocouple. As the burner warms up, banding is observed where the frequency will increase proportionally, then jump by 10-20 Hz, and continue to increase proportionally to the temperature.

H) Variation of the combustion chamber length resulted in no change to the instability. Increasing the plenum volume caused the frequency and amplitude to decrease. The largest changes to the instability occurred with variation of the chimney length and diameter. Increasing the length and decreasing the diameter caused the instability frequency to decrease and the amplitude to increase.

I) The frequency and amplitude of the instability are diminished if the walls of the combustor are thin quartz windows, as opposed to all steel walls. The heat transfer through the glass is higher and the amplification of the instability is not sustained to the same extent.

6.1.2 Flame Shape and Rayleigh Indices

A) The presence of the instability is highly correlated with the flame shape. Resonating flames are typically flat and have some degree of liftoff height. Quiet flames are V-shaped and may be anchored.

B) Syngas flames which tend to have high flame speeds, are anchored at higher hydrogen concentrations, which prevents amplification of the instability. Hydrocarbon flames are typically lifted and the flame does not interfere with the formation of flow structures, such as the PVC.

C) Rayleigh indices of the flame support the shape and amplitude correlation. Flame are amplified when the pressure and heat release oscillations are in phase. Flat flames are better at achieving this phase matching.

D) The change in flame shape is associated with the distribution of air flow through the swirlers.

6.1.3 Conceptual Instability Model

A) Concepts from the models presented by Hathout and Schuller provide the background to the mechanism conclusions drawn below. Hathout's model provides the theory needed to explain coupling between the resonance and the combustion, while Schuller's model captures the effects of the chimney and the decoupling of the chamber from the plenum. As well, Hathout's model for heat release incorporates fueling and flame speed effects, which captures some of trends seen in the parameter study conducted.

B) The primary motivator in the GTMC is plenum Helmholtz resonance, driven by turbulent combustion, whose frequency is set by coupling between the resonator, flame/fuel effects, and geometry impedances.

C) The spatial location of the combustion influences the convective time scales of the oscillations, which determines if the instability is amplified or dampened by the degree of satisfaction of the Rayleigh criterion.

D) The chamber is decoupled from the plenum due to the low coupling index, such that variations of chamber geometry are not accounted for because the coupling index renders them negligible. However the chamber experiences fluctuations in response to the velocity and pressure fluctuations induced out of the plenum.

E) The impedance is set as a restriction to the flow at the exit boundary. Decreasing the diameter of the chimney or increasing its length has the effect of increasing the impedance. Impedance in the chimney may act as a relieving effect to pressure oscillations in the chamber, such that larger pressure oscillations are capable at higher impedances.

F) The impedance acts to accentuate pressure fluctuations by acting as a theoretical valve on the exhaust due to an induced pressure drop across the chimney; the dampening of the combustion effect on the plenum is inversely proportional to the exhaust impedance.

G) The turbulence and combustion are the driving forces activating the Helmholtz resonance of the plenum. However the observed frequency is altered by a combination of flame effects and impedances. The effect of increased heat release is to increase the observed frequency.

6.2 Fuel-Air Mixing and Instability Mechanisms

The swirler air flow distribution plays a strong role in setting up flow patterns that enable the instability. Simultaneous pressure and chemiluminescence measurements capture the response of the flame to the instability. Acetone PLIF measurements indicate where unburned fuel lies with respect to the shear layers in the GTMC.

6.2.1 Swirler Air Flow Redistribution

A) From LDV measurements, high radial velocities create flow patterns which enable flat flames which resonate. Quiet flames exhibit low radial velocities and tend to be V-shaped.

B) Hydrocarbon flames, when resonating, displayed radial velocities that were constant with increasing air mass flow rate. Syngas flame velocities increased with flow rate. For steady operation, the flow was either dominated by one swirler or the other, there was no rapid back and forth change in flow between the two swirlers.

C) Lean blowout and intermittency can occur when the radial velocity of the flow drops below 2.5 m/s. Higher radial velocities are critical for good flame stabilization.

D) The degree of radial flow is controlled by the outer swirler, while the inner swirler controls the axial flow rate.

6.2.2 Pressure and Chemiluminescence Correlations

A) The pressure field, chemiluminescence, liftoff height all oscillate at the same frequency.

B) Chemiluminescence videos show a high degree of motion over the course of an oscillation cycle. As well, there is a large change in flame surface structure, and thus heat release during these cycles.

C) Resonating hydrocarbon and syngas flames exhibit large liftoff motions, whereas steady flames display very little vertical motion. Syngas flames tend to be anchored to the burner and the flame brush is lifted but flashes all the way back to the injector.

D) The vertical motion of the centroid of heat release occurs at the acoustic frequency, while the horizontal center oscillates at a low frequency, typical of a breathing motion, which may be due to low frequency precession of the PVC core.

E) The flame exhibits a combination of vertical and rocking motions. The rocking motions may be due to interaction with the PVC. The rocking motion corresponds to the rotation of the PVC as captured in the 2D plane such that the PVC asymmetrically disturbs the flame surface.

6.2.3 Flowfield Interaction with Unburned Fuel Localization

A) Acetone PLIF was added to the fuel stream to act as a marker of unburned fuel.

B) Unburned fuel in methane and propane was distributed to two lobes on each side of the burner. The location of fuel switched back and forth between these two lobes, which may be due to interaction with the PVC. This redistribution of fuel by the PVC can affect the instability by altering the heat release and flame shape, which controls the convective time scale.

C) In methane flames, the fuel concentration was equally strong in both lobes, however the concentration was stronger in one lobe or the other for propane cases.

D) The localization of fuel in syngas flames was relegated to a single location which showed no horizontal displacement. The fuel distribution moved vertically along what may be the location of the shear layer between recirculation zones. The syngas fuel was spatially located in the gap between the fuel lobes for hydrocarbon fuels. The location of the fuel in this position may also disrupt the formation of a PVC.

E) A rich, low flow propane case, showed that with poor mixing the fuel localization is very similar to the syngas fuel distribution. As well, there was no PVC present.

6.3 High-Speed Investigations of Preheat Zone Surfaces

High-speed formaldehyde PLIF measurements were used to track the time evolution of the preheat zone surface. Flame surface density measurements show the oscillation of wrinkling in response to the instability and flowfield. In comparison to high speed chemiluminescence, the time-resolved PLIF allows for spatially resolved measurements of the evolution of flame surface length and asymmetries induced in the flame surface by the PVC. Proper orthogonal decomposition was performed on the scalar field to observe the dominant influences on coherent structures in the flame surface. As well, POD describes the relative strength of particular effects in shaping the flame surface. POD analysis shows that the scalar field is controlled by either the acoustics or the PVC. Flame length and surface area vary with increased air flow rate or increased fueling. The PVC was not directly measured, however, indirect effects due to its precession and rotation can be observed in the motion of the flame surface. This influence can be captured through POD and frequency analysis of the scalar field.

6.3.1 Comparison of Resonating and Non-Resonating Flames

A) In resonating flames, the flame surface density in each lobe oscillated at the instability frequency, but the ratio of densities between lobes fluctuated at the PVC frequency. In non-resonating flames, the lobe behavior matches the PVC precession rate.

B) Wrinkling and surface area parameters were used to look at the distribution of wrinkling across the burner. Resonating flames showed wrinkling was distributed radially further from the centerline. Wrinkling at the edges of the flame contribute more to the 3D surface area of the flame. Resonating and non-resonating flames have about the same flame length in plane, but the convoluted surface area is greater in loud flames, which contributes to amplification of the instability.

C) The integrated formaldehyde signal fluctuates at a low velocity due to a breathing mode, while the resonating flames fluctuate at the acoustic frequency.

D) In resonating flames, the lobes independently fluctuate at the acoustic frequency, but the ratio of the signal in each lobe oscillates at the PVC precession rate, indicating coupling with both the acoustics and the PVC. In non-resonating flames, the independent signal from each lobe and their ratio fluctuate at the PVC frequency.

E) The phase shift of the oscillation from one lobe to the other is smaller for resonating flames.

F) Resonating flames show thickened formaldehyde structure due to higher turbulence intensities aiding in the diffusion of formaldehyde away from the flame surface.

Non-resonating flames show more structure closer to the centerline, while loud flames are radially distributed outward from the centerline.

G) The average formaldehyde structure in non-resonating flames display two lobes, each of which is made up of two zones, which lie on either side of the shear layer. This is similar in structure to the unburned fuel distributions in methane and propane. Average signal in resonating flames show two lobes distributed farther from the center of the burner.

H) The flame surface exhibits a rocking motion and flame rollup due to the interaction with the PVC. The lobes on either side switch in strength and intensity, over an oscillatory cycle. The rocking motion corresponds to the rotation of the PVC as captured in the 2D plane such that the PVC asymmetrically disturbs the flame surface.

I) A flame surface marking procedure was applied based thresholding, using the local gradient along edges in the formaldehyde signal. The method distinguishes between edges that mark preheat zone structure near to the flame, and edges that correspond to fuel decomposition without a flame surface nearby. However, this methods tends to be biased towards the selection of premixed flamelets because regions of fuel decomposition and diffusion flames are similar on a gradient basis.

J) Flame surface density patterns in both cases were similar to the average formaldehyde distributions. The length of the total flame surface in resonating flames oscillated at the acoustic frequency.

6.3.2 POD of the Scalar Formaldehyde Field

A) The average Mode 0 in resonating flames pulsates at the acoustic frequency, while in non-resonating flames, the pulsation occurs at a low-frequency corresponding to a breathing mode. This mode represents the time-averaged flame surface structure.

B) Mode 1 is the first fluctuating mode. In non-resonating flame it corresponds to a left-to-right motion at 475 Hz. In resonating flames, the motion corresponds to an oscillation in the flame spreading angle at 320 Hz.

C) In Mode 2, non-resonating flames experience a rocking motion at the PVC frequency. Resonating flames have both acoustic and PVC effects in Mode 2. However, the PVC influence is damped in comparison to the instability presence.

D) Modes 1 and 2 represent fluctuating coherent structures around the mean. They have much lower significance than the mean structure given in Mode 0, however, they contain information about asymmetric motions due to PVC interaction with the flame surface for both resonating and non-resonating flames.

E) The total scalar field is dominated by the first few modes in both cases. However in non-resonating flames, the PVC controls the motion of any coherent structures. In resonating flames, a combination of instability and PVC motions effect the time evolution of the structures.

6.3.3 Response to Parameter Variation

A) Increasing the air mass flow rate and equivalence ratio tends to increase the frequency and strength of the instability and the frequency of the PVC precession.

B) In weakly resonating flames, both instability and PVC effects are observed.

C) The surface area of the flame increases with instability presence and with increased thermal power. The RMS of the length of the flame and the surface area RMS also increase with instability presence and thermal power.

D) In weakly resonating ethylene flames, both instability and PVC effects are observed. The flame wrinkling is reduced in comparison to DME flames. This may be due to the high flame speed of ethylene causing wrinkles and cusps to smooth themselves.

6.4 Future Work

The study of combustion instabilities often causes more questions to arise than problems that are solved. While this study has shed light on coupling mechanisms, global flame behavior, and flame surface response, there is still much work that could be conducted to improve the understanding of these complex behaviors. In order to fully validate the conceptualized model presented, more acoustic data is needed to investigate the phase differences between the plenum and the chamber for various fueling conditions. As well, the validity of a bulk pressure oscillation in the chamber should be checked for other fuels and operating conditions. The impedance induced by the exhaust nozzle should also be determined so as to improve the conceptualized model.

Since the PVC was not directly measured in DME flames, it would be important to also perform high speed PIV alongside the high speed formaldehyde PLIF measurements. This will enable direct time-resolved tracking of the PVC and flame surface responses to the PVC. With regards to the breathing motion observed, it would be useful to conduct PIV measurements of the transverse plane to identify if the core of the PVC is precessing at a low frequency relative to its rotation rate. As well, the formaldehyde PLIF should be performed at a higher spatial resolution in order to be able to more accurately interpret gradients along the detected edges and to measure wrinkling more accurately. Finally, a more discerning method for marking flame surfaces should be developed in order to be able to distinguish between regions of fuel decomposition and diffusion flames.

6.5 Overall Conclusion

The combustion instability investigated in the GTMC is representative of complex interactions between the flame and flowfield. The instability responds strongly to variations in fueling and operating conditions. The GTMC is controlled by a Helmholtz resonation in the plenum which is altered by the geometry of the chamber and exhaust. The degree of heat release due to turbulent combustion drives the frequency and strength of the instability. Flame shape and geometry is strongly linked to the satisfaction of the Rayleigh criterion through control of a convective time constant. The inherent distribution of flow through the swirlers establishes flow patterns which enable flame shapes which cause amplification of the instability. Finally, the degree of flame wrinkling and surface area is increased for resonating flames and the wrinkling evolves in time at the acoustic frequency in response to the thermoacoustic oscillation.

BIBLIOGRAPHY

BIBLIOGRAPHY

[1] Lefebvre, A. H., *Gas Turbine Combustion*, Taylor & Francis, 1999.

[2] Correa, S. M., "A review of NOx formation under gas-turbine combustion conditions," *Combustion Science and Technology*, Vol. 87, No. 1-6, Jan. 1993, pp. 329–362.

[3] Gupta, A. K., Lilley, D. G., and Syred, N., *Swirl flows*, Abacus Press, 1984.

[4] Syred, N. and Beér, J., "Combustion in swirling flows: A review," *Combustion and Flame*, Vol. 23, No. 2, 1974, pp. 143–201.

[5] Hill, P. and Peterson, C., *Mechanics and Thermodynamics of Propulsion*, Addison-Wesley, 2nd ed., 1992.

[6] Lieuwen, T. and Yang, V., *Combustion Instabilities in Gas Turbine Engines (Progress in Astronautics and Aeronautics)*, AIAA, 2005.

[7] Sick, V., "High speed imaging in fundamental and applied combustion research," *Proceedings of the Combustion Institute*, Vol. 34, No. 2, Jan. 2013, pp. 3509–3530.

[8] Huang, Y., Sung, H., Hsieh, S., and Yang, V., "Large-eddy simulation of combustion dynamics of lean-premixed swirl-stabilized combustor," *Journal of Propulsion and Power*, Vol. 19, No. 5, 2003, pp. 782–794.

[9] Menon, S. and Patel, N., "Subgrid modeling for simulation of spray combustion in large-scale combustors," *AIAA Journal*, Vol. 44, No. 4, 2006, pp. 709–723.

[10] El-Asrag, H. and Menon, S., "Large eddy simulation of bluff-body stabilized swirling non-premixed flames," *Proceedings of the Combustion Institute*, Vol. 31, No. 2, 2007, pp. 1747–1754.

[11] Moin, P. and Apte, S., "Large-eddy simulation of realistic gas turbine combustors," *AIAA Journal*, Vol. 44, No. 4, 2006, pp. 698–708.

[12] Dhanuka, S. K., Temme, J. E., and Driscoll, J. F., "Lean-limit combustion instabilities of a lean premixed prevaporized gas turbine combustor," *Proceedings of the Combustion Institute*, Vol. 33, No. 2, 2011, pp. 2961–2966.

[13] Weigand, P. and Meier, W., "Laser based investigations of thermo-acoustic instabilities in a lean premixed gas Turbine model combustor," *Journal of Engineering for Gas Turbines and Power*, Vol. 129, No. 2007, pp. 664 – 671.

[14] Harrje, D. T. and Reardon, F. H., editors, *Liquid Propellant Rocket Combustion Instability, NASA Report SP-194*, 1972.

[15] de la Cruz García, M., Mastorakos, E., and Dowling, A., "Investigations on the self-excited oscillations in a kerosene spray flame," *Combustion and Flame*, Vol. 156, No. 2, 2009, pp. 374–384.

[16] Bellows, B., Bobba, M., and Forte, A., “Flame transfer function saturation mechanisms in a swirl-stabilized combustor,” *Proceedings of the Combustion Institute*, Vol. 31, No. 2, 2007, pp. 3181–3188.

[17] Preetham, Santosh, H., and Lieuwen, T., “Dynamics of laminar premixed flames forced by harmonic velocity disturbances,” *Journal of Propulsion and Power*, 2008.

[18] Stöhr, M., Arndt, C., and Meier, W., “Effects of Damköhler number on vortex-flame interaction in a gas turbine model combustor,” *Proceedings of the Combustion Institute*, Vol. 34, No. 2, Jan. 2013, pp. 3107–3115.

[19] Chigier, N. A. and Beér, J. M., “Velocity and static-pressure distributions in swirling air jets issuing from annular and divergent nozzles,” *Journal of Basic Engineering*, Vol. 86, No. 4, Dec. 1964, pp. 788.

[20] Boxx, I., Stöhr, M., Carter, C., and Meier, W., “Temporally resolved planar measurements of transient phenomena in a partially pre-mixed swirl flame in a gas turbine model combustor,” *Combustion and Flame*, Vol. 157, No. 8, Aug. 2010, pp. 1510–1525.

[21] Feikema, D., Chen, R.-H., and Driscoll, J. F., “Enhancement of flame blowout limits by the use of swirl,” *Combustion and Flame*, Vol. 80, 1990, pp. 183–195.

[22] Feikema, D., Chen, R.-H., and Driscoll, J. F., “Blowout of nonpremixed flames: Maximum coaxial air velocities achievable, with and without swirl,” *Combustion and Flame*, Vol. 86, 1991, pp. 347–358.

[23] Stopper, U., Aigner, M., Ax, H., Meier, W., Sadanandan, R., Stöhr, M., and Bonaldo, A., “PIV, 2D-LIF and 1D-Raman measurements of flow field, composition and temperature in premixed gas turbine flames,” *Experimental Thermal and Fluid Science*, Vol. 34, No. 3, 2010, pp. 396–403.

[24] Driscoll, J. F. and Temme, J., “Role of swirl in flame stabilization,” *49th AIAA Aerospace Sciences Meeting including the New Horizons Forum and Aerospace Exposition*, 2011.

[25] Syred, N., “A review of oscillation mechanisms and the role of the precessing vortex core (PVC) in swirl combustion systems,” *Progress in Energy and Combustion Science*, Vol. 32, No. 2, 2006, pp. 93–161.

[26] Roux, S., Lartigue, G., Poinsot, T., Meier, U., and Bérat, C., “Studies of mean and unsteady flow in a swirled combustor using experiments, acoustic analysis, and large eddy simulations,” *Combustion and Flame*, Vol. 141, 2005, pp. 40–54.

[27] Fokaides, P., Weiß, M., Kern, M., and Zarzalis, N., “Experimental and numerical investigation of swirl induced self-excited instabilities at the vicinity of an airblast nozzle,” *Flow, Turbulence and Combustion*, Vol. 83, No. 4, March 2009, pp. 511–533.

[28] Palies, P., Durox, D., Schuller, T., Morenton, P., and Candel, S., “Dynamics of premixed confined swirling flames,” *C.R. Mecanique*, Vol. 337, 2009, pp. 395–405.

[29] Palies, P., Durox, D., Schuller, T., and Candel, S., “The combined dynamics of swirler and turbulent premixed swirling flames,” *Combustion and Flame*, Vol. 157, 2010, pp. 1698–1717.

[30] Meier, W., Duan, X., and Weigand, P., “Investigations of swirl flames in a gas turbine model combustor,” *Combustion and Flame*, Vol. 144, No. 1, 2006, pp. 225–236.

[31] Peters, N., *Turbulent Combustion*, Cambridge University Press, 2000.

[32] Chen, Y.-C. and Bilger, R. W., “Simultaneous 2-D imaging measurements of reaction progress variable and OH radical concentration in turbulent premixed flames: Instantaneous flame-front structure,” *Combustion Science and Technology*, Vol. 167, No. 1, June 2002, pp. 187–222.

[33] Weigand, P., Meier, W., Duan, X., Stricker, W., and Aigner, M., "Investigations of swirl flames in a gas turbine model combustor," *Combustion and Flame*, Vol. 144, No. 1-2, Jan. 2006, pp. 205–224.

[34] Driscoll, J. F., "Turbulent premixed combustion: Flamelet structure and its effect on turbulent burning velocities," *Progress in Energy and Combustion Science*, Vol. 34, No. 1, 2008, pp. 91–134.

[35] Swaminathan, N. and Bray, K., editors, *Turbulent Premixed Flames*, Cambridge University Press, 2011.

[36] Law, C. and Sung, C., "Structure, aerodynamics, and geometry of premixed flamelets," *Progress in Energy and Combustion Science*, Vol. 26, No. 4, 2000, pp. 459–505.

[37] Schwarz, H., Zimmer, L., Durox, D., and Candel, S., "Detailed measurements of equivalence ratio modulations in premixed flames using laser Rayleigh scattering and absorption spectroscopy," *Experiments in Fluids*, Vol. 49, No. 4, Sept. 2010, pp. 809–821.

[38] Lee, T.-W., North, G., and Santavicca, D., "Surface properties of turbulent premixed propane/air flames at various Lewis numbers," *Combustion and Flame*, Vol. 93, No. 4, June 1993, pp. 445–456.

[39] Filatyev, S. A., Driscoll, J. F., Carter, C. D., and Donbar, J. M., "Measured properties of turbulent premixed flames for model assessment, including burning velocities, stretch rates, and surface densities," *Combustion and Flame*, Vol. 141, 2005, pp. 1–21.

[40] Steinberg, A., Boxx, I., Stöhr, M., Carter, C., and Meier, W., "Flow-flame interactions causing acoustically coupled heat release fluctuations in a thermo-acoustically unstable gas turbine model combustor," *Combustion and Flame*, Vol. 157, 2010, pp. 2250–2266.

[41] Trunk, P., Boxx, I., Heeger, C., Meier, W., Böhm, B., and Dreizler, a., "Premixed flame propagation in turbulent flow by means of stereoscopic PIV and dual-plane OH-PLIF at sustained kHz repetition rates," *Proceedings of the Combustion Institute*, Vol. 34, No. 2, Jan. 2013, pp. 3565–3572.

[42] Balachandran, R., Dowling, a. P., and Mastorakos, E., "Non-linear response of turbulent premixed flames to imposed inlet velocity oscillations of two frequencies," *Flow, Turbulence and Combustion*, Vol. 80, No. 4, May 2008, pp. 455–487.

[43] Kiefer, J., Li, Z., Zetterberg, J., Bai, X., and Aldén, M., "Investigation of local flame structures and statistics in partially premixed turbulent jet flames using simultaneous single-shot CH and OH planar laser-induced fluorescence imaging," *Combustion and Flame*, Vol. 154, No. 4, 2008, pp. 802–818.

[44] Bell, J. B., Day, M. S., Grcar, J. F., Lijewski, M. J., Driscoll, J. F., and Filatyev, S. a., "Numerical simulation of a laboratory-scale turbulent slot flame," *Proceedings of the Combustion Institute*, Vol. 31, No. 1, Jan. 2007, pp. 1299–1307.

[45] Bray, K. N. C. and Cant, R. S., "Some applications of kolmogorov's turbulence research in the field of combustion," *Proceedings of the Royal Society A: Mathematical, Physical and Engineering Sciences*, Vol. 434, No. 1890, July 1991, pp. 217–240.

[46] Rayleigh, J. and Lindsay, R., *The Theory of Sound, Vol 2*, Dover Publications, 1945.

[47] Lieuwen, T. C., *Unsteady Combustor Physics*, Cambridge University Press, 2012.

[48] Lieuwen, T., "Modeling premixed combustion-acoustic wave interactions: A review," *Journal of Propulsion and Power*, Vol. 19, No. 5, Sept. 2003, pp. 765–781.

[49] Dowling, A. P. and Stow, S. R., "Acoustic analysis of gas turbine combustors," *Journal of Propulsion and Power*, Vol. 19, No. 5, 2003, pp. 751–764.

[50] Ducruix, S., Schuller, T., Durox, D., and Candel, S., "Combustion dynamics and instabilities : Elementary coupling and driving mechanims," *Journal of Propulsion and Power*, Vol. 19, No. 5, 2003, pp. 722–734.

[51] Candel, S., "Combustion dynamics and control: Progress and challenges," *Proceedings of the Combustion Institute*, Vol. 29, No. 1, 2002, pp. 1–28.

[52] Kinsler, L. E., Frey, A. R., Coppens, A. B., and Sanders, J. V., *Fundamentals of Acoustics*, Wiley, 1999.

[53] Meier, W., Weigand, P., Duan, X., and Giezendanner-Thoben, R., "Detailed characterization of the dynamics of thermoacoustic pulsations in a lean premixed swirl flame," *Combustion and Flame*, Vol. 150, No. 1, 2007, pp. 2–26.

[54] Polifke, W., Fischer, A., and Sattelmayer, T., "Instability of a premix burner with nonmonotonic pressure drop characteristic," *Journal of Engineering for Gas Turbines and Power*, Vol. 125, No. 1, 2003, pp. 20.

[55] Samaniego, J. M., Yip, B., Poinsot, T., and Candel, S., "Low frequency combustion instability mechanismsin a side-dump combustor," *Combustion and Flame*, Vol. 94, No. 4, 1993, pp. 363–380.

[56] Steinberg, A. M., Boxx, I., Stöhr, M., Meier, W., and Carter, C. D., "Effects of flow structure dynamics on thermoacoustic instabilities in swirl-stabilized combustion," *AIAA Journal*, Vol. 50, No. 4, April 2012, pp. 952–967.

[57] Chakravarthy, S. R., Shreenivasan, O. J., Boehm, B., Dreizler, A., and Janicka, J., "Experimental characterization of onset of acoustic instability in a nonpremixed half-dump combustor." *The Journal of the Acoustical Society of America*, Vol. 122, No. 1, July 2007, pp. 120–7.

[58] Schuller, T., Durox, D., Palies, P., and Candel, S., "Acoustic decoupling of longitudinal modes in generic combustion systems," *Combustion and Flame*, Vol. 159, No. 5, May 2012, pp. 1921–1931.

[59] Zähringer, K., Durox, D., and Lacas, F., "Helmholtz behavior and transfer function of an industrial fuel swirl burner used in heating systems," *International Journal of Heat and Mass Transfer*, Vol. 46, No. 18, 2003, pp. 3539–3548.

[60] Schildmacher, K.-U., Hoffmann, a., Selle, L., Koch, R., Schulz, C., Bauer, H.-J., Poinsot, T., Krebs, W., and Prade, B., "Unsteady flame and flow field interaction of a premixed model gas turbine burner," *Proceedings of the Combustion Institute*, Vol. 31, No. 2, Jan. 2007, pp. 3197–3205.

[61] Selamet, A. and Lee, I., "Helmholtz resonator with extended neck," *The Journal of the Acoustical Society of America*, Vol. 113, No. 4, 2003, pp. 1975.

[62] Lieuwen, T., Torres, H., Johnson, C., and Zinn, B. T., "A mechanism of combustion instability in lean premixed gas turbine combustors," *Journal of Engineering for Gas Turbines and Power*, Vol. 123, No. 1, 2001, pp. 182.

[63] Rockwell, D. and Naudascher, E., "Review: Self-sustaining oscillations of flow past cavities," *Journal of Fluids Engineering*, Vol. 100, No. 2, June 1978, pp. 152.

[64] Yu, K. H., Trouvé, A., and Daily, J. W., "Low-frequency pressure oscillations in a model ramjet combustor," *Journal of Fluid Mechanics*, Vol. 232, April 1991, pp. 47–72.

[65] Stöhr, M., Boxx, I., Carter, C. D., and Meier, W., "Experimental study of vortex-flame interaction in a gas turbine model combustor," *Combustion and Flame*, Vol. 159, No. 8, Aug. 2012, pp. 2636–2649.

[66] Venkataraman, K. K., Preston, L. H., Simons, D. W., Lee, B. J., Lee, J. G., and Santavicca, D. A., "Mechanism of combustion instability in a lean premixed dump combustor," *Journal of Propulsion and Power*, Vol. 15, No. 6, Nov. 1999, pp. 909–918.

[67] Broda, J., Seo, S., Santoro, R., Shirhattikar, G., and Yang, V., "An experimental study of combustion dynamics of a premixed swirl injector," *Symposium (International) on Combustion*, Vol. 27, No. 2, Jan. 1998, pp. 1849–1856.

[68] Huang, Y. and Yang, V., "Bifurcation of flame structure in a lean-premixed swirl-stabilized combustor: transition from stable to unstable flame," *Combustion and Flame*, Vol. 136, No. 3, Feb. 2004, pp. 383–389.

[69] Tummers, M., Hübner, A., van Veen, E., Hanjalić, K., and van der Meer, T., "Hysteresis and transition in swirling nonpremixed flames," *Combustion and Flame*, Vol. 156, No. 2, 2009, pp. 447–459.

[70] Schuller, T., Durox, D., and Candel, S., "Dynamics of and noise radiated by a perturbed impinging premixed jet flame," *Combustion and Flame*, Vol. 128, No. 1, 2002, pp. 88–110.

[71] Durox, D., Schuller, T., and Gandel, S., "Self-induced instability of a premixed jet flame impinging on a plate," *Proceedings of the Combustion Institute*, Vol. 29, No. 1, 2002, pp. 69–75.

[72] Fernandes, E. and Leandro, R., "Modeling and experimental validation of unsteady impinging flames," *Combustion and Flame*, Vol. 146, No. 4, Sept. 2006, pp. 674–686.

[73] Smith, D. A. and Zukoski, E. E., "Combustion instability sustained by unsteady vortex combustion," *21st AIAA/SAE/ASME/ASEE Joint Propulsion Conference*, Dec. 1985, pp. Paper 85–1248.

[74] Lewis, B. and von Elbe, G., *Combustion, Flames and Explosions of Gases*, Academic Press, 3rd ed., 1987.

[75] Eckbreth, A. C., *Laser Diagnostics for Combustion Temperature and Species*, Gordon and Breach Publishers, 1996.

[76] Santoro, V. S., Liñán, A., and Gomez, A., "Propagation of edge flames in counterflow mixing layers: Experiments and theory," *Proceedings of the Combustion Institute*, Vol. 28, No. 2, 2000, pp. 2039–2046.

[77] Joedicke, A., Peters, N., and Mansour, M., "The stabilization mechanism and structure of turbulent hydrocarbon lifted flames," *Proceedings of the Combustion Institute*, Vol. 30, No. 1, 2005, pp. 901–909.

[78] Bombach, R. and Käppeli, B., "Simultaneous visualisation of transient species in flames by planar-laser-induced fluorescence using a single laser system," *Applied Physics B*, Vol. 68, 1999, pp. 251–255.

[79] Li, Z., Li, B., Sun, Z., Bai, X., and Aldén, M., "Turbulence and combustion interaction: High resolution local flame front structure visualization using simultaneous single-shot PLIF imaging of CH, OH, and CH2O in a piloted premixed jet flame," *Combustion and Flame*, Vol. 157, No. 6, June 2010, pp. 1087–1096.

[80] Peters, N., "Flame calculations with reduced mechanisms - An outline," *Lecture Notes in Physics Monographs*, edited by N. Peters and B. Rogg, Vol. 15 of *Lecture Notes in Physics Monographs*, Springer, 15th ed., 1993, pp. 3–14.

[81] Dhanuka, S. K., Temme, J. E., and Driscoll, J., "Unsteady aspects of lean premixed prevaporized gas turbine combustors: Flame-flame interactions," *Journal of Propulsion and Power*, Vol. 27, No. 3, May 2011, pp. 631–641.

[82] Gabet, K. N., Patton, R. A., Jiang, N., Lempert, W. R., and Sutton, J. A., "High-speed CH2O PLIF imaging in turbulent flames using a pulse-burst laser system," *Applied Physics B*, Vol. 106, No. 3, Jan. 2012, pp. 569–575.

[83] Duwig, C., Li, B., Li, Z., and Aldén, M., "High resolution imaging of flameless and distributed turbulent combustion," *Combustion and Flame*, Vol. 159, No. 1, Jan. 2012, pp. 306–316.

[84] Lee, J. G. and Santavicca, D. A., "Experimental diagnostics for the study of combustion instabilities in lean premixed combustors," *Journal of Propulsion and . . .* , Vol. 19, No. 5, 2003, pp. 735–750.

[85] Kim, K. T., Lee, J. G., Lee, H. J., Quay, B. D., and Santavicca, D. A., "Characterization of forced flame response of swirl-stabilized turbulent lean-premixed flames in a gas turbine combustor," *Journal of Engineering for Gas Turbines and Power*, Vol. 132, No. 4, 2010, pp. 041502.

[86] Kim, K. T. and Santavicca, D. A., "Interference mechanisms of acoustic/convective disturbances in a swirl-stabilized lean-premixed combustor," *Combustion and Flame*, Vol. 160, No. 8, Aug. 2013, pp. 1441–1457.

[87] Ayoola, B., Balachandran, R., Frank, J., Mastorakos, E., and Kaminski, C., "Spatially resolved heat release rate measurements in turbulent premixed flames," *Combustion and Flame*, Vol. 144, No. 1, 2006, pp. 1–16.

[88] Pun, W. and Palm, S. L., "Combustion dynamics of an acoustically forced flame," *Combustion Science and Technology*, Vol. 175, 2003, pp. 499–521.

[89] Huang, Y. and Ratner, A., "Experimental investigation of thermoacoustic coupling for low-swirl lean premixed flames," *Journal of Propulsion and Power*, Vol. 25, No. 2, March 2009, pp. 365–373.

[90] Nori, V. N. and Seitzman, J. M., "CH* chemiluminescence modeling for combustion diagnostics," *Proceedings of the Combustion Institute*, Vol. 32, No. 1, 2009, pp. 895–903.

[91] Lawn, C., "Distributions of instantaneous heat release by the cross-correlation of chemiluminescent emissions," *Combustion and Flame*, Vol. 123, No. 1-2, Oct. 2000, pp. 227–240.

[92] Weigand, P., Meier, W., Duan, X. R., Giezendanner-Thoben, R., and Meier, U., "Laser diagnostic study of the mechanism of a periodic combustion instability in a gas turbine model combustor," *Flow, Turbulence and Combustion*, Vol. 75, No. 1-4, Dec. 2005, pp. 275–292.

[93] Giezendanner, R., Weigand, P., Duan, X., Meier, W., Meier, U., Aigner, M., and Lehmann, B., "Laser-based investigations of periodic combustion instabilities in a gas turbine model combustor," *Journal of Engineering for Gas Turbines and Power*, Vol. 127, No. 3, 2005, pp. 492–496.

[94] Sadanandan, R., St, M., and Meier, W., "Flowfield-flame structure interactions in an oscillating swirl flame," *Combustion, Explosion, and Shock Waves*, Vol. 45, No. 5, 2009, pp. 518–529.

[95] Giezendanner, R., Keck, O., Weigand, P., Meier, W., Meier, U., Stricker, W., and Aigner, M., "Periodic combustion instabilities in a swirl burner studied by phase-locked planar laser-induced fluorescence," *Combustion Science and Technology*, Vol. 175, No. 4, April 2003, pp. 721–741.

[96] Duan, X., Meier, W., Weigand, P., and Lehmann, B., "Phase-resolved laser Raman scattering and laser Doppler velocimetry applied to periodic instabilities in a gas turbine model combustor," *Applied Physics B*, Vol. 80, No. 3, Jan. 2005, pp. 389–396.

[97] Giezendanner-Thoben, R., Meier, U., Meier, W., Heinze, J., and Aigner, M., "Phase-locked two-line OH planar laser-induced fluorescence thermometry in a pulsating gas turbine model combustor at atmospheric pressure," *Applied Optics*, Vol. 44, No. 31, 2005, pp. 6565.

[98] Giezendanner-Thoben, R., Meier, U., Meier, W., and Aigner, M., "Phase-Locked Temperature Measurements by Two-Line OH PLIF Thermometry of a Self-Excited Combustion Instability in a Gas Turbine Model Combustor," *Flow, Turbulence and Combustion*, Vol. 75, No. 1-4, Dec. 2005, pp. 317–333.

[99] Meier, W., Boxx, I., Stöhr, M., and Carter, C. D., "Laser-based investigations in gas turbine model combustors," *Experiments in Fluids*, Vol. 49, No. 4, May 2010, pp. 865–882.

[100] Sadanandan, R., Stöhr, M., and Meier, W., "Simultaneous OH-PLIF and PIV measurements in a gas turbine model combustor," *Applied Physics B*, Vol. 90, No. 3-4, Feb. 2008, pp. 609–618.

[101] Stöhr, M., Sadanandan, R., and Meier, W., "Experimental study of unsteady flame structures of an oscillating swirl flame in a gas turbine model combustor," *Proceedings of the Combustion Institute*, Vol. 32, No. 2, 2009, pp. 2925–2932.

[102] Stöhr, M., Boxx, I., Carter, C., and Meier, W., "Dynamics of lean blowout of a swirl-stabilized flame in a gas turbine model combustor," *Proceedings of the Combustion Institute*, Vol. 33, No. 2, 2011, pp. 2953–2960.

[103] Boxx, I., Carter, C. D., Stöhr, M., and Meier, W., "Study of the mechanisms for flame stabilization in gas turbine model combustors using kHz laser diagnostics," *Experiments in Fluids*, Vol. 54, No. 5, May 2013, pp. 1532.

[104] Wehr, L., Meier, W., Kutne, P., and Hassa, C., "Single-pulse 1D laser raman scattering applied in a gas turbine model combustor at elevated pressure," *Proceedings of the Combustion Institute 31*, 2007, pp. 3099 – 3106.

[105] Lammel, O., Geigle, K., Luckerath, R., Meier, W., and Aigner, M., "Investigation of soot formation and oxidation in a high-pressure Ggs turbine model combustor by laser techniques," *ASME Turbo Expo 2007: Power for Land, Sea, and Air*, 2007, pp. GT2007–27902.

[106] Kutne, P., Kapadia, B. K., Meier, W., and Aigner, M., "Experimental analysis of the combustion behaviour of oxyfuel flames in a gas turbine model combustor," *Proceedings of the Combustion Institute*, Vol. 33, No. 2, 2011, pp. 3383–3390.

[107] Stöhr, M., Sadanandan, R., and Meier, W., "Phase-resolved characterization of vortex-flame interaction in a turbulent swirl flame," *Experiments in Fluids*, Vol. 51, No. 4, June 2011, pp. 1153–1167.

[108] Stopper, U., Aigner, M., Meier, W., Sadanandan, R., Stöhr, M., and Kim, I. S., "Flow field and combustion characterization of premixed gas turbine flames by planar laser techniques," *Journal of Engineering for Gas Turbines and Power*, Vol. 131, No. 2, March 2009, pp. 021504.

[109] Rosenberg, D. A. and Driscoll, J. F., "A method to image flame index in partially premixed flames," *50th AIAA Aerospace Sciences Meeting including the New Horizons Forum and Aerospace Exposition*, No. January, 2012, pp. 1–12.

[110] Rosenberg, D. A., Allison, P. M., and Driscoll, J. F., "Flame index measurements to assess partially-premixed flame models," *8th US National Combustion Meeting, Park City, UT*, 2013.

[111] Lozano, A., Yip, B., and Hanson, R., "Acetone: A tracer for concentration measurements in gaseous flows by planar laser-induced fluorescence," *Experiments in Fluids*, Vol. 13, No. 6, Oct. 1992.

[112] Thurber, M. C., Grisch, F., Kirby, B. J., Votsmeier, M., and Hanson, R. K., "Measurements and modeling of acetone laser-induced fluorescence with implications for temperature-imaging diagnostics," *Applied Optics*, Vol. 37, No. 21, July 1998, pp. 4963.

[113] Clemens, N., "Flow Imaging," *Encyclopedia of Imaging Science and Technology*, edited by J. Hornak, John Wiley & Sons, Inc, New York, 2002, pp. 390–419.

[114] Pichon, S., Black, G., Chaumeix, N., Yahyaoui, M., Simmie, J., Curran, H., and Donohue, R., "The combustion chemistry of a fuel tracer: Measured flame speeds and ignition delays and a detailed chemical kinetic model for the oxidation of acetone," *Combustion and Flame*, Vol. 156, No. 2, 2009, pp. 494–504.

[115] Chong, C. T. and Hochgreb, S., "Measurements of laminar flame speeds of acetone/methane/air mixtures," *Combustion and Flame*, Vol. 158, No. 3, 2011, pp. 490–500.

[116] Aldén, M., Bood, J., Li, Z., and Richter, M., "Visualization and understanding of combustion processes using spatially and temporally resolved laser diagnostic techniques," *Proceedings of the Combustion Institute*, Vol. 33, No. 1, 2011, pp. 69–97.

[117] Böhm, B., Heeger, C., Gordon, R. L., and Dreizler, A., "New perspectives on turbulent combustion: Multi-parameter high-speed planar laser diagnostics," *Flow, Turbulence and Combustion*, Vol. 86, No. 3-4, Aug. 2010, pp. 313–341.

[118] Fuest, F., Papageorge, M. J., Lempert, W. R., and Sutton, J., "Ultrahigh laser pulse energy and power generation at 10 kHz." *Optics letters*, Vol. 37, No. 15, Aug. 2012, pp. 3231–3.

[119] Olofsson, J., Richter, M., Aldén, M., and Auge, M., "Development of high temporally and spatially (three-dimensional) resolved formaldehyde measurements in combustion environments," *Review of Scientific Instruments*, Vol. 77, No. 1, 2006, pp. 013104.

[120] Harrington, J. E. and Smyth, K. C., "Laser-induced fluorescence measurements of formaldehyde in a methane/air diffusion flame," *Chemical Physics Letters*, Vol. 202, No. 3-4, Jan. 1993, pp. 196–202.

[121] Brackmann, C., Li, Z., Rupinski, M., Docquier, N., Pengloan, G., and Aldén, M., "Strategies for formaldehyde detection in flames and engines using a single-mode Nd:YAG/OPO laser system." *Applied spectroscopy*, Vol. 59, No. 6, June 2005, pp. 763–8.

[122] Siegman, A. E., *Lasers*, University Science Books, 1986.

[123] Hecht, E., *Optics*, Addison-Wesley, 4th ed., 2001.

[124] Brockhinke, A., Hartlieb, A., Kohse-Höinghaus, K., and Crosley, D., "Tunable KrF laser-induced fluorescence of C 2 in a sooting flame," *Applied Physics B: Lasers and Optics*, Vol. 67, No. 5, Nov. 1998, pp. 659–665.

[125] Ehn, A., Johansson, O., Bood, J., Arvidsson, A., Li, B., and Aldén, M., "Fluorescence lifetime imaging in a flame," *Proceedings of the Combustion Institute*, Vol. 33, No. 1, 2011, pp. 807–813.

[126] Metz, T., Bai, X., Ossler, F., and Aldén, M., "Fluorescence lifetimes of formaldehyde (H2CO) in the A1A2 –> X1A2 band system at elevated temperatures and pressures," *Spectrochimica acta. Part A, Molecular and biomolecular spectroscopy*, Vol. 60, No. 5, April 2004, pp. 1043–53.

[127] Daly, C. A., Simmie, J. M., and Wu, J., "Burning velocities of dimethyl ether and air," *Combustion and Flame*, Vol. 125, No. 4, 2001, pp. 1329–1340.

[128] Gabet, K., Shen, H., Patton, R., Fuest, F., and Sutton, J., "A comparison of turbulent dimethyl ether and methane non-premixed flame structure," *Proceedings of the Combustion Institute*, Vol. 34, No. 1, Jan. 2013, pp. 1447–1454.

[129] Kang, D., Culick, F., and Ratner, A., "Combustion dynamics of a low-swirl combustor," *Combustion and Flame*, Vol. 151, No. 3, Nov. 2007, pp. 412–425.

[130] Yu, G., Law, C., and Wu, C., "Laminar flame speeds of hydrocarbon + air mixtures with hydrogen addition," *Combustion and Flame*, Vol. 63, No. 3, March 1986, pp. 339–347.

[131] Kumar, K., Mittal, G., Sung, C., and Law, C., "An experimental investigation of ethylene/O2/diluent mixtures: Laminar flame speeds with preheat and ignition delays at high pressures," *Combustion and Flame*, Vol. 153, No. 3, May 2008, pp. 343–354.

[132] Egolfopoulos, F. N., Zhu, D. L., and Law, C. K., "Experimental and numerical determination of laminar flame speeds: Mixtures of C2-hydrocarbons with oxygen and nitrogen," *Proceedings of the Combustion Institute*, Vol. 23, No. 1, 1991, pp. 471–478.

[133] Dong, C., Zhou, Q., Zhao, Q., Zhang, Y., Xu, T., and Hui, S., "Experimental study on the laminar flame speed of hydrogen/carbon monoxide/air mixtures," *Fuel*, Vol. 88, No. 10, Oct. 2009, pp. 1858–1863.

[134] Natarajan, J., Lieuwen, T., and Seitzman, J., "Laminar flame speeds of H2/CO mixtures: Effect of CO2 dilution, preheat temperature, and pressure," *Combustion and Flame*, Vol. 151, No. 1-2, Oct. 2007, pp. 104–119.

[135] Hathout, J. P., Fleifil, M., Annaswamy, A. M., and Ghoniem, A. F., "Combustion instability active control using periodic fuel injection," *Journal of Propulsion and Power*, Vol. 18, No. 2, March 2002, pp. 390–399.

[136] Allison, P. M., Driscoll, J. F., and Ihme, M., "Acoustic characterization of a partially-premixed gas turbine model combustor: Syngas and hydrocarbon fuel comparisons," *Proceedings of the Combustion Institute*, Vol. 34, No. 2, 2013, pp. 3145–3153.

[137] Berkooz, G., Holmes, P., and Lumley, J., "The proper orthogonal decomposition in the analysis of turbulent flows," *Annual Review of Fluid Mechanics*, Vol. 25, 1993, pp. 539–575.

[138] Boxx, I., Arndt, C. M., Carter, C. D., and Meier, W., "High-speed laser diagnostics for the study of flame dynamics in a lean premixed gas turbine model combustor," *Experiments in Fluids*, Vol. 52, No. 3, Dec. 2012, pp. 555–567.

[139] Danby, S. J. and Echekki, T., "Proper orthogonal decomposition analysis of autoignition simulation data of nonhomogeneous hydrogen-air mixtures," *Combustion and Flame*, Vol. 144, No. 1-2, Jan. 2006, pp. 126–138.

[140] Bizon, K., Continillo, G., Mancaruso, E., Merola, S., and Vaglieco, B., "POD-based analysis of combustion images in optically accessible engines," *Combustion and Flame*, Vol. 157, No. 4, April 2010, pp. 632–640.

[141] Chen, H., Reuss, D. L., Hung, D. L., and Sick, V., "A practical guide for using proper orthogonal decomposition in engine research," *International Journal of Engine Research*, Vol. 14, No. 4, Aug. 2012, pp. 307–319.